Aix-Marseille Université

ED 353 – Sciences pour l'ingénieur : Mécanique, Physique, Micro et Nanoélectronique

Laboratoire de Mécanique et d'Acoustique -CNRS- UPR 7051

Thèse présentée pour obtenir le grade universitaire de docteur

Discipline : Sciences pour l'Ingénieur
Spécialité : Acoustique

Gaultier REAL

An ultrasonic testbench for reproducing the degradation of sonar performance in a fluctuating ocean

Thèse soutenue le 12 Novembre 2015, devant le jury composé de:

William A. KUPERMAN	MPL - SCRIPPS - UCSD	Rapporteur
Philippe BLANC-BENON	LMFA CNRS - UMR 5509	Rapporteur
Philippe ROUX	ISTerre CNRS - UMR 5275	Examinateur (Président du Jury)
Dominique FATTACCIOLI	DGA-TN	Examinateur
Xavier CRISTOL	Thales Underwater Systems	Invité
Jean-Pierre SESSAREGO	LMA CNRS - UPR 7051	Invité
Dominique HABAULT	LMA CNRS - UPR 7051	Directrice de thèse

Acknowledgements

A three-year work period is a fairly long time, and despite so much things have to be left undone, this dissertation represents a considerable achievement for me. Not only because of the results presented in this document, but also because of the great opportunities to meet and work with competent and remarkable people. Despite the non-linearity of the process, I am glad that I was able to work not with one, but with two thesis advisors. Therefore I would like to thank Dr. Jean-Pierre Sessarego for his constant kindness, his experimental skills and wisdom, and the way he always thought of his students before anything else. I am thankful for having had the chance to work under the guidance of Dr. Dominique Habault, my improvised second advisor. I could not have asked for a better alternative after Jean-Pierre retirement in his Corsica.

Sometimes, anodyne encounters are the ones that mark you the most. This is what happened to me a few years ago when I started an internship at the Délégation Générale pour l'Armement. This doctorate is the latest (and hopefully not the last) step of my collaboration with Dr. Dominique Fattaccioli. I am really grateful for everything you did for me, and I hope to be able to give it back to you in the next few years. *Grazie assai*.

I do not think I would have been able to present half to work shown in this document without the help and guidance of Dr. Xavier Cristol. Thank you for mentoring me in the paths of differential-integral equations with non-linear terms, and all the topics that gave me sleepless nights at the very start of the thesis. Thank you also for your genuine kindness and constant implication in this project.

It is truly an honor to count Dr. Philippe Blanc-Benon and Dr. William A. Kuperman as evaluators of my work. Thank you for accepting to be part of my thesis committee and for giving me your highly praised opinion on my research.
I also would like to thank Dr. Philippe Roux for being part of this thesis committee, with no hesitation whatsoever when I asked him. I feel extremely lucky to read your name on my manuscript as well.
Overall, I thank the jury for its wisdom, its implication and its remarks that strongly contributed to the quality of the present document.

Merci à tous ceux qui, de près ou de loin, ont pu m'aider lors de ma thèse, notamment pendant les mesures: Régine Guillermin et Guy Rabau pour votre implication hors du commun, Patrick Sanchez pour ton expertise (et pas uniquement en blagues toujours fines) ainsi que le Service d'Etudes et Réalisations Mécaniques, et spécialement Vincent Long.
Merci également à Thales Underwater Systems de m'avoir accueilli pendant cette thèse, je suis

en particulier très reconnaissant envers Bruno Chalindar.
Merci beaucoup à mes camarades brestois Julien Bonnel et Angélique Drémeau pour le dépannage de fin de thèse et leur accueil chaleureux à l'ENSTA (en attendant la prochaine tournée aux fauvettes).
Je glisse également un merci à Sylvain Cheinet, pour son intérêt pour mon travail et les discussions que nous avons pu partager.
Je tiens également à remercier mes précédents encadrants de Master's thesis à Florida Atlantic University, Pierre-Philippe Beaujean, dont les méthodes de travail m'ont menées où je suis et Pierre-Jean Bouvet, dont les précieux conseils me suivent encore aujourd'hui.

Merci à toutes les personnes du Laboratoire de Mécanique et d'Acoustique avec qui j'ai pu passer de bons moments. Je pense en priorité aux copains de bâtiment, le maître crépier Arnaud Guillou, le pongiste J-B Doc, Joël Piraux pour les débriefs olympiens, mais aussi à Etienne "Tit'Back" Thoret, à Vincent Moscato et Eric di Meco qui m'ont tellement accompagné que je les compte comme collègues de travail, à Quentin Mesnildrey, Soizic Terrien, Simon – au sens large- Conan, ... Merci aux camarades -entre autres- de Sodexo, Sabine Meunier, Michèle Laurent et la bande de chez PA. Un clin d'œil particulier à Jacques Chatron, dont les qualités humaines n'ont d'égales que les goûts culinaires, on dirait...

Un immense merci à mes amis pour avoir représenté de vraies bouffées d'oxygène tout au long de cette thèse. Merci à Anthony Prebiski, *fratellu* rugbystique et compagnon de galère(s) mais pas que, à Seb Barale, colocataire de fortune lors de mes passages à Sophia (en garde alternée avec Claire Foucault, que je remercie aussi en passant), à M. et Mme Gus pour les émotions, à Aurélie Dick et Benja "Désiré B." Contri (sans oublier Phrypucs) pour tous ces bons moments et à tous les autres que je n'oublie pas mais la liste serait trop longue.

J'en profite aussi pour remercier mes proches pour leur soutien sans faille et leurs attentions à mon égard, en particulier mes parents bienveillants Nathalie et Olivier, et ma petite sœur Olivia, au coeur aussi grand que son caractère est fort.

Enfin, Anaïs, comment ne pas terminer en t'adressant ces quelques mots. Merci de me supporter et de m'accompagner dans ma qualité de névrosé cynico-idéaliste. Merci de me faire redescendre sur terre dans les moments où j'en ai besoin et merci de me faire planer dans les autres. Merci pour tout ce qui est à venir aussi... *you're the best I never had*...

"Then he'd sit down and look across the water and when you looked across the water, everything was hard to believe."

Charles Bukowski, *A dollar and twenty cents.*

"Puis il s'asséyait et regardait l'océan, et quand on regarde l'océan, tout parait incroyable."

Charles Bukowski, *Un dollar and vingt cents.*

Contents

List of Figures

List of Tables

Abbreviations

ABS	**A**crylonitrile **B**utadiene **S**tyrene
CAD	**C**omputer **A**ider **D**esign
CIR	**C**hannel **I**mpulse **R**esponse
CPD	**C**omplex **P**ressure **D**istribution
CW	**C**ontinuous **W**ave
FS	**F**ull **S**aturation
GM	**G**arrett & **M**unk
IMF	**I**nterplanetary **M**agnetic **F**ield
IW	**I**nternal **W**aves
MBW	**M**achinable **B**lue **W**ax
MCF	**Mutual C**oherence **F**unction
MHD	**M**agneto**H**ydro**D**ynamic
NDT	**Non D**estructive **T**esting
PE	**P**arabolic **E**quation
PS	**P**artial **S**aturation
P3DCOM	**P**ropagation through **3D C**orresponding **O**cean
P3DTEx	**P**ropagation through **3D T**ank **Ex**periment
RAFAL	**R**andom **F**aced **A**coustic **L**ens
RayTAL	**Ray T**racing trhough an **A**coustic **L**ens
rms	**r**oot-**m**ean **s**quare
SOFAR	**SO**und **F**ixing **A**nd **R**anging
SNR	**S**ignal-to-**N**oise **R**atio
SSA	**S**mall **S**lope **A**pproximation
US	**U**n**S**aturation
VLA	**V**ertical **L**inear **A**rray **L**ens

WPRM	**W**ave **P**ropagation in **R**andom **M**edia

Main Symbols

a	parameter in an expression of Λ
b	intercorrelation parameter
c	sound speed in water
c_i	sound speed in medium i
c_0	mean sound speed in water
d	intercorrelation parameter
d^T	transducer/hydrophone diameter
dx	ray path
f	source center frequency
f_c	source center frequency in water tank
h_{ks}	Kolmogorov-Smirnov test output
$h_n(t)$	impulse response of $n-$th realization at time t
j^*	internal waves wavenumber
k_i	wavenumber in medium i
$\hat{k}_i$	approached wavenumber in medium i
l	discrete sensor spacing
m	acoustic log-intensity mean
n	realization index
$n_{x,y,z}$	number of steps in numerical code
$\boldsymbol{n}$	normal vector to Σ
p_i	acoustic pressure in medium i
q	intercorrelation parameter
r	inverse acoustic correlation length to wavelength ratio
$\hat{\mathbf{r}}$	set of estimated parameters
s	hydrophone vertical displacement amplitude

$s_n(t)$	source signal for the $n-$th realization at time t
s_h	scale of medium heterogeneities
s_u	normalized standard deviation of the ray divergence
t	time
x_{dist}	distance between RAFAL's average output face and receiver
x_f	distance between source and RAFAL's input face
x_m	signal model
$x_n(t)$	received signal at time t
x_t	test source abscissa
x_t^{max}	maximum test source abscissa
x_0	average RAFAL's output face abscissa
x_1	RAFAL's input face abscissa
x_2	RAFAL's average output face abscissa
z_t	test source depth
z_t^{max}	maximum test source depth
A_t	source signal amplitude
$A_{1,2}$	intercorrelation constant
B_{-xdB}	$-x\ dB$ flat frequency response
C	spatial intercorrelation function
C_0	spatial intercorrelation constant
C_2	spatial intercorrelation constant
C_4	intensity spatial intercorrelation
D	water depth
$D(s_1, s_2)$	phase-structure function between spacings s_1 and s_2
D_a	array depth
D_s	source depth
D_Z	hydrophone total vertical shift
D_Z^S	source total vertical shift
E_i	statistical expectation under hypothesis i
F_s	sampling frequency
G	deflection
G_i	Green's function in medium i
G_{Th}	theoretical array gain

H	RAFAL's thickness
H_0	Hankel's function
H_i	i–th hypothesis
$H_{x,y,z}$	size of considered box in numerical code
H_ℓ	size of the RAFAL
I	acoustic intensity
J_0	Bessel function
J_1	Bessel function of the first kind
K_i	wavevector in medium i
L_a	array length
L_H	horizontal correlation of the RAFAL's randomly rough output face
L_{H_s}	horizontal correlation of the sound speed fluctuations
L_V	vertical correlation of the RAFAL's randomly rough output face
L_{V_s}	vertical correlation of the sound speed fluctuations
L_x	longitudinal acoustic correlation length
L_y	horizontal acoustic correlation length
L_y^ℓ	horizontal acoustic correlation length in the lens case
L_z^ℓ	vertical acoustic correlation length in the lens case
$\bar{M}$	average maximum of detection algorithm output
N	number of sensors on a linear array
N_{eig}	number of eigenrays
$\mathcal{N}$	inverse ratio of the propagation range to the wavelength
$N_{h,v}$	normalized horizontal, vertical acoustic correlation length
N_p	number of periods in the source signal
N_r	number of realization per RAFAL
N_R	normalized propagation distance
N_{RAFAL}	number of manufactured RAFAL per configuration
N_S	number of segments
N_s	number of virtual sensors
N_{Snap}	number of noise snapshots
$\tilde{P}_i$	i algorithm output
R	propagation range
R_c	discrete radius of coherence

R_F	Fresnel radius
R_S	slit radius
$\mathbf{R_{xx}}$	signal spatial covariance
R_δ	autocorrelation function of sound speed fluctuations
R_ξ	autocorrelation function of random roughness
S	Sombrero function
SI	scintillation index
T	temperature
U	ray divergence
U_0	depth function for the sound speed profile
V_i	statistical variance under the hypothesis i
$\mathbf{V}_i$	i–th eigenvector
α	L_z parameter (=0.174)
β	beam spread projection diameter
γ	hydrophone sensitivity
$\delta(.)$	Dirac function
δ_c	sound speed deviation
δc_0	standard deviation of sound speed deviation
δAG	array gain degradation
δ_x	PE resolution step in numerical code
δ_x^ℓ	PE resolution step inside the RAFAL in numerical code
ϵ	vertical sensor displacement error
η	small horizontal displacement
κ	pressure field
λ	signal wavelength in ocean
λ_c	signal wavelength in water tank
λ_i	i–th eigen value
$\boldsymbol{\eta}$	eigenvector matrix
χ	pressure derivative
ν	normal vector on Σ
ρ	transducer radius
ρ_c	radius of coherence

σ	acoustic log-intensity standard deviation
σ_N^2	noise power
θ	source elevation angle
θ_{3dB}	half beam spread angle at $-3\ dB$
τ	source signal duration
τ_n	time delay for the $n-$th realization
μ	Fourier variable dual to z
ω	angular frequency
ζ	small vertical displacement
ζ_{IW}	displacement due to internal waves
ξ	amplitude of random roughness
ξ_0	standard deviation amplitude of random roughness
Γ	MCF
Δ_c	normalized sound speed fluctuations
Δ_{Z_s}	source depth shift
Λ	Flatté's diffraction parameter
Λ_ℓ	Flatté's diffraction parameter in the lens case
Π_i	Fourier transform of the acoustic pressure field
Φ	Flatté's strength parameter
Φ_ℓ	Flatté's strength parameter in the lens case
Φ_δ	cumulative autocorrelation function of sound speed fluctuations
Σ	rough surface profile

Chapter 1

Introduction and State of the Art

Contents

1.1 General objective

The topic of acoustic wave propagating in a fluctuating ocean is tackled in this thesis. The ocean medium is in constant motion, and cannot always be considered as the steady and *flat sea* described by Hemingway in "The Old Man and the Sea" (Hemingway 1963). The influence of the medium fluctuations on wave propagation has been of a great and constant interest over the last decades, in various domains, such as optics (Tatarskii 1971), electromagnetism, and acoustics (in air and water) (Dashen et al. 2010). We focus here on the effects inside the volume of the medium of propagation, and let aside the scattering arising from the roughness of the interfaces (for instance, an agitated sea surface, or a rough sea bottom). Internal waves were proven to be responsible for the sound speed deviations from the mean value observed in shallow and coastal waters (Garrett and Munk 1972). Due to the high complexity of the physical phenomena involved, the evaluation of the influence of the resulting fluctuations on acoustic wave propagation is challenging. The final objective of the work presented throughout this document is the ability for detection systems to compensate for the observed signal distortions.

Indeed, degradation of the detection performance is noticed when the signals travel through a fluctuating medium. The research for corrective signal processing techniques allowing to mitigate this result is therefore of primary interest. Spectacular results in terms of enhancement of the resolution have been observed in the field of adaptive optics applied to observational astronomy (Metchev et al. 2003). Their results are encouraging researchers to address this topic in other domains such as underwater acoustics. The studies presented throughout this thesis focus on configurations involving the propagation of acoustic waves in the mid-frequency band ($1 - 15\ kHz$) over distances of the order $1 - 10\ km$. The configurations of interest here are those presenting short times of propagation compared to the daily period of medium fluctuations so that the studied phenomena are considered spatially random but frozen in time.
The first main objective of this work is to provide an experimental protocol allowing, under laboratory conditions, to reproduce similar effects of ocean fluctuations due to internal waves on the propagated acoustic waves. Let us underline that a protocol allowing to mimic the induced typical statistical features of the received signals is sought out, rather than the reenactment of the phenomenon responsible for the signal distortions.
In order for the developed experimental protocol to provide results representative of what can be observed during at-sea measurements, a scaling procedure is necessary. Based on a dimensional analysis, it permits a direct scaled match between the configurations studied in a water tank and real scale oceanic cases.
The degradation of the existing detection techniques performance is also studied in this thesis, enhancing the idea that corrective signal processing methods are needed.

The work and the results presented here represent a way to reproduce the effects of complex physical phenomena on acoustic wave propagation using a simple scaled experimental scheme in a water tank. The possibility of this protocol to be a benchmark allowing to validate or discard corrective signal processing techniques is the main reason for this research.

A state of the art is proposed in section 1.2.1 to 1.4. The topic of wave propagation in random media (WPRM) has been tackled by many different scientific fields. Section 1.2.1 explores the way spatial and temporal fluctuations impact the propagation of optical, electromagnetic (essentially radio), and acoustic waves. If major differences are noted in practice in all these domains, the original problem is mainly analogous to what can be observed in a fluctuating ocean. The complexity of the physical phenomena motivated the development of scaled experiments in controlled and reproducible environments. Some examples are provided in section 1.3. One of the major reasons for the development of these protocols is the ability to test signal processing techniques allowing to compensate for the degradation of performance that they experience when medium fluctuations occur. The existing adaptive techniques are briefly presented in section 1.4 and discussed in further details in Chapter 6.
Finally, the contributions of the work presented here are provided in section 1.5, as well as the plan of the dissertation.

1.2 Wave propagation through random media

1.2.1 Transverse review

The study of WPRM is shared by many fields since media from very small scales (rocks, organic layers) to extremely large ones (interstellar medium) exhibit inhomogeneities that induce scattering of the propagating waves (Ishimaru 1978), due to local changes in index of refraction. The case of the ocean is treated in section 1.2.2 in terms of sources of fluctuations and description of the physical impact on the traveling of acoustic waves. We focus here on the analogous phenomena existing in the nature.

The propagation of ultrasonic waves as a diagnostic tool in order to image organic tissues to prevent or monitor the evolution of diseases is a relevant example. In fact, sound speed inhomogeneities are found in large organs such as the liver, or breast, inducing some distortions of the propagated wavefronts (Zhu and Steinberg 1992). The resolution of the images is hence limited by the capability to correctly describe the observed fluctuations. On the other hand, the measurement of a scattered wave may represent a way to reveal the presence of an anomaly. Similarly, ultrasonic wavefront distortions can be observed in non-destructive testing (NDT) of materials. However, the presence of a scatterer in the medium of propagation in this context is often the reason of the testing in the first place. In this case, the perturbation of the propagated wave is sought out, since it may hint an unwilling intrinsic characteristic of the material (e.g. anisotropy, cracks).

The earth interior is also an important source of inhomogeneities. Understanding the effect of the multi-scale heterogeneities is essential to interpret the behavior of seismic waves. As an example, the multiple scattering was recognized to be the source of the so-called coda (i.e. late arrivals of signals) (Aki 1980). Probing geological media therefore requires some statistical knowledge of the characteristics of the medium.

Optical scintillation due to atmospheric turbulence has been recognized as a limitating factor for the size and the resolution of telescopes (Newton 1704). Indeed, the index of refraction variations due to temperature fluctuations induce what is known as the "'twinkling" of stars. The Kolmogorov spectrum allowing to statistically describe turbulence was developed in this context (Kolmogorov 1941). The topic of optical scintillation due to atmospheric turbulence was theorized by Tatarskii (Tatarskii 1971). Figure 1.2 shows an example of the star twinkling:

FIGURE 1.1: Twinkling of a star. From NASA.

Vincent Van Gogh's painting *Starry Night* is perhaps the most famous representation of the phenomenon. In fact, the study of the statistics of the luminance of the painting showed that it described quite accurately the Kolmogorov spectrum of turbulence (Aragón et al. 2008).

FIGURE 1.2: *Starry Night* by Vincent Van Gogh. From *vangoghgallery.com*.

Other examples of WPRM can be found in engineering applications such as radio communications. It was indeed demonstrated that fluctuations in the ionosphere in terms of electron density were responsible for the scintillation of radio sources (Briggs and Parkin 1963, Buckley 1975). Rickett (Rickett 1977) also gathered information about the fluctuations in the interstellar plasma which cause distortions of radio waves from far radio sources, such as quasars and pulsars. The interstellar scattering is described in more details in (Rickett 1990), highlighting the limitations caused by this phenomenon. The analogy between this phenomenon and the topic of this dissertation is shown in figure 1.3:

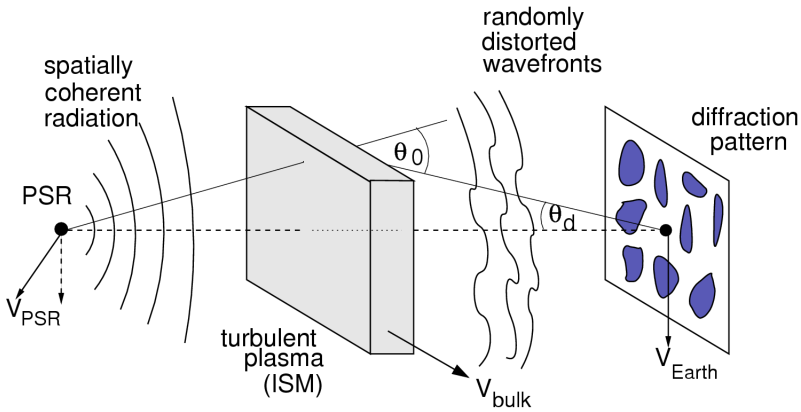

FIGURE 1.3: Schematic view of the wavefront distortion caused by interstellar plasma turbulence. From (Lorimer and Kramer 2005).

At interplanetary scale, solar wind is also considered to generate strong fluctuations leading to perturbations in the electromagnetic wave transmission. Magnetohydrodynamic (MHD) turbulence is, for example, caused by solar winds (Matthaeus and Goldstein 1982) which have also been proven to interact with interplanetary magnetic field (IMF) (Gosling et al. 1987, Zank 1999). Solar winds are also responsible for a well-known phenomenon, the appearance of *aurora borealis* (Dessler 1966).
All these examples emphasize the fluctuating aspect of any propagation medium. At all space and time scales, perturbations in the measurement environments are observed. The case of sound propagation through the ocean medium is not different, as presented in section 1.2.2.

1.2.2 Wave propagation in a random ocean

1.2.2.1 Sources of fluctuation

The ocean is in constant motion. Multiple physical phenomena contribute to the spatio-temporal variation of the world's oceans, from very large basin-scale heterogeinites, such as gyres, to small, meter-scale, turbulence. Driven by wind (Ekman transport) and the Coriolis effect, ocean gyres present a scale of the order of magnitude of the size of the ocean. Smaller events, such as eddies, are characterized by a diameter of 10 to 500 km and typical periods of days to months. Some examples of temperature and salinity heterogeneities induced by eddies are given in Tychensky and Carton (1998). The phenomenon of up-welling, of space and time scales up to respectively a few hundreds km and a few tens of days, is also well known to produce ocean temperature fluctuations. Tides are an example of non-wind driven event that cause ocean motion. In fact, the relationship between tides and the moon was raised by Pytheas as early as in the IVth century BC. A graphical representation of the space-time scale of the phenomena is proposed in Graham (1993)

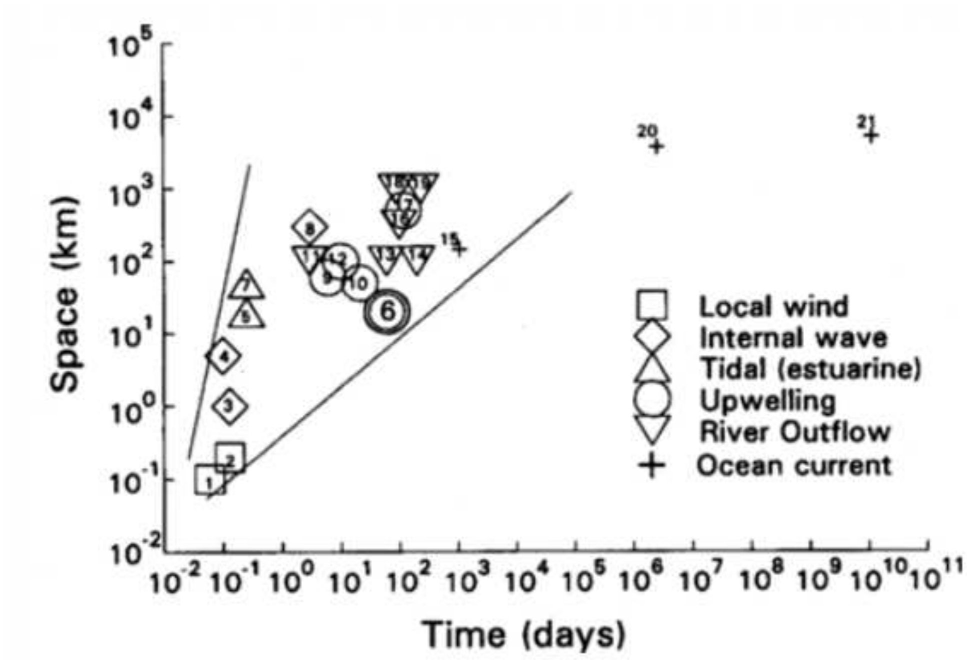

FIGURE 1.4: Space-time scale of some phenomena responsible for ocean fluctuations in northern Monterey Bay, California. From (Graham 1993).

However, these large-scale phenomena all present a quite long time period, which leads ocean engineering scientists to focus mainly on smaller-scale events such as those located in the bottom left corner of figure 1.4. For instance, the interactions of the propagated wave with the interfaces of the medium were proven to induce severe degradation in the signal coherence (Kuperman and Ingenito 1977, Kuperman and Schmidt 1989) when the interface is rough.

There is a tremendous amount of literature about the issue of scattering from rough surfaces, especially in the case of high-frequency acoustic waves interacting with an agitated sea surface. The studies conducted during World War II were extended by Eckart (Eckart 1953), where a theoretical analysis of the problem is provided. A comprehensive study of the ocean surface roughness and the associated model for sound propagation is presented in Marsh et al. (1961) and in Urick (1973). McDaniel (McDaniel 1993) also reviewed the topic of scattering from the sea surface, addressing it as a twofold problem: the scattering from the roughness of the surface and the volume attenuation due to the presence of bubbles or bubble layers and plumes. Statistical parameters such as the root-mean-square (rms) surface wave-height are classically used to describe the sea surface (Zhou et al. 2007). Statistical models for the sea surface can also be found, such as in Elfouhaily et al. (1997). The evaluation of the backscattering strength depends on the frequency of the signal since it involves the ratio between the acoustic wavelength and the surface rugosity. Several models are available in the literature, including the Chapman-Harris model for mid-frequencies (Chapman and Harris 1962), the Ogden-Erskine model for low frequencies (Ogden and Erskine 1992) and the Crowther model for high frequencies (Crowther 1980). The problem, overall, lies in the spatio-temporal dependence of the ocean channel impulse response (CIR), when the surface is agitated. The coherence time of such CIR, defined as the time during which the channel remains constant, can be as small as a few seconds (Li and Preisig 2007) which leads to a fading of the underwater acoustic channel response.

The roughness of the seabed is also a source of loss of coherence of acoustic signals propagated in the sea. Due to its extraordinary variability both in sediment nature and roughness, it is excruciatingly difficult to provide a model for the seabed. High-frequency signals show a high sensitivity to the grain size and Rayleigh scattering can be observed (Jackson et al. 1996). On the other hand, lower frequency signals penetrate inside the sea bottom and are therefore impacted by the internal burrowed geological structure. Similarly to what was presented for the sea surface agitation case, several models are used to evaluate the scattering strength of the rough seabed: for example, the formula proposed by DelBalzo (Leclere et al. 1997) is accurate for the 300 $Hz - 1.5\ kHz$ frequency band, whereas the Jackson model can be applied for waves around the 30 kHz center frequency (Jackson et al. 1986).

Besides the effects of ocean interfaces, an increasing interest is found in volume fluctuations. Especially, internal waves (IW) have been proven to induce spatial and temporal fluctuations in the sound speed distribution. In the early to mid 1970s, observations and analytical descriptions of the IW spectrum have been the subject of numerous studies (Boyce 1975, Garrett and Munk 1972; 1975, Munk and Zachariasen 1976, Desaubies 1976). The resulting model of these contributions is known as the GM model (for Garret and Munk model). The idea is to synthesize the available measurements of internal wave energy and to propose a model spectrum describing the variation of energy in terms of wavenumber (vertical and horizontal) and frequency. The internal wave energy per unit mass can therefore be expressed as a function of frequency ω and mode number j:

$$E_{GM}(\omega; j) = H^2 N_0 N(z) E_0 B(\omega) \lambda(j), \tag{1.1}$$

where $B(\omega) = \frac{2}{\pi}\frac{f^C}{\omega}\frac{1}{\sqrt{\omega^2-(f^C)^2}}$, $\lambda(j) = \frac{1}{j^2+j_*^2} \Big/ \sum_{j=1}^{\infty} \frac{1}{j^2+j_*^2}$. In the previous equations, for a typical ocean (Munk profile (Garrett and Munk 1972)) $E_0 = 6.10^{-5}\ J.m^{-2}$, the buoyancy frequency $N(z) = N_0 e^{(z-H)/H}$, where N_0 is the Brunt-Väisälä frequency (or buoyancy frequency), the SOFAR (SOund Fixing and Ranging) depth is $H = 1.3\ km$, f^C is the Coriolis parameter and $j_* = 3$.

Besides the GM model, qualitative descriptions of the sound field fluctuations induced by IW were provided in Munk and Zachariasen (1976). Waveguide invariant studies also allowed to relate the medium fluctuations to the phase and group velocities of the propagated wave (Kuperman et al. 2012, Roux et al. 2013). Ocean acoustic tomography was proven to provide spatial and temporal measurements on the temperature fluctuations due to IW at ultrasonic scale as well (Roux et al. 2011).

The ratio between vertical and horizontal fluctuations due to internal waves is found to be approximately 10, which imparts to the sound speed fluctuations field an anisotropic behavior. Internal waves are also found to be the main source at the origin of volume inhomogeneities, over cycles as long as hours or days (Kuperman and Lynch 2004). They are predominant with respect to meter-scale turbulence (Levine and Irish 1981). Various at-sea measurements demonstrate the influence of internal waves on acoustic wave propagation. Section 1.2.2.2 shows how such fluctuations impact the formulation of the wave equation and the way some classical theories can tackle this issue. The range dependency of the sound speed is illustrated by the measurements presented in Rouseff et al. (2002)

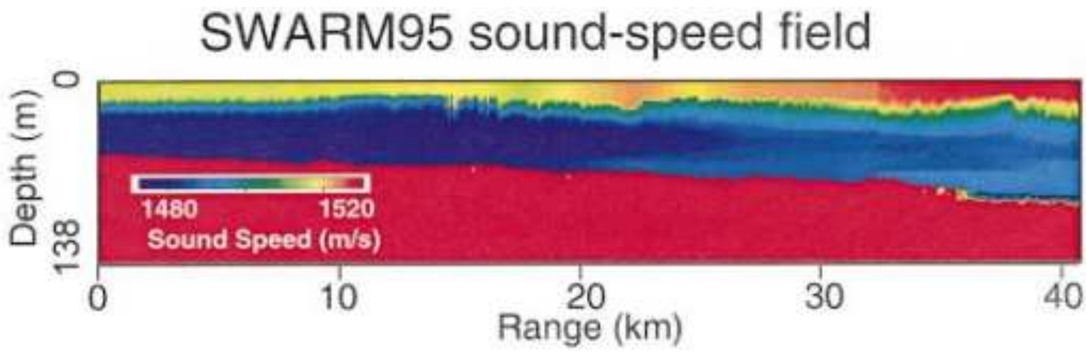

FIGURE 1.5: Sound speed field reconstructed using measurements carried out during the SWARM95 experiment. From (Rouseff et al. 2002).

Other examples of field measurements and the corresponding data processing are given in the following sections.

1.2.2.2 Effects on wave propagation

Propagation of sound in the ocean is governed by the wave equation:

$$\Delta^2 p = \frac{1}{c^2}\frac{\partial^2 p}{\partial t^2}, \tag{1.2}$$

and its time-independent version, the Helmholtz equation:

$$\left(\Delta + k^2\right) p = S, \tag{1.3}$$

where $k = \omega/c$ and S denotes the source term (classically either an initially plane wave or a point source). Sommerfeld conditions are usually considered (Sommerfeld 1912), as well as pressure release conditions at the surface, such that $p\,(x, y, z = 0) = 0$ and continuity conditions at the bottom:

$$\begin{cases} p = p_b \\ \rho^{-1}\partial p/\partial z = \rho_b^{-1}\partial p_b/\partial z \end{cases} \tag{1.4}$$

In the case of propagation through internal waves, fluctuations of the space distribution of sound speed are observed. Thus, c can be written as (Dashen et al. 2010)

$$c(\mathbf{x},t) = c_0\left(z\right) + \delta c(\mathbf{x},t), \tag{1.5}$$

where c_0 is the deterministic mean sound speed profile and $\delta c(\mathbf{x},t)$ is the internal wave-induced sound speed fluctuation term. In practice, $\delta c(\mathbf{x},t)$ is related to the magnitude of the displacement due to internal waves, noted $\zeta_{IW}(\mathbf{x},t)$, so that:

$$\delta c(\mathbf{x},t) = \left[\partial_z U_0\left(z\right)\right]_p \zeta_{IW}(\mathbf{x},t), \tag{1.6}$$

where $\left[\partial_z U_0\left(z\right)\right]_p$ is the fractional gradient of the sound speed profile (with the pressure effect removed) (Flatté 2002).

The Helmholtz equation is classically solved using either ray theory (high frequency hypothesis), or normal modes theory (low-frequency hypothesis), when the configuration studied is "range-independent" (Jensen et al. 2011). In the case of an ocean medium perturbed by internal waves, the dependence in range appears in the term $\delta c(\mathbf{x},t)$. Therefore, the range-dependent Helmholtz equation is solved using either, in the high-frequency case, ray theory taking into account the effects of the sound speed fluctuations (Esswein and Flatté 1980; 1981), or, in the low-frequency case, coupled mode theory (Evans 1983). Nevertheless, strong limitations of these techniques are observed: in fact, ray theory fails near caustics and shadow zones induced by sound speed fluctuations (Flatté and Rovner 2000), and mode theory is too expensive in terms of numerical calculations at high frequencies, since the number of modes becomes very important.

An efficient way to tackle the middle-frequency band ($100\ Hz - 10\ kHz$) is the parabolic equation (PE) (Jensen et al. 2011). Based on the two main hypotheses of weak fluctuations of the medium and narrow-angle propagation, the parabolic equation was applied to optical wave propagation through weak turbulence (Tatarskii 1971) and allows to perform a step-by-step solving with a given initial condition (Flatté and Tappert 1975, Dashen et al. 2010). This procedure is valid because of the first order derivative in distance of propagation presented by the standard PE. It was shown otherwise in Flatté and Vera (2003) that full wave equations are not necessary to accurately describe the influence of IW on underwater acoustic propagation. The radiation transport equation was also used in order to extend PE methods to higher frequency cases (Wilson and Tappert 1979). Analytical solutions for the parabolic equation in a randomly fluctuating ocean have also been proposed, using Rytov's method particularly (Munk and Zachariasen 1976). Path-integral techniques can also be used to solve the standard parabolic equation (Dashen et al. 1985).

An *a priori* qualitative characterization of the acoustic field using dimensional parameters is classically used in WPRM (Wolf 1975) and its most spread version in underwater acoustic was developed by Flatté (Dashen et al. 2010). In this case, the dimensional parameters are

- the *strength* parameter, Φ, which characterizes the amplitude of the acoustic field distortions. In the geometrical limit, it is defined as the standard deviation of the random phase fluctuations of the signal.
- the *diffraction* parameter, Λ, which characterizes the qualitative nature of the distortions.

Regimes of fluctuations are then defined, depending on the values of Λ and Φ, as depicted by figure 1.6, in the case of a single-scale medium:

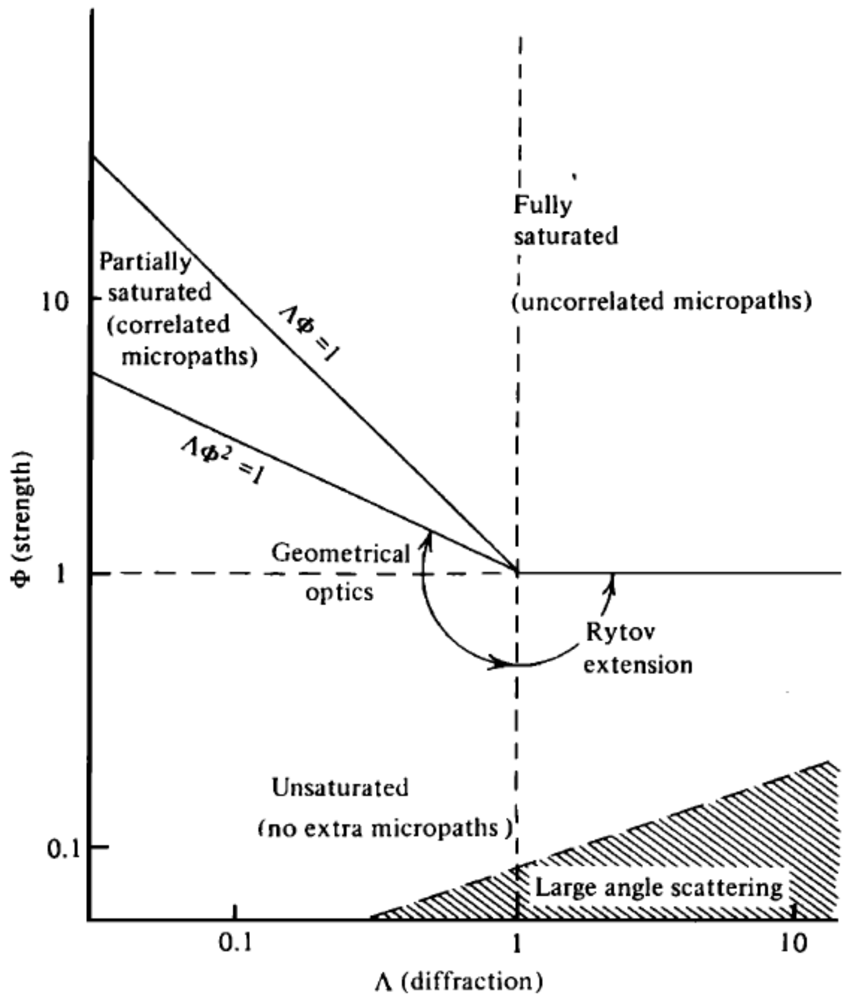

FIGURE 1.6: Λ-Φ plane. From (Dashen et al. 2010).

If $\Lambda >> 1$ and $\Phi < 1$, the Rytov approximation can be applied, which means that the pressure field may be approached using a perturbation expansion. When $\Lambda < 1$ and $\Phi \approx 1$, a single eigenray occurs, exhibiting a small displacement in vertical correlation length: this is the unsaturated regime. The configuration were $\Phi > 1$ and $\Phi^2\Lambda > 1$ is called partial saturation. The eigenray splits into multiple well-correlated eigenrays. Finally, if $\Phi > 1$ and $\Phi\Lambda > 1$, the eigenray splits into uncorrelated eigenpaths. The appearance of caustics and shadow zones is characteristic of the saturation. Physically, the unsaturated case corresponds to configurations where weak fluctuations occur at short ranges of propagation, and the saturated regime correspond to cases where strong fluctuations or long range propagation occurs. The boundaries between the various regimes of fluctuations should not be considered as strict delimiters, since their domain of validity may overlap. They are used in the present manuscript in order to provide qualitative information about the signals propagated through fluctuating media and they should not be taken as absolute predictions. Examples of the interpretation of the images resulting from atmospheric turbulence in terms of regimes of fluctuation can also be found, such as shown in figure 1.7 (Texereau 1948):

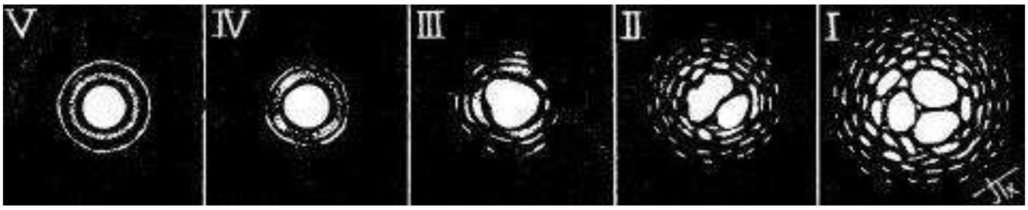

FIGURE 1.7: Evolution of an image at the output of a telescope in presence of very calm atmosphere (V), calm atmosphere (IV), agitated atmosphere -or unsaturation- (III), strongly agitated atmosphere -or partial saturation- (II), and very strongly agitated atmosphere - or full saturation- (I). From (Texereau 1948)

Most of the published materials focus on the calculation of the moments of the acoustic field, since derivations and predictions of the detailed realization of the pressure field in a complex random environment itself seem unreasonable and deprived of interest. Statistics of the pressure field propagated through IW have been provided, using the various theories described earlier. For example, path-integral resolution of the parabolic equation was used to derive expressions for the mutual coherence function (MCF), second-order moment of the sound pressure, noted Γ. The spatial MCF was therefore approximated as follows in Esswein and Flatté (1980)

$$\Gamma\left(\Delta s\right) \approx e^{-\frac{1}{2}D(\Delta s)} \tag{1.7}$$

where Δs denotes the spacing between two sensors and $D\left(\Delta s\right)$ is the phase-structure function, defined in (Dashen et al. 2010). It was shown in Flatté (2002) that the second-order moment for changes in depth could be expressed as a Gaussian function, i.e. a quadratic form for the phase-structure function:

$$\Gamma\left(\Delta s\right) \approx e^{-\frac{1}{2}\left(\frac{\Delta s}{\rho_c}\right)^2} \tag{1.8}$$

where ρ_c denotes the radius of coherence, defined in Carey (1998) as the sensor spacing for which $\Gamma(\rho_c) = e^{-\frac{1}{2}}$.

The measurement and the modeling of the loss of spatial (horizontal and vertical) and temporal coherence were extensively investigated using path-integral methods (Flatté and Stoughton 1988, Flatté and Vera 2003, Yang 2008), coupled and adiabatic modes (Voronovich and Ostashev 2006), transport theory (Colosi et al. 2013, Chandrayadula et al. 2013) and numerical PE codes (Tielbürger et al. 1997, Oba and Finette 2002, Flatté 2002, Vera 2007). Alternative methods, such as polynomial chaos, can also be found (Finette 2006, Creamer 2006). Combinations of horizontal ray theory and vertical mode theory is also used (Badiey et al. 2005) in order to characterize the variation of acoustic intensity. This last method is used to cope with the strong anisotropy of the sound speed fluctuations induced by internal waves. The statistical distribution of the acoustic pressure field (Dashen et al. 2010) and intensity (Flatté et al. 1987, Colosi et al. 2001) are also of great interest, since it was shown in these papers that a discrimination between the regimes of fluctuations was possible from the analysis of these quantities.
The direct link between WPRM and the limitation and degradation of the array gain was studied in Laval and Labasque (1981), Carey (1998). This means that the fluctuations of the propagating medium have to be considered in the design of sonar arrays, especially in the case of large arrays. In an ocean perturbed by internal waves, horizontal coherence lengths of 10 to 100 wavelengths and vertical coherence lengths less than 10 wavelengths are found (Gorodetskaya et al. 1999). It is nonetheless difficult to anticipate for the degradation solely caused by the effect of internal waves, since at-sea measurements involved numerous phenomena concurrently, including surface and bottom scattering, distortions of the array and dispersion of sensors properties. The development of signal processing techniques in order to mitigate the detection gain degradation is hence limited to numerical configurations. Could scaled experiment performed in a controlled and reproducible manner emulate the array gain degradation due to fluctuations in the ocean ? We will try to answer this question throughout the present document. Section 1.3 investigate the emulators of WPRM in various domains, mainly in optics.

1.3 Emulators of WPRM

Due to the tremendous complexity of the phenomena described in section 1.2.1, researchers found an interest in trying to reproduce the physical phenomena, or their impact on wave propagation, in controlled environments. We present here the main motivations behind these developments of scaled experimental protocols, and we provide examples in various domains of physics.

1.3.1 Motivations

The numerous phenomena concurrently involved in measurements of WPRM induces uncertainties on the quantification of the influence of the phenomenon of interest. For example, in the case of fluctuations of acoustic signals propagated in an ocean perturbed by IW, it is difficult to evaluate the influence of the process studied with respect to other sources of fluctuations (listed in section 1.2.2). Moreover, models describing extremely complicated phenomena such as IW are based on at-sea measurements involving high costs. A (cheap) way to isolate the involved phenomena and quantify its influence on wave propagation and signal processing represents therefore a strong interest. This can be performed in controlled environments, such as water tanks, where the development of a reproducible protocol allowing to acquire acoustic data perturbed in a similar fashion to what can be observed in the ocean is possible. The question is now to give a more accurate meaning to the word "similar".
The ability to work with acoustic data acquired in controlled environments represents a way to benchmark signal processing techniques developed in order to mitigate the loss of coherence of the signals. This procedure can also be performed using numerical models as well, but we see a vivid interest in being able to compare the results with experimental data.
Several fields related to WPRM were investigated using a comparable approach. A non-exhaustive review is given in the following section.

1.3.2 Existing protocols

In the 1960s, the fluctuations of high frequency sound waves traveling through temperature microstructure were investigated in water tanks under laboratory conditions. The range-dependence of the coefficient of variation was studied in (Stone and Mintzer 1962; 1965), where sound pulses were propagated in a water tank heated from below. The time dependence of ultrasonic waves amplitude was measured using a similar protocol (Campanella and Favret 1969). The frequency-dependence of this phenomenon is presented in LaCasce Jr et al. (1962). Transverse spatial correlations close to the definition of the coherence function described earlier were provided in Sederowitz and Favret (1969). In 1979, Chotiros and Smith (Chotiros and Smith 1979) compared measurements under similar conditions to theoretical description of turbulence (Tatarskii 1971). In his Ph.D. dissertation, Dobbins summarizes the results presented in these papers (Dobbins 1989). The measurement of the effect of turbulence in the propagation medium of ultrasonic waves was enhanced in Blanc-Benon and Juvé (1993), where the experiment was conducted in air instead of water tanks, avoiding the appearance of air bubbles, possibly responsible for a bias in the analysis of the measurements. A classification of the experimental configuration in terms of regimes of fluctuations is proposed, as well as an analysis of the intensity distribution, whose shape is characteristic of the associated regime of fluctuations.
All these protocols provided interesting results and explored the path of scaled experiments to reproduce larger scale phenomena, but our approach is somewhat different in the sense

that the induced fluctuations must resemble that of the process of interest here. For instance, the subject of the work presented here, propagation in an ocean perturbed by internal waves, is characterized by a strong anisotropy in the sound speed distribution. In our opinion, this property is not achievable following the protocols presented in the previous paragraph.
Another way to produce distortions of the propagated waves is therefore needed. In 1985, Booker (Booker et al. 1985) studied the non-intuitive representativeness of perturbations induced by an almost-2D rough phase screen, compared to those induced by an extended 3D fluctuating medium. This analysis was applied successfully to directive Gaussian beams in Andrews et al. (1997), with the conclusion that such protocols may be representative of extended medium configurations, under some specific conditions, such as the continuity in rms phase fluctuations in the two cases. We see a vivid interest in combining this observation with Flatté's dimensional analysis in order to provide an experimental protocol using a manufactured product, characterized by a few statistical parameters, to reproduce the effects of 3D propagation in a fluctuating medium. The induced sequences of perturbed medium measurements would hence be perfectly controlled and reproducible.
Numerous examples of this type of laboratory experiments are available in the field of optics. Phase screens emulating the turbulence in the atmosphere are used in order to validate or discard some adaptive optics procedures allowing to mitigate the effects of the fluctuations of the medium on optical waves propagation. The analogy between this approach and our objectives is straightforward. Systems involving liquid crystal light modulator (Wilcox et al. 2007), oil-filled (Rhoadarmer et al. 2001) or spray-filled phase plates (Rampy et al. 2012), computer-generated holography (Neil et al. 1998), optical glass and near-index matching polymer (Mantravadi et al. 2004) and surface-etched phase screens (Hippler et al. 2006) were studied, leading to considerable progress in the development of adaptive optics. The dynamic aspect of atmospheric turbulence is also studied in protocols involving rotating single or double phase plates (Petit et al. 2011).

1.4 Corrective Signal Processing

The distortions of the wavefront due to fluctuations of the medium of propagation degrade the performance of detection and localization of the source. Nevertheless, this assessment is not inevitable, and efforts have been made in the last decades to develop corrective processing techniques allowing to compensate for the effects related to environmental fluctuations.

The fluctuations of the medium of propagation can cause the detection of a source of interest to be impossible. The degradation of array gain due to the loss of signal coherence was investigated in Cox (1973a), where the main source of distortions was believed to be the unknown deviations of hydrophone location along the array. Other examples (Ancey 1973, Laval and Labasque 1981, Wilson 1998) show that the gain of an array is strongly dependent on the coherence function. Degradation of array gain due to internal waves effects were studied by Carey (Carey 1998) and (Gorodetskaya et al. 1999), enhancing on the fact that underwater acoustic scenarios often involved very low signal-to-noise ratios (SNRs), which may make the detection performance degradation critical. In other domains, such as optics or medical imaging, the main issue lies in the resolution of the output image produced by the processing. This issue may be considered as secondary in the case of underwater acoustics, since the detection problem is the main source of interest, but we can nonetheless imagine successive signal processing techniques allowing to address firstly the issue of detection and, in a second time, localization of acoustic sources of interest (direction of arrival, range). A detailed, but non-exhaustive review of the main existing corrective signal processing techniques is given in Chapter 6. The methods covered in this chapter include practical techniques arising from the adaptive optics community, more theoretical techniques based on the optimal filter, robust time-reversal methods, medical imaging corrective techniques, more original and, at first glance, unlikely successful techniques, such as speckle imaging (Labeyrie 1970) and lucky imaging (Hufnagel 1966, Fried 1966). We also explain why the techniques presenting the highest potential of applicability in the case of underwater acoustic wavefront distortion are the methods based on the incoherent combination of sub-arrays and the techniques arising from radio wave studies (Jin and Friedlander 2004, Lee et al. 2008).

1.5 Thesis Content

A scaled experiment in a water tank allowing to reproduce the impact of random ocean fluctuations on acoustic wave is described in this dissertation. Presented in Real et al. (2014b), the experimental scheme consists in transmitting an ultrasonic wave through an acoustic lens consisting of a plane input face and a randomly rough output face, called RAFAL (RAndom Faced Acoustic Lens).

A scaling procedure ensures the representativeness of the experimental configuration: the dimensional analysis *a priori* predicts typical features of the received signal based on the evaluation of Flatté's parameters and the acoustic correlation length. The analytical calculation of the acoustic pressure field propagated through the RAFAL is provided following approximations detailed and justified throughout the document. Especially, a comparison between the statistical moments (of order 1, 2 and 4) of the pressure field in the cases of a confined perturbation and of an extended 3D fluctuating medium is given.

The results obtained following the developed scaled experimental protocol are analyzed, emphasizing on the validity of the predictions in terms of regime of fluctuations. The distribution of the complex pressure and acoustic intensity, as well as the spatial mutual coherence function are investigated for all the configurations studied.

The influence of the distortions of the acoustic signals acquired in the water tank on the detection capability of classically used array beamforming techniques is studied. These techniques are proven to exhibit strong degradation in terms of detection performance. The existing corrective signal processing techniques are presented and the methods showing, in our opinion, the highest potential are listed. Finally, a description and an analysis of an at-sea measurement campaign is described and compared to the results obtained in the laboratory experiment.

The present document is organized as follows:
Chapter 2 presents the scaling procedure based on a dimensional analysis in order to ensure the representativeness of the presented experimental protocol.
This protocol is detailed in Chapter 3, where the measurements are described.
The results associated with the data acquired in the water tank are analyzed in Chapter 4. A statistical analysis of the studied configurations is proposed, in terms of distribution of the complex pressure and acoustic intensity, as well as MCF investigation.
The degradation of detection performance using classical techniques is investigated in Chapter 5, where a detailed review of the corrective signal processing techniques is also provided.
Chapter 6 focuses on a glimpse of results obtained during an at-sea campaign.

Concluding remarks and ideas for future work are given in the final chapter.

Chapter 2

Dimensional Analysis

Contents

2.1 Introduction

In order to provide a reliable and meaningful analogy between various configurations involving wave propagation through random media and in an artificial, small scale facility, a way to analyze the involved physical phenomena is needed. Since a large variability of the environmental conditions is observed in this field of study (in terms of signal frequency, propagation range and, of course, environmental parameters related to the fluctuations of the medium), the use of an as-small-as-possible set of dimensional parameters should help sorting out different configurations. Moreover, it is frequent, in WPRM, to characterize *a priori* the qualitative properties of the propagated acoustic field in terms of such dimensional parameters. As an example, in geophysics, the scattering regimes are often displayed as functions of the normalized distance R/s_h and the product $k_0 s_h$, where R is the propagation distance, s_h is the scale length of the heterogeneities and k_0 is the wavenumber (Wu and Aki 1988). In ocean acoustics, the Λ-Φ plane defined by Flatté (Dashen et al. 2010) is used to sort out various oceanic configurations into regimes of fluctuations presenting typical features. This particularly pertinent dimensional analysis was presented in Chapter 1 and is detailed in section 2.2.1.

In Booker et al. (1985), a comparison between the fourth-order moments (scintillation index and intensity correlation function) in the extended fluctuating medium configuration and through two thin phase screens setups (ten times and a hundred times smaller than the propagation distance) is proposed. The two configurations are comparable when the same value of rms phase fluctuation is ensured, for example by tuning the fluctuations to be ten times stronger in the first phase screen case. A condition for the position of the phase screen is given: the best match is found for central position between the source and the receiver. A continuity in terms of ratio of the Fresnel radius to the scale of fluctuations is also required (Booker et al. 1985, Andrews et al. 1997).

We propose an adaptation of this work using Flatté's dimensional analysis. The rms phase fluctuations in the "natural" 3D case and in the "artificial" almost-2D setup are set to be equal using the strength parameter Φ. In our case, the "artificial" almost-2D setup consists in an acoustic lens presenting a plane input face and a randomly rough output face. It is denoted RAFAL, as said in Chapter 1. A continuity in the diffraction parameter Λ - analogous to the ratio of the Fresnel radius to the scale of fluctuations - is also proposed in our scheme. The fluctuations intensity are tuned in order to retrieve the same statistical behavior of the propagated wave by adjusting the parameters of the roughness of the output face of the lens. Distortions resembling those observed in an extended fluctuating medium are therefore induced.
Most of the bulk consists in carrying out statistical studies for the propagated wave (order 1 for the mean field, order 2 for the coherence and order 4 for the intensity fluctuations). Analytical evaluations of the first and second-order moments both in the "natural" and "artifical" configurations are proposed in this chapter. In particular, it allows us to equate the acoustic correlation lengths (normalized with the wavelength) in both cases.

An analytical expression of the fourth-order moment is proposed in Appendix A and it is found to be very similar in the extended medium case and in the locally perturbed setup.

The link between the moments equations and Flatté's typology and classification into regimes of fluctuations is confirmed in Appendix B. The analytical expression of the mean number of eigenrays $< N_{eig} >$ as a function of the normalized standard deviation of the ray divergence, $s_u = \sigma_u / < U >$, is proposed, based on the resolution of the PE applied to the Fourier transforms of the second and fourth-order moments of the acoustic pressure field. The evidence of the existence of three distinct regimes of fluctuations is underlined by the behavior of $< N_{eig} >$ in figure B.2.

Our objective is twofold:

1. we first want to guarantee the consistency between our scaled experiment and a realistic ocean configuration in terms of regimes of fluctuations in the Λ-Φ plane. To do so, expressions for the strength and the diffraction parameters in our experimental protocol configuration are required. The calculations leading to these expressions are detailed in this chapter (section 2.4.1 for the strength parameter and 2.5 for the diffraction parameter);

2. the other dimensional parameter involved in our analysis is the ratio of acoustic correlation lengths (either in the horizontal or in the vertical direction) to the acoustic wavelength L_y/λ and L_z/λ. This ratio was proven to be fully characterized by the properties of sound speed fluctuations in an ocean medium perturbed by internal waves type fluctuations (Fattaccioli et al. 2009) based on the calculations in Tatarskii (1971). Equating L_y/λ and L_z/λ in our scaled experimental case and in an ocean configuration would ensure the agreement between the second-order moment of the acoustic pressure. The derivation of L_z/λ, based on the analytical evaluation of the second-order moment and its radius of curvature, is given in section 2.4.2. The radius of curvature is the radius of the circular arc fitting the second-order moment at his maximum. Since Gaussian statistics are used, it corresponds to the typical scale of the second-order moment, as depicted by figure 2.3.

The "natural" and "artificial" configurations will be considered as analogous or equivalent if these three characteristic parameters are equal. Our final conclusion will be that this three-parameter-set seems to be enough for ensuring analogy, when considering qualitative structure and moments up to the order 4.

2.2 Characteristic parameters in the "natural" oceanic case

We first present the calculations leading to the three quantities described in the introduction of this chapter. The calculations presented here are dedicated to their evaluations in the case of a fluctuating ocean.

2.2.1 Flatté's dimensional analysis

Introduced by Wolf (Wolf 1975) and widely popularized by Flatté (Dashen et al. 2010), the dimensional analysis allows to classify the signal distortions into qualitative regimes of fluctuations. In fact, the measure of the decorrelation induced by medium fluctuations is not sufficient to fully understand the underlying mechanisms leading to the loss of signal coherence, or to the appearance of uncorrelated multipath propagation. For wavelengths smaller than the typical size of inhomogeneities, the so-called regimes of fluctuations are separated into three types:

- (A) the unsaturated regime, where phase fluctuations mostly arise from the medium inhomogeneities;
- (B) the partially saturated regime, where correlated multipath propagation may be observed ;
- (C) the fully saturated regime, where uncorrelated eigenrays are observed.

For the same given value of L_z/λ, any of the three regimes is possible. Figure 2.1 depicts the three regimes of fluctuations in a schematic way, using ray theory, such as in Flatte (1983):

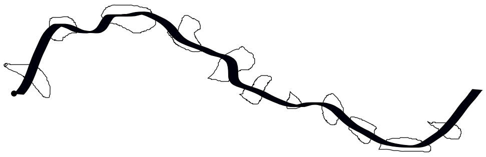

(A) Unsaturation.

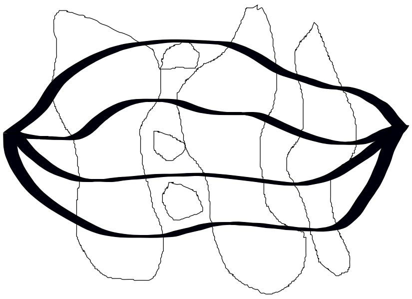

(B) Partial Saturation.

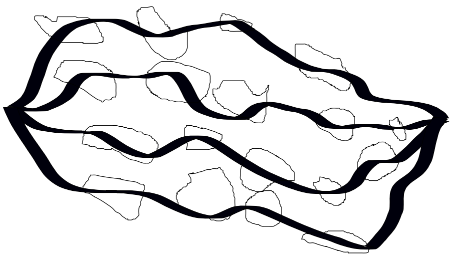

(C) Full Saturation.

FIGURE 2.1: Ray splitting due to celerity inhomogeneities in the medium of propagation: comparison between schematic behavior in the saturated and unsaturated regimes. Adapted from (Flatte 1983)

In order to sort out experimental configurations into a given regime of fluctuation, two dimensional parameters were defined (Wolf 1975, Dashen et al. 2010). First, the strength parameter, denoted Φ, accounts, in the geometrical limit, for the variance of the phase of the received signal. It is defined as follows:

$$\Phi^2 = k_0^2 \int_0^R dx \int_{-\infty}^{\infty} R_\delta \left(u \right) du \tag{2.1}$$

where k_0 is the wave number in water, R is the range of propagation and R_δ is the sound speed fluctuations intercorrelation function. The integral is performed along a ray dx, following the *path integral* terminology (Dashen et al. 2010). Assuming a Gaussian shape for the sound speed fluctuations intercorrelation, the strength parameter can be approximated with the following formula:

$$\Phi^2 \approx k_0^2 \sqrt{2\pi} \left(\frac{\delta c_0}{c_0} \right)^2 L_{H_s} R \tag{2.2}$$

where δc_0 is the standard deviation of the sound speed fluctuations amplitude and L_{H_s} is their horizontal correlation length.
The other dimensional parameter is the diffraction parameter Λ. It allows to evaluate how widely the signal fluctuations are spread by comparing the vertical correlation length of the sound speed inhomogeneities to the Fresnel radius R_F. Λ is defined as:

$$\Lambda = \frac{1}{R} \int_0^R dx \frac{1}{2\pi} \left(\frac{R_F(x)}{L_{V_s}} \right)^2 \tag{2.3}$$

The diffraction parameter can be approximated as:

$$\Lambda \approx \frac{R}{a k_0 L_{V_s}^2} \tag{2.4}$$

where $a = 2$ for a plane wave or $a = 6$ for a point source. L_{V_s} is the sound speed fluctuations vertical correlation length.

Interpretations and alternative definitions of dimensional parameters in terms of number of eigenrays are given in Appendix B.
Especially, the statistical distribution of the complex acoustic pressure and intensity can be related to the behaviors of rays in the various regimes. Figure 2.2 depicts the travel of rays transmitted through a fluctuating medium in different configurations. The depth of ray Z_R is displayed as a function of the distance x and the launch angle θ_0.

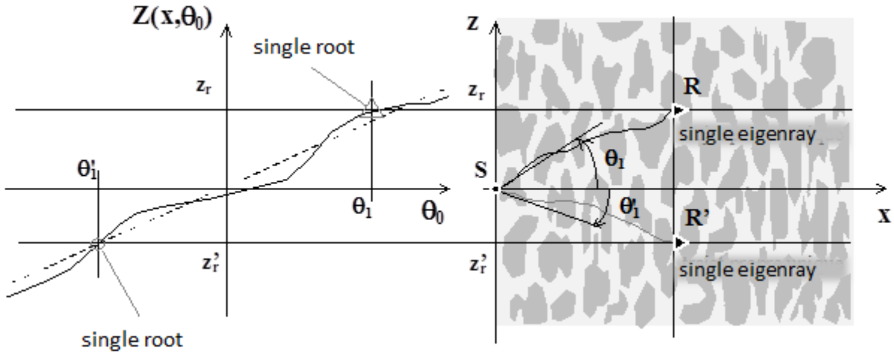

(A) Unsaturation.

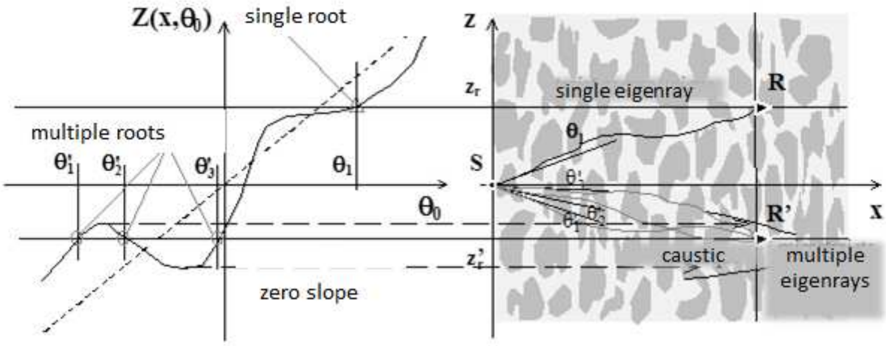

(B) Partial saturation.

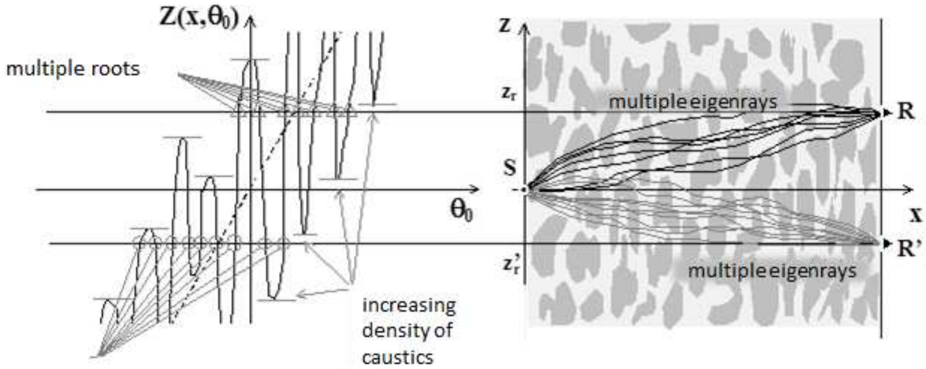

(C) Full saturation.

FIGURE 2.2: Rays behavior in the various regimes of fluctuations. From (Cristol 1996).

In figure 2.2a, small deviations from the unperturbed ray trajectory are noticed. In this unsaturated regime, a perturbation expansion around the mean value can describe the acoustic pressure or the acoustic intensity. The probability density functions (pdf) of these two quantities should therefore be centered around their mean values. As the saturation increases (figures 2.2b and 2.2c), multiple roots of the equation $Z(x_R, \theta_0) = z_R$ can be found, leading to multiple eigen rays. The zero-slope points appear frequently in the fully saturated regime, leading to a strong concentration of zeros in the pdf of acoustic pressure and intensity.

These qualitative physical analyses of the problem will be verified in Chapter 4, where the pdf of complex pressure and intensity are computed for measured and simulated data.

2.2.2 Acoustic field correlation length

For the sake of simplicity and readability, the calculations carried out throughout this section are presented in 2D. Conceptually, they can easily be extended to 3D, but at a high cost in terms of notations and readability. In order to characterize the loss of coherence of the acoustic signals, the evaluation of the acoustic correlation length is essential. It provides the quantitative information about the size of the random fluctuations of the pressure field and complete the qualitative examination performed with Flatté's dimensional analysis.

In Fattaccioli et al. (2009) (following results developed in Tatarskii (1971)), for the case of a fluctuating ocean, the correlation lengths of the acoustic fields in both transverse directions, denoted here L_y and L_z, are related to the acoustic wavelength. In the case of a statistically random homogeneous medium and a point source, an approximation can be analytically calculated for the intercorrelation of the sound field. The intercorrelation of the fluctuations of the sound speed is assumed to be a Gaussian function :

$$R_\delta(\eta,\zeta) = \left\langle \delta c\left(x-\eta/2, z-\zeta/2\right)\ \delta c\left(x+\eta/2, z+\zeta/2\right)\right\rangle \approx \frac{4\delta c_0^2}{c_0^2}\ e^{-\frac{\eta^2}{2L_{H_s}^2}}\ e^{-\frac{\zeta^2}{2L_{V_s}^2}} \tag{2.5}$$

where $\delta_c = c - c_0$. The terms L_{H_s} and L_{V_s} are the correlation lengths of the sound velocity in horizontal and vertical directions. According to (Tatarskii 1971), the acoustic fluctuations only depend on the cumulative effect of the variations of the medium. The so-called δ–correlation approximation leads to the following definition for the cumulative autocorrelation of the sound speed fluctuations, underlining the fact that the sole dependence on ζ remains:

$$\Phi_\delta(\zeta) = \int_{\infty}^{\infty} R_\delta(\eta,\zeta)d\eta \tag{2.6}$$

The transverse intercorrelation function of the sound field is defined by :

$$C(x,z,\zeta) = \left\langle p(x,z-\zeta/2)p^*(x,z+\zeta/2)\right\rangle \tag{2.7}$$

It is the solution to the parabolic equation (Wilson and Tappert 1979):

$$\left[2\imath k_0\frac{\partial}{\partial x} - 2\frac{\partial^2}{\partial\zeta\partial z} + \frac{k_0^3}{2}\left(\Phi_\delta(0) - \Phi_\delta(\zeta)\right)\right]C(x,z,\zeta) = 0 \tag{2.8}$$

and can be solved by :

$$C(x,z,\zeta) = \frac{k_0^2}{4\pi^2 x^2} e^{\left(-\frac{k_0^2}{4}\int_0^x \left(\Phi_\delta(0)-\Phi\left(\zeta\frac{x'}{x}\right)\right)dx'\right)} e^{\left(-\imath k_0 \frac{\zeta z}{x}\right)} \tag{2.9}$$

Replacing the function Φ by its expression and introducing some classical approximations leads to

$$C(x,z,\zeta) \approx \frac{k_0^2}{4\pi^2 x^2} e^{\left(-\sqrt{\frac{\pi}{2}}\,\frac{\delta c_0^2}{c_0^2}\,k_0^2\,L_{H_s}\,\frac{\zeta^2}{L_{V_s}^2}\,\frac{x}{3}\right)} \tag{2.10}$$

As a function of ζ, C is a Gaussian function of the form $e^{-\frac{1}{2}\frac{\zeta^2}{L_z^2}}$.

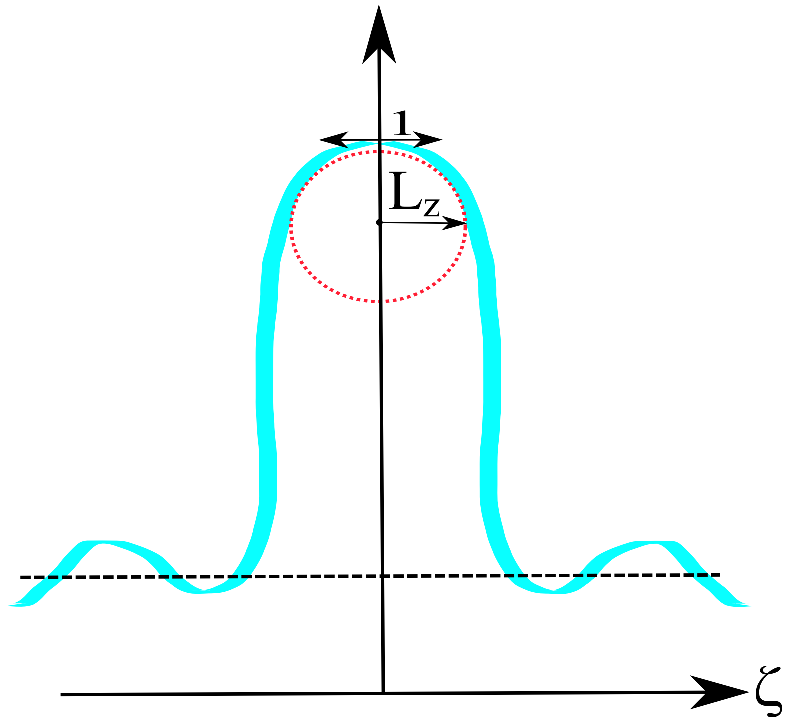

FIGURE 2.3: Sketch of the intercorrelation function radius of curvature evaluation.

This defines a parameter L_z which is denoted here the radius of curvature of the Gaussian function. Comparing this general form and the last expression of C leads to :

$$L_z = \alpha\,\lambda_s\,\frac{c_0}{\delta c_0}\left(\frac{L_{V_s}^2}{x L_{H_s}}\right)^{1/2} \tag{2.11}$$

with $\alpha \approx 0.174$.

In section 2.4.2, the radius of curvature of the Gaussian function equivalent to the intercorrelation function of the acoustic field in the case of a wave propagating through a randomly rough acoustic lens will be evaluated.

2.3 Sound field calculation in the lens case

The geometry of the propagation problem is shown in figure 2.4. It is assumed that the sound field $p(x, y, z)$ is emitted by a harmonic source (pulsation ω) located at $x = 0$ and propagates to a receiver through the RAFAL. The x axis is perpendicular to the plane of the lens. The transverse directions are y (horizontal) and z (vertical). The flat side of the RAFAL is located at $x = x_1$ and its rough face is at $x = x_2 = H + \xi(y, z)$. The function $\xi(y, z)$ stands for the roughness of the face. It is assumed that the function $\xi(y, z)$ follows a normal Gaussian law ; its mean value is equal to zero and its standard deviation is ξ_0. Medium 1 ($x < x_1$ and $x > x_2$) corresponds to fresh water and is characterized by a constant sound speed c_1 and a constant density ρ_1. Medium 2 corresponds to the wax lens ($x_1 < x < x_2$) and is characterized by a constant sound speed c_2 and the same density $\rho_2 = \rho_1$. The densities of the two materials do not appear in the following calculations since they are very close in both cases (see table 3.2). The calculation procedure has been conducted in 3D but for the sake of simplicity, the study is presented here in 2D (2 variables (x, z)) since for the 3D geometry most formulas are similar in both y and z directions. In the following, we therefore write $p(x, z)$ and $\xi(z)$.
The diagram presented in figure 2.4 displays the parameters involved with our calculations:

- the standard deviation of the random roughness amplitude ξ_0;
- the vertical and horizontal correlation lengths L_V and L_H of the random roughness amplitude;
- the distance between the source and the RAFAL's plane input face x_1;
- the RAFAL average thickness $H = x_2 - x_1$;
- the distance between the average random output face and the receiver x_{dist}.

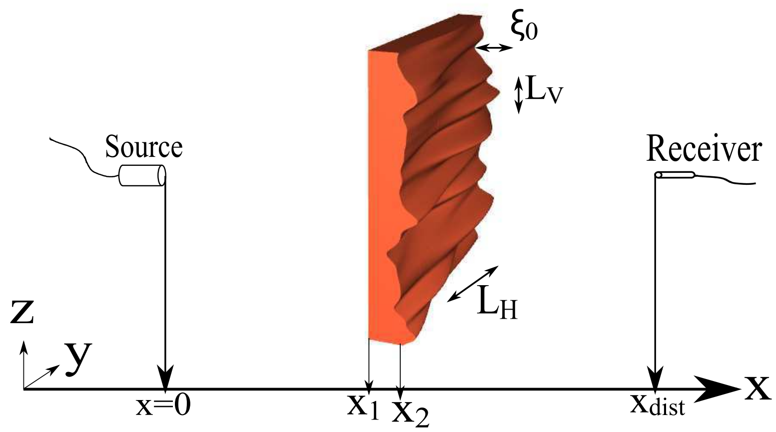

FIGURE 2.4: Experimental diagram: definition of the physical parameters.

The aim of this section is to provide an analytical expression for the pressure field propagated through the RAFAL. In this configuration, the acoustic pressure is ruled by the Helmholtz equation:

$$\begin{cases} \left(\Delta + k_1^2\right) p_1 = S, & \text{in water} \\ \left(\Delta + k_2^2\right) p_2 = 0, & \text{in RAFAL} \end{cases} \tag{2.12}$$

where $k_j = \omega / c_j$ and S is the source term. The boundary conditions write into:

$$\begin{cases} p_1 = p_2, \\ \partial_n p_1 = \partial_n p_2 \ (\rho_1 \approx \rho_2) \end{cases} \tag{2.13}$$

with Sommerfeld conditions (Sommerfeld 1912).
In section 2.3.1, the simplified case of two semi-infinite spaces is studied. Fourier transforms are used to describe the propagation. The main challenge lies in the dependence on the RAFAL's output face roughness. However, if the roughness of the surface is small, it is possible to use an approximation called Small Slope Approximation. The details of the method are summarized section 2.3.1. Its applications to the lens case is presented in section 2.3.2.

The first step is to calculated the $z-$Fourier transform of the sound field $p\,(x,z)$ defined by:

$$\Pi(x,\mu) = \int dz\, e^{-i\mu z} p(x,z), \tag{2.14}$$

In the following equations we define the component of the wave vector in the $x-$direction, denoted K_j, as follows:

$$K_j = k_j \left(1 - \frac{\mu^2}{k_j}\right)^{1/2}, \tag{2.15}$$

where k_j is the wavenumber in medium j, defined as $k_j = \omega / c_j$. In medium j, the propagation along the x axis is therefore described by terms of the form $e^{iK_j x}/2iK_j$. Boundary conditions at $x = x_1$ and $x = x_2$ are taken into account through a transmission coefficient. For instance at $x = x_1$ this coefficient is equal to $2K_1/(K_2 + K_1)$ since the density is the same on both sides and the surface is plane. Such a simple result is however not available if the surface is rough.
The transducer directivity can be approximated by the *Sombrero* function corresponding to the directivity of a circular piston of radius ρ (Gaskill 1978, Kinsler et al. 1999). It is written $S\,(\mu\rho)$ in the following equations.
Since forward and small-angle (due to the transducer narrow directivity) propagation is considered here, the parabolic approximation can be applied. We also note that the length scale of the medium fluctuations is much longer in the propagation direction than in the transverse

direction.

In the following sections, the source term is denoted $p_0(x, z)$. Its Fourier transform is noted $\Pi_0(x, \mu)$.

2.3.1 The Small Slope Approximation in the case of two semi-infinite media

In the case of a sound transmission problem between two semi-infinite media separated by a thin rough surface $\Sigma : x = \xi(z)$, it is possible to derive an approximate expression for the sound field transmitted through the surface, especially if its slope can be considered to be small. The so-called integral Small Slope Approximation (SSA) is used to derive the expression of the sound field in our case (Meecham-Lysanov approach in Voronovich (2012), adapted from the reflection case (Cristol 2008) to the transmission problem). As shown in figure 2.5, the source is here located in the medium 1 ($x < \xi(z)$) and the incident pressure on Σ is noted $p_0(M)$, for any point M. Integral representations of the reflected and transmitted fields on the boundary Σ are first sought out. To do so, let us express the Green's function defined in the 2D infinite space with the same characteristics as respectively medium 1 (in our case, freshwater) and medium 2 (the material composing the acoustic lens, referred to as *Machinable Blue Wax*). The Green's function is given by:

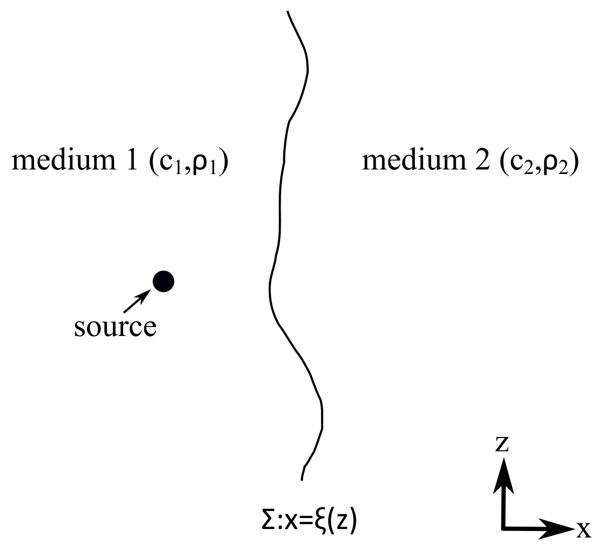

FIGURE 2.5: Configuration for the SSA in the case of two semi-infinite media.

$$G_j(S, M) = -\frac{i}{4} H_0^{(1)}(k_j R(S, M)) \text{ for } j = 1, 2 \tag{2.16}$$

where $R(S, M)$ is the distance between two points S and M and $H_0^{(1)}$ is the Hankel function of order zero and of the first kind. The transverse Fourier transforms of the Green's function is written:

$$\hat{G}_j(x, \mu) = \frac{e^{iK_j|x|}}{2iK_j} \tag{2.17}$$

The integral representation of the total pressure $p_1(M)$ for a point M in medium 1 can be written:

$$p_1(M) = p_0(M) + \int_\Sigma dP'\left[p_1(P')\frac{\partial G_1(P', M)}{\partial \boldsymbol{n}(P')} - \frac{\partial p_1(P')}{\partial \boldsymbol{n}(P')}G_1(P', M)\right], \tag{2.18}$$

where p_1 is the sound pressure and $\partial p_1/\partial \boldsymbol{n}$ its normal derivative on Σ. P' is a point on Σ. Similarly, for medium 2 we obtain:

$$p_2(M) = -\int_\Sigma dP'\left[p_2(P')\frac{\partial G_2(P', M)}{\partial \boldsymbol{n}(P')} - \frac{\partial p_2(P')}{\partial \boldsymbol{n}(P')}G_2(P', M)\right], \tag{2.19}$$

We obtain the integral equations for the pressure $\kappa(P') = p_i(P')$ and its first normal derivative $\chi(P') = \partial p_1(P')/\partial \boldsymbol{n}(P')$ on Σ. $\nu(P')$ denotes the vector normal to the surface, oriented towards the incident side (medium 1). For any point $P(\xi(z), z)$, in medium 1:

$$\frac{1}{2}\kappa(P') = p_0(P) + \int dP'\left[\kappa(P')\frac{\partial G_1(P', M)}{\partial \boldsymbol{n}(P')} - \chi(P')G_1(P, P')\right] \tag{2.20}$$

Similarly, in medium 2:

$$\frac{1}{2}\kappa(P') = -\int dP'\left[\kappa(P')\frac{\partial G_2(P', M)}{\partial \boldsymbol{n}(P')} - \chi(P')G_2(P, P')\right] \tag{2.21}$$

The SSA consists here in replacing the Green's functions G_j in the integral equations 2.20 and 2.21 by their asymptotic approximations for $|\xi(z') - \xi(z)| << |z - z'|/R(P, P')$. In other terms, the idea is to replace inside the integrals the Green's function $G_j(\xi(z'), z'; \xi(z), z)$ by the Green's function $G_j(0, z'; 0, z))$, which may be understood as a first term in a Taylor expansion along the powers of the maximum slope. This procedure is enough for the Dirichlet problem (reflection on an impenetrable free boundary) ; for the interface problem with transmission, or for an irregular rigid boundary (Neumann problem), the normal gradient of the Green function must be considered inside the integrals; as illustrated by figure 2.6b), this gradient is canceled on a plane tangent to the local tangent plan to point $(\xi(z), z)$; if the slope is weak enough, the irregular boundary remains inside the region where the normal gradient is small.

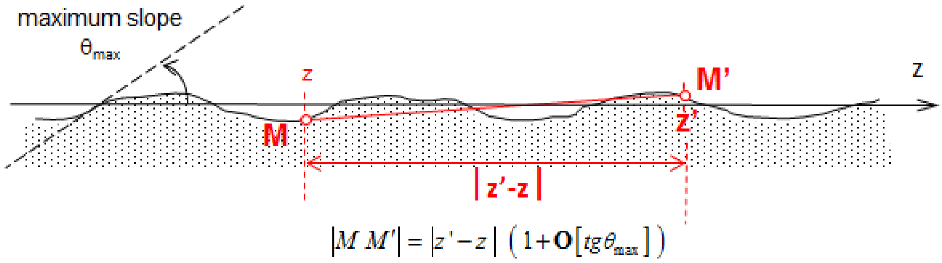

(A) Green's function between two point on the irregular interface.

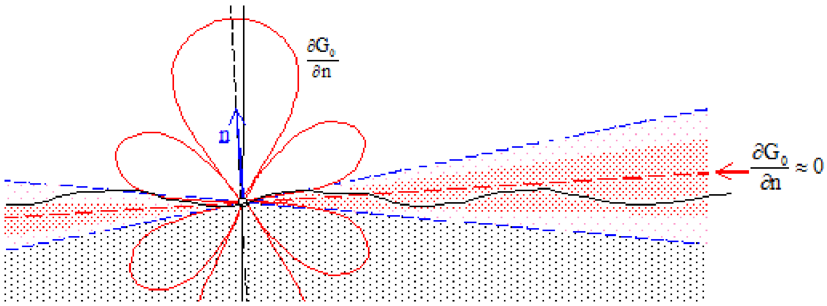

(B) normal gradient of Green's function between two point on the irregular interface.

FIGURE 2.6: Meaning of the Small Slope Approximation.

Subtracting the last two equations (2.20 and 2.21) leads to:

$$-p_0\left(\xi\left(z\right),z\right) \approx \int dz'\chi\left(\xi\left(z'\right),z'\right)\left[G_1\left(0,z-z'\right)+G_2\left(0,z-z'\right)\right] \tag{2.22}$$

The right-hand side of equation 2.22 is a classical convolution, which may be easily inverted. The Fourier transform of χ is therefore found:

$$\hat{\chi}\left(\mu\right) = \int dz\; e^{-i\mu z}\chi\left(\xi\left(z'\right),z'\right) \approx -2i\frac{K_1K_2}{K_1+K_2}\Pi_0\left(x,\mu\right), \tag{2.23}$$

where we recall that Π_0 is the Fourier transform of the incident pressure field p_0. Similarly, the Fourier transform of κ is obtained:

$$\hat{\kappa}\left(\mu\right) = \int dz\; e^{-i\mu z}\kappa\left(\xi\left(z'\right),z'\right) \approx i\frac{\hat{\chi}\left(\mu\right)}{K_2} \approx -2\frac{K_2}{K_1+K_2}\Pi_0\left(x,\mu\right). \tag{2.24}$$

Finally, it is possible to obtain the Fourier transform of the pressure field by inverting the order of integrations:

$$\Pi\left(x,\mu\right) \approx \int dz\; e^{-i\mu z}\frac{e^{-iK_1\xi(z)}}{K_1}\left(\int d\mu'\; e^{i\mu' z}2\frac{K_1'K_2'}{K_1'+K_2'}\Pi_0\left(x,\mu'\right)e^{iK_1'x}\right) \tag{2.25}$$

2.3.2 Application to the lens case

In the case of the RAFAL, the classical transverse Fourier method is applied for the propagation between the source and inside the RAFAL. We then use the integral SSA in order to derive the sound pressure field transmitted from inside the RAFAL to the receiver.

The expression for the initial field (in $x = 0$) in the Fourier domain is:

$$\Pi_0(x=0,\mu) = \frac{-i}{4\pi^2}\frac{1}{K_1}S(\mu) \tag{2.26}$$

Hence, we can express the Fourier transform of the acoustic pressure in the region between the source and the RAFAL's plane input face:

$$\Pi_0(x,\mu) = \Pi_0(x=0,\mu)e^{iK_1x}. \tag{2.27}$$

The transmission term between medium 1 (water) and 2 (RAFAL) is given by the following relationship (at $x = x_1$):

$$\Pi(x=x_1,\mu) = \Pi_0(x=x_1,\mu)\frac{2K_1}{K_1+K_2}. \tag{2.28}$$

The transmitted field in region 2 can therefore be expressed in a similar fashion to what was done in equation 2.27:

$$\Pi(x,\mu) = \Pi(x=x_1,\mu)e^{iK_2(x-x_1)} \tag{2.29}$$

Finally, according to the formula given by the SSA, the Fourier transform of the pressure field transmitted through the RAFAL's randomly rough output face ($x = x_2 + \xi\left(z\right)$) is:

$$\begin{aligned}
&\Pi(x=x_2+\xi\left(z\right),\mu)\\
&=\frac{1}{2\pi}\int dz\; e^{-i\mu z}e^{-iK_1\xi(z)}\int d\mu' e^{i\mu' z}\frac{K_2}{K_1+K_2}\Pi\left(x=x_2,\mu\right)\\
&=\frac{1}{2\pi}\int dz\; e^{-i\mu z}e^{-iK_1\xi(z)}\int d\mu' e^{i\mu' z}\frac{2K_2K_1}{\left(K_1+K_2\right)^2}e^{iK_1x_1}e^{iK_2(x_2+\xi(z)-x_1)}\Pi_0(x=0,\mu)
\end{aligned} \tag{2.30}$$

As explained earlier, the parabolic approximation applies to our configuration. Hence, we can write $K_i = k_i$ for amplitude terms and $K_i = k_i - \frac{1}{2}\frac{\mu^2}{k_i}$, denoted $\hat{k_i}$, so that equation 2.30 can be rewritten as :

$$\begin{aligned}&\Pi(x = x_2 + \xi(z), \mu) \\ &\approx \frac{1}{2\pi}\int dz\, e^{-i\mu z} e^{-i\hat{k}_1\xi(z)} \int d\mu' e^{i\mu' z} \frac{2k_2k_1}{(k_1+k_2)^2} e^{i\hat{k}_1 x_1} e^{i\hat{k}_2(x_2 - x_1 + \xi(z))} \Pi_0(x = 0, \mu)\end{aligned} \tag{2.31}$$

The *Sombrero* function contained in the $\Pi_0(x = 0, \mu)$ term can be approximated with a Gaussian, with the same height and curvature: $S(\mu) \approx \frac{1}{2} e^{-\mu^2\rho^2/8}$, where ρ is the radius of the transducer. It follows:

$$\begin{aligned}&\Pi(x = x_2 + \xi(z), \mu) \\ &\approx C_0 \frac{1}{2\pi}\int dz\, e^{-i\mu z} e^{-i\hat{k}_1\xi(z)} \int d\mu' e^{i\mu' z} e^{-\mu'^2\rho^2/8} e^{i\hat{k}_1 x_1} e^{i\hat{k}_2(x_2 - x_1 + \xi(z))}\end{aligned} \tag{2.32}$$

where C_0 is a constant coefficient. Equation 2.32 simplifies into:

$$\Pi(x = x_2 + \xi(z), \mu) \approx C_0 e^{-\mu^2\rho^2/8} e^{i\hat{k}_1 x_1} e^{i\hat{k}_2(x_2 - x_1)} e^{-i(\hat{k}_1 - \hat{k}_2)\xi(z)} \tag{2.33}$$

Finally, the sound field is approached by:

$$p(x, z) \approx \int d\mu\, e^{i\mu z} \Pi(x = x_2 + \xi(z), \mu)\, e^{i\hat{k}_1(x - x_2)} \tag{2.34}$$

2.4 Sound field statistics

In this section, we derive statistics of the sound field evaluated in section 2.3.2. Indeed, the evaluation of the strength parameter Φ can be performed with the average of the sound pressure transmitted through the RAFAL. This calculation is presented in section 2.4.1. Otherwise, the acoustic field correlation length can be obtained with the intercorrelation function of the sound field.

2.4.1 First-order statistics

By definition of Φ (Dashen et al. 2010), the mean value of the random sound field can be written $< p > \approx e^{-\Phi^2/2}$. Evaluating $< p >$ in the experimental configuration presented here would allow to retrieve the corresponding strength parameter, noted Φ_ℓ. Taking the average of the transmitted field at abscissa $x = x_2 + \xi(z)$ (equation 2.33) gives:

$$\left\langle \Pi\left(\mu, x = x_2 + \xi(z)\right)\right\rangle = C_0 e^{-\mu^2\rho^2/8} e^{i\hat{k}_1 x_1} e^{i\hat{k}_2(x_2 - x_1)} \left\langle e^{-i\left(\hat{k}_1 - \hat{k}_2\right)\xi(z)}\right\rangle \tag{2.35}$$

Because of the normal statistics, equation 2.35 gives:

$$\left\langle \Pi\left(\mu, x = x_2 + \xi(z)\right)\right\rangle = C_0 e^{-\mu^2\rho^2/8} e^{i\hat{k}_1 x_1} e^{i\hat{k}_2(x_2 - x_1)} e^{-\frac{1}{2}\left(\hat{k}_1 - \hat{k}_2\right)^2 \xi_0^2} \tag{2.36}$$

The argument in the last exponential function in equation 2.36 corresponds to the variable part of the pressure field. We can therefore identify a term corresponding to the scaled strength parameter Φ_ℓ, such that:

$$e^{-\frac{1}{2}\left(\hat{k}_1 - \hat{k}_2\right)^2 \xi_0^2} = e^{-\frac{1}{2}\Phi_\ell^2}. \tag{2.37}$$

Using a first order approximation, this provides an expression for the scaled strength parameter Φ_ℓ:

$$\Phi_\ell^2 = \left(k_1 - k_2\right)^2 \xi_0^2 \tag{2.38}$$

which can be written as:

$$\Phi_\ell = k_1 \xi_0 \left(1 - \frac{c_1}{c_2}\right) \tag{2.39}$$

2.4.2 Second-order statistics

As seen in section 2.2.2, the width of the second-order moment around its maximum can be used to obtain the correlation length of the acoustic field L_z. The spatial intercorrelation, noted C, is calculated hereafter using the Fourier transform of the pressure field transmitted through the randomly rough acoustic lens. The radius of curvature of C corresponds to the quantity of interest L_z. Hence, L_z is the inverse of the radius of curvature of the Fourier transform of C. Let us write the analytical expression for the Fourier transform of the intercorrelation function of the sound field :

$$\tilde{C}(x, z, \Theta) = \frac{1}{2\pi} \int d\zeta e^{i\Theta\zeta} \left\langle p\left(x, z - \frac{1}{2}\zeta\right) p^*\left(x, z + \frac{1}{2}\zeta\right)\right\rangle \tag{2.40}$$

The term in brackets can be written using inverse Fourier transforms, so that:

$$\begin{aligned}
&\tilde{C}(x,z,\Theta)\\
&= \frac{1}{2\pi}\int d\zeta e^{i\Theta\zeta}\int d\Theta_1 e^{-i\Theta_1\left(z-\frac{1}{2}\zeta\right)}\int d\Theta_2 e^{-i\Theta_2\left(z+\frac{1}{2}\zeta\right)}\left\langle \Pi(x,\Theta_1)\Pi^*(x,\Theta_2)\right\rangle\\
&= \frac{1}{2\pi}\int d\zeta e^{i\Theta\zeta}\int d\Theta'\int d\upsilon e^{i\upsilon z}e^{i\Theta'\zeta}\left\langle \Pi\left(x,\Theta'-\frac{1}{2}\upsilon\right)\Pi^*\left(x,\Theta'+\frac{1}{2}\upsilon\right)\right\rangle
\end{aligned} \tag{2.41}$$

where $\upsilon = \Theta_2 - \Theta_1$ and $\Theta' = \frac{\Theta_1+\Theta_2}{2}$. Noticing in equation 2.41 that $\frac{1}{2\pi}\int d\zeta e^{i\Theta\zeta}e^{i\Theta'\zeta} = \delta(\Theta+\Theta')$, where $\delta(.)$ is the Dirac function, this turns into:

$$\tilde{C}(x,z,\Theta) = \int d\upsilon e^{i\upsilon z}\left\langle \Pi\left(x,-\Theta-\frac{1}{2}\upsilon\right)\Pi^*\left(x,-\Theta+\frac{1}{2}\upsilon\right)\right\rangle \tag{2.42}$$

Elementary but tedious calculations lead to a relatively simple analytical expression for the term between brackets in the last integral. The details of these calculations are given in Appendix C. The result is the following, where $b = \frac{x_1}{k_1} + \frac{x_2-x_1}{k_2}$, $d^2 = k_1^2\xi_0^2\left(1-\frac{c_1}{c_2}\right)^2\frac{1}{L_V^2}$, $q = 1+\frac{d^2\rho^2}{2}$ and $\mathcal{R} = \rho^2/8 + \frac{b^2d^2}{1+d^2\rho^2/2}$:

$$\begin{aligned}
&\left\langle \Pi\left(x,\Theta-\frac{1}{2}\upsilon\right)\Pi^*\left(x,\Theta+\frac{1}{2}\upsilon\right)\right\rangle\\
&= C_1^2\frac{1}{\rho/\sqrt{2}}\frac{1}{(2\pi)^{3/2}}e^{-\frac{1}{2}\upsilon\mathcal{R}}e^{i\Theta\frac{\upsilon b}{q}}\frac{e^{-\frac{1}{2}\Theta^2/\left(2q/\rho^2\right)}}{\sqrt{2\pi(2q/\rho^2)}},
\end{aligned} \tag{2.43}$$

Using the definition of the intercorrelation proposed in equation 2.40 and the property written in equation 2.42, it is possible to obtain an expression for the Fourier transform of the intercorrelation based on the result of equation :

$$\tilde{C}(x,z,\Theta) = C_2^2\frac{1}{\sqrt{2\pi\frac{2q}{\rho^2}}}e^{-\frac{1}{2}\frac{\Theta^2}{2q/\rho^2}}\frac{e^{-\frac{1}{2}\frac{(z-\Theta b/q)^2}{\mathcal{R}}}}{\sqrt{2\pi}\sqrt{\mathcal{R}}} \tag{2.44}$$

where C_2 is a constant coefficient.
The Fourier transform of the intercorrelation function is a solution of the parabolic equation in the Fourier domain, written as the Fourier transform of equation 2.8:

$$\left[2\imath k_0\frac{\partial}{\partial x} + \Theta\frac{\partial^2}{\partial z^2} + \frac{k_0^2}{2}\left(\Phi_\delta(0)-\Phi_\delta(\zeta)\right)\right]\tilde{C}(x,z,\Theta) = 0. \tag{2.45}$$

In the case of propagation through a non-fluctuating media -it is here the case since we are at the output of the RAFAL- the term $(\Phi_\delta(0)-\Phi_\delta(\zeta)) = 0$ and equation 2.45 is a transport equation. In this case, with the help of $\tilde{C}(x,z,\Theta) = \tilde{C}\left(0, z - \frac{\Theta}{k_1}x, \Theta\right)$, the x−dependence is carried by the term $z = \frac{\Theta}{k_1}x$ and equation 2.44 rewrites into:

$$\tilde{C}(x,0,\Theta) = C_2^2 \frac{1}{\sqrt{2\pi\frac{2q}{\rho^2}}} e^{-\frac{1}{2}\frac{\Theta^2}{2q/\rho^2}} \frac{e^{-\frac{1}{2}\Theta^2\left(\frac{x}{k_1}+\frac{b}{q}\right)^2/\mathcal{R}}}{\sqrt{2\pi}\sqrt{\mathcal{R}}} \tag{2.46}$$

Examining equation 2.44 leads to the conclusion that the decorrelation due to the roughness of the RAFAL's output face appears in the term $e^{-\frac{1}{2}\frac{\Theta^2}{L_\Theta^2}}$, which is comparable to a Gaussian function whose radius of curvature can be analytically evaluated. The vertical correlation length of the acoustic field propagated through the RAFAL, denoted L_z^ℓ, is finally obtained using the fact that $L_z^\ell = \frac{1}{L_\Theta}$, which gives:

$$L_z^\ell = \sqrt{\frac{\rho^2}{2q} + \frac{\left(\frac{x}{k_1} + \frac{b}{q}\right)^2}{\mathcal{R}}} \tag{2.47}$$

The ratio L_z^ℓ/λ can therefore be evaluated in the case of our scaled experiment. We already saw in section 2.2.2 that this ratio could be otherwise calculated for an oceanic configuration presenting continuous sound speed fluctuations. Equating the radii of acoustic correlation length to the wavelength in both cases would hence ensure the representativeness of our scaled experimental scheme in terms of loss of coherence.

2.5 The Fresnel radius and the *diffraction* parameter

This section focuses on the evaluation of the diffraction parameter in the case of the scaled experiment presented here. In this configuration, let the diffraction parameter be noted Λ_ℓ. Since, as noticed for the strength parameter, its evaluation using Flatté's definition is not possible in the experimental scheme described in this thesis, a different approach is proposed. It is essentially based on the fact that the diffraction parameter and the Fresnel radius are connected in the following manner:

$$\Lambda_\ell = \frac{1}{2\pi}\left(\frac{R_F}{L_V}\right)^2. \tag{2.48}$$

Equation 2.48 implies that the evaluation of R_F is necessary in order to obtain Λ_ℓ. Since, to our knowledge, no published work offers an expression for the Fresnel radius in the case of a directive source, we propose a calculation, based on the historical methodology of Fresnel, which is further compared to the classical Fresnel radius obtained for a point source.

Therefore, we propose to calculate R_F by analytically evaluating the acoustic pressure propagated through an acoustic lens with a plane input face and an opaque plane output face presenting a circular slit with a variable diameter. Note that the calculation is here performed in 3D. The pressure on the central propagation axis is computed as a function of the radius of the slit. The first maximum of this function corresponds to the radius of the first Fresnel zone, since it gathers all the constructive interference, as originally explained in optics in Sears (1949) and extended to geophysics in Knapp (1991), Brühl et al. (1996).

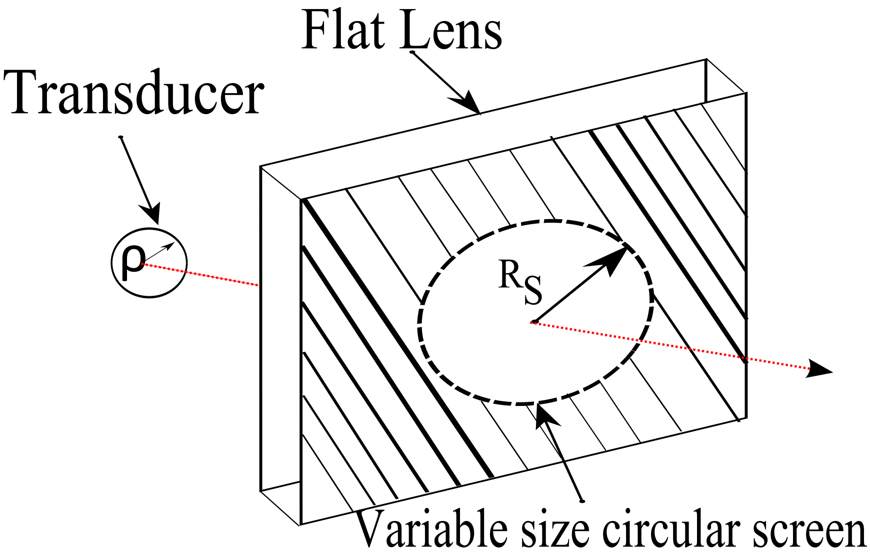

FIGURE 2.7: Configuration for the evaluation of the Fresnel radius.

The acoustic pressure on the central axis is given by:

$$p(x,0,0) = \iint dy\, dz\, cyl\left(\frac{\sqrt{z^2+y^2}}{R_S}\right) p\left(x_2,y,z\right) \frac{1}{4\pi^2} \iint d\mathcal{L}\, d\mu\, e^{-i(\mu z+\mathcal{L}y)} e^{-i\frac{1}{2}\frac{k}{k_1}x}, \tag{2.49}$$

where the cylindrical function defined in Gaskill (1978), denoted $cyl(.)$, is used to take into account the propagation through the slit only. Equation 2.49 can be rewritten using $r = \sqrt{y^2+z^2}$:

$$p(x,0,0) = \int_{-\pi}^{\pi} d\varphi \int_0^{R_S} dr\, r\, p\left(x_2,r\right) \frac{1}{4\pi^2} \int_{-\pi}^{\pi} d\varphi' \int_0^{\infty} dk\, k\, e^{-ikr\cos\varphi'} e^{-i\frac{1}{2}\frac{k}{k_1}x}, \tag{2.50}$$

we recognize in the last two integrals a classical Bessel transform (Gaskill 1978). Equation 2.50 becomes:

$$
\begin{aligned}
&p(x,0,0)\\
&= \int_0^{R_S} dr\, r\, p\left(x_2, r\right) \int_0^{\infty} dk\, k J_0\left(kr\right) e^{-i\frac{1}{2}\frac{k}{k_1}x}\\
&= \int_0^{R_S} dr\, r\, p\left(x_2, r\right) \frac{-ik_1}{x} e^{i\frac{1}{2}\frac{k_1 r}{x}}.
\end{aligned}
\tag{2.51}
$$

Figure 2.8 displays an example of the calculation of the pressure field on the central axis, for an output face / receiver distance of 250 mm.

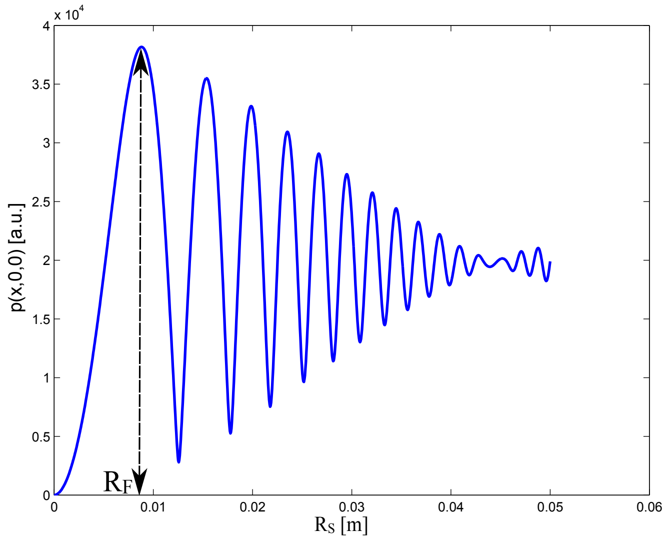

FIGURE 2.8: Calculation of the acoustic pressure on the central axis for $x_{dist} = 250\ mm$. The Fresnel radius is equal to $8.8\ mm$.

The final result regarding the Fresnel radius is presented in figure 2.9a. It is compared to the case of the Fresnel radius calculated for a point source, and the agreement between the two quantities is found to be quite good. The relative departure is displayed in figure 2.9b and is large at very short ranges (typically $x_{dist} < 0.025m$). The departure is of the order of one percent for longer propagation ranges.

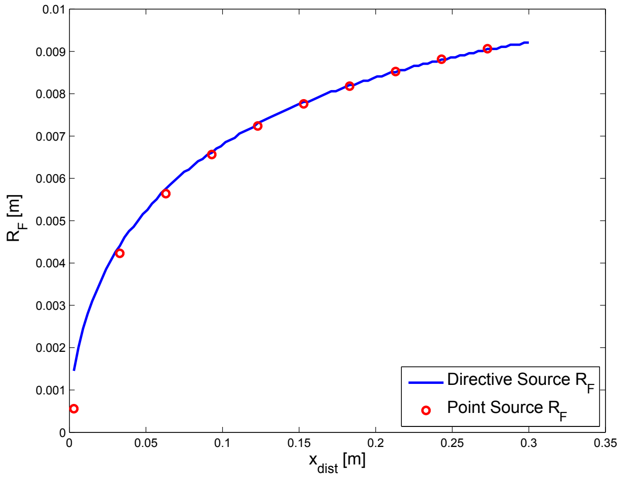

(A) Fresnel radius calculation: comparison between a directive source (blue solid line) and a point source (red dots).

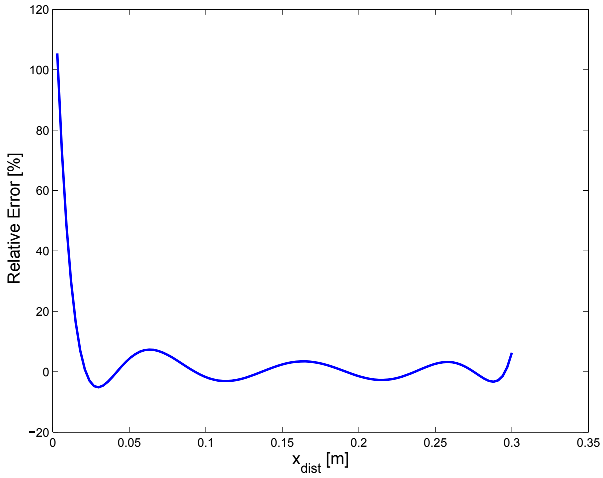

(B) Relative departure between the R_F calculated for a directive source and for a point source (red dots).

FIGURE 2.9: Fresnel radius calculation results.

2.6 Summary and conclusion

Finally, we derived all the quantities involved in the evaluations of our three dimensional parameters. Expressions for Flatté's dimensional parameters Φ_ℓ and Λ_ℓ were obtained in the case of our experimental case. First order statistics of the sound field calculated using the SSA lead to a simple expression for the strength parameter Φ^ℓ. The Fresnel radius R_F was evaluated in the lens case as well in order to obtain a formula for the diffraction parameter. Second-order statistics of the sound field allowed us to obtain an expression for the vertical acoustic correlation length in the tank experiment case as well. The expressions for these parameters in the scale experiment case and in the oceanic case are summarized in Table 2.1:

	"Natural" Ocean	"Artificial" RAFAL
Strength parameter	$\Phi^2 = k_0^2\sqrt{2\pi}\left(\frac{\delta c_0}{c_0}\right)^2 L_{H_s} R$	$\Phi_\ell^2 = k_1^2 \xi_0^2 \left(1 - \frac{c_1}{c_2}\right)^2$
Diffraction parameter	$\Lambda = \frac{dx}{ak_0 L_{V_s}^2}$	$\Lambda_\ell = \frac{1}{2\pi}\left(\frac{R_F}{L_V}\right)^2$
Acoustic vertical correlation length	$L_z = \alpha\, \lambda_s\, \frac{c_0}{\delta c_0}\left(\frac{L_{V_s}^2}{x L_{H_s}}\right)^{1/2}$	$L_z^\ell = \sqrt{\frac{\rho^2}{2q} + \frac{\left(\frac{x}{k_1} + \frac{b}{q}\right)^2}{\rho^2/8 + \frac{b^2 d^2}{1 + d^2\rho^2/2}}}$

TABLE 2.1: Comparison between dimensional parameters in the oceanic case and in the scaled experiment case.

The expressions for the dimensional parameters presented in this chapter in the scaled experiment case allow to predict the regimes of fluctuations that one would be able to induce with our experimental protocol. Indeed, it is possible to tune Λ_ℓ and Φ_ℓ with the experimental parameters (frequency, distance, RAFAL's randomly rough output face statistics). Equating these dimensional parameters in the lens case with those obtained in the oceanic case also provides the representativeness of our experimental scheme. Furthermore, equating the acoustic correlation as well not only yields to a continuity in terms of regimes of fluctuations, but also in radius of coherence. Hence, if we write:

$$\begin{cases} \Lambda = \Lambda_\ell \\ \Phi = \Phi_\ell; \\ L_z/\lambda_s = L_z^\ell/\lambda \end{cases} \tag{2.52}$$

then we are able to directly compare the parameters involved in our scaled experiments with those corresponding to a realistic oceanic configuration. As a matter of fact, the comparison is made using the following process:

1. the parameters of the scaled experiment are chosen so that Λ_ℓ and Φ_ℓ span over different regimes of fluctuations;
2. L_z^ℓ/λ is deduced;
3. a series of combination of dimensional parameters, involving the oceanic environmental variables, are defined, so that they appear in the original dimensional parameters expressions:

$$\begin{cases} \mathcal{N} = \frac{\lambda_s}{R} \\ N_{h,v} = \frac{\lambda_s}{L_{H,V_s}} \\ \Delta_c = \frac{\delta c_0}{c_0} \\ r = \frac{\lambda_s}{L_z} \end{cases} \tag{2.53}$$

which leads to:

$$\begin{cases} \Phi^2 = (2\pi)^{5/2}\,\Delta_c^2 \frac{1}{\mathcal{N}_h N} \\ \Lambda = \frac{1}{12\pi}\frac{N_v^2}{\mathcal{N}} \\ r^2 = \frac{N_v^2}{\mathcal{N} N_h}\frac{1}{\alpha^2}\Delta_c^2 \end{cases} \tag{2.54}$$

4. the oceanic environmental parameters are the range R, the vertical sound speed fluctuations correlation length L_{V_s} and their standard deviation δc_0. Rigorously, one should also consider the frequency f_s and the ratio L_{V_s}/L_{H_s} as parameters to evaluated as well, but, in order to limit the degrees of freedom of our problem, we chose to fix $f_s = 1\ kHz$ and tune L_{V_s}/L_{H_s}.

5. finally we obtain:

$$\begin{cases} N_v = \frac{\alpha(2\pi)^{5/4}}{\Phi} \\ \mathcal{N} = \frac{\alpha^2 r^2 (2\pi)^{5/2}}{12\pi\Phi^2\Lambda} \\ \delta c_0 = c_0\frac{\sqrt{(L_{V_s}/L_{H_s})N_v\mathcal{N}\Phi}}{(2\pi)^{5/4}} \end{cases} \tag{2.55}$$

This is a way to establish a comparison between signals propagated through a randomly rough acoustic lens and acoustic pressure field resulting from propagation through continuously fluctuating sound speed distribution, such as sketched in figure 2.10:

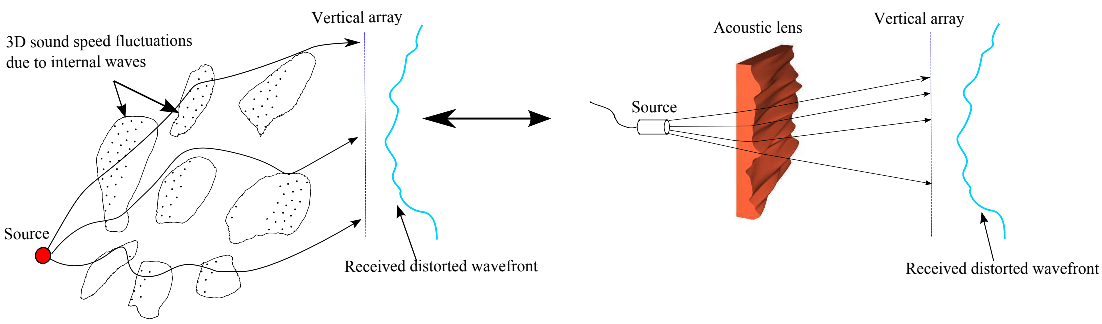

FIGURE 2.10: Comparison between continuous 3D medium fluctuation and local perturbation influence on the received wavefront on a linear array.

This comparison will be carried out using simulated and measured data, as well as theoretical results, in Chapter 4.

Chapter 3

Development of a Scaled Experiment

Contents

3.1 Introduction

In this chapter, the developed experimental protocol is detailed. Tank experiments including thermal turbulence have been carried out using heating grids to generate the medium fluctuations (Stone and Mintzer 1962; 1965, Sederowitz and Favret 1969, Campanella and Favret 1969, Chotiros and Smith 1979) summarized in Dobbins (1989). As noticed by Blanc-Benon and Juvé (Blanc-Benon and Juvé 1993), this type of protocol can induce the appearance of air bubbles pertubating the medium in an undesired manner. An alternative is proposed in Blanc-Benon and Juvé (1993), where the protocol was adapted in air instead of water, solving the bubbles appearance issue. Nevertheless, the turbulence generated using thermistors produced fluctuations of the propagated acoustic signals that are not perfectly reproducible in a deterministic manner, meaning that only the statistical features of the fluctuations are reproducible.

Therefore, we propose a radically different experimental protocol driven by the motivation of obtaining representative and reproducible results. The main objective is to simplify the measurements in order to enhance the reproducibility and expand the possible configurations to study. Preliminary measurements revealed interesting features of sound propagation through

Plexiglas plano-concave lens (Real et al. 2013). In fact, the refraction of the transmitted ultrasonic signal produces shadow zones and caustics, which are typical features of the propagation of sound waves through IW in the saturated regime. Hence, the idea of reproducing IW effects on sound wave propagation using acoustic lenses seemed to represent an interesting path to explore. It was shown otherwise in Chapter 2, that it was possible to reproduce the final statistical qualitative and quantitative effects of 3D propagation in random media using almost-2D acoustic lenses, or phase screen (Andrews et al. 1997).

We first present the experimental protocol itself, including the studied configurations. In section 3.3, the manufacturing process of the acoustic lenses is described. Section 3.4 presents the equipment used to perform the measurements. Finally, numerical tools developed in support of the experiment are presented in section 3.5.1.

3.2 Experimental protocol

The experimental scheme consists in propagating an ultrasonic signal through a RAndom Faced Acoustic Lens (RAFAL), made of a material featuring a sound speed higher than water (Real et al. 2014b). The RAFAL presents a plane input face and a randomly rough output face which induces refraction and diffraction of the acoustic wave. Its dimensions are $H_\ell \times H_\ell \times (H+\xi)$, where $H_\ell = 150\ mm$, $H = 20\ mm$ and ξ is the random roughness amplitude. Features of the propagation of acoustic waves through IW, such as focal points and shadow zones, can therefore be observed. The signal acquisition is performed by a mobile hydrophone at various vertical positions, allowing to simulate virtual vertical linear arrays. A diagram of the experimental configuration is given in Fig. 3.1:

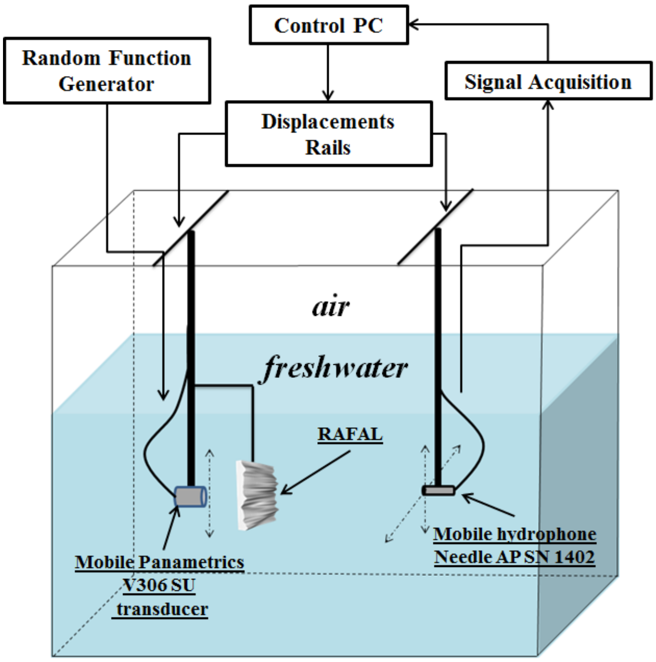

FIGURE 3.1: Tank experiment configuration.

On the receiver end, computer controlled displacements of the hydrophone simulate vertical linear arrays. The vertical displacement amplitude between two positions of the hydrophone was set to $s = 0.3\ mm$ in order to respect the sampling criterion ($s < \lambda/2$). In fresh water at $T = 20°C$, for $f_c = 2.25\ MHz$, $\lambda = 0.658\ mm$.

Automatic displacements of the various elements allow us to provide several realizations for the same fluctuation regime and to carry out statistical studies: the measurements are repeated for several source depths in order to acoustically highlight different decorrelated regions of a RAFAL (see figure 3.2). The amplitude of the source depth displacement is chosen to be at least twice the vertical correlation length of the output face roughness of the RAFAL, such that the different zones highlighted can be considered to be independent. In figure 3.2, the diameter of the beam spread projection on the RAFAL's input face is noted β. It is given by:

$$\beta = x_1\ \tan\left(\theta_{3dB}\right); \tag{3.1}$$

where x_1 is the distance between the source and the RAFAL's plane input face and θ_{3dB} is the half beam spread angle at $-3dB$ given by the following approximation:

$$\theta_{3dB} \approx 58\frac{\lambda}{d^T}. \tag{3.2}$$

In equation 3.2, d^T is the diameter of the transducer used in this experiment. Its value is given later in Table 3.3. The corresponding half beam spread angle is found to be approximately 3°.

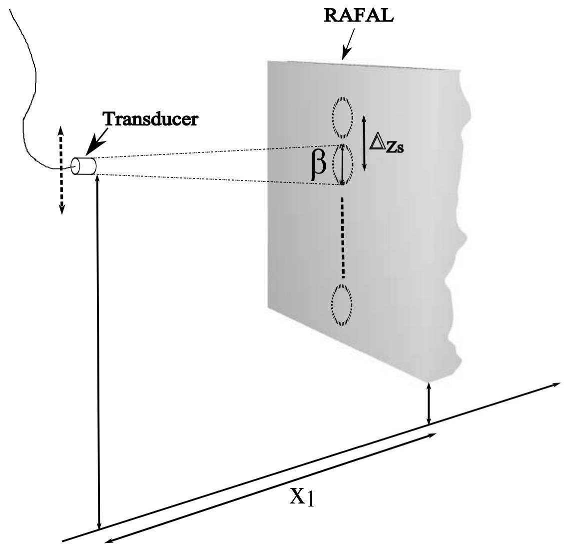

FIGURE 3.2: Source depth shift calculated to acoustically highlight indepedent RAFAL areas.

In order to be in the far field of the transducer, x_1 is chosen to be $200\ mm$. In this experimental configuration, we obtain $\beta \approx 10\ mm$. This result is in good agreement with the measured directivity, displayed in figure 3.3, where the width of the $-3\ dB$ lobe is approximately $10\ mm$.

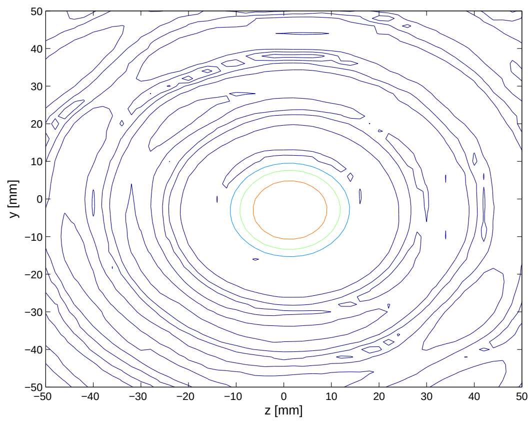

(A) Contour plot of the measured directivity pattern.

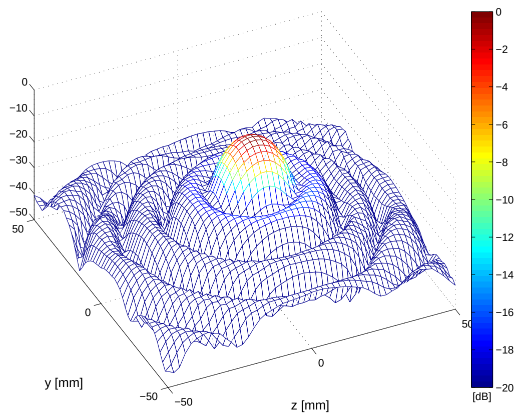

(B) 3D plot of the measured directivity pattern.

FIGURE 3.3: Measured source directivity pattern.

The number of RAFALs that need to be manufactured is determined by the number of independent realizations available on a single lens. It depends on the statistical characteristics of this lens. In order for the realizations to be independent, the shift in source depth was chosen to be equal to at least twice the vertical correlation length of the random roughness of the output face (denoted L_V). Table 3.1 gathers the source depth shifts and the number of lenses that were manufactured. In the first column, FS, PS and US stand for Full Saturation, Partial Saturation and UnSaturation, respectively.

TABLE 3.1: Source depth shift Δ_{Z_s}, in mm, vertical correlation length L_V, in mm, number of realizations per RAFAL N_r and number of manufactured RAFALs per configuration N_{RAFAL}.

Config. #	L_V $[mm]$	Δ_{Z_s} $[mm]$	N_r	N_{RAFAL}
FS	4	10	22	2
PS	7	15	21	3
US	8	20	24	4

We measured the physical properties of the material composing the acoustic lens and list them in Table 3.2. The material chosen here is referred to as *Machinable Blue Wax (MBW)* (used in Calvo et al. (2008)).

TABLE 3.2: Measured physical properties - *Machinable Blue Wax*.

Relative Density	$0.98 \pm 4.3.10^{-5}$
Longitudinal Wave Sound Speed $[m/s]$	1975 ± 15
Shear Wave Sound Speed $[m/s]$	772 ± 16
Longitudinal Wave Attenuation at 2.25 MHz $[dB/cm]$	13.1 ± 0.25

The density of the *MBW*, as shown in Table 3.2, is very close to that of water. It is therefore possible to neglect a density discontinuity at the interface water/*MBW* in computer simulations. Moreover, the shear wave attenuation was too important to be accurately measured, meaning that the propagation of shear wave could be disregarded as well.

3.3 RAndom Faced Acoustic Lens manufacturing

Once the statistical parameters of the RAFAL's output face are chosen, the propagation of acoustic wave through the designed RAFAL is tested using computer simulations. The randomly rough output face is determined by a Gaussian sampling. The roughness amplitude ξ is considered to be centered, so that $< \xi >= 0$, uniform and normal, characterized by its autocorrelation function R_ξ:

$$R_\xi = \left\langle \xi \left(z - \frac{1}{2}\zeta, y - \frac{1}{2}\eta \right) \xi \left(z + \frac{1}{2}\zeta, y + \frac{1}{2}\eta \right) \right\rangle. \tag{3.3}$$

R_ξ is a Gaussian function of the form:

$$R_\xi = \xi_0^2 \, e^{-\frac{1}{2}\frac{\zeta^2}{L_V^2}} \, e^{-\frac{1}{2}\frac{\eta^2}{L_H^2}} . \tag{3.4}$$

ξ_0 is the standard deviation of the roughness amplitude , x_0 is the average output face abscissa and L_V and L_H are respectively the vertical and horizontal correlation lengths of the randomly rough output profile.

If the original set of parameters is validated by the simulation results coupled with the dimensionless analysis, the RAFAL is manufactured in order to correspond as much as possible to the model used in the simulations. Section 3.5.1 will present some numerical tools used to anticipate for the experimental results. A ray tracing program and a code based on a parabolic equation provide outputs that allow us to validate or discard the relevance of a set of parameters for an experiment (mainly related to the RAFAL's output face random roughness).

We developed a process in four steps leading to the preparation of a sample in MBW.
Step one: the profile defined by the scaling process is interpolated and edited using a CAD (Computer Aided Design) software. This step is displayed in figure 3.4.

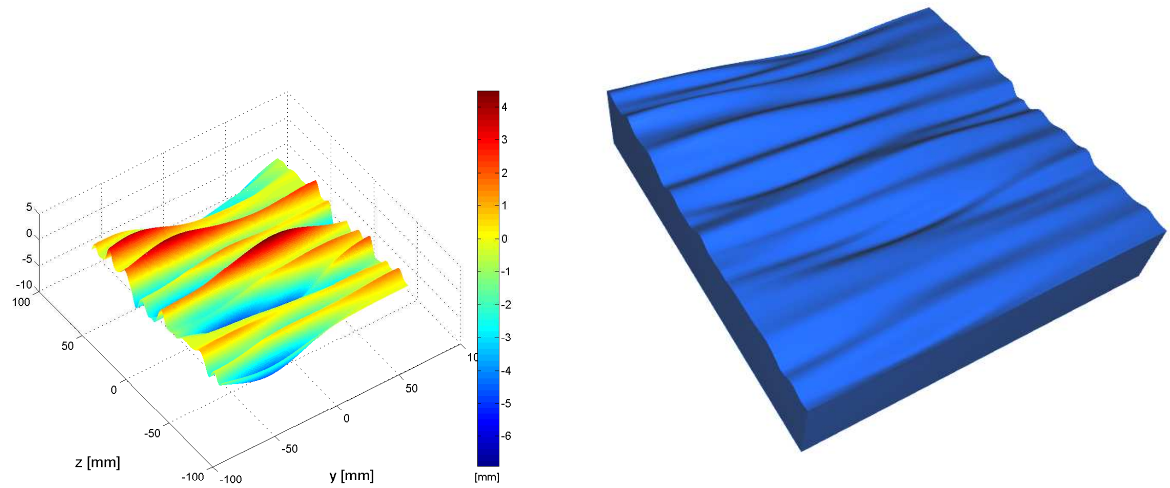

(A) Matlab generated RAFAL's randomly rough output face.

(B) CAD extruded RAFAL.

FIGURE 3.4: Numerical design of the RAFAL.

Step two: the output file of the CAD software is then sent to a 3D printer, producing a first version of the sample:

FIGURE 3.5: 3D printed RAFAL.

Nevertheless, the thermoplastic material used by the 3D printer (acrylonitrile butadiene styrene or ABS) does not feature the appropriate acoustical properties (due to its highly porous honeycomb structure unadapted to ultrasound propagation in water and inhomogeneous regarding the wavelength involved in the experiment).

Since the ABS melts at $80°C$, we can not use directly the printed object to mold the final sample (because the *Machinable Blue Wax* melts above $115°C$).

Step three: we therefore use a molding silicone (RTV 2-RTV 123) in order to obtain a "negative" mold of the original profile (step three). The steps in the realization of this negative mold are displayed by figure 3.6.

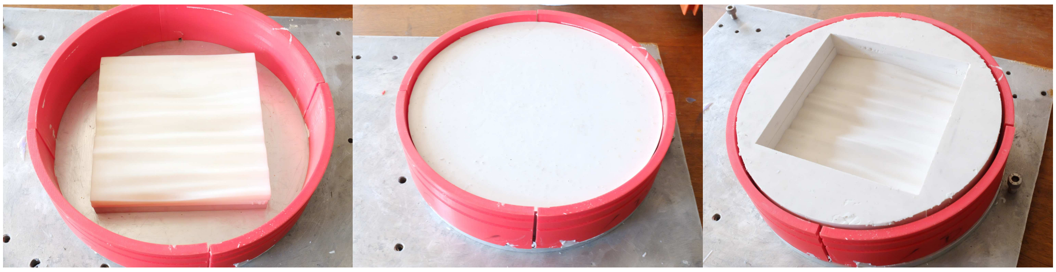

(A) 3D printed RAFAL container. (B) Pouring of the liquid silicone (C) Negative silicone mold.

FIGURE 3.6: RAFAL's negative silicone mold manufacturing.

This silicone maintains its shape at high temperature, and therefore, it allows us to perform step four: pouring the melted *MBW* in the mold. This particular step of the manufacturing process was realized under the dome of an air pumping system in order to avoid the presence of air bubbles at the surface of the RAFAL. If this step is omitted, the appearance of air bubbles at the *MBW*/silicone interface can produce unusable samples. Figure 3.7 displays a RAFAL manufactured without the air pumping step. This destructive impact of the air bubbles is evident.

FIGURE 3.7: RAFAL realized whithout the air pumping system.

Figure 3.8 shows the dome and the motor of the air pumping system. The melted MBW is poured into the silicone negative mold placed inside the dome. The pump is activated for a duration of a few seconds, which is long enough for the air bubbles to be removed from the MBW/silicone interface. The MBW then solidifies and presents the suitable shape.

FIGURE 3.8: Final step: RAFAL manufacturing under the air pumping system.

Figure 3.9 displays the final RAFALs (bottom), classified as a function of the regime of saturation that they refer to. A zoom at the RAFAL corresponding to the fully saturated regime is provided on the top figure of figure 3.9.

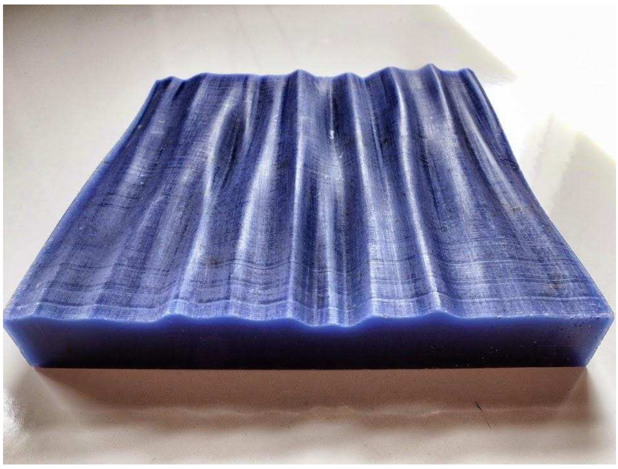

(A) Final RAFAL.

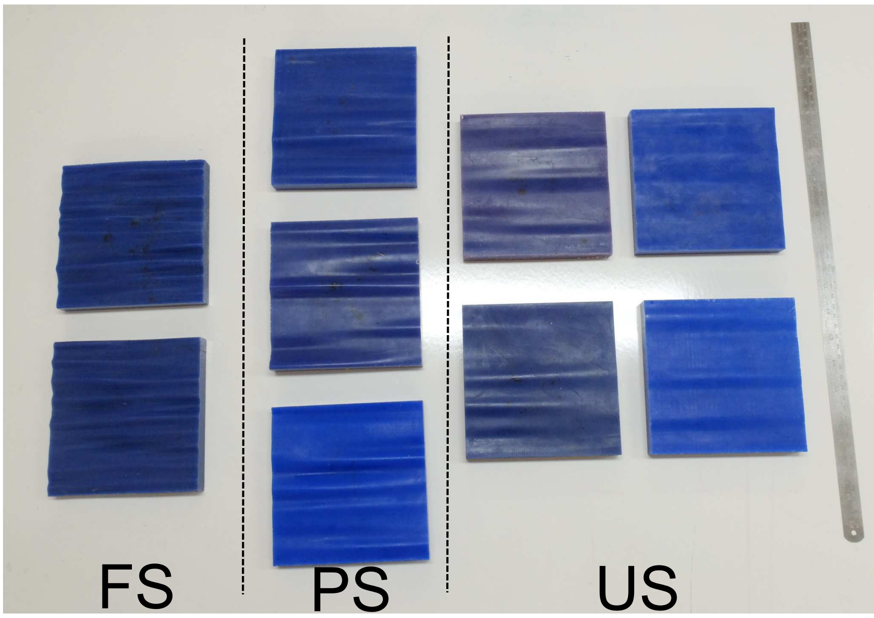

(B) All designed RAFALs. We recall that FS stands for Full Saturation, PS stands for Partial Saturation and US for UnSaturation.

FIGURE 3.9: Final manufactured RAFALs.

3.4 Laboratory equipment

The measurements are conducted in a $3\ m$ long, $1\ m$ deep and $1\ m$ wide water tank, represented in Fig. 3.10 (bottom). It is filled with fresh water. The temperature is continuously controlled using a probe. This way, the sound speed in water is known accurately at any time from the table in reference (Del Grosso and Mader 1972), assuming that its distribution is uniform throughout the water tank. The acoustical equipment is placed on motorized rails driven by a computer interface (see reference (Papadakis et al. 2008) for more details).

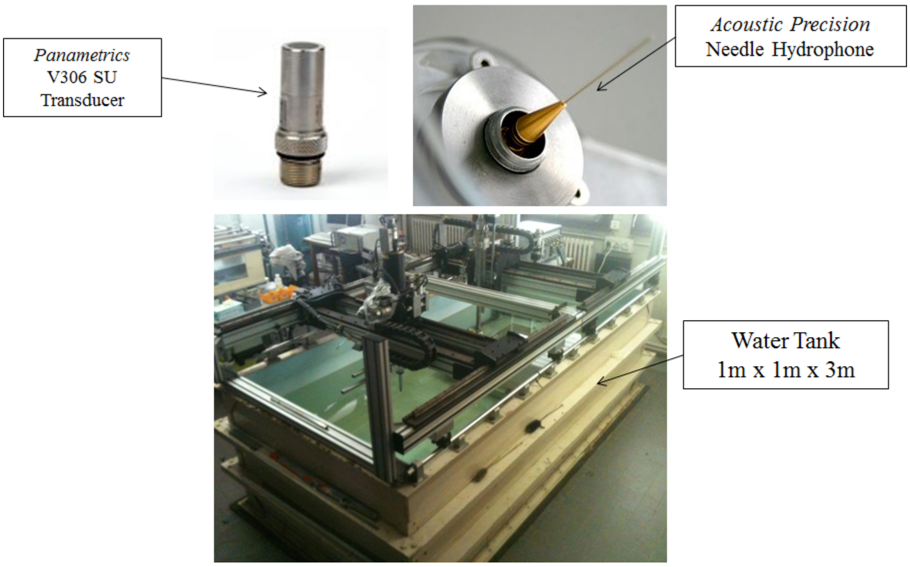

FIGURE 3.10: Experimental equipment - top left: Panametrics V306 SU transducer; top right: AP Needle hydrophone; bottom: water tank.

The transmitted signal is a continuous wave (CW) chirp at $f = 2.25\ MHz$ with a duration of $22.2\ \mu s$ ($N_p = 50$ periods) and an amplitude of $A_t = 10\ V$ (see figure 3.11) generated using a *HP* 33120A Arbitrary Waveform Generator and sent through a *Panametrics* V306 transducer (Fig. 3.10 top left) after $\times 10$ amplitude amplification by a NF 4005 High Speed Power Amplifier.

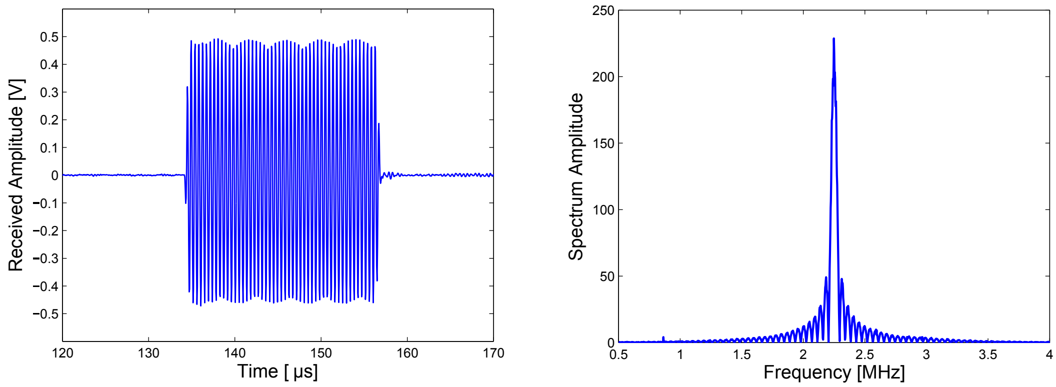

(A) Transmitted signal in the time domain.

(B) Transmitted signal spectrum.

FIGURE 3.11: Transmitted CW wavetrain.

The choice of this high frequency is justified by the narrowness of the beam spread of the transmitted signal. Indeed, it allows to carry out more realizations for a given RAFAL (see figure 3.2). A change in signal frequency would also impact the calculations of the parameters involved in the dimensional analysis (Chapter 2). Hence, frequency can here be seen as a tunable parameter allowing to span various scaled oceanic configurations. Besides, the duration of the transmitted signal was chosen so that the signal can be detected in all configurations. A fairly long signal is detected without much trouble despite the attenuation in the RAFAL, even for the longest propagation ranges.

The receiver is an *Acoustic Precision (AP)* Needle hydrophone (Fig. 3.10 top right) and the signal is collected on the control computer after high-pass filtering and amplification by a Sofranel Pulse Receiver Model 5055PR. The displacement of the receiving hydrophone is triggered on the signal acquisition so that the displacement is commanded only once the data recording is complete. We perform as many displacements as necessary to simulate virtual linear arrays: N_s positions of the hydrophone correspond to a N_s-elements virtual array. The physical and acoustical characteristics of the transducer (diameter d^T and $-6dB$ frequency band B_{-6dB}) and the hydrophone (diameter d^T, $-2dB$ flat frequency response B_{-2dB}, $-4dB$ flat frequency response B_{-4dB} and sensitivity γ) are given in Table 3.3. A block diagram of the experimental configuration is also proposed in Figure 3.12.

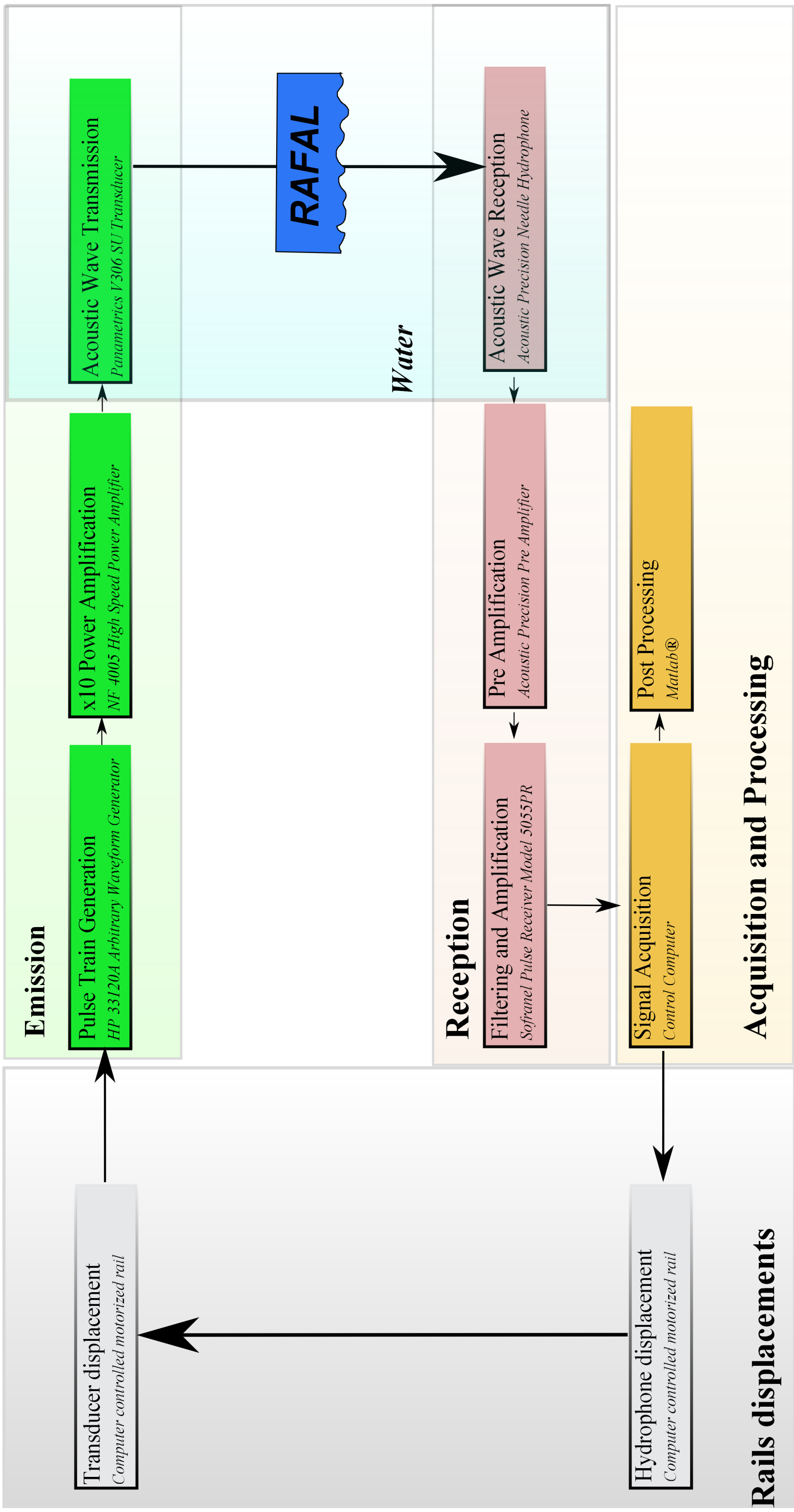

FIGURE 3.12: Block diagram of the scaled experimental protocol.

TABLE 3.3: Panametrics V306 SU transducer and AP Needle hydrophone acoustic characteristics .

	Panametrics V306 SU transducer	AP Needle hydrophone
d^T $[mm]$	13	1
$B_{-6dB}[MHz]$	$0.8 - 3.7$	-
$B_{-2dB}[MHz]$	-	$3 - 12$
$B_{-4dB}[MHz]$	-	$0.5 - 15$
$\gamma[dBre1V/\mu Pa]$	-	-241.1

3.5 Numerical tools

In support to the tank experiment, numerical tools have been developed. First, a ray tracing program and a code modeling the propagation through the RAFAL based on the parabolic equation (PE) were designed. They were used to anticipate for experimental results and also as tools to provide more realizations for a given configuration. The results obtained in the experimental framework will be compared to these numerical results in Chapter 4. Then, another PE propagation code was developed to compare the results in our experimental configuration to the corresponding oceanic medium. Indeed, since the scaling procedure presented in Chapter 2 allows to compare the tank experiment setups to realistic oceanic configurations, a comparison between the acoustic pressure fields in these two cases is of main interest. The concepts of these PE codes are presented in this section. More technical details concerning the numerical procedures are provided in Appendix E.

3.5.1 Simulation tools in the scaled experiment configuration

First, a program allowing to trace rays throughout the RAFAL was developed. This code was named RayTAL for Ray Tracing through an Acoustic Lens. Taking into account Snell's law and the sound speed discontinuity between freshwater and the material composing the RAFAL permits to model the refraction of rays. A first attempt to qualify the results obtained in various cases into regimes of saturation can be made. In fact, figure 3.13 displays the results of RayTAL in the cases of :

- the unperturbed medium, consisting in a RAFAL presenting a flat output face (figure 3.13a);
- the unsaturated regime in figure 3.13b;
- the partially saturated regime (figure 3.13c);
- the regime of full saturation in figure 3.13d;

Only the main lobe of the transducer directivity pattern was represented in figure 3.13 for the sake of clarity.

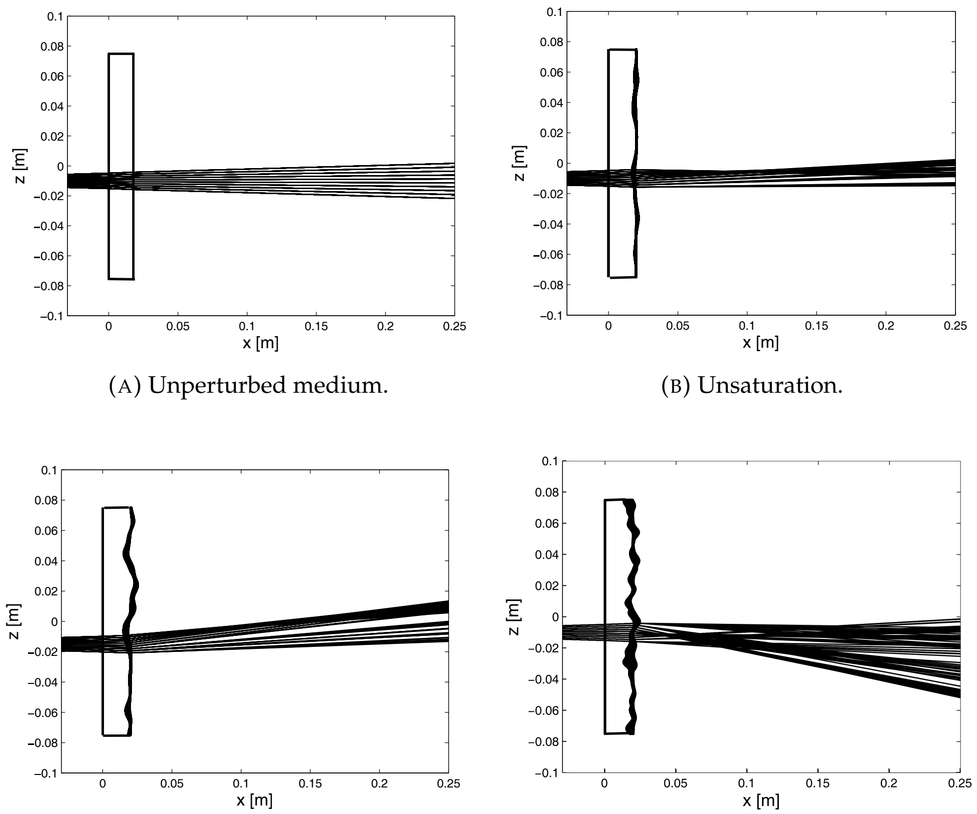

(A) Unperturbed medium.

(B) Unsaturation.

(C) Partial saturation.

(D) Full saturation.

FIGURE 3.13: RAYTAL outputs.

The unperturbed case (figure 3.13a) reveals that very little refraction is observed when the output face is flat. The difference in sound speed between water and Machinable Blue Wax is not important enough to refract the rays significantly. On the other hand, the unsaturated case, shown in figure 3.13b, displays a more important refraction of the rays. Still, the main lobe is deflected and some perturbation in the propagation can be observed. In the partially saturated study (figure 3.13c), a more significant refraction of the rays is noticed, leading to the appearance of foci. Finally, the fully saturated case, represented in figure 3.13d, displays some important refraction of the rays and an alternation between focal points, caustics and shadow zones, or speckle. The features described here are typical of the propagation of sound waves through internal waves fields. Especially, the focusing and defocusing effects described in Badiey et al. (2005) can be observed in our experimental scheme.

For comparing the results obtained with the tank measurements, a numerical program allowing to propagate an acoustic wave through the RAFAL in three dimensions was developed under the parabolic approximation. This code is an adaptation of the algorithm described in section 3.5.2. The directivity pattern of the source is fully taken into account and the results of this code, called P3DTEx (Propagation in 3D in the Tank Experiment setup) (Real et al. 2014a), are given in figure 3.14. The numerical parameters for this code are given in table 3.4:

TABLE 3.4: P3DTEx numerical parameters.

Bounds of the considered box	$[m]$
H_z	$4H_\ell$
H_y	$4H_\ell$
H_x	x_{max}
Number of calculation steps for the acoustic field	$[]$
n_z	2048
n_y	2048
n_x^ℓ	$\left[\max\left(H+\xi\right)/\delta_x^\ell\right]$
n_x	$\left[x_{max}/\delta_x\right]$

where $\delta_x^\ell = 0.1\ mm$ is the step used for the PE resolution inside the lens and $\delta_x = 1\ mm$ is the step used for the PE resolution in water. We recall that x_{max} denotes the total range of propagation and that H_ℓ denotes the dimension of the RAFAL.

The configurations studied are the same as that studied with RayTAL.

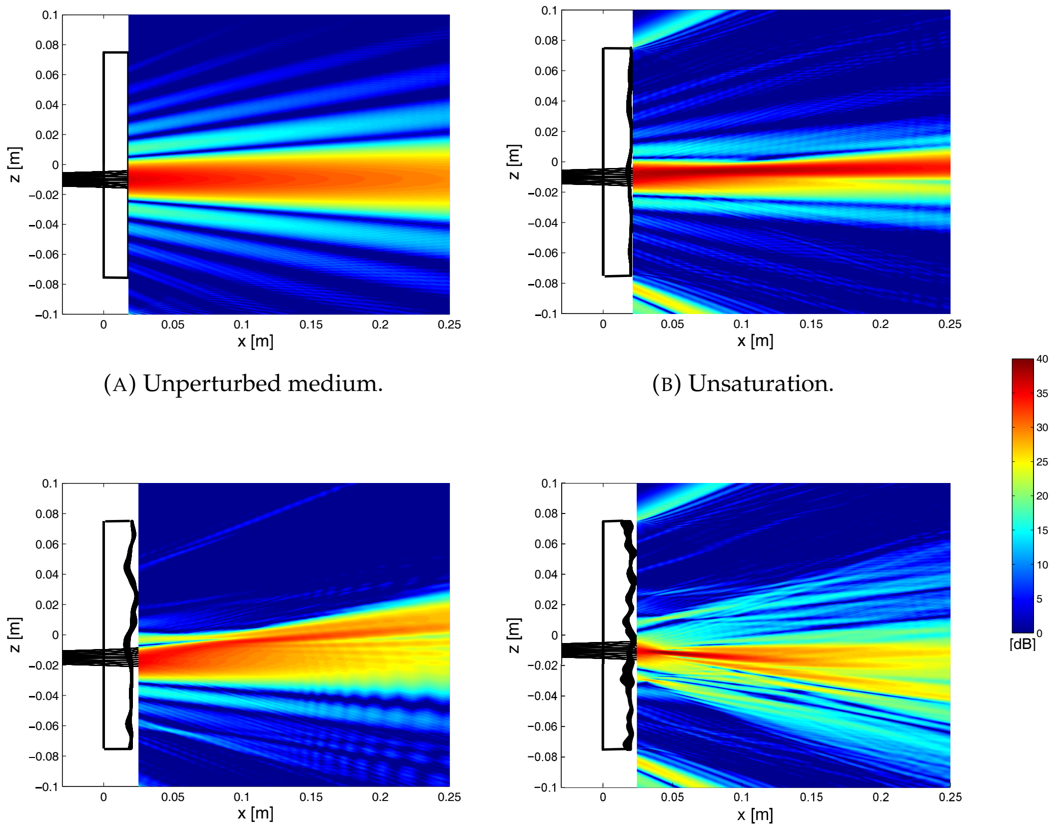

(A) Unperturbed medium.

(B) Unsaturation.

(C) Partial saturation.

(D) Full saturation.

FIGURE 3.14: P3DTEx outputs.

Similar conclusions to the RayTAL analysis can be drawn from the P3DTEx results: the unperturbed case (figure 3.14a) displays no important variation of the acoustic pressure field, which is, in this case, consistent with the source directivity pattern. In the unsaturated case (figure 3.14b), the refraction seen in figure 3.13b is again observed, leading to a pressure field slightly different than the one obtained in the unperturbed case. The focal points witnessed with RayTAL in the partial saturation (figure 3.13c) are clearly noticeable in figure 3.14c and their location is in good agreement in both cases. Eventually, the focal points, caustics and shadow zones also appear in the fully saturated configuration (figure 3.14d). As noticed in the partially saturated case, their locations is in concordance with the results obtained with RayTAL. These tools are useful since they permit to anticipate for the tank measurements and they provide a way to compare the results obtained experimentally with numerical calculations as well. This last step will be presented in Chapter 4.

3.5.2 Simulation tool in the corresponding oceanic configuration

It is also interesting to compare the measurements to the analogous "natural" oceanic configuration they correspond to, according to the scaling process detailed in Chapter 2. A PE code was developed in order to simulate the effect of sound speed fluctuations on sound propagation in the ocean (Cristol et al. 2012), based on the work of Wilson and Tappert (Wilson and Tappert 1979). The signal is transmitted from a point source located in the middle of the water column (at the point ($x_s = 0; y_s = 0; z_s = D/2$), where D is the water depth). The sound speed profile is not taken into account since we supposed an iso-velocity like environment. Also, the interaction with the sea surface and the seabed are not included: the focus is put on the effects of the sound speed fluctuations. A Split-Step Fourier algorithm is used to solve the standard parabolic equation. 3D propagation through the field of fluctuating sound speed can therefore be simulated. The numerical parameters of the code are given in table 3.5

TABLE 3.5: P3DCOM numerical parameters.

Bounds of the considered box	$[m]$
H_z	500
H_y	5000
H_x	R
Number of calculation steps for the random sound speed field	[]
n_z^{SS}	120
n_y^{SS}	60
n_x^{SS}	$[6R/L_x]$
Number of calculation steps for the acoustic field	[]
n_z	1024
n_y	8192
n_x	$[R/\delta_x]$

L_x is the longitudinal correlation length of the random sound speed field and $\delta_x = 25\ m$ denotes the step used for the resolution of the PE. Typical configurations are displayed in figure 3.15: the unperturbed case, where no sound speed fluctuations are observed (figure 3.15a, the unsaturated case (figure 3.15b, the partially saturated case (figure 3.15c) and finally, the fully saturated case (figure 3.15d). This code's name is P3DCOM, for Propagation in 3D in the Corresponding Oceanic Medium, since its aim is to compare the results obtained in our experimental configurations to the equivalent ocean medium setup, according to our scaling procedure (see Chapter 2).

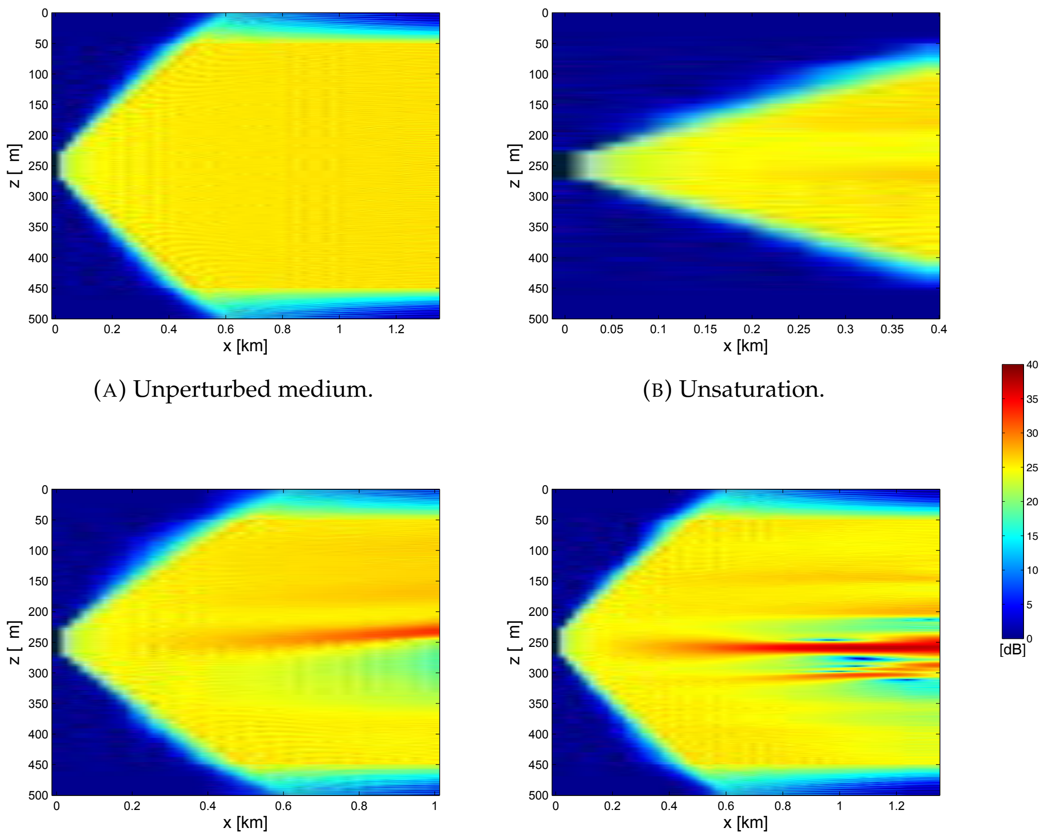

(A) Unperturbed medium. (B) Unsaturation.

(C) Partial saturation. (D) Full saturation.

FIGURE 3.15: P3DCOM outputs.

Figure 3.15a displays no variability of the sound pressure field, as expected. The unsaturated case presents weak variations in the sound field (figure 3.15b), whereas focal points can be observed in the partial saturation configuration (figure 3.15c). Focal points, shadow zones and caustics are seen in the fully saturated case (figure 3.15d). P3DCOM is a tool that reproduces the features of wave propagation through a fluctuating ocean perturbed by internal waves. Nevertheless, some limitations are important enough to be highlighted: the representativeness of the results obtained with this code is relatively arguable since the effects of the sound speed gradient and the interactions with the interfaces are not accounted for. The calculation is limited to the study of the effects of the sound speed fluctuations, which is, after all, the goal of this work. Moreover, the numerical conditioning of this code confers other limitations: at very short ranges (typically for $R << 1\ km$), the results are not exploitable in terms of large linear array statistics due to the appearance of interference linked to the Gibbs effect. One point functions, such as the complex pressure distribution and the probability density function of intensity, are, on the contrary, workable in this type of configuration. Finally, very long range propagation setup (for $R > 7-8\ km$), the relevance of the calculated sound field is questionable, since the width of the beam transmitted by the point source becomes fairly larger than the box used for the numerical calculations. In configuration where the sound waves propagate with a range between $1\ km$ and $5\ km$, the results between P3DCOM, P3DTEx and the tank experiment measurements can be compared meaningfully.

3.6 Conclusion

An experimental protocol aiming to reproduce the effects of propagation in a 3D random media with an thin acoustic lens presenting a plane input face and a randomly rough output face is presented. As explained in Chapter 2, this protocol can indeed provide acoustic data representative of the fluctuations that occur when sound waves propagate through a fluctuating ocean. The procedure leading to the manufacturing of the RAFAL allows a great number of configurations to be simulated, since the 3D printer leave room to many possibilities.

We see an interesting contribution in this experiment, since it is conducted in a controlled and reproducible manner. The capability to measure acoustic signals distorted by the sole influence of volume effects such as IW is, to us, extremely valuable.

Numerical tools allowing to anticipate for the experimental results were developed and are presented in this section. The comparison between the measurements and the synthetic data obtained with these simulations will be provided in Chapter 4.

Chapter 4

Experimental results

Contents

We show hereafter some of the results obtained using water tank measurements, under the conditions described in Chapter 3. We first focus on the identification of the regimes of fluctuations and the characteristics of the oceanic medium corresponding to our scaled experiment setup. The analysis of the complex pressure distribution (CPD) is proposed in section 4.2. The behavior of this quantity reveals some qualitative pieces of evidence of the affiliation of a particular setup to a regime of fluctuation. Some statistics of the signals studied are then presented: first, the second-order moment, or mutual coherence function (MCF) is analyzed in section 4.3. The agreement between the radius of coherence (measured and simulated) and the normalized vertical correlation length Lz/λ, defined in Chapter 2 is examined. Finally, the probability density functions (pdf) of the acoustic intensity is investigated in the various configurations.

The purpose of this chapter is to demonstrate that the proposed scaled experimental scheme faithfully reproduces the effects of 3D propagation through random medium, both qualitatively (in terms of typical features of the various regimes of fluctuations) and quantitatively (with the expected radius of coherence).

4.1 Investigated configurations

We present here the setups studied in order to be representative of realistic oceanic configurations. From the procedure detailed in Chapter 2, we adopted a set of configurations shown in Table 4.1.

The tank experiment parameters are the RAFAL's amplitude standard deviation ξ_0, vertical correlation length L_V, horizontal correlation length $L_H = 10 \times L_V$, and the propagation range between the averaged output face and the receiver array x_{dist}, all expressed in mm. The associated ocean medium parameters are the sound speed fluctuations amplitude standard deviation δc_0, in m/s, the vertical correlation length L_{V_s}, horizontal correlation length L_{H_s}, in m, and the propagation range R, in km. These parameters are listed in Table 4.1. The scaling procedure was conducted between a f_c=2.25 MHz signal in the tank experiment setup and a f=1 kHz signal in the corresponding oceanic configuration. Nonetheless, this choice is arbitrary and motivated by our will to compare the experimental results to numerical configurations. The latters are obtained with the P3DCOM code which performs best at a frequency of 1 kHz. Conceptually, other frequencies could be considered.

TABLE 4.1: Scaled experiment and corresponding oceanic medium parameters.

Frequency	f_c = 2.25 MHz			f = 1 kHz			
Config. #	$\xi_0[mm]$	$L_V[mm]$	$x_{dist}[mm]$	$\delta c_0[m/s]$	$L_{V_s}[m]$	$L_{H_s}[m]$	$R[km]$
1:FS1	2	4	250	0.77	31.9	106.3	19.9
2:FS2	2	4	150	1.04	19.9	199	5.89
3:FS3	2	4	100	1.99	14	140	2.26
4:PS1	2	7	150	1.46	23	230	2.58
5:PS2	2	7	125	1.88	20.2	202	1.78
6:US1	1	8	100	1.79	15.1	151.3	0.65
7:US2	1	8	50	2.24	12.4	247.5	0.25

The fluctuations generated in the tank experiment configuration and in the corresponding oceanic medium can be analyzed in terms of spectrum, since their spatial intercorrelation function is known (equation 3.4 for the RAFAL and equation 2.5 for the fluctuating ocean). The vertical component of these spectra of fluctuations are depicted in figure 4.1:

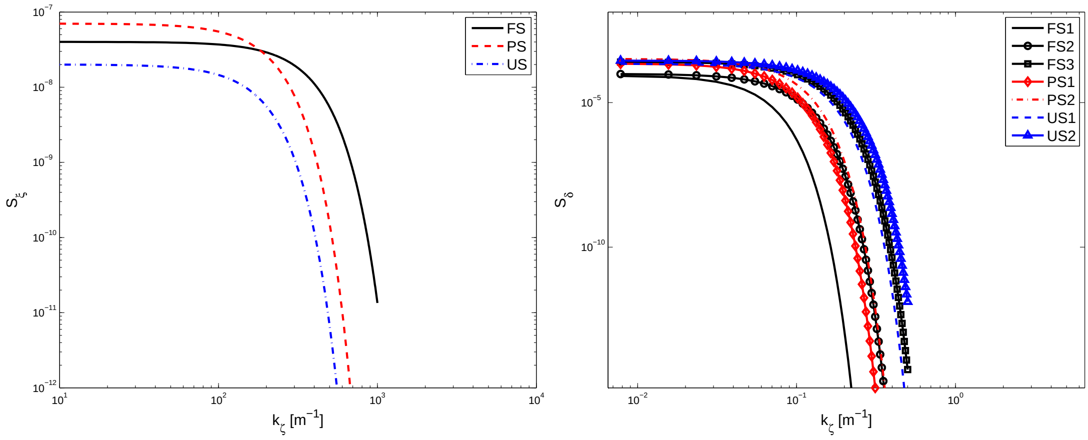

(A) Spectrum of RAFAL's randomly rough thickness

(B) Spectrum of sound speed fluctuations

FIGURE 4.1: Vertical spectra of RAFAL's thickness variations and sound speed fluctuations for each configuration in Table 4.1

As expected, the spectrum presents a single scale in both cases, as opposed to a von Karman spectrum, classically used to model the spectrum of turbulence (Blanc-Benon 1981, Cotté and Blanc-Benon 2007). This is explained by the fact that both the RAFAL's randomly rough face amplitude and the sound speed distributions follow a Gaussian law. For the latter, this corresponds to a simplified version of the IW spectrum. Nonetheless, the involved parameters ensured the realism of the investigated configurations: the sound speed fluctuations standard deviation is of the order of $1\ m/s$, with a minimum value of $0.77\ m/s$ (FS1 configuration) and a maximum value of $2.24\ m/s$ (US2 configuration). These values are typical of what can be observed in the case of perturbations due to linear internal waves (Dashen et al. 2010). The vertical correlation length of the sound speed fluctuations is also quite representative of what can be observed in the reality: from $12.4\ m$ (US2) to $31.9\ m$ (FS1). The ratio of vertical to horizontal sound speed fluctuations correlation lengths is a parameter that was tuned in order to obtain realistic results in terms of δc_0. Nevertheless, the tuning of this parameter was performed with respect to the value of the horizontal correlation length of the sound speed fluctuations, which is typically of a few hundred meter. Here L_{H_s} lies between $106.3\ m$ (FS1) and $247.5\ m$ (US2). Finally, the range of propagation is a critical parameter in an oceanic medium, since the saturation increases with the propagation distance (in the case where the environmental parameters are the same). It can be observed that R spans from a few hundred meter (R = $250\ m$ in the US2 setup) to more than ten kilometers (R = $19.9\ km$ in the FS1 configuration). .

Fig. 4.2 represents the locations of the configurations studied in the scaled experiment and oceanic medium in the $\Lambda - \Phi$ plane.

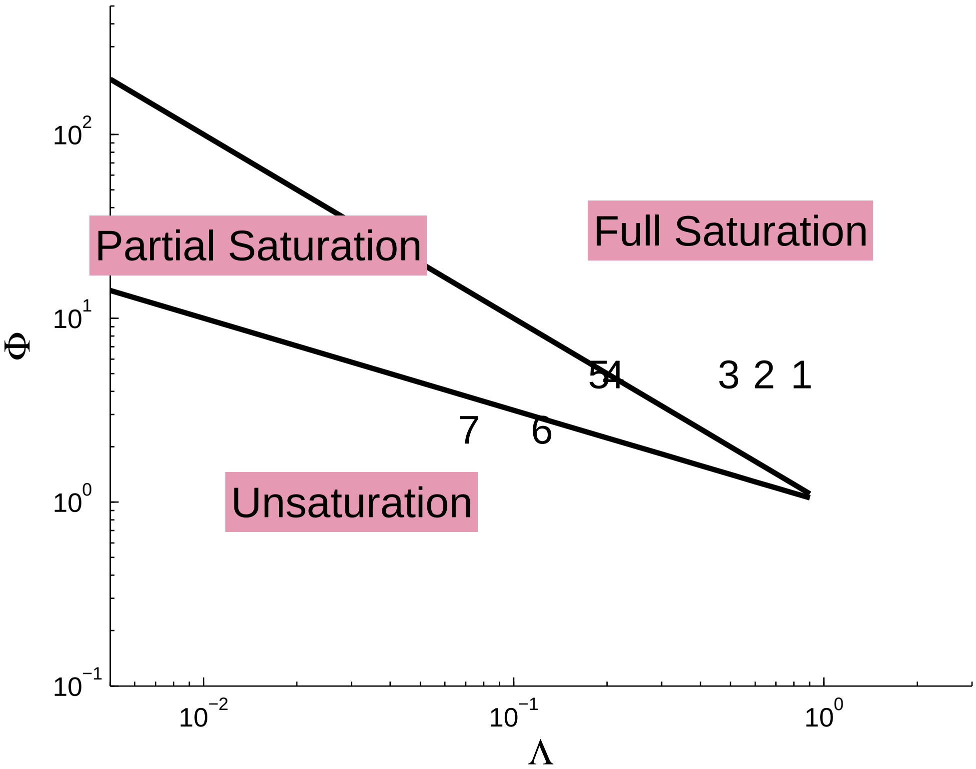

FIGURE 4.2: Experimental configurations in the $\Lambda - \Phi$ plane.

Three configurations were classified as fully saturated (FS1, FS2 and FS3), three as partially saturated (PS1, PS2) and, finally, two setups lead to unsaturation: US1 and US2.

4.2 Complex Pressure Distribution

In this section, we evaluate the behavior of the complex pressure distribution (CPD). The CPD, also called *phasor* (Dashen et al. 2010), was calculated on 8 hydrophones (corresponding to the 8 central sensors of the vertical linear array) in various configurations (using experimental or synthetic data). The real and imaginary parts of the complex pressure are displayed for each realization of the medium. The distribution of the complex pressure is compared to the mean pressure distribution ($p_0 = \sqrt{\left\langle |p|^2 \right\rangle_{N_r}}$ - where $< . >$ is the ensemble average, displayed with the dashed line) in all the following figures. The CPDs show characteristic behaviors (Dashen et al. 2010, Ehrhardt et al. 2013) that would help the classification into regimes of fluctuations. The following sections analyze the experimental and simulated data in terms of CPD for each regime of fluctuation: the unsaturated case is studied in section 4.2.1, the partially saturated case is studied in section 4.2.2 and the fully saturated case is studied in section 4.2.3.

4.2.1 Unsaturated regime

Figure 4.3 displays the CPD for the unsaturated configurations. The left figures (figures 4.3a, 4.3c and 4.3e) show the results corresponding to US1, whereas the right figures (figures 4.3b, 4.3d and 4.3f) show the US2 results. The top figures (4.3a and 4.3b) were obtained using the experimental data, the middle figures (4.3c and 4.3d) were obtained with the P3DTEx results and the bottom figures (4.3e and 4.3f were obtained with the P3DCOM results).

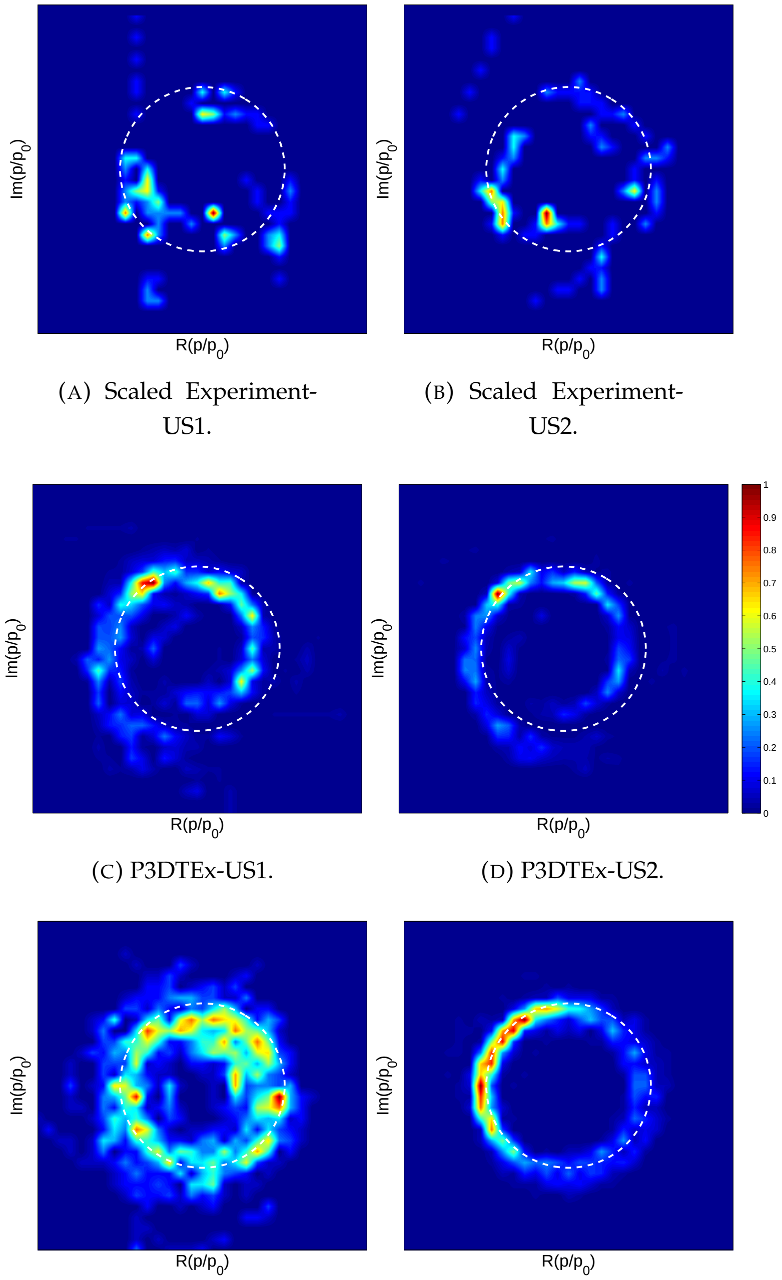

(A) Scaled Experiment-US1.

(B) Scaled Experiment-US2.

(C) P3DTEx-US1.

(D) P3DTEx-US2.

(E) P3DCOM-US1.

(F) P3DCOM-US2.

FIGURE 4.3: Complex pressure distribution (CPD) and mean complex pressure distribution (dashed circle) - Unsaturated configurations.

In all the cases studied and displayed in figure 4.3, the CPD follows relatively closely the mean complex pressure distribution, represented with the white dashed line. This analysis is quite difficult to conduct on the experimental data (figures 4.3a and 4.3b), since only 24 realizations were available, but the simulations of the experiment (figures 4.3c and 4.3d), conducted with P3DTEx with ten times more realizations, confirms the trend sensed in the experimental case. Moreover, the phasors obtained with the results of P3DCOM (figures 4.3e and 4.3f) are in excellent qualitative agreement with the results obtained in our experimental configuration. The agreement is not only good between the calculations (using experimental and simulated data) is found, but the pattern observed in the CPD in the configurations studied here also reveals a excellent concordance with the observations classically made in the unsaturated regime (Dashen et al. 2010, Ehrhardt et al. 2013). Here the CPD remains confined near the circumference of the mean pressure circle, especially in the US2 case which corresponds to the clearer case of unsaturation (see figure 4.2).

4.2.2 Partially saturated regime

Figure 4.4 displays the CPD for the partially saturated configurations. The PS1 and PS2 are shown from left to right (figures 4.4a, 4.4b, figures 4.4c and 4.4d,and figures 4.4e, 4.4f respectively). The top figures (4.4a and 4.4b) were obtained using the experimental data, the middle figures (4.4c and 4.4d) were obtained with the P3DTEx results and the bottom figures (4.4e and 4.4f) were obtained with the P3DCOM results. The results in terms of CPD are quite hard to anticipate in the partially saturated regime, since it mostly translated the transition between the unsaturated regime, which follows the mean CPD, and the fully saturated regime, which concentrates the energy in the center of the phasor (Dashen et al. 2010).

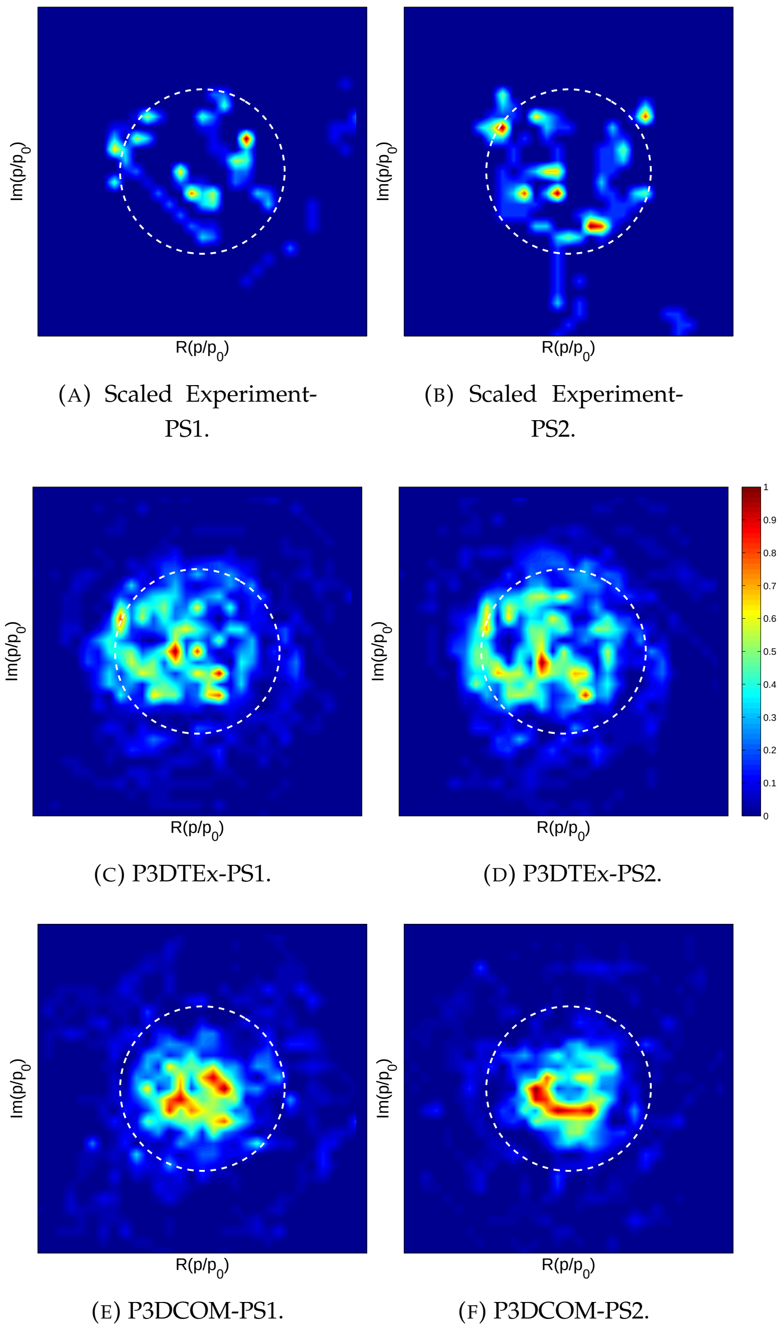

(A) Scaled Experiment-PS1.

(B) Scaled Experiment-PS2.

(C) P3DTEx-PS1.

(D) P3DTEx-PS2.

(E) P3DCOM-PS1.

(F) P3DCOM-PS2.

FIGURE 4.4: Complex pressure distribution (CPD) and mean complex pressure distribution (dashed circle) - Partially saturated configurations.

As expected, the analysis of figure 4.4 is not straightforward. Nonetheless, a radical change is observed when we compare the results presented in figure 4.4 to those obtained in the unsaturated regime (figure 4.3): the complex pressure is no longer distributed following the circle of mean CPD, but its distribution is somewhat more chaotic. Peaks of high energy can be observed close to the center of the phasor in the experimental configuration (for example, in figure 4.4a). This trend is confirmed by the corresponding result obtained with P3DTEx (figure 4.4c), where a lot of occurences are noticed in the center of the circle, with still non negligible energy outside the *zero* area. Once again, the results of P3DCOM confirm this analysis, as depicted by figure 4.4e. If it can be difficult to clearly identify the regime of fluctuation, it is quite obvious here that the unsaturated regime is not a credible candidate.

4.2.3 Fully saturated regime

Figure 4.5 displays the CPD for the fully saturated configurations. The representation of the results is similar to the one used in section 4.2.2: the FS1, FS2 and FS3 configurations are shown from left to right (figures 4.5a, 4.5d and 4.5g, figures 4.5b, 4.5e and 4.5h and figures 4.5c, 4.5f and 4.5i respectively). The top figures (4.5a, 4.5b and 4.5c) were obtained using the experimental data, the middle figures (4.5d, 4.5e and 4.5f) were obtained with the P3DTEx results and the bottom figures (4.5g, 4.5h and 4.5i) were obtained with the P3DCOM results.

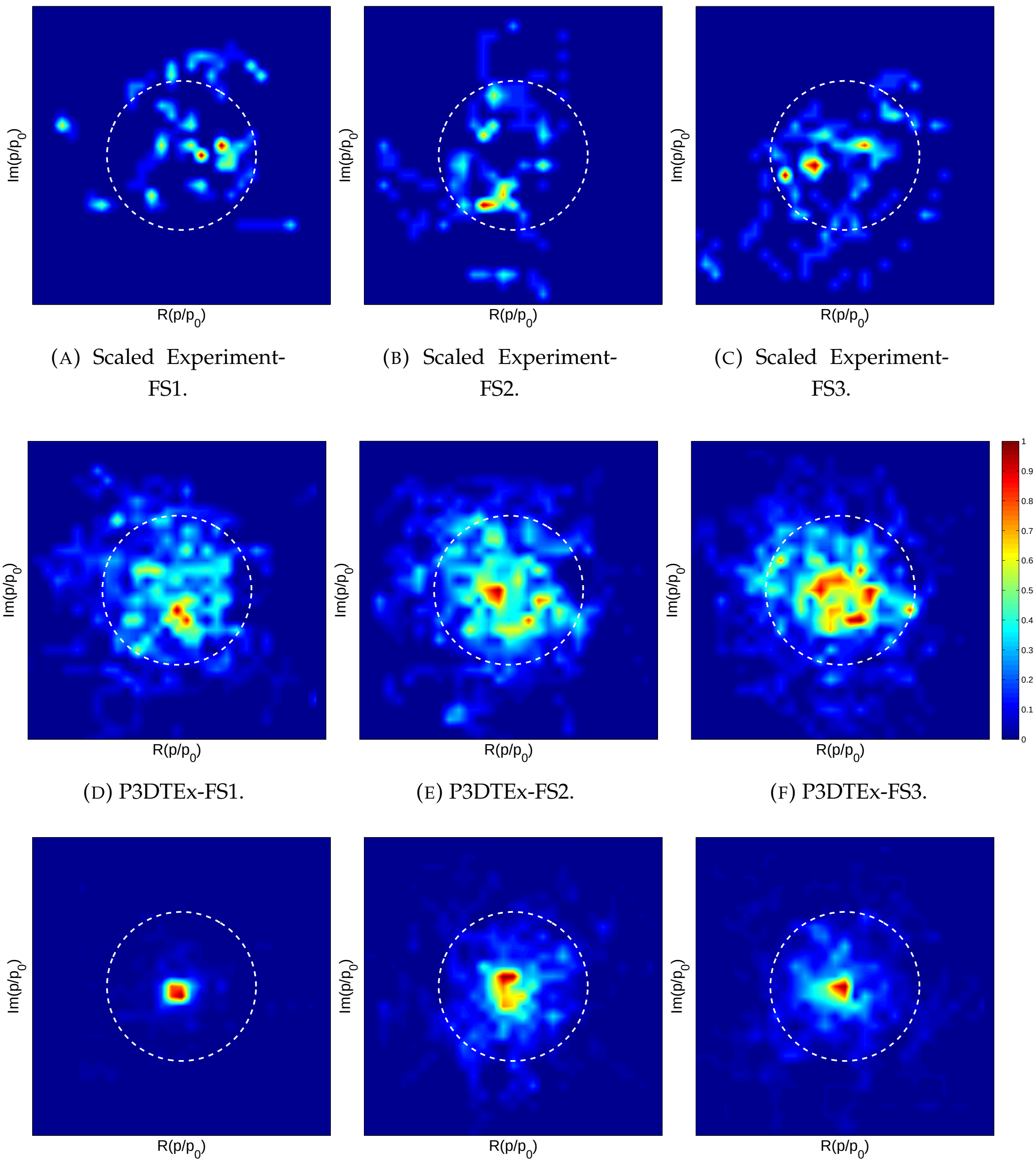

(A) Scaled Experiment-FS1.

(B) Scaled Experiment-FS2.

(C) Scaled Experiment-FS3.

(D) P3DTEx-FS1.

(E) P3DTEx-FS2.

(F) P3DTEx-FS3.

(G) P3DCOM-FS1.

(H) P3DCOM-FS2.

(I) P3DCOM-FS2.

FIGURE 4.5: Complex pressure distribution (CPD) and mean complex pressure distribution (dashed circle) - Fully saturated configurations.

The analysis of the experimental results displayed in figure 4.5 shows very little difference with the partially saturated case: some peaks are denoted at the center of the phasor, but we can still observe some occurences outside the very centered area. This result might be related to the number of realizations available with the experimental data, because the results associated with P3DTEx show a less ambiguous behavior. Indeed, most of the energy is concentrated at the center of the image, and an extremely chaotic representation of the CPD is observed. The agreement with the results provided by P3DCOM is not perfect, but the same conclusion regarding the high concentration at the center of the phasor can be drawn in both cases, for all the fully saturated configurations studied.

4.2.4 Discussion

The analysis of the CPD reveals that a discrimination can be done between the saturated and the unsaturated cases. In fact, even when a few realizations only are available, as it is the case for the experimental results, the CPD features a very different pattern. In the unsaturated regime, the CPD follows the circle of the mean pressure distribution, whereas in full saturation, the highest and most concentrated peaks are found in the center of the phasor. This difference becomes clearer when the results are compared with a great number of realizations, as observed in the P3DTEx configuration. Similar remarks can be made, but the results are more evident. This analysis is quite satisfying, since it echoes what can be noticed in the corresponding oceanic medium case (P3DCOM calculations). This is a proof of representativeness of our experimental scheme concerning the distribution of the random phase of the sound field.

Nonetheless, it is still quite difficult to distinguish the partially saturated regime from the fully saturated regime. In both cases, a chaotic representation of the phasor is obtained, which is the proof of high variability in the received signal (Dashen et al. 2010).

A blind analysis (i.e. an analysis carried out without knowing which regime of saturation is involved) may clearly identify the unsaturated regime from the saturated regimes, but it could be very difficult to differentiate the partially and fully saturated regimes. This holds true throughout the various configurations studied (experimental and simulated data). Overall, the CPD is an efficient, but limited tool to classify an experiment in terms of regime of fluctuation. It allowed us, nevertheless, to assess the relevance of our scaled experimental setup, with satisfying conclusions.

4.3 Second-order moment analysis

In this section, we compare the second-order moment results (or mutual coherence function, MCF) obtained in various configurations. The MCF, denoted Γ, provides information on how the signal is correlated along a vertical linear array. The cross-spectrum matrix is first calculated and averaged across the whole number of realizations. The obtained quantity is then averaged across the iso-spaced sensors, leading to a function of the sensor spacing. More precisely, Γ is defined as (Wilson 1998, Carey et al. 2006, Collis et al. 2008):

$$\Gamma(l) = \left\langle \left\langle \frac{p\,(n)\,p^*\,(n+l)}{|p\,(n)\,||p\,(n+l)\,|} \right\rangle_N \right\rangle_{N_r}; \tag{4.1}$$

where l is the discrete sensor spacing, p is the complex received signal (at frequency f_c = 2.25 MHz), $.*$ denotes the complex conjugate, $< . >_N$ is the ensemble average over the VLA (variable n) and $< . >_{N_r}$ is the ensemble average over the number of realizations.

In this section, $\Gamma(l)$ is evaluated for several configurations and for all the regimes of fluctuations. In figures 4.6b to 4.8d, the scaled experiments results are represented by the red circles and the P3DTEx are plotted using magenta diamonds. When available, the results associated with P3DCOM are displayed with cyan squares.

The experimental and simulated results are compared to the theoretical solution for the MCF (Flatté and Rovner 2000, Flatté 2002, Collis et al. 2008, Dashen et al. 2010), displayed using a black solid line in figures 4.6b to 4.8d. In these references, the MCF is described as an exponential function parameterized by the radius of coherence ρ_c. The quadratic form of the phase-structure function is used (Flatté 2002). We compare our experimental and simulation results using the ratio L_z/λ as the radius of coherence. The results associated with this formula will be referred to as simplified theory (ST) :

$$\Gamma^{ST}(l) = e^{-0.5\left(\frac{l}{R_c}\right)^2}; \tag{4.2}$$

where R_c is the discrete radius of coherence.
Note that the theoretical solutions for the 3D fluctuating ocean and for our experimental scheme is the same, according to the calculations and the scaling procedure detailed in Chapter 2.

The comparisons obtained from the simulations provides a tool to test the results obtained in the water tank. The idea that the MCF should behave differently depending on a specific regime of fluctuation is counterintuitive: the radius of coherence can be greater in a fully saturated case than in a unsaturated case. Therefore, no comparison between the results obtained in various regimes of fluctuations is significant. A comparison between the different sections 4.3.1 to 4.3.3 present the results in terms of the MCF for a $64-$sensor VLA. We emphasize on the fact that a consistency in terms of the evolution of the MCF as a function of the saturation regime is sought out, rather than a perfect agreement between the different calculations.

4.3.1 Unsaturated regime

In this section, we present the results associated with the unsaturated regime (US1, US2). As presented in Table 3.1, 24 realizations were performed in order to obtain the results presented here. Figures 4.6b and 4.6c display the MCF obtained for the US1 and the US2 configurations respectively. As explained in Chapter 3, section 3.5.2, the results in terms of MCF corresponding to the P3DCOM calculations are not available for the configurations considered here, because of the numerical interference generated by the code at the very short distances involved in the US1 and US2 setups (respectively R = 650 m and R = 250 m).

Nevertheless, the agreement is excellent between the calculations in US1 and US2 configurations, as depicted by Fig. 4.6.

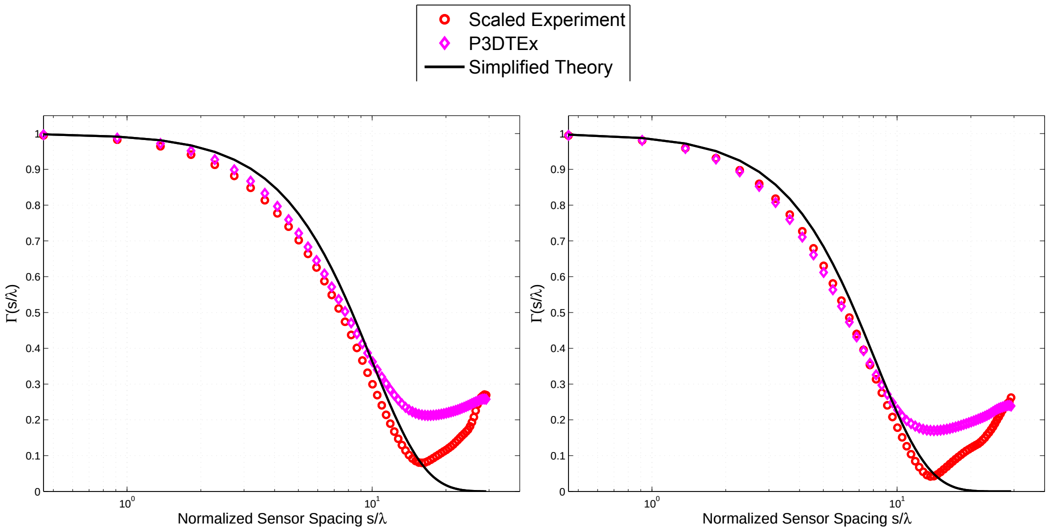

(B) US1.

(C) US2.

FIGURE 4.6: MCF - 64-sensor vertical linear array- Unsaturated configurations.

First, the MCF corresponding to the scaled measurements and P3DTEx are in excellent agreement, which reveals a high accuracy of the experimental protocol realization. Despite the fact that the number of realizations is much higher in the P3DTEx case (N_r = 240, whereas in the scaled measurements case, N_r = 24), the agreement between the main lobe of the MCF is good. This is a sign that the number of realizations carried out in the tank experiment is sufficient to analyze the MCF. Then, the curves corresponding to the simplified theory is almost superimposed with the scaled measurements and the P3DTEx results. This shows remarkable realism of the scaled experiment configuration: the objective of obtaining a pressure field with a predetermined radius of coherence is here completed.

4.3.2 Partially saturated regime

The results associated with the configurations classified as partially saturated are studied in this section. Figure 4.7 represents the results in terms of MCF for the PS1 (figure 4.7b), and PS2 (figure 4.7c) configurations. The agreement between the results provided by the scaled measurements, the numerical code (P3DTEx and P3DCOM) and the simplified theory is excellent in the PS1 and PS2 configurations.

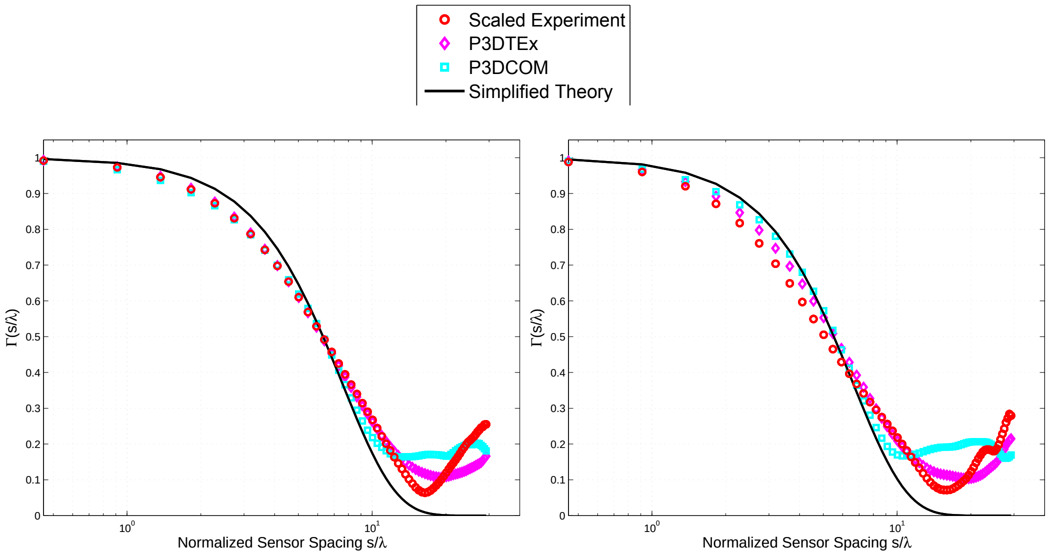

(B) PS1. (C) PS2.

FIGURE 4.7: MCF - 64-sensor vertical linear array- Partially saturated configurations.

As denoted in the unsaturated case (section 4.3.1), the agreement between the scaled measurements results and the scaled measurements simulations (P3DTEx) is excellent in all cases. The measurements were, here also, conducted with good care and accuracy. The agreement with the theoretical curve is very good in all cases, especially in the PS1 configurations (figure 4.7c), where all calculations are almost superimposed. A few differences are observed with the results obtained with P3DCOM in the PS2 case(figure 4.7c). Indeed, in this configuration, the MCF obtained with the scaled experiment data in the corresponding oceanic medium is slightly narrower. Nevertheless, the agreement between our scaled experimental protocol and P3DTEx is good throughout the two partially saturated configurations. Overall, the slight deviation observed in the PS2 configuration does not mitigate the excellent agreement between the various calculations in the presented cases.

4.3.3 Fully saturated regime

We present here the results associated with the configurations identified as fully saturated in section 4.1. For the experimental cases, the number of realization N_r was taken equal to 22 according to Table 3.1. The simulations allowed us to obtain ten times more realizations in the P3DCOM and P3DTEx frameworks. If the agreement between the various calculations is good overall, some deviations more important than in the partially saturated regime (section 4.3.2) and the unsaturated regime (section 4.3.1). In spite of that assessment, the evolution of the MCF throughout the setups studied here is consistent: as we follow the configurations from FS1 (figure 4.8b) to FS3 (figure 4.8d) through FS2 (figure 4.8c), the theoretical radius of coherence L_z/λ decreases, meaning that the MCF should narrow. This is clearly observed in figure 4.8:

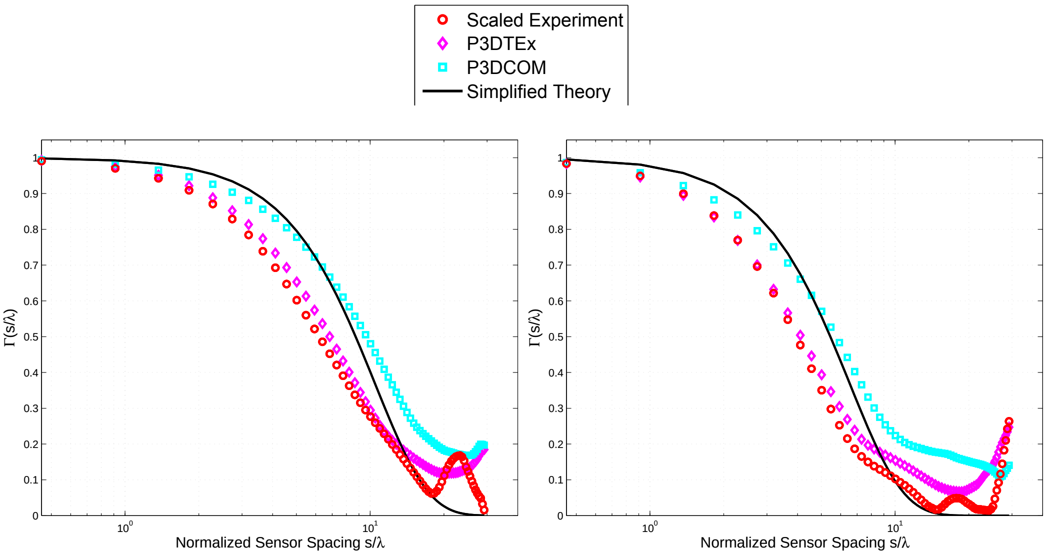

(B) FS1. (C) FS2.

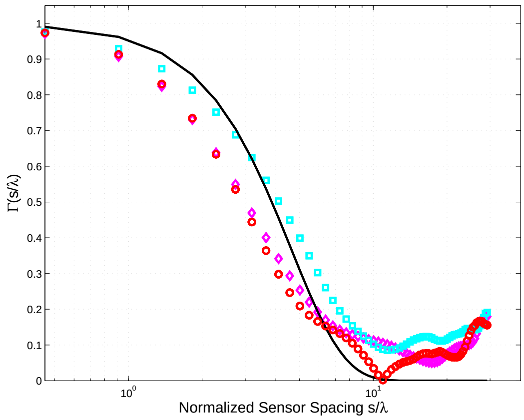

(D) FS3.

FIGURE 4.8: MCF - 64-sensor vertical linear array- Fully saturated configurations

Again, the agreement between the water tank measurements and P3DTEx is excellent in all cases, meaning that the differences should not be attributed to measurements uncertainties. Moreover, the results obtained with P3DCOM are in good concordance with the theoretical results, especially in the FS1 (figure 4.8b) and FS3 (figure 4.8d) configurations. Overall, the MCF obtained in our experimental framework (with experimental or synthetic data) is narrower than the expected MCF. This result can be explained by the approximations used to derive an expression for the theoretical radius of coherence in Chapter 2. In fact, the Small Slope Approximation was used and, as depicted by table 4.1, the statistical parameters of the output face of the RAFAL in the fully saturated cases provide an important roughness amplitude and a small vertical correlation length. This could cause the SSA to be slightly inaccurate in these cases, since the slope of the RAFAL's roughness may be relatively important. Notwithstanding this explanation, the results found in this section still provide results in good concordance, since the behavior of the MCF is very consistent as the theoretical radius of coherence diminishes.

4.3.4 Discussion

The study of the MCF was meaningful in several ways: it first validated the experimental setup, since, in all cases, the measured MCF is in excellent agreement with the MCF computed with P3DTEx for the same configuration. This reveals the highly accurate control of the measurements conducted in the water tank, ensuring the reproducibility of the experiment.

Comparing these results with the output of P3DCOM was also satisfying, meaning that the scaling method proposed in this section is quite relevant for the second-order moment of the sound field.

The theoretical curve, presented for all the cases and tuned with scaling parameter L_z/λ, tends to underestimate the results in terms of width of the coherence function. However, the evolution of Γ is very consistent in all cases for every regime (Real et al. 2015b).

Fig. 4.9 displays the match between the estimated radii of coherence using simulated data (both using P3DTEx and P3DCOM), recorded data and simplified theory. The radius of coherence was defined as the sensor spacing $l = R_c$, so that, in our case, $\Gamma(R_c) = e^{-0.5}$ (Carey 1998). In the continuous domain, the radius of coherence is noted ρ_c.
The statistical stability of $\Gamma(s/\lambda)$ is evaluated in the P3DTEx case by repeating the calculation ten times. The standard deviation of Γ was therefore calculated and is represented in Fig. 4.9. Similarly, the standard deviation of Γ in the P3DCOM case was computed. They are respectively noted σ^{P3DTEx} and σ^{P3DCOM} in Fig. 4.9. Note that it was not possible to compute the same standard deviation for experimental data, since it would have required ten times more realizations. Considering the time needed to manufacture a RAFAL and conduct the acoustic measurements, this would have been unrealistically long. On the other hand, other sources of uncertainty in the evaluation of ρ_C^{Exp} are discussed later in this section.

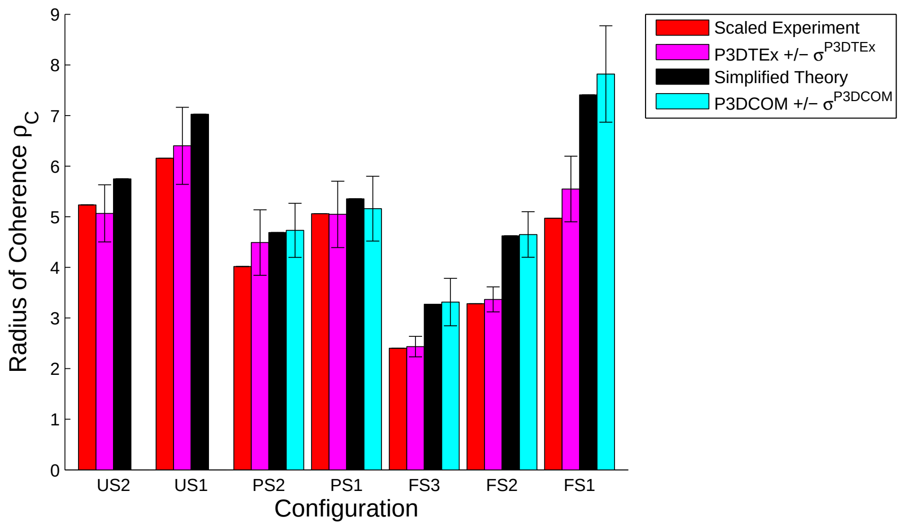

FIGURE 4.9: Comparison of radii of coherence ρ_C obtained with P3DCOM, experimental data, P3DTEx and simplified theory from left to right in all configurations.

The analysis of Fig. 4.9 echoes the previous conclusions: the match between theoretical, simulated and measurements is good for most cases. As an example, in FS3 configuration, $\rho_C^{ST} = L_V/\lambda = 3.27$, in the experimental case $\rho_C^{Exp} = 2.4$, and the simulated data showed $\rho_C^{P3DTEx} = 2.4$ in the tank experiment setup and $\rho_C^{P3DCOM} = 3.31$. The analysis carried out in section 4.3.3 holds true here: the theoretical solution and P3DCOM are in excellent agreement; similarly, the scaled experiment and P3DTEx results are also in remarkable concordance, but a difference is noted between these two groups, due to the relative validity of the SSA in this configuration. On the other hand, the PS1 configuration displays a great agreement between all calculations, since $\rho_C^{ST} = L_V/\lambda = 5.35$, $\rho_C^{Exp} = 5.1$, $\rho_C^{P3DTEx} = 5.05$ and $\rho_C^{P3DCOM} = 5.1$.

It is interesting to notice the slight differences between the results obtained using the tank measurements and P3DTEx: the results are very similar, but the radius of coherence calculated in the simulation framework exceeds the scaled experiment radius in all cases. This may be explained by the uncertainty on several experimental parameters. For example, the vertical displacement step of the hydrophone undergoes some errors up to $0.1\ mm$. Assuming that the error in vertical displacement ϵ follows a normal distribution (zero mean, variance σ_ϵ^2), so that $\epsilon \in \mathcal{N}\left(0, \sigma_\epsilon^2\right)$, where $\sigma_\epsilon^2 = 0.01^2$, we can calculate the resulting error in the estimation of the radius of coherence. This error is of the order of 0.05 (normalized by the wavelength) and does not represent a significant influence on the final result, as hinted in section 4.3.3.

In addition to the sensor dispersion, other factors may impact the accuracy of the MCF analysis: The plane input face of the RAFAL is not guaranteed to be perfectly normal to the direction of propagation, although retrodiffusion measurements were conducted to ensure this orthogonality. The latter was in fact measured by comparing the time travel of signal reflected from various locations of the RAFAL's plane input face. Furthermore, slight local errors in the randomly rough face amplitude of the RAFAL are induced, due to the manufacturing process. Finally, the physical characteristics of the *Machinable Blue Wax* composing the RAFAL were measured within uncertainties (see Table 3.2). This could lead to possible differences between the results obtained with the experimental data and P3DTEx.

Again, these differences are so small that the overall appraisal of this section is that the measurement were carried out with very good accuracy and close attention. Despite some gaps between the radii of coherence estimated in the fully saturated regime, we can state that our experimental protocol fulfills its second objective: its allows to produce acoustic pressure field with the expected radius of coherence, in other words, it generates the wished decorrelation of the acoustic data.

4.4 Fourth-order moment analysis: intensity fluctuations

We evaluate in this section a third objective connected with the fourth-order moment: the distribution of the acoustic intensity in all the considered configurations. The probability density function (pdf) of acoustic intensity, defined as $I = |p|^2$, is indeed a relevant tool to sort out the configuration into the saturation regimes, since very different qualitative behaviors may be expected for the unsaturated and saturated cases. In the fully saturated case, the pdf of normalized acoustic intensity $I/<I>$, decreases from the low $I/<I>$ to the higher $I/<I>$ exponentially (Flatté et al. 1987, Blanc-Benon and Juvé 1993). On the contrary, in the unsaturated case, the pdf of $I/<I>$ follows a log-normal distribution (Blanc-Benon and Juvé 1993, Flatté et al. 1987), meaning that the log of the intensity $\iota = \log(I/<I>)$ is normally distributed, with highest values around $I/<I>= 1$. The histograms of normalized intensity are calculated in all the regimes of fluctuations considered, using experimental and synthetic (P3DTEx and P3DCOM) data. They are computed following the Freedman-Diaconis rule (Freedman and Diaconis 1981) for the bin size s_B, so that:

$$s_B = 2\frac{\mathrm{IQR}(x)}{n_I^{1/3}}, \tag{4.3}$$

where IQR is the interquartile range and n_I the length of the intensity vector (i.e. the number of realizations N_r times the number of sensors);

Comparison with theoretical pdfs are also provided throughout this section. Three theoretical solutions are computed here: first, the exponential distribution, defined as (Strohbehn et al. 1975):

$$W(I) = \frac{I}{<I>}e^{-\frac{I}{<I>}}, \tag{4.4}$$

The exponential distribution is classically used to describe the normalized intensity pdf in the case of full saturation (Blanc-Benon and Juvé 1993). Nevertheless, a better agreement (Colosi et al. 2001) was found when modulating the exponential distribution with the scintillation index SI, defined as:

$$SI = \frac{<I>^2}{<I^2>} - 1, \tag{4.5}$$

A second solution, the modulated exponential (ME) distribution is given by (Colosi et al. 2001):

$$W(I) = e^{-\frac{I}{<I>}}\left[1 + \frac{(SI-1)}{4}\left(\frac{I^2}{<I>^2} - 4\frac{I}{<I>} + 2\right)\right]. \tag{4.6}$$

Finally, as a third solution, the log-normal pdf is also computed, since, in the unsaturated regime, the log intensity ι is supposed to be normally distributed (Tatarskii 1971). The log-normal pdf is defined as:

$$W(I) = \frac{1}{\sqrt{2\pi} I \sigma} e^{-\left[\left(ln\left(\frac{I}{m}\right)+\frac{\sigma^2}{2}\right)^2 \frac{1}{2\sigma^2}\right]}; \tag{4.7}$$

where σ and m are respectively the standard deviation and mean of the normalized log intensity ι. It was otherwise shown in Blanc-Benon and Juvé (1993) that the normalized intensity distribution in all the regimes of fluctuation could be described by a generalized Gamma distribution.

The main objective of this section is to attest the capability of our experimental scheme to satisfy a third objective: mimicing the behavior of acoustic waves propagation through a fluctuating medium in terms of normalized intensity distribution. Besides the qualitative comparison between the obtained histograms, the two-sample Kolmogorov-Smirnov test (Massey 1951) is computed. This test compares two distributions and rejects or accepts the null hypothesis H_0 that states that both distributions are not sufficiently different to come from different distributions. The output of the test, denoted h_{KS} is either 0 if the null hypothesis is accepted, or 1 if the null hypothesis is rejected and opposite hypothesis H_1 is accepted.

The unsaturated case is discussed in section 4.4.1, whereas the partially saturated and fully saturated cases are analyzed in sections 4.4.2 and 4.4.3 respectively.

4.4.1 Unsaturated regime

Figure 4.10 displays the results in terms of normalized intensity pdf for the unsaturated configurations. The first line displays the results obtained with the experimental data in the US1 (figure 4.10b) and in the US2 (figure 4.10c) configurations, the middle line displays the results obtained with P3DTEx in the US1 (figure 4.10d) and in the US2 (figure 4.10e) configurations and the bottom line displays the results obtained with P3DCOM in the US1 (figure 4.10f) and in the US2 (figure 4.10g). Again, the results in the experimental framework were obtained with N_r realizations ($N_r = 24$ in the unsaturated case), and the simulations were carried out with ten times more realizations, which explains the differences regarding the number of points represented in figure 4.10. The histograms were computed on the 8 central sensors of the vertical linear array.

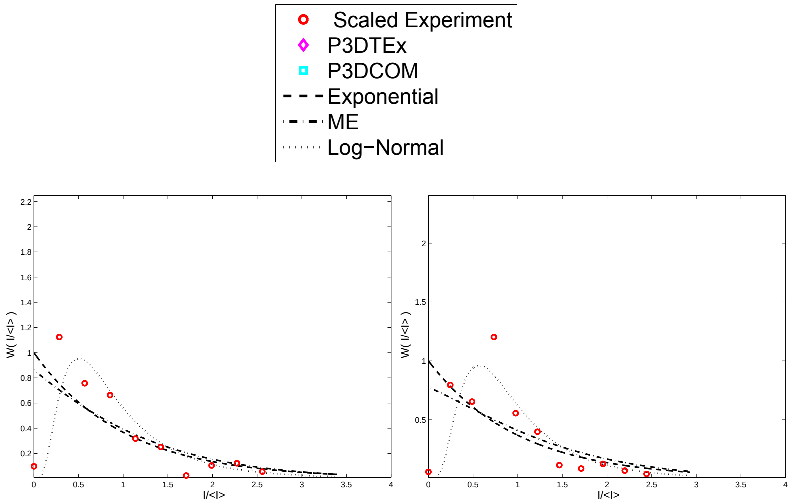

(B) Scaled experiment - US1.

(C) Scaled experiment - US2 .

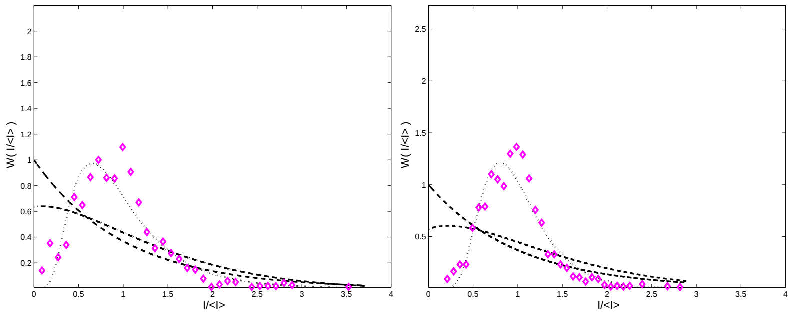

(D) P3DTEx - US1.

(E) P3DTEx - US2.

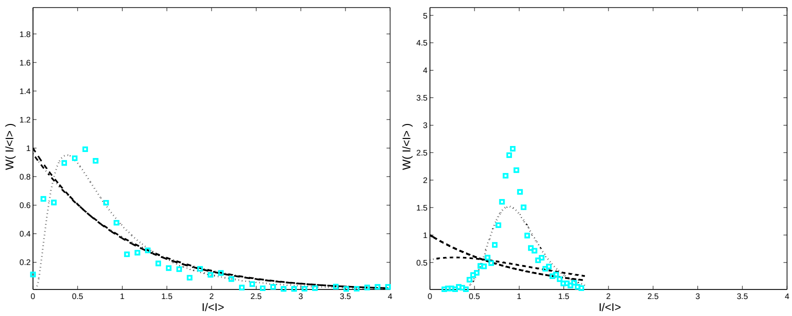

(F) P3DCOM - US1.

(G) P3DCOM - US2.

FIGURE 4.10: Intensity distributions (on 8 sensors) per regime (left: US1 and right: US2) and configuration (top: scaled experiment, middle: P3DTEx, bottom: P3DCOM. The dashed line is the exponential distribution, the dashed-dotted line is the ME distribution and the dotted line is the log-normal distribution.

In the scaled experiment cases, even if only a few realizations are available, the normalized intensity pdf seems to fit the log-normal distribution. This is confirmed by the results obtained with P3DTEx, where, in the US1 (figure 4.10d) and in the US2 (figure 4.10g) configurations, the log-normal distribution is the best candidate. As explained in Chapter 3, the short range configurations lead to numerical interference which can perturb the results. This explains the aspect of the histogram in figures 4.10f and 4.10g, where the log-normal distribution can still be presumed. It is more obvious in the US2 case. The latter was already displaying feature of unsaturation in the CPD study because of its position in the $\Lambda - \Phi$ plane. In fact, it is the most unsaturated case. However, US1 is closer to the boundary between unsaturation and partial saturation which can explain the pdf observed here.

The Kolmogorov-Smirnov test can be used to compare the pdfs obtained in the unsaturated case. Despite the fact that numerical artifacts lead to results difficult to interpret, the Kolmogorov-Smirnov validates the null hypothesis that the distributions are similar in all configurations. The results of this test are provided in table 4.2.

h_{KS}	US1	US2
(Scaled Experiment; P3DTEx)	0	0
(Scaled Experiment; P3DCOM)	0	0
(P3DTEx; P3DCOM)	0	0

TABLE 4.2: Kolmogorov-Smirnov test value h_{KS}: comparison between the unsaturated cases.

4.4.2 Partially saturated regime

Figure 4.11 displays the results in terms of normalized intensity pdf for the partially saturated configurations. As in section 4.4.1, the first line displays the results obtained with the experimental data in the PS1 and PS2 configurations (figures 4.11b, 4.11c respectively) , the middle line displays the results obtained with P3DTEx in the same configurations (figures 4.11d to 4.11g) and, similarly, the bottom line displays the results obtained with P3DCOM (figures 4.11f to 4.11g).

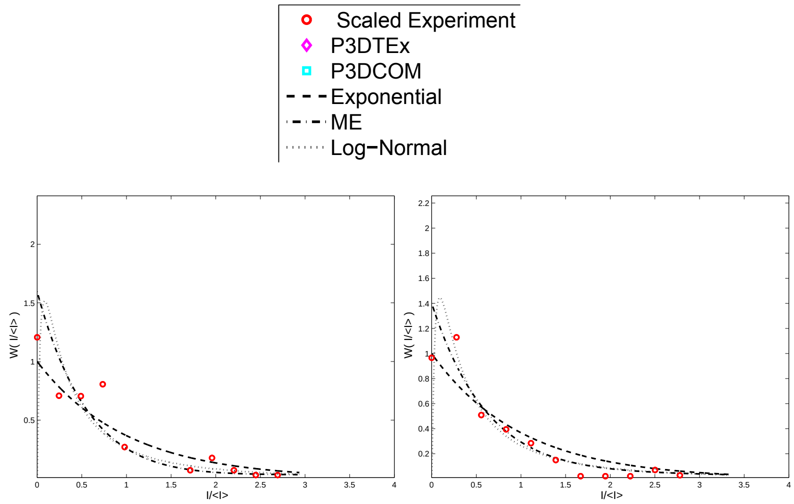

(B) Scaled experiment - PS1.

(C) Scaled experiment - PS2.

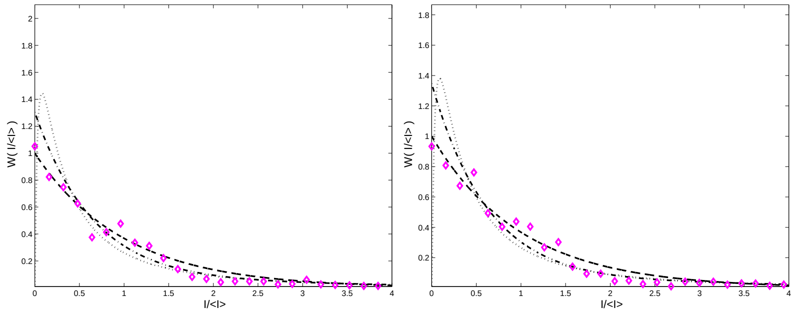

(D) P3DTEx - PS1.

(E) P3DTEx - PS2.

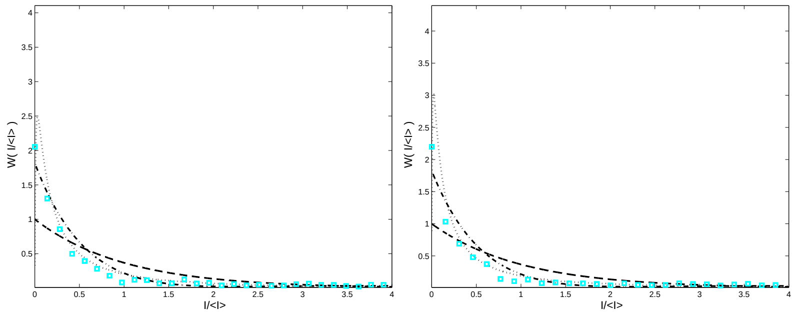

(F) P3DCOM - PS1.

(G) P3DCOM - PS2.

FIGURE 4.11: Intensity distributions (on 8 sensors) per regime (left: PS1 and right: PS2) and configuration (top: scaled experiment, middle: P3DTEx, bottom: P3DCOM. The dashed line is the exponential distribution, the dashed-dotted line is the ME distribution and the dotted line is the log-normal distribution.

The results displayed in figure 4.11 show a good agreement between the scaled experiments and P3DTEx in the PS1 and PS2 configurations, were the pdf follows relatively closely the exponential distribution. In the P3DCOM calculation, PS1 also displays a good agreement with the exponential distribution. Nevertheless, PS2 in the scaled experiment and in P3DTEx frameworks do not show a clear decay from the low normalized intensity values. Indeed, a lobe is observed in these cases and the log-normal distribution is also a credible candidate. In spite of these remarks, table 4.3, reveals a good concordance between all the configurations studied here.

h_{KS}	PS1	PS2
(Scaled Experiment; P3DTEx)	0	0
(Scaled Experiment; P3DCOM)	0	0
(P3DTEx; P3DCOM)	1	0

TABLE 4.3: Kolmogorov-Smirnov test value h_{KS}: comparison between the partially saturated cases.

Overall, the behavior of the pdf in the partially saturated regime is ambiguous since it consists of a tradeoff between the exponential and the log-normal distributions. The equivocal study of the partially saturated case is highlighted by the mismatch between the intensity distributions obtained in the PS1 case (P3DCOM and P3DTEx). This echoes the observation of figures 4.11d and 4.11f, where, in the scaled experiment case, a secondary lobe appears as a residual of a log-normal distribution, whereas, in the equivalent oceanic case, this phenomena is not present. This analysis is consistent with the fact that the partially saturated regime represents a transition between the unsaturated case and the fully saturated case, studied in the following section.

4.4.3 Fully saturated regime

The results corresponding to the fully saturated regime are presented in figure 4.12. Similarly to what was done in the two previous sections, the first line displays the results obtained with the experimental data in the FS1, FS2 and FS3 configurations (figures 4.12b, 4.12c and 4.12d respectively) , the middle row is the results obtained with P3DTEx in the same configurations (figures 4.12e to 4.12j) and, similarly, the bottom row displays the results obtained with P3DCOM (figures 4.12h to 4.12j). The number of realizations used here is given in table 3.1: $N_r = 21$. The 8 central sensors were taken into account.

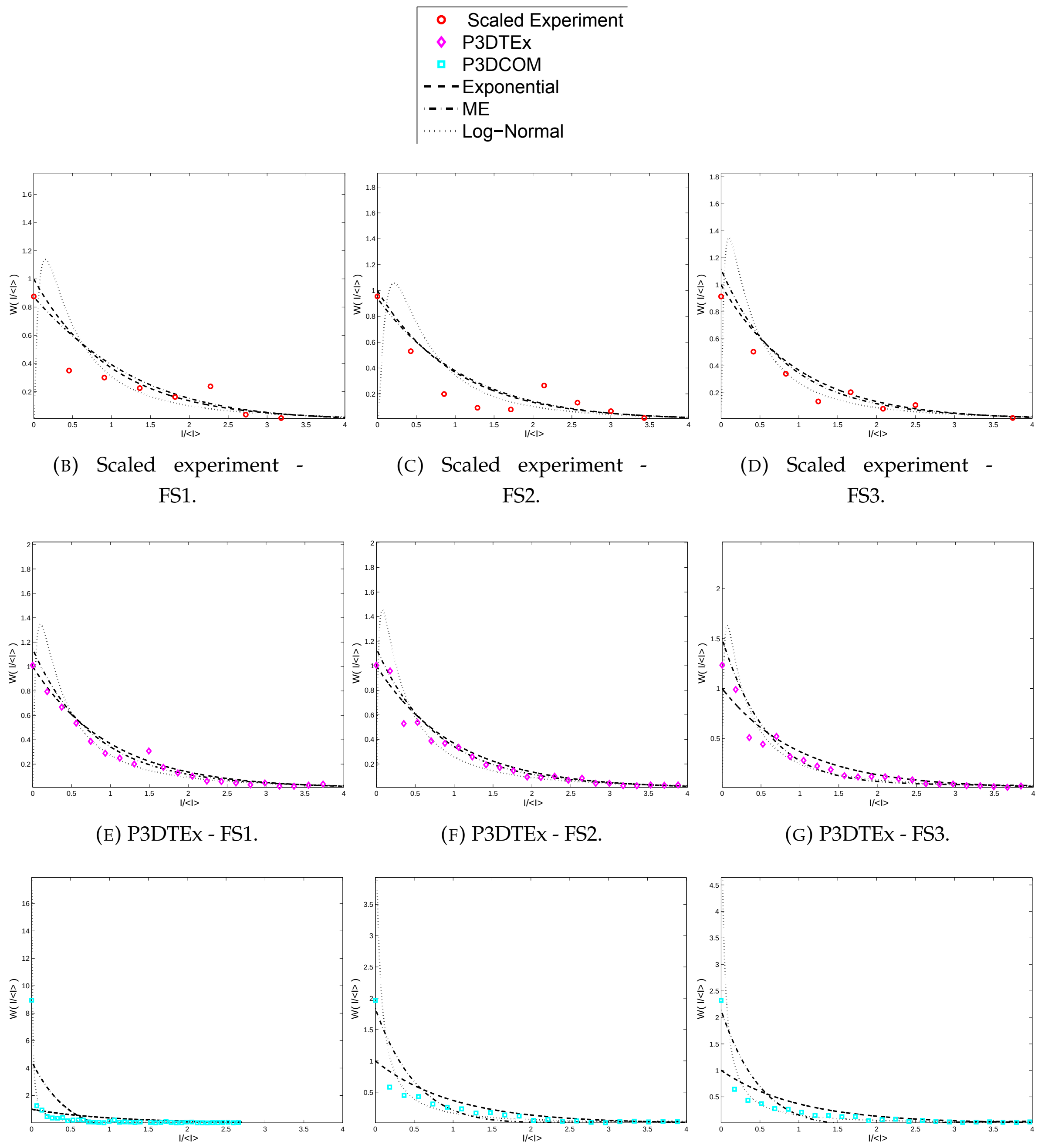

(B) Scaled experiment - FS1.

(C) Scaled experiment - FS2.

(D) Scaled experiment - FS3.

(E) P3DTEx - FS1.

(F) P3DTEx - FS2.

(G) P3DTEx - FS3.

(H) P3DCOM - FS1.

(I) P3DCOM - FS2.

(J) P3DCOM - FS3.

FIGURE 4.12: Intensity distributions (on 8 sensors) per regime (left: FS1, center: FS2 and right: FS3) and configuration (top: scaled experiment, middle: P3DTEx, bottom: P3DCOM. The dashed line is the exponential distribution, the dashed-dotted line is the ME distribution and the dotted line is the log-normal distribution.

Overall, an excellent agreement is found between our measurements and the P3DTEx results: the distribution decays from the $I/ < I > \approx 0$ to the higher values of normalized intensity. The same observation can be made for the P3DCOM, although some differences can be noticed: in particular, in the FS1 configuration, the best fit for the normalized intensity pdf is the log-normal distribution. In all other cases, the ME distribution is the best candidate for the normalized intensity pdf, confirming the results obtained in Colosi et al. (2001). Traditionally, the exponential distribution was used to described strong fluctuations configurations (Blanc-Benon and Juvé 1993), and the results presented here can not completely contradict this outcome, since the exponential distribution is still a good match.

The match between the normalized intensity distributions is summarized in table 4.4. A good agreement is found between all distributions, expect in the FS1 configuration, where, as explained in Chapter 3, section 3.5.2, the range of propagation was so important that it may induce difficultly analyzable results. The agreement is found otherwise to be good, as the Kolmogorov-Smirnov does not reject the null hypothesis in all saturated configurations. The essential feature typical of strong fluctuations is here respected: the decay from the maximum obtained for very weak normalized intensity towards higher $I/<I>$.

h_{KS}	FS1	FS2	FS3
(Scaled Experiment; P3DTEx)	0	0	0
(Scaled Experiment; P3DCOM)	0	0	0
(P3DTEx; P3DCOM)	1	0	0

TABLE 4.4: Kolmogorov-Smirnov test value h_{KS}: comparison between the fully saturated cases.

4.5 Conclusion

Two important conclusions can be drawn from the results presented in this chapter.

1. the MCF was calculated over the total number of realizations per configurations and over a 64-sensor vertical linear array. In the unsaturated and the partially saturated regimes, an excellent agreement was found between the measured, simulated (P3DTEx and P3DCOM when available) and predicted radii of coherence, as depicted by figure 4.9, where this quantity is shown along with its standard deviation, computed in the computer simulations. In particular, the US1 and US2 show remarkable agreement between all the calculations. The PS1 case also presents outstanding concordance. The correspondence is slightly less satisfying in the fully saturated cases, where the scaled measurements and the simulation of the tank experiment match remarkably, but the expected and the P3DCOM values are greater. As discussed in section 4.3.4, the small slope approximation used to obtain the analytical expressions for the radius of coherence may be in limit of validity for these cases, since the slopes of the corresponding RAFALs may not be considered very small. The Kirchoff approximation may be used to study these cases with more precision.

2. Two tools indicating signs of assignation to a specific regime of fluctuation were studied. In section 4.2, the phasor, or CPD, was calculated for the different configurations using measurements and synthetic data. Section 4.4 focused on the distribution of the

normalized acoustic intensity in the same cases. It was shown that the data acquired in our tank experiment featured typical characteristics of the different aimed regimes of fluctuations: in the unsaturated regime, the CPD followed the circle of mean pressure as expected (Dashen et al. 2010, Ehrhardt et al. 2013). Similarly, the histograms of normalized intensity displayed a log-normal distribution in this regime of weak fluctuation, as noticed in Flatté et al. (1987), Blanc-Benon and Juvé (1993). In the fully saturated case, a more formless representation of the CPD was obtained, indicating strong signal fluctuations in phase and amplitude. This assessment can be made in all the cases considered (measurements, simulations) and this results is in good agreement with what can be expected from the full saturation (Dashen et al. 2010). The evidence that the expected fully saturated regime are indeed classified into this regime was also provided by the histogram distribution study. In fact, the exponential like distribution defined in Colosi et al. (2001) as ME is the most likely candidate to match the pdf of normalized intensity in these cases. If some differences can be noticed with the P3DCOM results, they should mostly be attributed to numerical limitations rather than to physical interpretations. Finally, the partially saturated regime cases can be analyzed as a transition between unsaturation and fully saturation, both in terms of phasors and normalized intensity pdfs, which was expected.

These concluding remarks are in very good agreement with the physical interpretation of the regimes of saturation in terms of rays detailed in Chapter 2.

Overall the objectives were fulfilled and the capability of our experimental scheme to reproduce faithfully the effects of wave propagation in 3D random media was demonstrated.

Chapter 5

Influence of Medium Fluctuations on Detection Performance

Contents

5.1 Introduction

Numerous examples in the literature show that the loss of signal coherence induces a decrease in terms of array gain or resolution. This phenomena was first discussed by Sir Isaac Newton in Optics (Newton 1704) when he described the *constant tremor* experienced by the propagating medium as the limitating factor for the size of the telescopes. The failure of classical detection and localization techniques when they are applied to signal perturbed by the fluctuations of the propagation medium was tackled in many different fields, such as electromagnetism, optics or acoustics. Especially, the limitations in array gain due to atmospheric turbulence were studied (Wilson 1998). This assessment was the main motivation for the development of corrective techniques, such as adaptive optics (Beckers 1993), enhancing the performance of the detection/localization systems. This main issue with underwater acoustics is slightly different, since very low signal-to-noise ratios (SNR) are often involved. The detection problem is hence prominent, and the issues related to localization and resolution are secondary, but still worth of some interest.

In this chapter, the detection issue and especially the limitation of array gain in the case of sound waves perturbed by a fluctuating ocean are studied. Section 5.2 relates the MCF to a parameter accounting for the degradation of the array gain. In section 5.3, the performance of "classical" techniques, such as matched-field beamforming or high-resolution algorithm is investigated. These algorithms are applied to the signals acquired during the tank measurements (Chapter 3 and 4). The influence of the input signal-to-noise ratio and of the regime of fluctuation is studied. Corrective signal processing techniques are discussed in section 5.4.

5.2 Array gain degradation

The degradation of the array gain in a fluctuating medium is investigated in this section. This issue was tackled in underwater acoustics (Laval and Labasque 1981, Carey 1998, Gorodetskaya et al. 1999, Collis et al. 2008). The link between the loss of coherence (evaluated using the MCF) and the degradation of the array gain is highlighted in these papers. The array gain is here defined as the ratio between the output of the signal processing technique using signal only as an input to the output of the same technique using noise only as an input, normalized by the SNR on each sensor (Cox 1973a). In the case of fluctuations of the medium of propagation, the array gain is weighted by the coherence function $|\Gamma|$ (Ancey 1973, Graham 1979; 1982, Morgan and Smith 1990). We therefore deduce an expression for an array gain. We provide here a rather simple expression of an array gain degradation parameter, denoted δAG, in the case of linear array and a point source:

$$\delta AG = G_{Th} - 10\ \log\left(1 + \sum_{l=1}^{N} \frac{2\,(N-l)}{N} |\Gamma\,(l)\,|\right); \tag{5.1}$$

where we recall that N is the number of sensors, l is the discrete sensor spacing, Γ is the MCF defined in 4.1, and $G_{Th} = 10\ \log\,(N)$. In the case of perfect coherence ($\Gamma = 1$ for all sensor spacings), formula 5.1 becomes $\delta AG = 0\ dB$.

The objective of this calculation is not to determine precisely the exact loss of array gain, but to provide an order of magnitude of the degradation that one should expect when working with signals propagated through a perturbed medium.

The results obtained with formula 5.1 are provided for various calculations, following the approach proposed in Chapter 4, section 4.3. The results in terms of array gain degradation are also compared to the empirical formula presented in Fattaccioli et al. (2009):

$$\delta AG \approx \begin{cases} 10log\left(\frac{L_a}{L_z} - 4\right) & \text{if } L_a > 5L_z \\ 0.9\frac{L_a}{L_z} - 0.6 & \text{if } L_z \leq L_a \leq 5L_z \\ \frac{1}{3}\left(\frac{L_a}{L_z}\right)^{1.8} & \text{if } L_a < L_z \end{cases} \tag{5.2}$$

where L_a is the length of the array and L_z is the vertical correlation length of the acoustic field. Formula 5.2 was obtained after Monte-Carlo simulations of direct propagation from a point source to a linear array throughout an oceanic medium presenting Gaussian random sound speed fluctuations. The frequency range was $300\ Hz\ -\ 5\ kHz$, the propagation range was $1\ km\ -\ 30\ km$. The sound speed fluctuations were characterized by their amplitude (between $0.5\ m/s$ and $2\ m/s$, their horizontal and vertical correlation lengths (respectively included in the $0.2\ -\ 0.4\ km$ range and in the $10\ -\ 20\ m$ range). A regression lead to formula 5.2. More details are available in Fattaccioli et al. (2009).

In figures 5.1a to 5.1d, the δAG associated with the scaled measurements are displayed with dots, the simulations of the scaled experiment (P3DTEx) are displayed with diamonds, when available, the results associated with the equivalent ocean medium (P3DCOM) are displayed with squares, and the simplified theoretical results are provided with black dotted solid line. The latter are obtained using the theoretical coherence function given in equation 4.2:

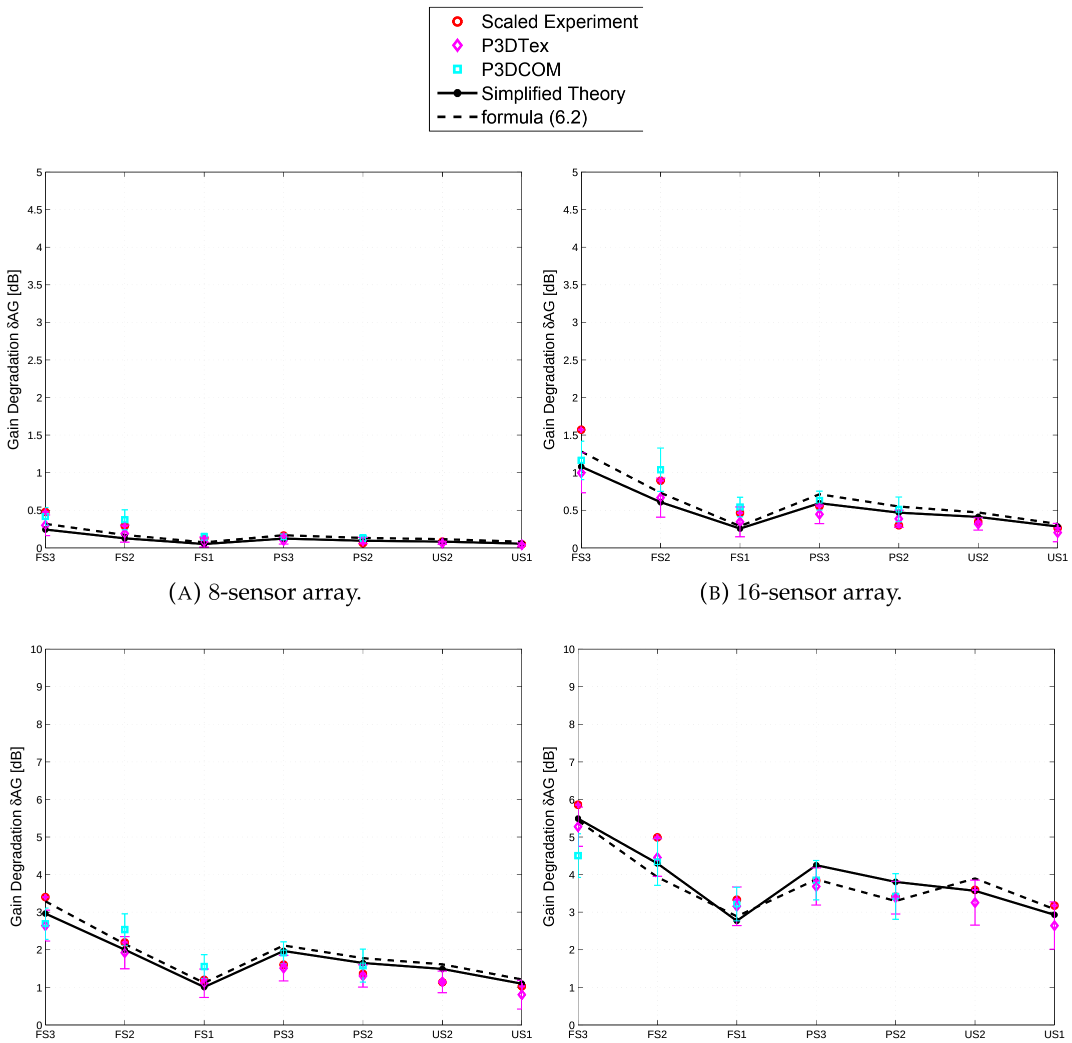

(A) 8-sensor array. (B) 16-sensor array.

(C) 32-sensor array. (D) 64-sensor array.

FIGURE 5.1: δAG as a function of the regime of saturation and the array size.

The influence of the array size is investigated by the comparison of figures 5.1a to 5.1d. Indeed, it is commonly assumed that the array resolution increases with the array size, but when fluctuations in the medium occur, the degradation of the array gain also increases with the size of the array. This leads very large arrays to be fairly more sensitive to perturbations in the propagation medium (Wilson 1998, Gorodetskaya et al. 1999). This assessment is verified here, since, for a given configuration, an increase in array size is followed by an increase in δAG, for all figures. Especially, for the measured data, in the US1 configuration, δAG was $0.05\ dB$ with a $8-$sensor array, and $3.2\ dB$ for a $64-$sensor array. Similarly, still for our experimental data, in the FS3 configuration, the shortest array leads to $\delta AG = 0.5\ dB$ and the longest array to $\delta AG = 5.8\ dB$. In our case, the fact that small arrays are less sensitive to the fluctuations of the medium than large arrays is therefore verified. Throughout all the configurations and array sizes, an excellent agreement is found between the array gain degradation estimated using equation 5.1 for the measured, simulated, and theoretical data. This result was expected since it simply echoes the analysis of the MCF performed in Chapter 4, section 4.3. Nonetheless, the agreement is also accurate with the empirical calculation proposed in formula 5.2. This points out the good representativeness of our experimental scheme, whose original aim was to reproduce the degradation of sonar gain in fluctuating environments such as an ocean perturbed by internal waves.

On the other hand, we can observe that the degradation of the array gain does not necessarily increase with the saturation. As an example, for the largest array, δAG is $3.6\ dB$ in the unsaturated US2 case, and $3.3\ dB$ in the fully saturated configuration FS1. This also echoes the analysis carried out in Chapter 4, where we stated that the MCF is not fundamentally or necessarily narrower in a fully saturated case than in an unsaturated case. Nevertheless, we can reasonably anticipate the fact that corrective signal processing techniques would mitigate the degradation of performance more easily in an unsaturated case than in a fully saturated case, since most of the signal fluctuations are linked to phase aberrations in the first context. Indeed, in the fully saturated regime, strong amplitude fluctuations or several neighboring paths are also noticed, which makes it even more complicated for source detection and localization.

5.3 Performance of *classical* techniques

In this section, the performance of *classical* source detection and localization techniques are studied. Two specific algorithms are tested using the signals acquired with the tank experiment: a Matched Field BeamForming (MFBF) algorithm and a high resolution (MUltiple SIgnal Classification or MUSIC) (Bienvenu and Kopp 1983) algorithm. The performance of these two techniques is analyzed in terms of deflection rather than classical detection gain as defined in Cox (1973a), Van Trees (2004). The deflection is shown to be a more suitable criterion for the detection capability in Picinbono (1995) since it allows to evaluate the detection performance in more practical configurations. In the case of the MFBF, it is identical to the classical array gain, but this does not hold for other techniques, such as MUSIC. The deflection is defined in Morgan and Smith (1990) as the difference between the average maximum output with signal plus noise as input and the average maximum output with noise only as input, normalized with the standard deviation of the maximum output with noise only as input:

$$G = \frac{E_1\left[\tilde{M}\right] - E_0\left[\tilde{M}\right]}{\sqrt{V_0\left[\tilde{M}\right]}}, \tag{5.3}$$

where $E_1[.]$ is the statistical expectation in the signal plus noise hypothesis, $E_0[.]$ is the statistical expectation in the noise hypothesis, $V_0[.]$ is the variance in the noise hypothesis and $\tilde{M}$ is the maximum of the algorithm output, averaged across N_r realizations.

5.3.1 Matched-Field Beamforming

In this section and the next one, the performance of these two detection and localization techniques is evaluated.

The detection, in the case of the MFBF, relies on the match between the received signal and a modeled signal (Bucker 1976). Here, the parameters of the modeled signal are not related to the environmental characteristics of an acoustic waveguide (sound speed profile, sea bottom characteristics), as it is usually the case (Baggeroer et al. 1988), but they are linked to the source model. Especially, the transducer radius $\rho = 6.5\ mm$ and its directivity pattern provide the model. The signal model x_m is therefore given by:

$$x_m\left(R\right) = S\left(k\ \rho\ \sin\left(\theta\right)\right)e^{-ikR} \tag{5.4}$$

where R is the propagation distance, θ is the source elevation angle, k is the wavenumber, and $S\left(.\right)$ is the *Sombrero* function defined in Gaskill (1978). In this configuration, the wavelength of the signal is $\lambda \approx 0.66\ mm$. The linear array is sampled at $\lambda/2.2$, so that the array size is 29λ. The output of the MFBF, noted $\tilde{P}_{MFBF}$ is given by:

$$\tilde{P}_{MFBF}\left(\hat{\mathbf{r}}\right) = \left|\frac{\mathbf{x}_m^H\left(\hat{\mathbf{r}}\right)}{\left|\mathbf{x}_m\left(\hat{\mathbf{r}}\right)\right|}.\mathbf{x}\right|^2 \tag{5.5}$$

where $.^H$ is the Hermitian operator and $\hat{\mathbf{r}}$ is the estimated parameters of the source location (here they are the test abscissa x_t and test depth z_t). $\mathbf{x}$ is the vector containing the received signal x on each receiver.

$$x_n\left(t\right) = \sum_{n=1}^{N} h_n\left(t\right) * s\left(t-\tau_n\right) + n_n\left(t\right) \tag{5.6}$$

where $h_n(t)$ is the impulse response of the $n-$th sensor, $s_n(t)$ is the signal radiated from the source, $n_n(t)$ is additive white Gaussian noise (AWGN), with power σ_N^2 and τ_n is the delay associated with the $n-$th sensor. The AWGN is supposed to be uniform along the array and uncorrelated between sensors.

In the case of an unperturbed medium, that is, in our case, a lens presenting plane input face ($\xi_0 = 0$), the deflection of the MFBF , denoted G^0, can be computed as a function of the input SNR:

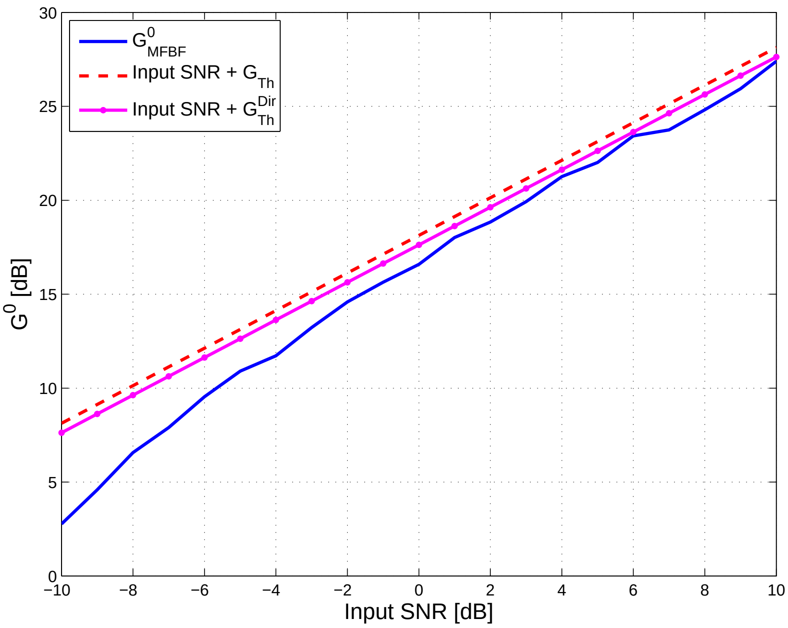

FIGURE 5.2: Deflection G^0 obtained with the flat lens for the MFBF (blue).

Figure 5.2 shows that increasing the input SNR leads to an increase of the deflection for the MFBF. For a $64-$sensor array, the deflection in absence of medium fluctuation can be interpreted as the sum SNR + G_{Th}, which is close to the value of G^0_{MFBF} for the largest SNR ($> 0\ dB$), as expected. Note that a correction due to the source directivity leads to an even better match between G^0_{MFBF} and the theoretical value.

We present hereafter snapshots of the performance of the MFBF in terms of detection and 2D localization. First, the sensitivity of the MFBF to the SNR is evaluated in figures 5.3 and 5.4, where the SNR is respectively of $10\ dB$ and $-10\ dB$. In these figures, the left figure (5.3a and 5.4a) display the MFBF output with signal and noise as input and the right figure (5.3b and 5.4b) displays the algorithm output with noise only as input. A large difference between the signal+noise output and the noise output is sought out, since it would imply a strong contrast between the two cases and would therefore reveal an efficient detection capability.
In order to highlight the contrast between the two cases, the outputs are normalized with respect to the maximum of the signal output. The range of the test abscissa is chosen to be $0\ m < x_t < 1\ m$ and the test source depth interval is given by:

$$z_t^{max} = 3 \, \tan\left(\theta_{3dB}\right) \, x_t^{max}, \tag{5.7}$$

where $\theta_{3dB} = \frac{1.39}{\pi} \frac{\lambda}{N\,s}$ (Waite 2001). Our configuration provides $z_t^{max} = 0.045 \; m$.

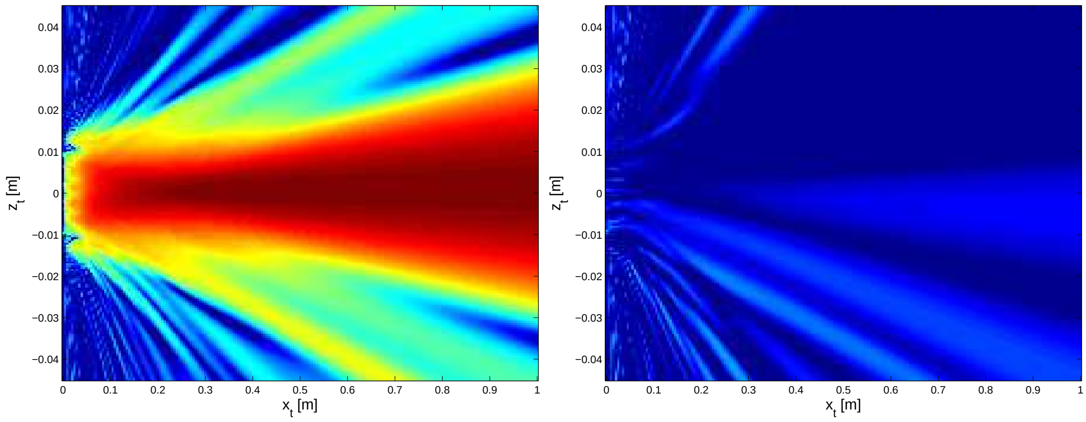

(A) MFBF - Flat lens - SNR = 10 dB.

(B) MFBF - Flat lens - Noise only.

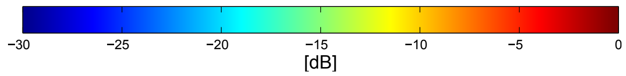

FIGURE 5.3: MFBF performance - “Signal + Noise” (left) and “Noise” only (right) - $SNR = 10 \; dB$.

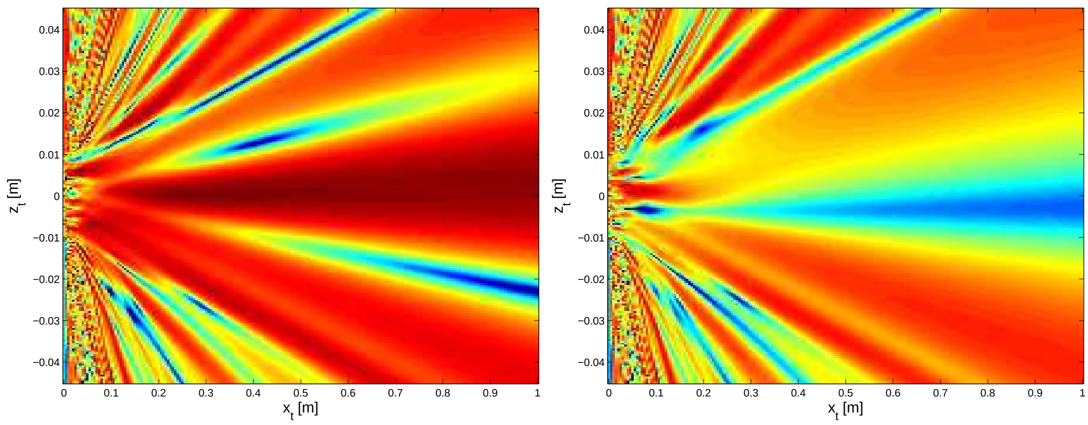

(A) MFBF - Flat lens - SNR = $-10 \; dB$.

(B) MFBF - Flat lens - Noise only.

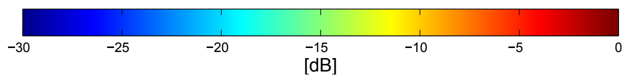

FIGURE 5.4: MFBF performance - “Signal + Noise” (left) and “Noise” only (right) - SNR = $-10 \; dB$.

In the favorable (SNR=10 dB) case, the source is clearly detected. The level difference between signal + noise and noise only outputs is significant in the high SNR case, where $G^0_{MFBF} = 27.4 \; dB$. In the low SNR case (SNR=$-10 \; dB$), the source is detected by with a rather small deflection: $G^0_{MFBF} = 2.8\ dB$. This echoes the result provided by figure 5.2, where the low SNR case corresponds to the detection limit. It will be interesting to measure the impact of medium fluctuations on the detection in this low SNR configuration. In an unperturbed environment, the source detection procedure seems therefore to be providing satisfying results. Examples of its behavior in various experimental configurations spanning from the unsaturated to the fully saturated regime are given in figures 5.6 to 5.9.

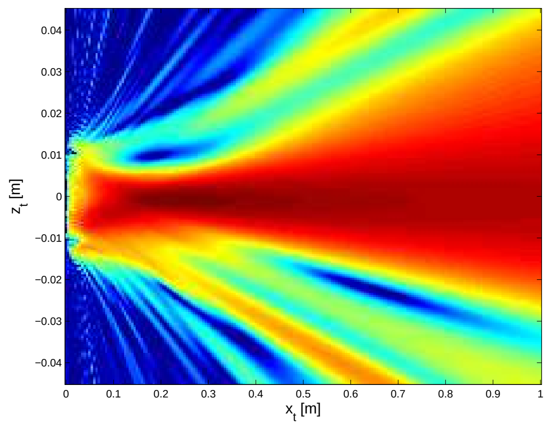

(A) MFBF - US2 case - SNR = $10\ dB$.

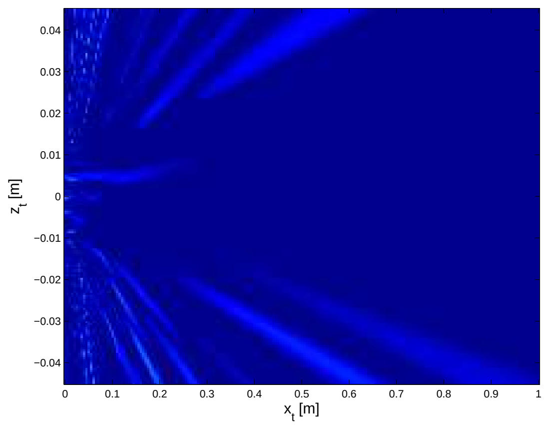

(B) MFBF - US2 case - Noise only.

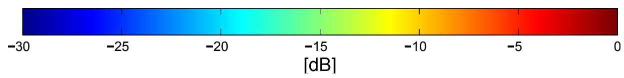

FIGURE 5.5: MFBF performance US2 case - "Signal + Noise" (left) and "Noise" only (right) - SNR = $10\ dB$.

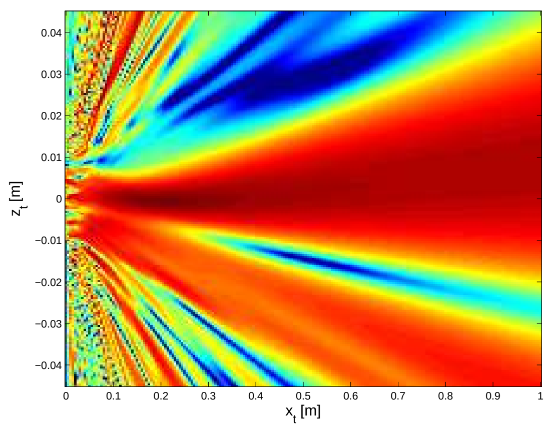

(A) MFBF - US2 case - SNR = $-10\ dB$.

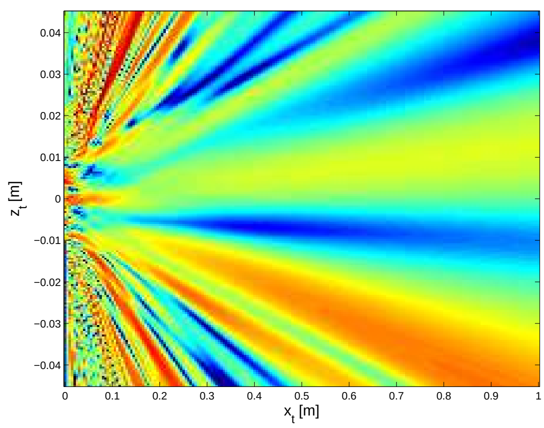

(B) MFBF - US2 case - Noise only.

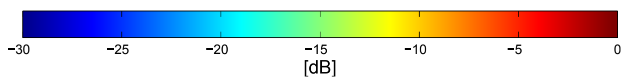

FIGURE 5.6: MFBF performance US2 case - "Signal + Noise" (left) and "Noise" only (right) - SNR = $-10\ dB$.

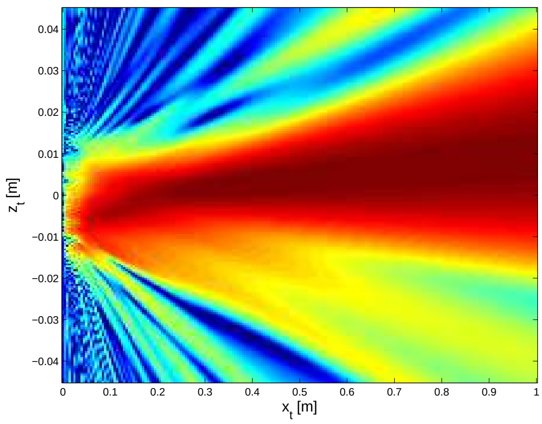

(A) MFBF - PS2 case - SNR = $10\ dB$.

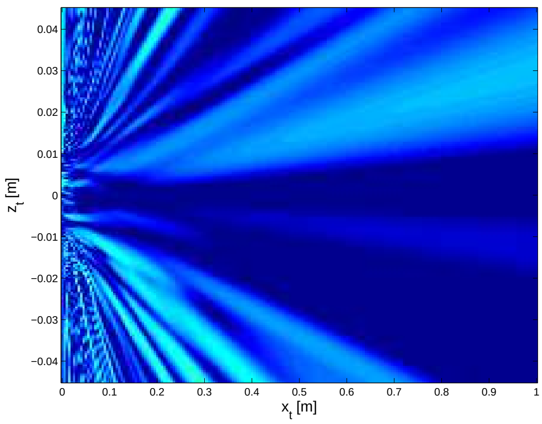

(B) MFBF - PS2 case - Noise only.

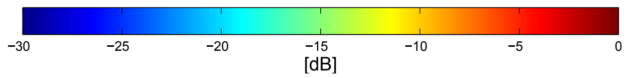

FIGURE 5.7: MFBF performance PS2 case - "Signal + Noise" (left) and "Noise" only (right) - SNR = $10\ dB$.

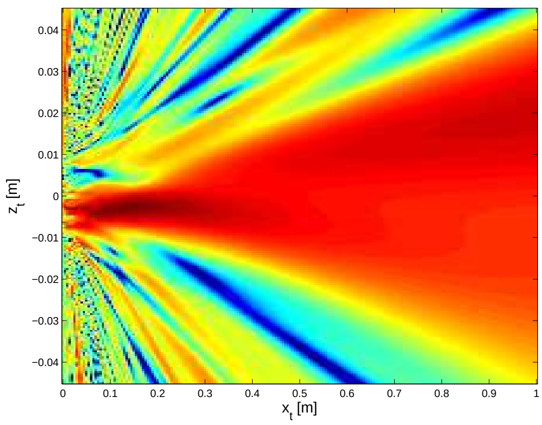

(A) MFBF - PS2 case - SNR = $-10\ dB$.

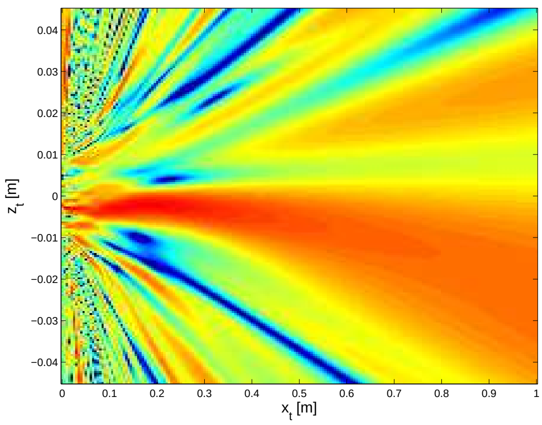

(B) MFBF - PS2 case - Noise only.

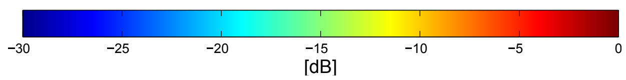

FIGURE 5.8: MFBF performance PS2 case - "Signal + Noise" (left) and "Noise" only (right) - SNR = $-10\ dB$.

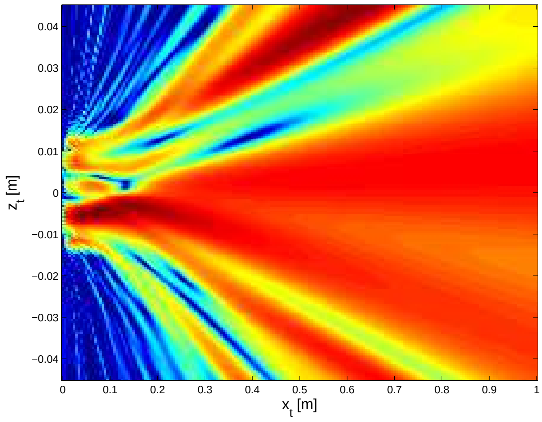

(A) MFBF - FS3 case - SNR = 10 dB.

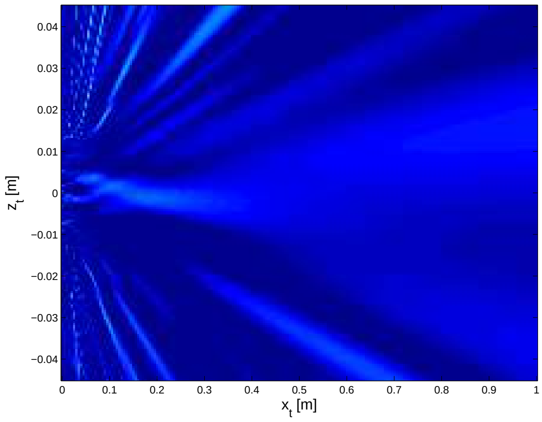

(B) MFBF - FS3 case - Noise only.

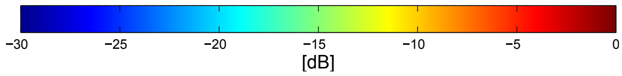

FIGURE 5.9: MFBF performance FS3 case - "Signal + Noise" (left) and "Noise" only (right) - SNR = 10 dB.

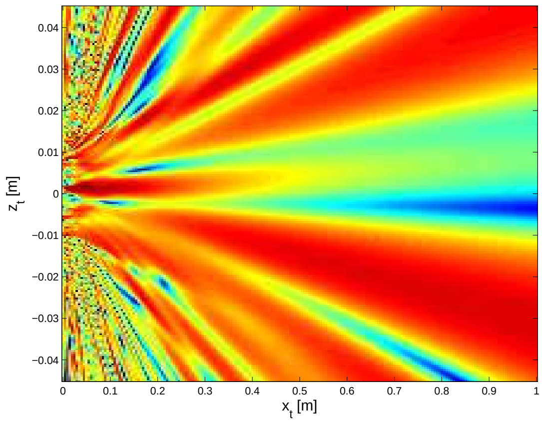

(A) MFBF - FS3 case - SNR = -10 dB.

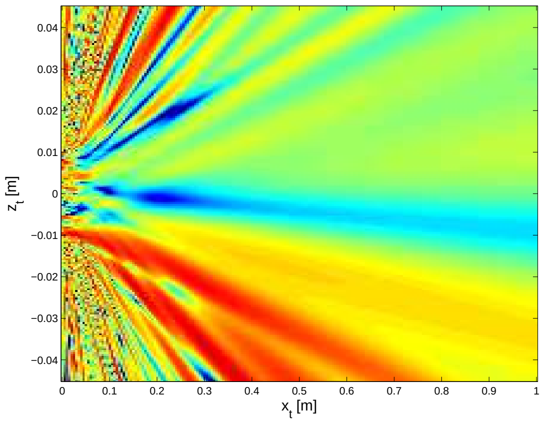

(B) MFBF - FS3 case - Noise only.

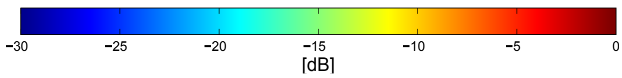

FIGURE 5.10: MFBF performance FS3 case - "Signal + Noise" (left) and "Noise" only (right) -SNR = -10 dB.

The unsaturated case (configuration US2) is presented in figures 5.5 and 5.6. We observe a slight decrease of the gain in this case, as the contrast between signal + noise and noise only outputs is smaller. In fact, $G_{MFBF} = 25\ dB$ in the high SNR scenario, and $G_{MFBF} = 1.2\ dB$ in the low SNR scenario. Note that in the high SNR case the induced detection capability degradation $\delta AG^{MFBF} = G^0_{MFBF} - G_{MFBF}$ is of the order of $2.3\ dB$.
The partially saturated regime (PS2 configuration) is investigated in figures 5.7 and 5.8. In the low SNR scenario, $G_{MFBF} = 1.8\ dB$, whereas in the high SNR case, $G_{MFBF} = 24.8\ dB$. This translates into a degradation of the deflection of $1\ dB$ and $2.6\ dB$ respectively.

The influence of the fluctuations of the medium on the degradation of the deflection is hence larger than in the US2 case.
The fully saturated case is displayed in figures 5.9 and 5.10. The degradation of the deflection induced by the propagation through the RAFAL is here more pronounced: in the case of a $10\ dB$ SNR, $\delta AG^{MFBF} = 3.8\ dB$ and in the case of a low ($-10\ dB$) SNR, $\delta AG^{MFBF} = 2.3\ dB$. The degradation of the deflection is quite large in this configuration. Figure 5.10a displays a case where it is excruciatingly difficult to detect the source correctly. The case where the input of the algorithm is signal plus noise and the case where only noise is used as an input are almost indistinguishable.
Table 5.1 summarizes the degradation of the deflection described in the previous paragraphs:

$\delta AG^{MFBF}\ [dB]$	Configurations		
SNR $[dB]$	US2	PS2	FS3
$-10\ [dB]$	1.5	1	2.3
$10\ [dB]$	2.3	2.6	3.8

TABLE 5.1: δAG^{MFBF} as a funtion of the configuration studied and the input SNR.

The results in terms of δAG^{MFBF} are gathered in figure 5.11, where the degradation of the deflection is represented as a function of the experimental configuration (and hence, the saturation regime) and of the input SNR.

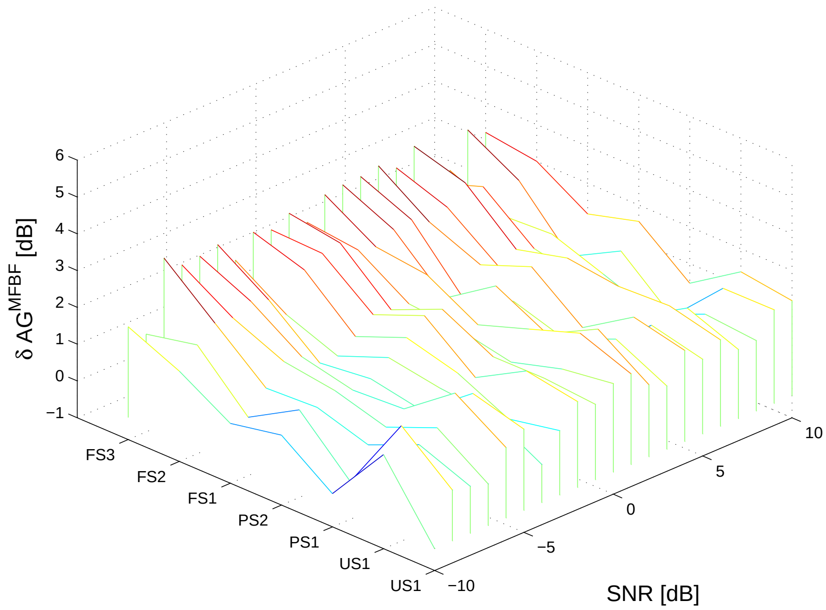

FIGURE 5.11: Degradation of the deflection as a function of the input SNR and the configuration for MFBF.

The behavior of the degradation of the deflection shows a high dependence in the configuration studied. The δAG^{MFBF} values for very low SNR seem to be smoothed, but still present the same qualitative analysis in terms of link between the degradation and the regime of fluctuation. Typically, for the lowest ($-10\ dB$) SNR, the highest δAG^{MFBF} is obtained in the FS3 configuration and the lowest value is obtained for the US1 case.

5.3.2 High-resolution MUSIC algorithm

High-resolution algorithms have been used for many decades in order to tackle the source detection and localization problem (Bienvenu and Kopp 1983, Schmidt 1986). The MUSIC output provides an estimation of the source position by the locations of the smallest value of the function:

$$\tilde{P}_{MUSIC}\left(\hat{\mathbf{r}}\right) = \frac{1}{\mathbf{x}_m^H\left(\hat{\mathbf{r}}\right)\left(I - \boldsymbol{\eta}^H\boldsymbol{\eta}\right)\mathbf{x}_m\left(\hat{\mathbf{r}}\right)} \tag{5.8}$$

where I is the $N \times N$ identity matrix and $\boldsymbol{\eta}$ contains the eigen vectors $\mathbf{V}_i$ associated with the eigen values λ_i of the covariance matrix $\hat{\mathbf{R}}_{\mathbf{xx}}$, so that:

$$\hat{\mathbf{R}}_{\mathbf{xx}}\mathbf{V}_i = \lambda_i\mathbf{V}_i \qquad i = 1, .., N \tag{5.9}$$

$\hat{\mathbf{R}}_{\mathbf{xx}}$ is here defined as:

$$\hat{\mathbf{R}}_{\mathbf{xx}} = \mathrm{SNR}\,\mathbf{y}.\mathbf{y}^H + \frac{1}{\alpha_N N_{Snap}}\sum_{m=1}^{N_{Snap}}\mathbf{n}_m.\mathbf{n}_m^H, \tag{5.10}$$

where $\mathbf{y}$ is the received signal vector, normalized so that $|\mathbf{y}|^2 = N + 1$, α_N is a normalization parameter, so that $\sum_{n=1}^{N}|B_{nn}|^2 = N + 1$ as well, and N_{Snap} is the number of noise snapshots per realizations.

Similarly to what was shown in the MFBF case, the deflection in the case of the unperturbed environment can be computed for MUSIC:

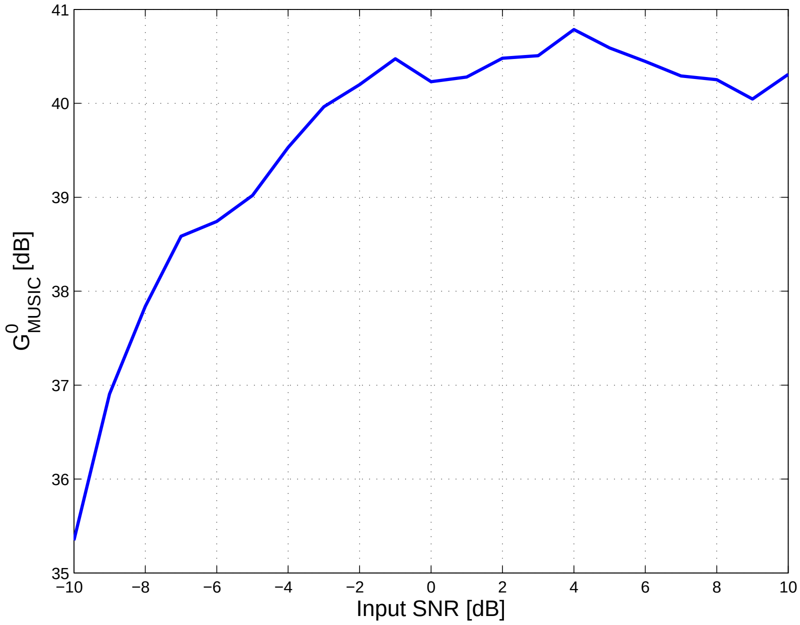

FIGURE 5.12: Deflection G^0_{MUSIC} obtained with the flat lens for MUSIC.

As depicted by figure 5.12, the dynamic of the deflection in the unperturbed case is smaller for MUSIC than in the MFBF case. The performance of MUSIC in terms of deflection is therefore less sensitive to the input SNR. It is evaluated in the unperturbed environment in figures 5.13 and 5.14 for high ($10\ dB$) and low ($-10\ dB$) values of the SNR. Although the deflection in the case of the MFBF was shown to correspond to the theoretical sum SNR + G_{Th}, this concordance is not necessarily true in the case of MUSIC, where the noise only as input case is not easily interpreted. The outputs of the MUSIC algorithm for two types of inputs are provided: from figure 5.13 to 5.10, the left figure is the MUSIC output with a noisen signal as an input and the right figure is the algorithm output with only noise as an input, similarly to what was shown in section 5.3.1. The normalization is also identical to what was done in the MFBF case.

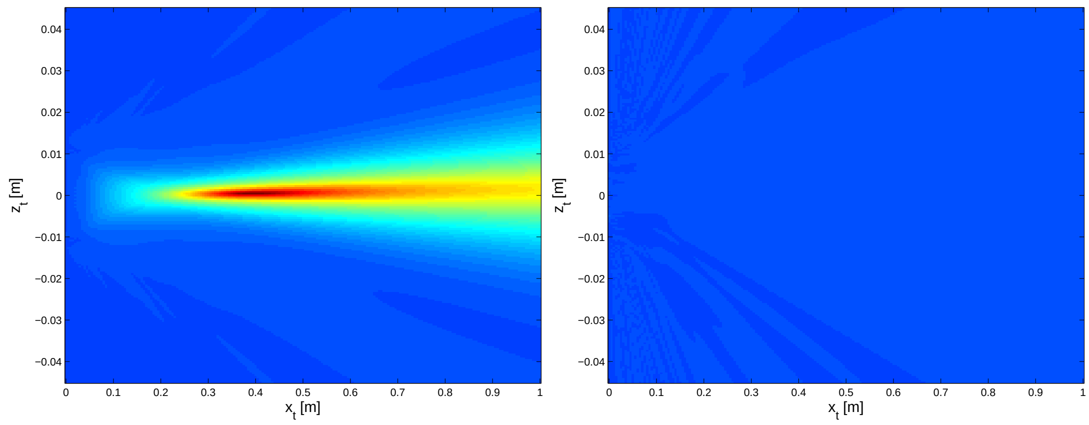

(A) MUSIC - Flat lens - SNR = 10 dB.

(B) MUSIC - Flat lens - Noise only.

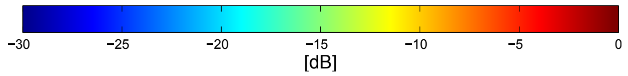

FIGURE 5.13: MUSIC performance - "Signal + Noise" (left) and "Noise only "(right) - SNR = 10 dB.

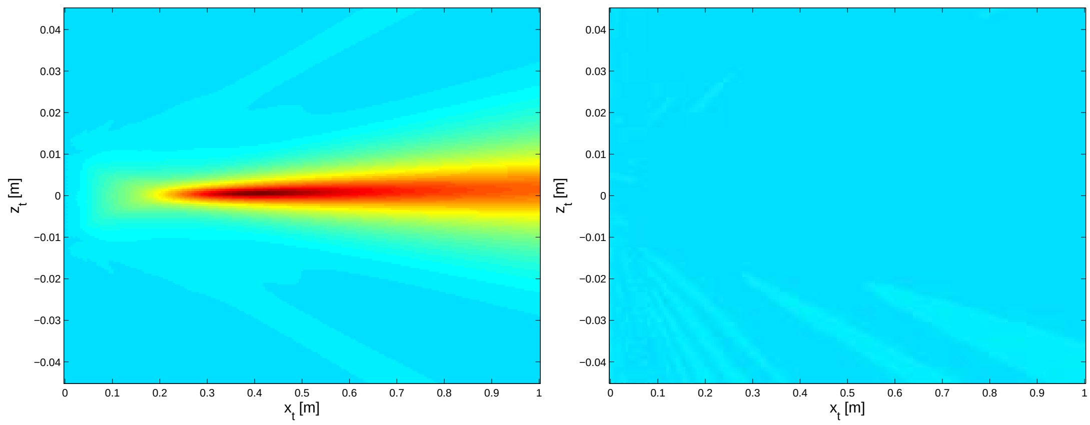

(A) MUSIC - Flat lens - SNR = -10 dB.

(B) MUSIC - Flat lens - Noise only.

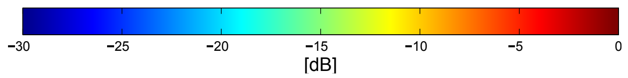

FIGURE 5.14: MUSIC performance - "Signal + Noise" (left) and "Noise only" (right) - SNR = -10 dB.

In both cases the source is detected significantly: in the low SNR case, G^0_{MUSIC} = 35.3 dB and in high SNR scenario, G^0_{MUSIC} = 40.3 dB. The resolution of the detection map given in figures 5.13 and 5.14 is actually fairly higher than the one provided by the MFBF (see figures 5.3 and 5.4).

The following figures display the results associated with MUSIC : first, the unsaturated regime is studied with the US2 configuration in figures 5.15 and 5.16, then the partially saturated case (in particular, the PS2 configuration) is studied throughout figures 5.17 and 5.8. Finally, the fully saturated case (FS3) is studied in figures 5.19 and 5.20.

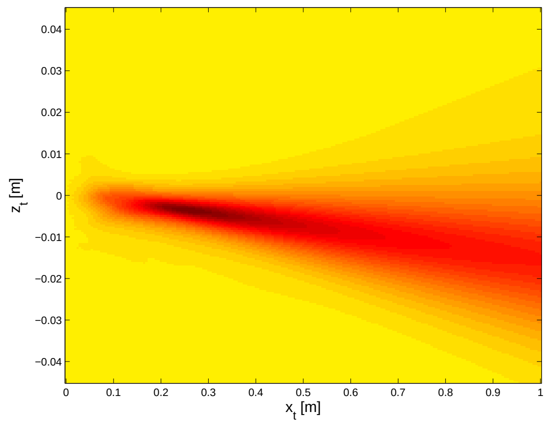

(A) MUSIC - US2 case - SNR = $10\ dB$.

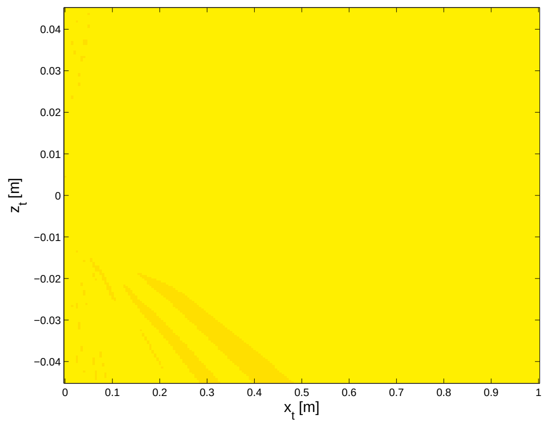

(B) MUSIC - US2 case - Noise only.

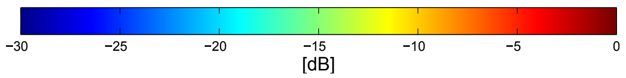

FIGURE 5.15: MUSIC performance US2 case - "Signal + Noise" (left) and "Noise" only (right) - SNR = $10\ dB$.

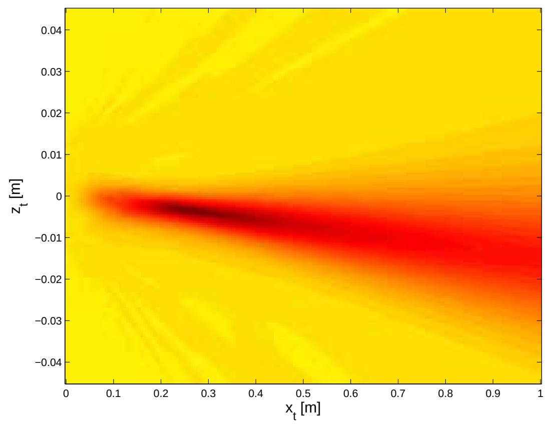

(A) MUSIC - US2 case - SNR = $-10\ dB$.

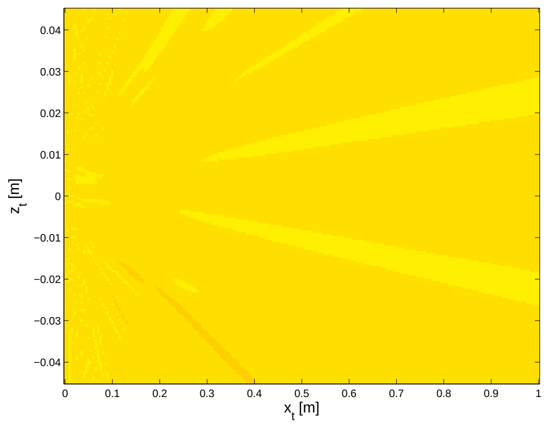

(B) MUSIC - US2 case - Noise only.

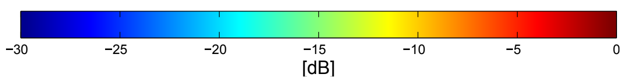

FIGURE 5.16: MUSIC performance US2 case - "Signal + Noise" (left) and "Noise" only (right) - SNR = $-10\ dB$.

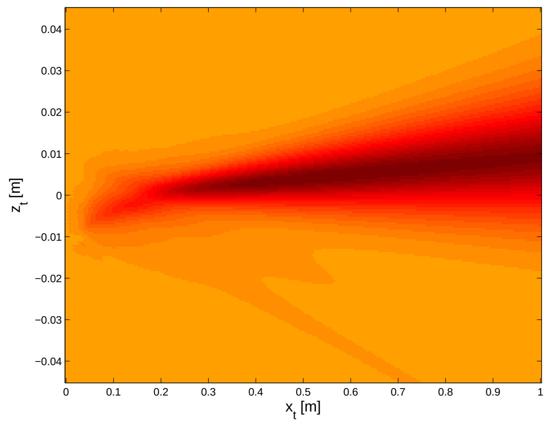

(A) MUSIC - PS2 case - SNR = 10 dB.

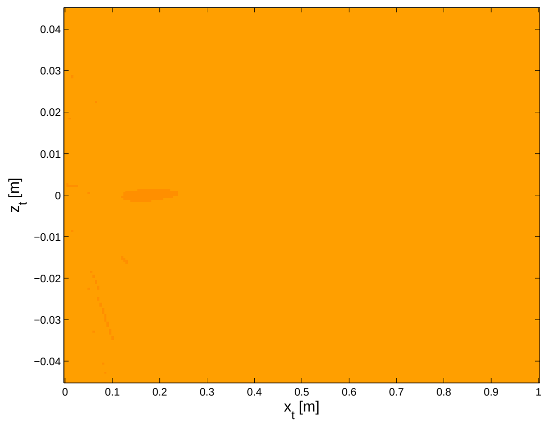

(B) MUSIC - PS2 case - Noise only.

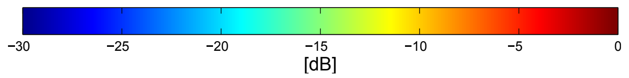

FIGURE 5.17: MUSIC performance PS2 case - “Signal + Noise” (left) and “Noise” only (right) - SNR = 10 dB.

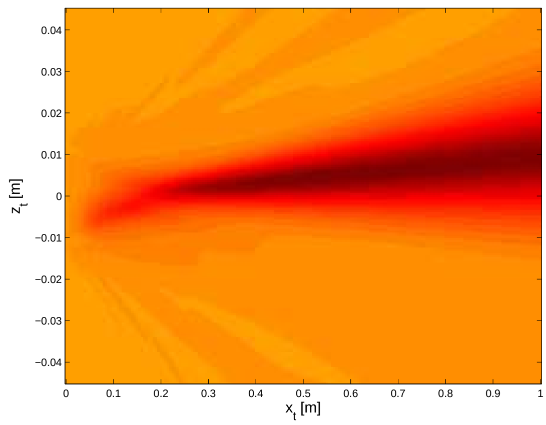

(A) MUSIC - PS2 case - SNR = -10 dB.

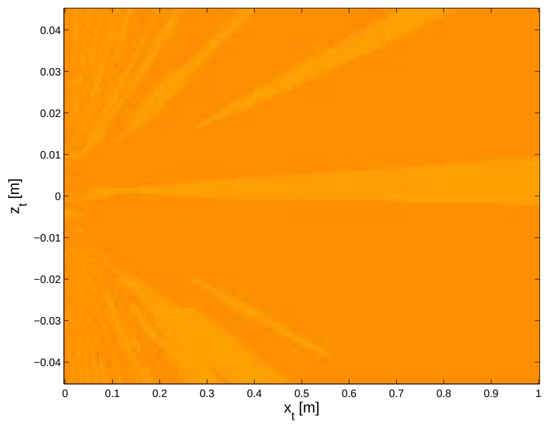

(B) MUSIC - PS2 case - Noise only.

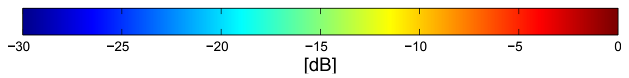

FIGURE 5.18: MUSIC performance PS2 case - “Signal + Noise” (left) and “Noise” only (right) - SNR = -10 dB.

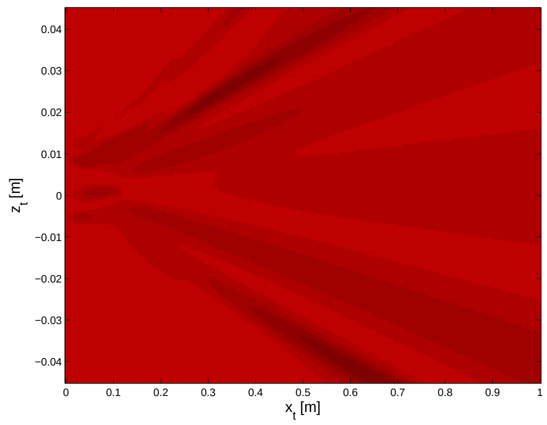

(A) MUSIC - FS3 case - SNR = 10 dB.

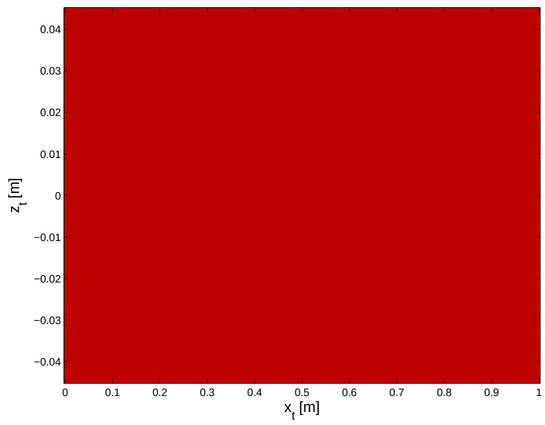

(B) MUSIC - FS3 case - Noise only.

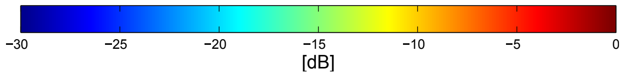

FIGURE 5.19: MUSIC performance FS3 case - "Signal + Noise" (left) and "Noise" only (right) - SNR = 10 dB.

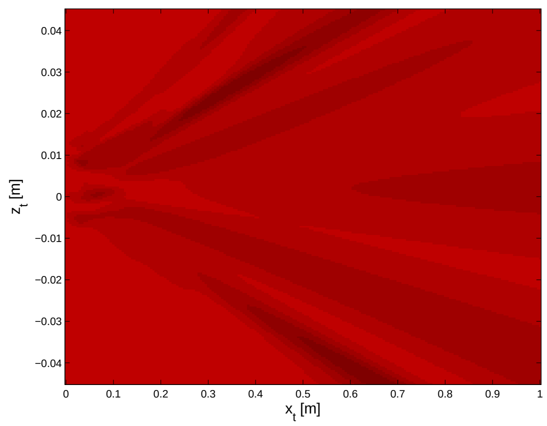

(A) MUSIC - FS3 case - SNR = -10 dB.

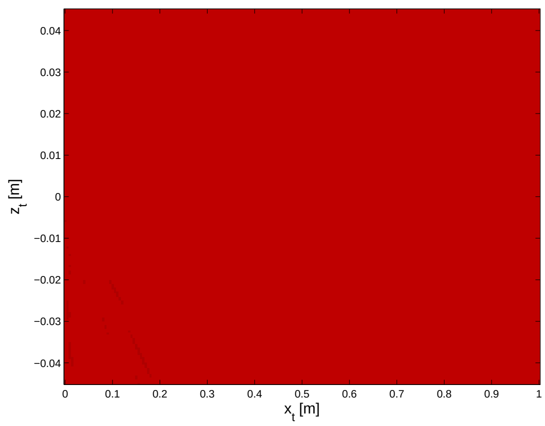

(B) MUSIC - FS3 case - Noise only.

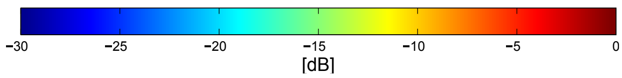

FIGURE 5.20: MUSIC performance FS3 case - "Signal + Noise" (left) and "Noise" only (right) - SNR = -10 dB.

First, we can observe that MUSIC seems to be more sensitive to the propagation through a fluctuating medium than the MFBF. Indeed, in the US2 configuration, for the high SNR case, $G_{MUSIC} = 25.6\ dB$ and in the low SNR case, $G_{MUSIC} = 24\ dB$ which respectively represents a degradation of $14.7\ dB$ and $11.3\ dB$ respectively. Compared to the loss experienced by the MFBF in the same configuration ($\delta AG_{MFBF} = 3\ dB$), MUSIC displays a more important deflection degradation. This can be related to the fact that the deflection of MUSIC is already higher than the MFBF gain for unperturbed environment, at high SNR (see figure 5.2).
The performance analysis of MUSIC in this partially saturated case echoes the analysis carried

out in the unsaturated case. In fact, $G_{MUSIC} = 25.3\ dB$ and $G_{MUSIC} = 23.4\ dB$ respectively in the high and low SNR cases. This translates into a gain degradation of $15\ dB$ and $12.5\ dB$ respectively. Once again the observed gain degradation is more important than the one noticed with the MFBF (in the same conditions, $\delta AG_{MFBF} = 4.1\ dB$ in the high SNR case, and $\delta AG_{MFBF} = 1.9\ dB$ for a SNR of $-10\ dB$).
The fully saturated case exhibits a strong array gain degradation. In fact, for the high SNR case ($10\dot{d}B$), the deflection is $G_{MUSIC} = 19.1\ dB$, which represents a degradation of $21.2\ dB$. The degradation of the deflection induced by the propagation through the fluctuating medium in the case of a $-10\ dB$ SNR is $17.2\ dB$.
Table 5.2 summarizes the array gain degradation described in the previous paragraphs:

δAG^{MUSIC} $[dB]$	Configurations		
SNR $[dB]$	US2	PS2	FS3
-10 $[dB]$	11.3	12.5	17.2
10 $[dB]$	14.7	15	21.2

TABLE 5.2: δAG^{MFBF} as a function of the configuration studied and the input SNR.

The overall behavior of MUSIC as a function of the configuration studied and the SNR is represented by the performance degradation parameter δAG^{MUSIC} in figure 5.21:

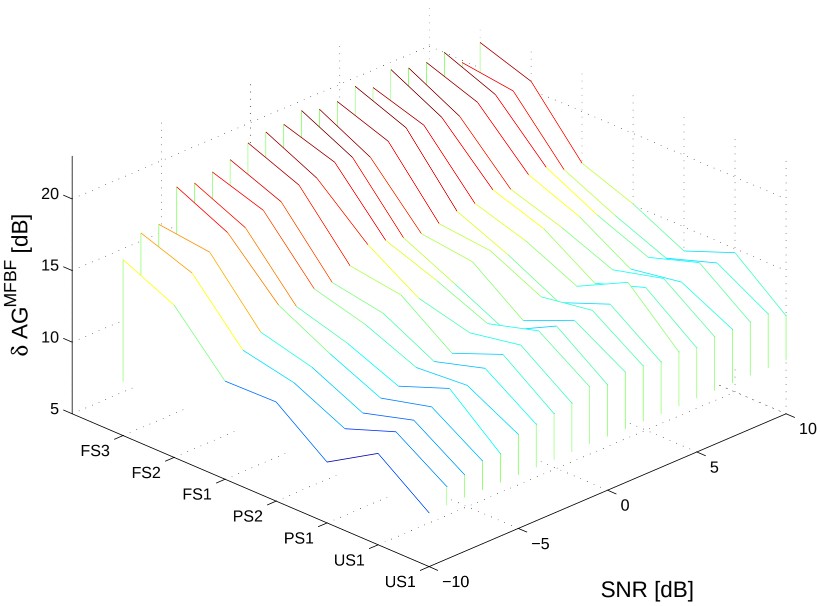

FIGURE 5.21: Detection gain degradation as a function of the input SNR and the configuration for MUSIC.

The analysis of the degradation of the MUSIC performance in presence of fluctuations is somewhat biased by the spectacular values of deflection in the unperturbed case. This explains the tremendous values of δAG^{MUSIC}. Note that the degradation of performance of MUSIC is fairly independent of the input SNR. The influence of the regime of fluctuation is otherwise very important. The analysis carried out on the performance of the MFBF algorithm lead to similar conclusions. In essence, our main objective was the ability to reproduce the degradation of array gain when acoustic waves travel through an ocean characterized by random sound speed fluctuations. The study of the performance of existing techniques on experimental data acquired in a very controlled and reproducible fashion, display array gain degradation comparable to what can be observed in the ocean case (Carey 1998, Carey et al. 2006). The techniques presented and studied in this section displayed some important array gain degradation since they are completely blind, meaning that they do not use any information regarding the propagation medium. In order to mitigate the influence of the propagation medium fluctuations, signal processing techniques adapted to the environment are needed.

5.4 Corrective signal processing techniques

The degradation of the performance of blind signal processing techniques implies a need for corrective algorithms, adapted to the environment and its fluctuations. The research of such adaptive techniques takes an important part in signal processing publications in various domains and applications. The propagation of sound waves through an ocean perturbed by internal waves is indeed analogous to other phenomena such as wavefront distortions due to atmospheric turbulence (observed in the design of high-resolution telescopes for example) or ultrasonic waves propagating through layers of heterogeneous tissues (for medical imaging or non-destructive techniques (NDT) applications).
In this section, we gather the relevant techniques allowing to compensate for wavefront distortions due to fluctuations of the propagation medium.

The most advanced domain in this area is adaptive optics. Indeed, spectacular results in terms of increase in the resolution of very large telescopes were found. The separation of binary stars was therefore enhanced (Metchev et al. 2003). The techniques developed in this domain can be classified into two categories, based on the use (or not) of a reference. The most commonly used techniques not using any sort of reference is the Buffington system. This technique relies on the estimation of the signal phase fluctuations using a Monte-Carlo method. A tunable phase shifter is used in order to compensate for the phase variations before the beamforming step. A diagram of the system is proposed in Muller and Buffington (1974):

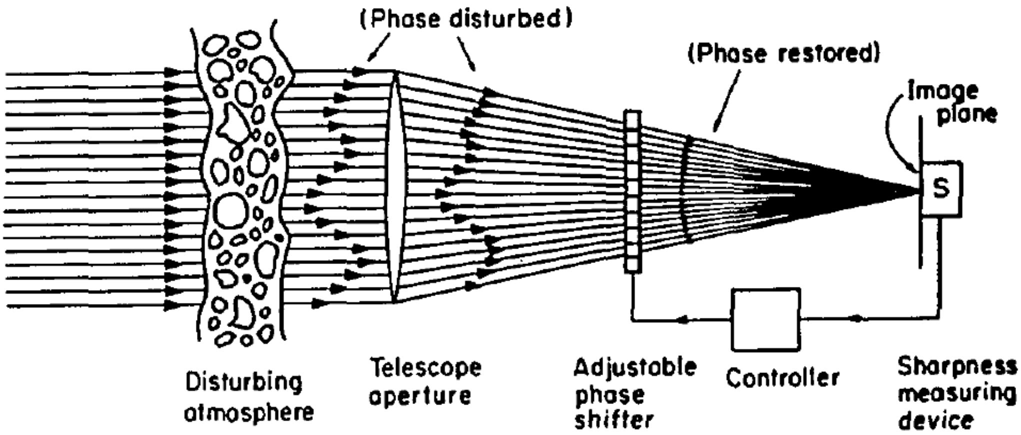

FIGURE 5.22: The Muller and Buffington system. From (Muller and Buffington 1974).

The idea is then to maximize the sharpness of the output. Experimental results validating this system are provided in Buffington et al. (1977). The implementation of this technique in the case of sonar detection can be performed quite easily, since an artificial phase shift of the received signals can be realized. Nevertheless, this technique implies that a peak can be detected in the output image, which is far from being ensured in the case of low SNR. The concept of noise is indeed missing in the derivation of this technique. On the contrary, low SNRs are frequently involved with source detection in the ocean problems.
In adaptive optics, techniques involving the use of beacons to obtain information about the medium of propagation are also numerous. A natural bright star may be used as a beacon, and referred to as guide star (Muller and Buffington 1974). An "artificial star" may be created using a high-altitude yellow laser that is resonant wit sodium; a thin sodium layer is therefore excited near the direction of the beam of the telescope, resulting in a beacon.

A very widespread system is the Shack-Hartmann wavefront sensor (Platt et al. 2001). The system generates focal points on a sensor using lenses. The position of the measured focal points is then compared to a position of reference and hence, the wavefront distortion can be measured. Finally, a set of deformable mirrors allows to compensate for the perturbed wavefront. The Shack-Hartmann setup is presented in figure 5.23:

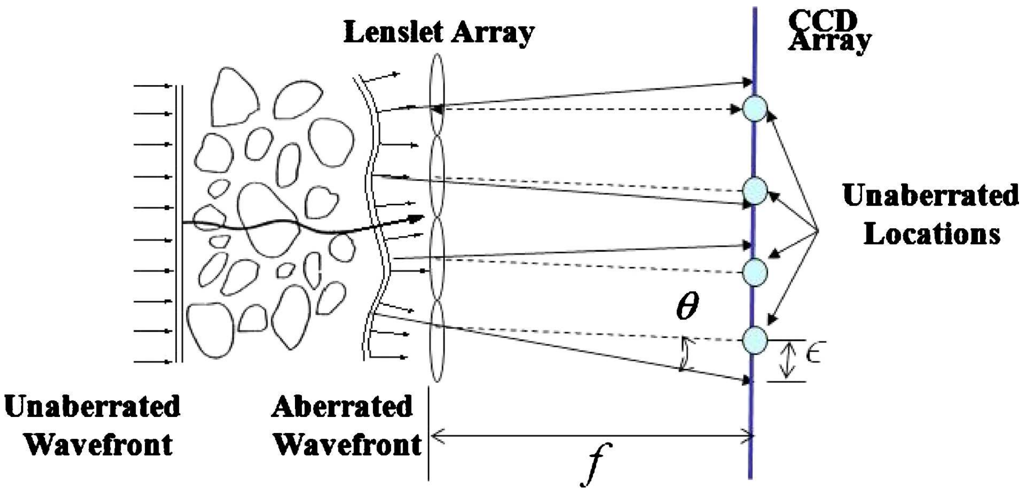

FIGURE 5.23: The Shack-Hartmann system. From (Abado et al. 2010).

Applications of this setup can be found in various domains such as high-energy laser applications (Schwiegerling and Neal 2005), astronomy (Wilson et al. 2003) and ophthalmology (Liang et al. 1994). The adaptation of this setup to sonar techniques could be realized by estimating the local wavefronts orientations on each group of hydrophones. Nonetheless, the approach relies on the use of a source of opportunity as a reference which is , in the ocean and in passive sonar configurations, very unlikely. Other techniques using artificial beacons, such as scattering in the upper atmosphere generated by a ground-based laser, were developed (Primmerman et al. 1991, Fugate et al. 1994). The idea of applying these techniques to underwater acoustics was tackled in Dobbins (1994). However, this method is only conceivable in an active sonar scenario, unless a source of noise could provide information about volume scattering and hence be used as an artificial beacon.

Other methods, more classical, tackled the issue of signal processing in presence of perturbed wavefronts. Historically, the uncertainty of the sensor position on the receiver array was considered as the primary source of loss of spatial coherence (Cox 1973b). In reality, as shown throughout this thesis, the ocean fluctuations, in particular internal waves in shallow and coastal waters, are also responsible for the degradation of array gain. Methods involving the exploration of the space of possible coherence functions combined with the use of optimal filters have been studied (Morgan and Smith 1990, Van Trees 2004). Nevertheless, the cost of these methods is extremely high since it involves an examination of the possible characteristics of the coherence function.

A model for the coherence function can be included in this type of methods (Ballard et al. 2009), but it involves strong assumptions on the type of fluctuations of the propagated signals. In practice, many different phenomena interact and influence each other, making delicate the choice of a specific coherence model .

Also, techniques including the combination of sub-arrays were developed. In fact, while the gain of a linear array does not follow the $G_{Th} = 10\log(N)$ rule in case of loss of coherence (an increase and a saturation of the gain is actually observed), an incoherent combination of N_{sub} sub-arrays of N_e elements induces a gain of $G_{Th}^{Sub} = 10\log(N_e) + 5\log(N_{sub})$ which does not saturate. The main advantage of this technique is its simplicity. The optimal size of the sub-arrays and the best way to combine them are nonetheless practical issues inherent to this method (Graham 1979).

Based on the capability of a receiver to transmit the recorded signal reversed in time, time-reversal (TR) techniques were proven to be an efficient way to focus the acoustic field on its source. This was demonstrated experimentally at the ultrasonic scale (Derode et al. 1995) and at the oceanic scale (Kuperman et al. 1998). The concept is nonetheless extremely sensitive to the fluctuations in the propagation medium (Dungan and Dowling 2000), especially for high-frequency signals traveling through a dynamic ocean (Hodgkiss et al. 1999). Robust TR techniques were therefore investigated, based on the use of waveguide invariant and singular value decomposition of the signal prior to back-propagation (Kim et al. 2003) or adaptive channel equalizers (Song et al. 2006).

Medical and especially ultrasonic imaging are domains that contributed to the research of corrective signal processing techniques as well. The main issues rely on the sound speed discontinuities between the tissues and scattering induced by the thickness of fat layers (Hinkelman et al. 1994, Anderson et al. 2001). Sound speed variations are also noticed in large tissue beds, such as the liver, or the breast (Zhu and Steinberg 1992). Figure 5.24 illustrates the analogy between the medical imaging issue and the problem studied in this thesis.

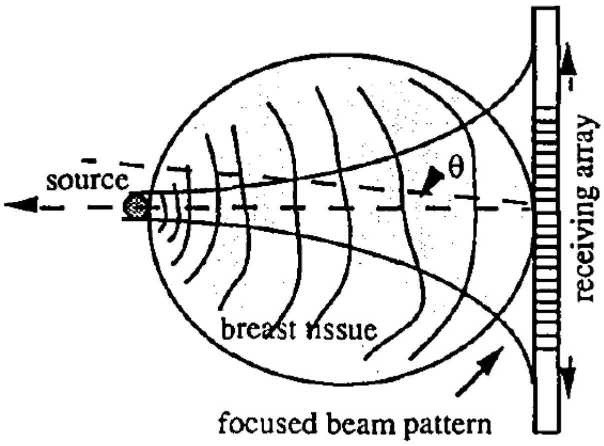

FIGURE 5.24: Schematic view of the wavefront distortions observed in breast imaging. From (Zhu and Steinberg 1992).

Adaptive signal processing techniques rely on the presence of a scatterer allowing to focus the array (similar to the guide star method). Since such scatterers are unlikely in these medical imaging scenarios, techniques using speckle regions as targets were developed (Robert and

Fink 2008). A method based on a lower-frequency transmission in order to create a source of reference in the medium was successfully applied (Dianis and von Ramm 2011). A second method, using the spatial properties of the propagated wave to perform self-calibration, was shown to be successfully applied to wavefront distortions caused by local sound speed perturbations in homogeneous tissues. Nevertheless, when strong scattering and amplitude fluctuations are observed, more robust techniques are necessary (Zhu and Steinberg 1992). Overall, these methods were developed in order to enhance the resolution of ultrasonic images, which is quite different than the results aimed here. In fact, the detection issue is the main interest of our study. However, the medical imaging techniques presented here could be applied in order to enhance the localization of underwater sound sources.

The fact that fluctuations of the propagation medium induces some degradation of the detection/localization/imaging performance has been explored. However, somewhat paradoxically, the heterogeneities of the medium can be used to perform imaging. Indeed, the fluctuations of the received signals can be used to extract meaningful information. Speckle-interferometry was first introduced by Labeyrie (Labeyrie 1970) in order to enhance the resolution of telescopes and hence mitigate the effect of atmospheric turbulence. Speckle is defined as the grainy structure produced by the reflection or the propagation of a laser beam from a scattering surface or through a 3D scattering environment (Labeyrie 1970). Assuming that the conditions of observation do not change (implying a short exposure duration), the image intensity distribution can be expressed as a function of the object intensity distribution and a transfer function, defined as the autocorrelation function of the speckle (perturbed received signal). Speckle-interferometry has been favorably applied to the detection of companions or exoplanets (Gladysz and Christou 2008a). In practice, this method does not provide information about the phase. Recent techniques allow to recover the phase information and could be applied to underwater acoustics. They are listed in Svet (2014).

The detection and photometry of exoplanets was recently improved by a series of techniques based on the stochastic difference between real sources and speckle. Gladysz proposed a blind, iterative deconvolution process allowing based on the discrimination between the probability density functions corresponding to the detected source and that corresponding to the *off-axis* speckle (Gladysz and Christou 2008a). Spectacular results in terms of discrimination between faint companions and speckle are obtained with this technique (Gladysz and Christou 2008b), even at low SNR, which is of considerable interest in our field of study. This method was also successfully applied to the issue of estimation of the brightness of the detected exoplanet (Gladysz et al. 2010). The reference-less property of this technique is especially interesting in the context of underwater acoustic detection. Moreover, it permits not only to enhance the detection capability, but the classification capability as well (Gladysz and Christou 2009).

Another concept, established heuristically in Hufnagel (1966) and developed in Fried (1966), is based on the idea that if the images are sufficiently close in terms of recording time, the atmospheric turbulence can be considered as fixed. The hypothesis is that there is a finite probability for the wavefront distortion to be negligible at a given time. This method is referred to as "lucky" imaging. The calculation of the probability that at a given time, the wavefront distortion is weak, is aimed, and the number of images necessary to obtain a satisfying result is deduced. An experimental validation of this concept is proposed in Bensimon et al. (1981). An adaptation of the lucky imaging in the Fourier domain is proposed in Mackay (2013), it is referred to as "lucky Fourier" and provides considerable sharpness improvement. The application of this technique to the random ocean problem depends on the signal integration time compared to the period of the studied phenomena, in order to make sure to obtain lucky outputs in a shorter time than the internal or surface waves period.

Finally, the last category of methods listed in this section is called here "robust" techniques. An exhaustive review of these techniques is proposed in Li and Stoica (2006). A particularly interesting process is presented in Jin and Friedlander (2004), where the problem tackled is the distribution of the source of interest. This issue is analogous to the wavefronts distortions due to internal waves in the ocean, since they both result in a spreading of the source position, or in the direction of arrival (DOA), and therefore, an array gain degradation. in Jin and Friedlander (2004), the described method is based on the evaluation of the generalized likelihood ratio (GLR) of the probability density functions (pdf) of the measured signal under the signal hypothesis, with the pdf of the measured signal under the noise hypothesis. This calculation is a function of the input SNR, the radius of coherence of the signal and the source elevation angle, in an oceanic configuration. An adaptation of this method to the measurements carried out in the water tank would consist in replacing the last parameter (elevation angle) by the source position in $(x_t; z_t)$, similarly to what was done in sections 5.3.1 and 5.3.2. A four parameter (five in the water tank case) estimation is therefore needed. Note that in the case where signal and noise can be considered as Gaussian random variables, the GLR method is similar to the "classical" beamforming when the radius of coherence is infinite. In the case of angular spreading of the source(s), the GLR technique exhibits degradation significantly less important than classical beamforming (Jin and Friedlander 2004). Another "robust" method related to the estimation of the DOA of distributed source is presented in Lee et al. (2008). The Cholesky factorization of the signal covariance matrix is proposed before conventional beamforming is applied. The performance is evaluated in terms of root-mean square error (RMSE) in DOA. The proposed method outperforms the covariance based least-square estimator and is close to the Cramer-Rao bound. The two latter methods present, to us, the highest potential to mitigate the degradation of array gain related to the fluctuations of the propagation medium.

5.5 Discussion

In this chapter, we focus on the degradation of sonar array gain when the received signal presents large phase and amplitude fluctuations. The calculation of a parameter accounting for the array gain degradation, δAG, is related to the MCF, and compared, with good agreement, to an empirical formula. The dependence in array size of δAG is investigated, with the conclusion that large arrays are more sensitive to the fluctuations of the propagation medium (Wilson 1998, Gorodetskaya et al. 1999). The influence of the regime of saturation is also studied. The analysis of δAG as a function of the saturation reveals that, paradoxically, an unsaturated case can exhibit gain degradation larger than a saturated case. This assessment was anticipated in the MCF analysis, since the same observation can be made regarding the radius of coherence.
The performance of blind classical source detection techniques (Matched Field BeamForming -MFBF- and MUltiple SIgnal Classification -MUSIC-) is also studied here. The deflection is calculated for a $64-$sensor array by comparing the output of each algorithm using the measured signals (plus WGN) and WGN only as inputs. The connection between the deflection and the input SNR is therefore investigated for each technique, as well as the link between the detection performance and the regime of saturation. Both techniques exhibit strong degradation when the saturation increases.
This highlights the need for adaptive signal processing techniques allowing to mitigate the effect of wavefront distortions on the detection capability.
Such techniques are listed in section 5.4. Various domains contributed to the development of corrective techniques adapted to the signal distortions due to fluctuations of the medium issue. The methods studied span from adaptive optics wavefront sensing and compensation to robust detection algorithms and originate from the effects of turbulent atmosphere on optical wave propagation, the sound speed heterogeneities in tissues on medical imagine, or non-destructive testing algorithms, and the distributions of source in radio waves propagation. The first two focus on the enhancement of the resolution of the used instrument and the detection problem is not really tackled. Especially, the influence of the noise is not, or only partially, studied, whereas, in underwater acoustics, it is critical. Nonetheless, as stated in introduction, the localization issue is secondary, since the source must be detected in the first place, but also of interest and these techniques may offer some improvements in this domain. On the other hand, the methods based on the incoherent combination of sub-arrays and the techniques issued from radio wave studies (GLR (Jin and Friedlander 2004) and Cholesky factorization (Lee et al. 2008)) are, to us, the candidates presenting the highest potential.

Chapter 6

At-sea Measurements: the ALMA Experiment.

Contents

6.1 Introduction

In this chapter, an analysis of the acoustic signals collected during an at-sea experiment is presented. The experimental system is called ALMA, for Acoustic Laboratory for Marine Applications, and was first deployed in October 2014 in Corsica, France. The development and the realization of ALMA was conducted by DGA Naval Systems, in collaboration with the ALSEAMAR and CESIGMA companies, with the objective of providing experimental data in shallow and coastal environments. The goal of this acoustic system is, *in fine*, to enhance the understanding of the ambient noise and to develop some adaptive sonar processing techniques. The first objective is linked to the civil community, since the main challenges are related to environmental and ecological issues. The development of sonar techniques adaptive to the environment is a challenge for the Defence community, since large arrays have to deal with highly fluctuating environments and are more sensible to the loss of spatial coherence. In the context of WPRM studies, only a few well-studied at-sea experiments were presented in the literature (Reynolds et al. 1985, Badiey et al. 2002, Tang et al. 2007), and there is a vivid interest

in developing what could be an underwater acoustic observatory dedicated to the study of sound wave propagation in a fluctuating marine environment.
The experimental configuration is presented in section 6.2. The first data gathering is detailed in section 6.3. Some results associated with the data acquired during the first trial are given in section 6.4.

6.2 Experimental configuration

The system was presented in Fattaccioli (2015). ALMA is a bi-static system composed of a pinger and a receiver array. They are respectively detailed in the next sections.

6.2.1 Source sub-system

The source sub-system consists in a wideband omnidirectional transmitter. The bandwidth of the pinger spans from $1\ kHz$ to $14\ kHz$. The transmission level can be adjusted up to $160\ dB\ ref\ \mu Pa@1m$. The duration of the transmitted sequence varies from $1\ ms$ to $1mn$, at sampling frequency $F_s = 48\ kHz$.
A schematic representation of the active sub-system is given in figure 6.1:

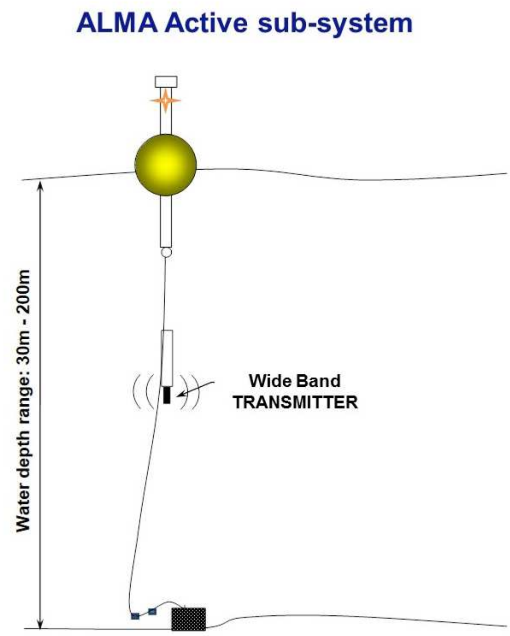

FIGURE 6.1: ALMA active sub-system scheme.

As shown in figure 6.1, the source system is deployable in water from $30\ m$ to $200\ m$ deep. The mooring is ensured by a surface buoy and the anchoring by a reinforced concrete half cube.

During the 2014 experiment, the transmitted signal was a sequence of several CW chirps at frequency $(2,\ 5,\ 7$ and $11\ kHz)$, a linear frequency modulation (LFM) and a sequence of white noise, assembled following the schematic source signal given in figure 6.2:

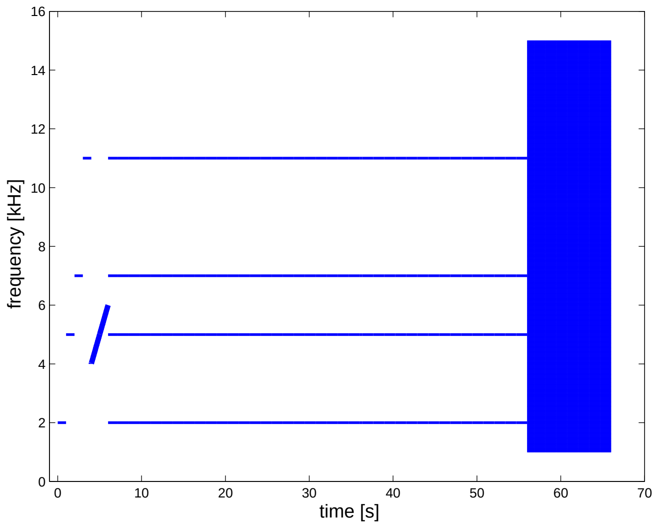

FIGURE 6.2: ALMA source signal sequence.

6.2.2 Receiver sub-system

At the receiver end, an acoustic array composed of four rigid sections of $2.7\ m$ length, each composed of 16 hydrophones, is proposed. The spacing between the hydrophones is adjustable (from $11\ cm$ to $15\ cm$), as well as the signal sampling frequency (from $7.5\ kHz$ to $48\ kHz$). A schematic representation of the passive sub-system is presented in figure 6.3:

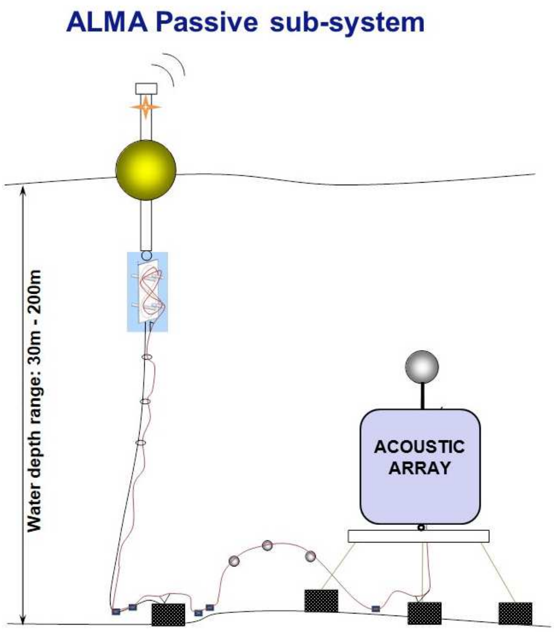

FIGURE 6.3: ALMA passive sub-system scheme.

A continuous temperature monitoring is ensured by 16 temperature sensors on the array. Moreover, the orientation of the receiver system is controlled at any time using 3D positioning sensors. As depicted by figure 6.3, the anchoring is guaranteed by 3 concrete blocks (1 × 550 kg, 2 × 125 kg in water). The noise level in the hydrophonic chain is less than sea state 0, up to $20\ kHz$.
The collected data are transmitted to a surface buoy via an optical fiber cable. The surface buoy ensures a $200\ h$ autonomy and a $1\ TB$ storage capability. Also, long range data transmission is available via WIFI. The anchoring of the surface buoy is done with a reinforced concrete cube of $1000\ kg$ in water.
The acoustic array modules were designed in order to be assembled in different ways; therefore, the following structures are available:

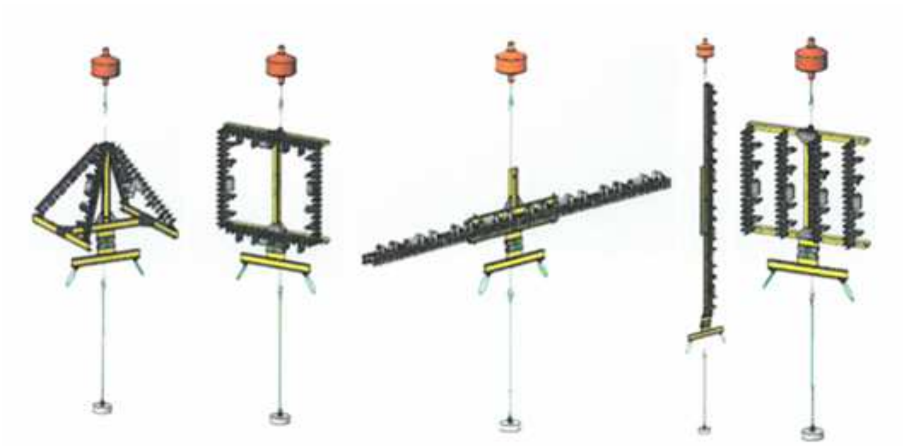

FIGURE 6.4: Different arrangements of ALMA passive sub-system (from left to right: pyramidal, square, linear horizontal, linear vertical, comblike).

The comblike configuration was chosen for the first data gathering, presented in section 6.3.

6.3 First data gathering

The first gathering of acoustic data was conducted in October (13^{th} – 24^{th}), 2014. The aim of this first data gathering was to acquire experimental data in a shallow water environment perturbed by internal waves. The deployment of the complete system was conducted by the COMEX company, in particular with the JANUS II research vessel. The area of deployment was the coast of Alistro, Corsica, France, as displayed in figure 6.5:

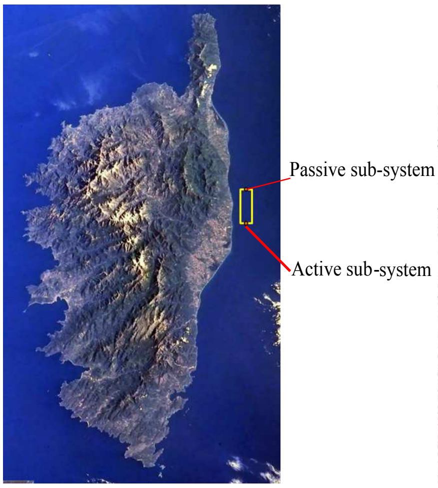

(A) Area of deployment of the first data gathering.

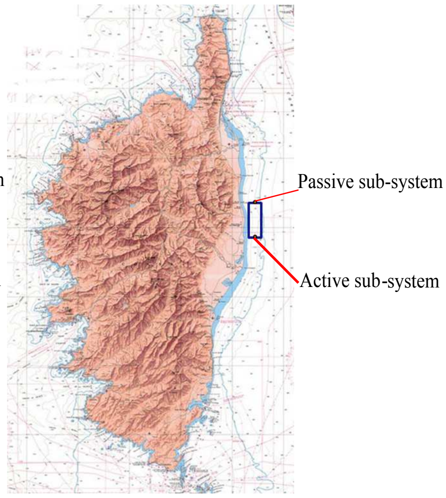

(B) Map of the deployment area.

FIGURE 6.5: Deployment area: 5 km away from the shores of Alistro, Corsica.

The active/passive sub-systems distance was of 9 km and the bottom was composed of coarse sand. A remarkably flat bottom was noticed, as well as a singularly flat sea surface (sea state 0). The source depth, D_s, was 40 m and the array depth, D_a, was 60 m . The passive sub-system and surface buoy are displayed in figure 6.6. Figure 6.7a reveals the presence of internal waves in the deployment area. The receiver array in water is shown in figure 6.7b using a snapshot from the COMEX remotely operated vehicle (ROV) camera.

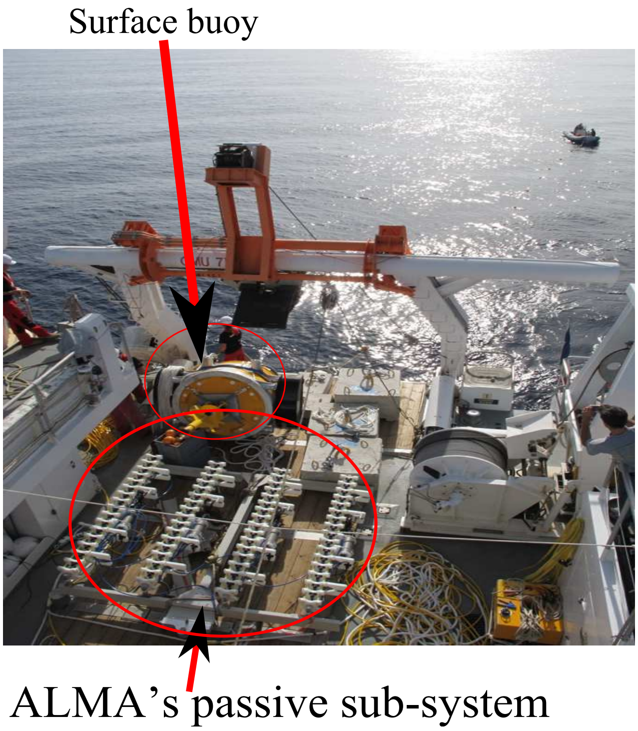

FIGURE 6.6: Passive sub-system on the deck of the JANUS II.

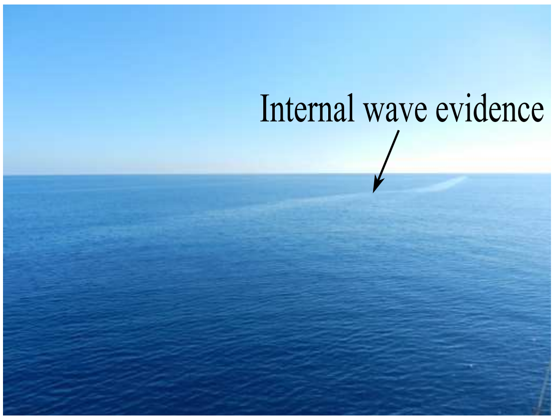

(A) Evidence of the presence of internal waves.

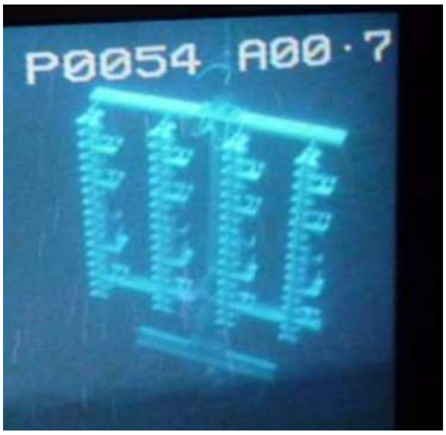

(B) ALMA's passive sub-system at a 60 m depth.

FIGURE 6.7: Passive sub-system in a medium perturbed by internal waves.

The evidence of the presence of internal waves was confirmed by the measurements of sound speed profiles using a CTD (Conductivity, Temperature and Depth) cast. The measured SSPs (sound speed profiles) are shown in figure 6.8. The recordings were conducted at the source and receiver locations, in order to investigate the dependence in range of the SSP. The temporal variability was also explored since the measurements were carried out on the 19/10/2014, and on the 20/10/2014. Each time the CTD cast was operated downwards (from the surface to the sea bottom) and upwards.

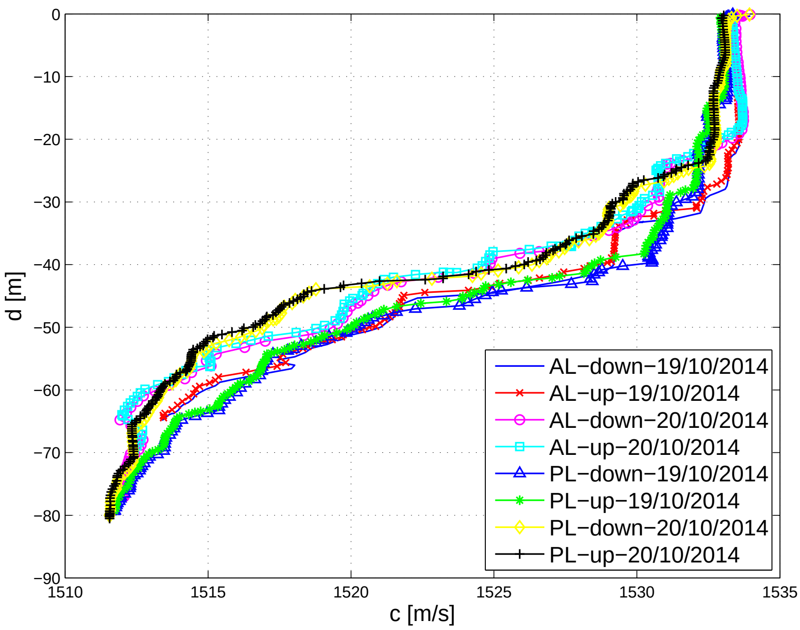

FIGURE 6.8: Sound speed profiles (SSPs) acquired with a CTD cast at two different locations: the Array Locatio (AL) and the Pinger Location (PL), at two different times: the 19/10/2014 and the 20/10/2014. Each measurements was carried out upwards and downwards.

According to figure 6.8, the sound speed is fairly constant near the interfaces: over the ten first meters ($-10\ m < d < 0\ m$), the eight measurements provide approximately the same value of $c = 1533\ m/s$. Similarly, in the region where $-80\ m < d < -70\ m$, the slight variations of the sound speed in these two regions are consistent throughout all the measurements, the curves are almost superimposed. The fact that internal waves are responsible for most of the sound speed fluctuations is confirmed by the depth of the most important deviations which occur in the $-60\ m < d < -40\ m$ region (thermocline). Typically, sound speed fluctuations up to $3\ m/s$ at a depth of $48\ m$ between the measurements conducted at the source and receiver locations on the 20/10/2014 are observed. Similarly, temporal deviations up to $5\ m/s$ showed up on both days.

The receiver array depth being $60\ m$ and the source depth being $40\ m$, there is a great chance that the influence of internal waves could be observed on the propagated signals. In section 6.4, a portion of the signals acquired on the 20/10/2014 are analyzed, as an example of results.

6.4 A glimpse of the experimental results

We present in this section, a glimpse of the results associated with the measurements conducted on the 20/10/2014. For technical reasons, it is not possible to present all results in this thesis. Therefore, we propose here a study of a portion of the acquired data. We focus on a $0.65\ s$ slice of the $7\ kHz$ CW. The signal acquired on the first sensor of the array is shown in figure 6.9:

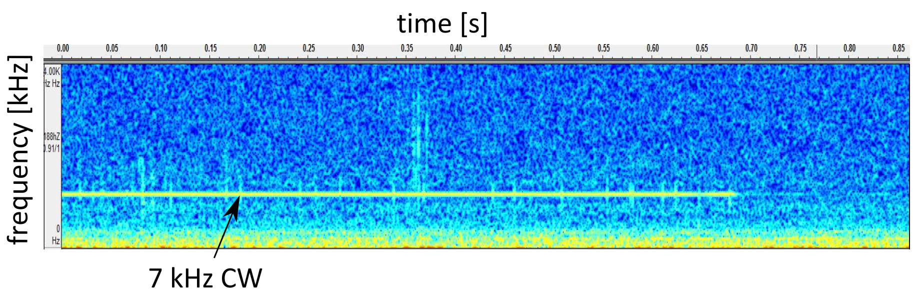

FIGURE 6.9: Time-frequency representation of the $7\ kHz$ CW acquired by the first sensor of the array.

Furthermore, since this thesis focuses on the influence of the propagation medium on linear arrays, the analysis of the experimental results is carried out on a 16–element linear block. Segments of 50 periods were considered in order to perform the MCF calculation. The MCF provided by $N_S = 91$ segments were then averaged (similarly to what was done with the N_r realizations in equation 4.1, in section 4.3).

The magnitude of the MCF, noted $|\Gamma(s/\lambda)|$ (we recall that s is the sensor spacing), is displayed in figure 6.10:

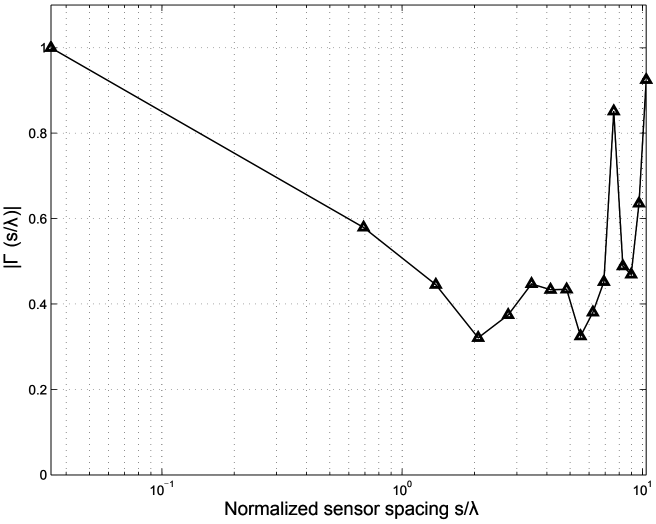

FIGURE 6.10: MCF of the 7 kHz CW.

The analysis of figure 6.10 shows a loss of coherence quite large, since the classical radius of coherence ($|\Gamma\left(s/\lambda\right)| = e^{-0.5}$) is reached for $s/\lambda = 0.7$, which corresponds to the normalized spacing between two consecutive hydrophones. The oscillations and the increase of the MCF magnitude observed for large normalized sensor spacings can be explained by the fact that only a few statistically independent realizations of the medium are available here. In fact, the N_S segments chosen to perform the MCF calculations were not significantly different and therefore, they do not lead to an accurate calculation of the MCF for these spacings. In other words, the coherence time is here more important than the individual duration of the N_S segments. The calculation of $|\Gamma|$ on signals recorded at more isolated times should provide results more exploitable. Moreover, this would allow temporal coherence to be computed.

The array gain degradation associated with the loss of coherence is also investigated. The array gain was calculated following formula 5.1, proposed in section 5.2. The result is shown in figure 6.11:

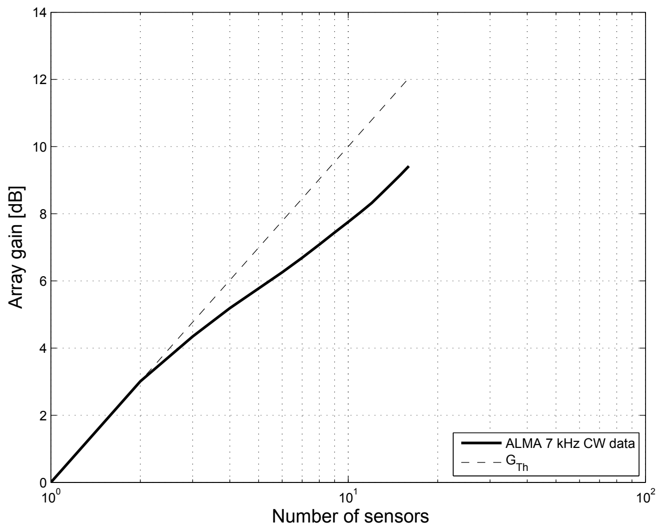

FIGURE 6.11: δAG calculated on a $0.65\ s$ section of the $7\ kHz$ CW.

The comparison between the array gain calculated here and the theoretical array gain ($G_{Th} = 10\ \log(N)$) highlights the degradation induced by the ocean fluctuations. For the maximum array length (16 sensors), the degradation of the array gain is almost $3\ dB$, which, for a $16-$sensor array, is huge. For comparison, the array gain degradation experienced by a $16-$sensor array in the case of the scaled experiment (figure 5.1b) was at most $1.5\ dB$. However, as explained in the MCF case, the analysis of the observed array gain degradation has to be taken with great care, since the statistical relevance of the data processed here is not ensured.

In order to characterize the experiment in terms of regime of fluctuation, the tools used in sections 4.2 and 4.4 are applied to the data analyzed in this section. First, the CPD (Complex Pressure Distribution) is computed. We recall that the behavior of the CPD can help classifying a given experiment as unsaturated or saturated (partially or fully). In the unsaturated case, the CPD follows relatively closely the circle of mean pressure, whereas in the saturated regimes, the complex pressure is more randomly distributed and peaks are concentrated around zero. The CPD calculated for the $7\ kHz$ CW is given in figure 6.12:

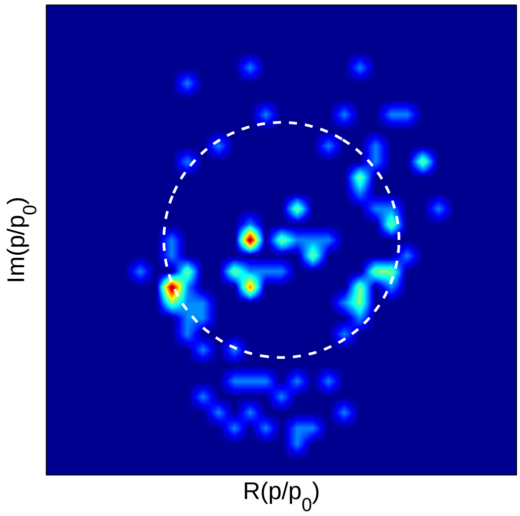

FIGURE 6.12: CPD calculated on a $0.65\ s$ section of the $7\ kHz$ CW.

As explained earlier, the moderate number of realizations available here tends to make the analysis difficult. Nonetheless, the CPD displays some interesting features: in fact, a non negligible portion of the pressure is distributed along the circle of mean pressure, but some occurences are also observed inside the circle, in particular in the zero area. Without any pretention to make any absolute statement, we can deduce from this analysis that the experiment studied here could display some of the features of the partially saturated regime.

The experiment is also studied using the normalized intensity distribution analysis. The histograms of normalized intensity $I/<I>$ are calculated. Comparisons with typical theoretical distributions such as the log-normal, the modulated exponential (ME) and the exponential distributions are provided as well. The mathematical details of these classical distributions are given in section 4.4. We expect the analysis conducted here to provide more information on the qualitative characteristic of the experiment studied in this section. Substantially, a good agreement between the observed distribution of $I/<I>$ and the log-normal distribution would hint that the experiment could be classified as unsaturated. On the other hand, if the exponential, or ME distributions are better candidates then the fully saturated regime would represent a more appropriate solution. The normalized intensity distribution is displayed in figure 6.13:

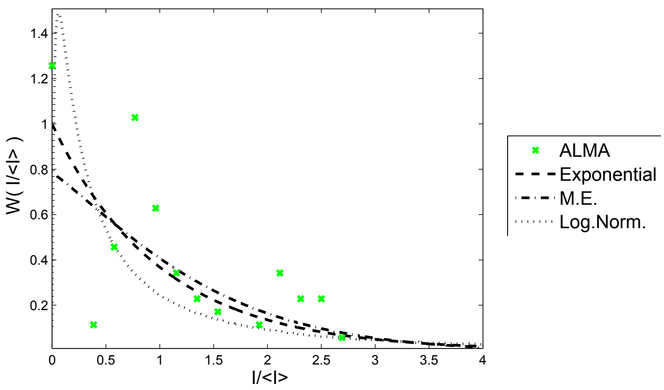

FIGURE 6.13: Normalized intensity distribution of the $0.65\ s$ section of the $7\ kHz$ CW.

The analysis of figure 6.13 leads to a similar conclusion than what could be observed in the CPD case. In fact, a decrease from the $I/<I>\approx 0$ to the higher values of normalized intensity is noticed, which implies that the unsaturated hypothesis can be rejected. However, a rise of the intensity distribution around $I/<I>\approx 1$ is observed. This suggests that the distribution is indeed an exponential-type distribution with a log-normal remainder, meaning that the experiment considered here might be interpreted as a transition from the unsaturation towards the full saturation. The partial saturation seems therefore to be the most plausible choice for characterizing the experiment studied here.

6.5 Conclusion

Overall, we presented an at-sea experimental facility that will allow to address issues of interest in underwater acoustics, such as ambient noise characterization, or data acquisition in coastal waters, almost constantly subject to the propagation of internal waves. The modularity of the system presented here was highlighted: in particular, the various configurations available for ALMA's passive sub-system allows to tackle various issues.
The measurements of the sound speed profile at various locations and times confirmed the hypothesis of presence of internal waves in the acquisition area. We focused on a $7\ kHz$ CW sequence acquired during the first sea trail in October 2014 and the demonstration that internal waves impacted the coherence of the received signal was made clear. This chapter does not pretend to exhaustively analyze the data acquired during the trial. However, the aim is to show, using the tools developed and used to study the data recorded with our scaled experiment protocol, that the typical characteristics of the acoustic data fluctuations can be analyzed, at least qualitatively. More statistically independent realizations (in particular, at different recording times) would help quantifying the loss of coherence and the related degradation of array gain with more confidence than the partial results presented here. Indeed, a $3\ dB$ array gain loss was measured on a $16-$sensor array, which is tremendous when compared to the corresponding results in our scaled experiment (see figure 5.1b).

The complex pressure and normalized intensity distributions analyses otherwise lead to confirm the hypothesis that the experiment studied here could be classified as partially saturated, in some measure.
Finally, a more complete analysis and more diverse measurements (in terms of times and locations) of the sound speed profiles will help retrieving the typical correlation scales and amplitude of the sound speed fluctuations, using the Garrett and Munk model for example (Garrett and Munk 1972; 1975). The adaptation of this commonly used model to shallow water environments was proposed in Yang and Yoo (1999) and could represent an interesting tool to accurately describe the environment. The adaptation of the GM model is actually quite simple in this case, since it simply consists in tuning the characteristic mode number for the internal wave spectrum j^* to 1 instead of 3.
An interesting perspective of work would therefore be, once the environment is characterized according to the procedure described in the previous paragraph, to use the scaling procedure presented in Chapter 2 in order to manufacture an acoustic slab presenting the suited characteristics allowing to reproduce the signal fluctuations with our scaled experimental protocol. A direct comparison between the real ocean data and the acoustic signals acquired in a controlled environments could hence be available. A better understanding of the physical phenomena involved with sound waves propagation through a coastal oceanic environment could be aimed, as well as a validation of our scaling procedure, throughout confrontations between real and scaled measured data.

Chapter 7

Conclusion and Future Work

Contents

7.1 Concluding remarks

In this thesis, an experimental protocol allowing to reproduce, under controlled laboratory conditions, the effects of fluctuations in the water column on underwater acoustic propagation is proposed. These fluctuations are essentially related to internal waves, occurring extremely frequently in shallow and coastal waters. Numerous examples of theoretical and numerical studies of the statistics of the acoustic waves propagated through an internal waves field are available in the literature, exhibiting the complexity of the intrinsic physical phenomenon. This assessment motivated the work presented here.
Our protocol involves the propagation of ultrasonic waves through RAndom Faced Acoustic Lenses (RAFALs) immersed in water and used to reproduce the wavefront distortions similar to those observed in the case of sound waves propagating through IW. In order to develop the experimental protocol presented here, the work of Booker (Booker et al. 1985) and Andrews (Andrews et al. 1997) was studied: they justify the similarity in terms of statistics of the propagated wave between the traveling through an extended 3D fluctuating medium and the propagation through an almost-2D perturbation. The conditions of validity of this result are achieved using the dimensional analysis popularized by Flatté (Dashen et al. 2010). The latter consists in classifying configurations where the waves propagate through short ranges, weak fluctuations (unsaturation), long ranges or strong fluctuations (saturation) and a transition region in between (partial saturation) using dimensional parameters. In this document, analytical calculations of the acoustic field propagated through the RAFAL using the Small-Slope Approximation (SSA), the parabolic approximation and Fourier transforms are presented. They lead to the evaluation of the first, second and fourth-order moments of the received pressure.

These statistical quantities, along with the Fresnel radius, are used to obtain expressions of the *strength* and *diffraction* parameters, used in the dimensional analysis in the ocean configuration (Dashen et al. 2010). Another parameter is derived: the acoustic correlation length, whose expression was found to depend on the environmental parameters, the propagation range and the frequency (Tatarskii 1971, Fattaccioli et al. 2009), under the conditions of applicability corresponding to the configurations studied here (frequency of 1 to 15 kHz, range between 1 and 10 km). Hence, a continuity between these parameters is ensured by tuning the statistical characteristics of the RAFAL's output face, as well as other experimental parameters, such as the signal frequency and the distance of propagation.

Using a relatively simple manufacturing procedure and making use of the experimental facilities (automatic displacements of the motorized rails of a water tank), a series of measurements was conducted. The representativeness of the experimental scheme is evaluated in Chapter 4, where the Complex Pressure Distribution (CPD), the Mutual Coherence Function (MCF) and the normalized intensity distributions were calculated using the data acquired in the water tank, synthetic data produced by numerical codes based on a parabolic equation (PE) (in the scaled experiment configuration and in the equivalent oceanic medium) and theoretical results. A satisfying agreement in terms of CPD and normalized intensity distribution was found for all the regimes of fluctuations considered and allowed to validate the results provided by dimensional analysis, used to *a priori* sort out the various configurations in terms of regimes of fluctuations. The work of (Reynolds et al. 1985, Blanc-Benon and Juvé 1993, Colosi et al. 2001) established the link between the behaviors of the distribution of complex pressure and intensity and the involved regime of fluctuations. The unsaturated and partially saturated configurations lead to excellent agreements for all the performed calculations in terms of MCF. The radius of coherence was found to be very accurately estimated using scaled experimental data. This result is essential since the radius of coherence and overall the loss of coherence was proven to be related to the degradation of the array gain Cox (1973a), Ancey (1973), Laval and Labasque (1981), Carey (1998), Gorodetskaya et al. (1999). The full saturation case exhibits small deviations between the measured and theoretical radius of coherence, which might be explained by the limit of validity of the SSA in this scenario. In this case, the RAFALs manufactured in order to produce acoustic fields representative of the fully saturated regime are in fact quite rough, since the standard deviation of the roughness amplitude is $2mm$ ($\approx 3\lambda$) and the vertical correlation of the roughness is $4mm$ ($\approx 6.5\lambda$). Another approach, such as the Kirchoff approximation, might provide more accurate results in this case.

The long-term objectives of this study is to evaluate the limits of performance of the signal processing techniques and to mitigate the influence of the fluctuations of the propagation medium on the detection performance. The detection capabilities of two traditionally used algorithm were measured using the data measured in the scaled experiment detailed here. The link between the loss of coherence highlighted by the narrowing of the MCF and the array gain degradation is underlined in Chapter 5. In fact, as the saturation increases, the source detection capability decreases. In practice, some configurations where the array gain degradation is more important in an unsaturated case than in a saturated configuration may be observed, however, the overall analysis of the detection capability leads to the conclusion that phase aberrations combined with strong amplitude fluctuations induce the most important degradation. This emphasizes the fact that corrective signal processing techniques are required. A review of the existing techniques in various domains analogous to the case of interest show that some methods already in use in other physical domains may be used in our sonar case. If numerous studies focus on the improvement in terms of resolution in a context of high SNR, which is secondary in the context of our study, some techniques are promising. Especially, the incoherent combination of subarrays and two techniques derived for the case of distributed radio sources are, to us, paths to explore uppermost.

Finally, a non-extensive analysis of at-sea experimental results was provided in Chapter 6. The experimental facility was presented, as well as the results from part of the data acquired during the first sea trial. The tools used to perform the data analysis of the signals measured following the tank experiment scheme were also used here. The data presented here are not necessarily relevant in terms of direct comparisons with one of the configurations explored by the scaled experiment, but the objective of this analysis was to show that this comparison could be performed in the future.

7.2 Future work

If the relevance of the experimental protocol presented here was demonstrated, it would be interesting to modify it in order to obtain more independent realizations of the medium. The fact that the measurements were conducted using a single receiver limited the number of realizations due to the time required to perform an experiment. Working with high-frequency linear arrays borrowed from the medical imaging field would help solving this issue, since a parallel recording on independent channels would be possible. Also, the manufacturing process of the RAFAL could be improved in order to produce more samples.
One of the major limitations of the scaled experimental protocol is the fact that only a single-scale spectrum of fluctuations was considered. In fact, the amplitude of the randomly rough output face of the RAFAL and the sound speed fluctuations both follow Gaussian distributions, which translate into single-scale spectra. However, the RAFAL manufacturing process theoretically allows any shape to be realized. We could therefore imagine that a more sophisticated distribution could be chosen for the amplitude of the roughness. For instance, a von Karman spectrum was used in a similar approach in Buckley (1975). The broadband spectrum of IW could therefore be simulated. Nevertheless, such a modification would have a cost in terms of calculations of the various dimensional parameters involved in this thesis, since their

evaluation and the scaling of typical quantities are based on their statistical behavior.

The at-sea measurement facility presented in Chapter 6 represents an astounding source of real-scale experimental data. A more exhaustive measurement of the environmental parameters would allow to generate the RAFAL corresponding to a given at-sea configuration, and hence to replay the scenario under laboratory conditions. A dual objective may be seen in this comparisons: enhancing the representativeness of the scaled experimental protocol, and improving the understanding of the physical phenomena taking place at sea.

The topic of wavefront distortions due to scattering from the sea surface or the sea bottom was let aside in this thesis. We see however, a non negligible possibility that the experimental protocol presented here could be representative of the space scales of signals distorted by an interaction with a rough surface. The correlation scales selected for the RAFAL presented here are adapted to internal waves-induced acoustic fluctuations, but they are also tunable and could very much be illustrative of a loss of coherence due to surface agitation, or seabed roughness. The NARCISSUS-2005 model, developed by Cristol (Cristol 2005) can provide the vertical and horizontal acoustic correlation scales in the case of a rough sea surface. Parameters such as the range of propagation, the angle between the surface waves crest and the direction of propagation, and the signal frequency are used to calculate the ratio of acoustic correlation length to the wavelength. Preliminary calculations revealed that the loss of coherence was larger horizontally than vertically, whereas the contrary was observed for internal waves. Configurations at a center frequency of $1\ kHz$ in a summer sound speed profile environment lead to values of L_y/λ of the order of 3 to 10 and values of L_z/λ of the order of 14 to 25 for propagation ranges from 1 up to $3\ km$. According to figure 4.9, these values are achievable with our experimental protocol. The dynamic aspect of the process shall nonetheless be taken into consideration, since the coherence time is much shorter in the case of surface fluctuations than in the IW configuration. Overall, the issue of loss of coherence due to scattering from a rough surface might be addressed using an adaptation of the experimental protocol proposed in this thesis.

The concepts and results presented in this thesis fit into a wider project aiming to develop corrective techniques allowing to mitigate the degradation of sonar performance. The path is still long until such techniques can be found and the experimental protocol shown here might contribute to the development and validation of novel algorithms. The most important part of the future work lies in this topic. The retained techniques presented in Chapter 6 constitute, to us, the starting point of the future studies. The procedure proposed in Lee et al. (2008) was tested and showed some promising results (Real et al. 2015a). Nonetheless, the development of new techniques, or the adaptation of methods let aside from the review proposed in Chapter 5 can contribute to the effort.

Appendix A

Fourth-order moment calculations

Contents

It was shown in Chapter 2 that the continuous 3D perturbed medium and the locally perturbed case show similar expressions for the first and second-order moments. Especially, the mean pressure field is directly related to the strength parameter Φ and the spatial intercorrelation calculation leads to the evaluation of the acoustic correlation length L_z (here in the vertical direction). We present in this Appendix, the calculation of the fourth-order moment, noted C_4, both in the extended 3D medium and the local perturbation cases.

A.1 C_4 in the 3D perturbed medium

We consider throughout the calculations showed in this section, random sound speed fluctuations. The fourth-order moment satisfies the following parabolic equation:

$$ik_0 \frac{\partial C_4}{\partial x} - \frac{\partial^2 C_4}{\partial \zeta \partial y} + ik_0^3 \left[2\Phi(0) - 2\Phi(y) - 2\Phi(\zeta) + \Phi(y+\zeta) - \Phi(y-\zeta)\right] C_4 = 0 \tag{A.1}$$

where $C_4 = \left\langle p\left(x, z - \frac{\zeta}{2}, \frac{1}{2}y\right) p^*\left(x, z - \frac{\zeta}{2}, -\frac{1}{2}y\right) p\left(x, z + \frac{\zeta}{2}, \frac{1}{2}y\right) p^*\left(x, z + \frac{\zeta}{2}, \frac{1}{2}y\right)\right\rangle$. Setting $\acute{\psi} = k_0^3 \Phi(0) L_z^2$ we can apply the change of variables showed in Frankenthal et al. (1984)

$$\begin{cases} \acute{x} = k_0^2 \Phi(0)\, x \\ \acute{\zeta} = \sqrt{\acute{\psi}} \frac{\zeta}{L_z} \\ \acute{y} = \sqrt{\acute{\psi}} \frac{y}{L_z} \end{cases} \tag{A.2}$$

In addition, writing $\Phi(z) = \Phi(0)\, p\left(\frac{z}{L_z}\right)$ leads to the following expression for equation A.1:

$$\frac{\partial C_4}{\partial \acute{x}} + i\frac{\partial^2 C_4}{\partial \acute{\zeta}\acute{y}} + 2\left[1 - p\left(\acute{\psi}\acute{y}\right) - p\left(\acute{\psi}\acute{\zeta}\right) + \frac{1}{2}p\left(\acute{\psi}\left(\acute{\zeta}+\acute{y}\right)\right) + \frac{1}{2}p\left(\acute{\psi}\left(\acute{\zeta}-\acute{y}\right)\right)\right]C_4 = 0; \tag{A.3}$$

with the initial condition $C_4\left(\acute{x}=0,\acute{\zeta},\acute{y}\right) = 1$. Let know $\chi_4\left(\acute{x},\acute{u},\acute{y}\right)$ be the Fourier transform of C_4 along the $z-$ direction. Equation A.3 becomes:

$$\frac{\partial \chi_4}{\partial \acute{x}} + \acute{u}\frac{\partial \chi_4}{\partial \acute{y}} + 2\left(1 - p\left(\acute{\psi}\acute{y}\right)\right)\chi_4 = \int d\acute{u}\chi_4\left(\acute{x},\acute{u}-\acute{v},\acute{y}\right)\frac{1}{2\pi}\int d\acute{\xi}e^{i\acute{v}\acute{\xi}}F\left(\acute{\xi},\acute{\psi}\acute{y}\right) \tag{A.4}$$

where $F(z,y) = 2p(z) - p(y+z) - p(z-y)$ and $\chi_4\left(0,\acute{u},\acute{y}\right) = \delta\left(\acute{u}\right)$.
In the case of multiple scale medium, χ_4 can be written:

$$\chi_4\left(\acute{x},\acute{u},\acute{y}\right) = \chi_4\left(\acute{x},\acute{u},\acute{y},\underline{u},\underline{y},\right) \tag{A.5}$$

And equation A.4 becomes:

$$\frac{\partial \chi_4}{\partial \acute{x}} + \acute{u}\frac{\partial \chi_4}{\partial \acute{y}} + \underline{u}\frac{\partial \chi_4}{\partial \underline{y}} + 2\left(1 - p\left(\acute{\psi}\acute{y}\right)\right)\chi_4 = \int d\acute{u}\chi_4\left(\acute{x},\acute{u}-\acute{\psi}\acute{v},\acute{y},\underline{u}-\acute{\psi}^2\underline{v},\underline{y}\right)\frac{1}{2\pi}\int d\acute{\xi}e^{i\acute{v}\acute{\xi}}F\left(\acute{\xi},\acute{\psi}\acute{y}\right) \tag{A.6}$$

Letting $\hat{\chi}_4(\acute{x},\acute{\xi},om\acute{e}ga,\underline{u},\underline{y}) = \frac{1}{2\pi}d\acute{u}\;d\acute{y}\;e^{-i\acute{u}\acute{\xi}}e^{i\acute{\omega}\acute{y}}\chi_4$, it can be demonstrated that:

$$\acute{u}\frac{\partial \chi_4}{\partial \acute{y}} = \acute{\omega}\frac{\partial \hat{\chi}_4}{\partial \acute{\xi}} \tag{A.7}$$

which leads to equation A.8:

$$\frac{\partial \hat{\chi}_4}{\partial \acute{x}} + \acute{u}\frac{\partial \hat{\chi}_4}{\partial \acute{\xi}} + \underline{u}\frac{\partial \hat{\chi}_4}{\partial \underline{y}} + 2\left(1 - p\left(\acute{\psi}\acute{y}\right)\right)\hat{\chi}_4 = \int d\acute{u}\hat{\chi}_4\left(\acute{x},\acute{\xi},\acute{\omega},\underline{u}-\acute{\psi}^2\underline{v},\underline{y}\right)\frac{1}{2\pi}e^{-i\acute{v}\acute{\xi}}\int d\acute{\xi}e^{i\acute{v}\acute{\xi}}F\left(\acute{\xi},\acute{\psi}\acute{y}\right) \tag{A.8}$$

Operating the following change of variables $\hat{\chi}_4\left(\acute{x},\acute{\xi},\acute{\omega},\underline{u},\underline{y}\right) = \hat{\sigma}\left(\acute{x},\acute{\xi},\acute{\omega},\acute{\psi}\acute{\xi},\acute{\psi}\acute{\omega},\underline{u},\underline{y}\right)$ and carrying out a Taylor's expansion in $\acute{\psi}^2$ at the $0-$th and $1-$st order leads to:

$$\frac{\partial \hat{\sigma}_1}{\partial \acute{x}} + \omega\frac{\partial \hat{\sigma}_1}{\partial \acute{\xi}} + \underline{\omega}\frac{\partial \hat{\sigma}_1}{\partial \underline{\xi}} + \underline{u}\frac{\partial \hat{\sigma}_1}{\partial \underline{y}} = -2\left(1 - p\left(\acute{y}\right)\right)\hat{\sigma}_1 - i\left(2p'\left(\underline{\xi}\right) - p'\left(\underline{\xi}+\underline{y}\right) - p'\left(\underline{\xi}-\underline{y}\right)\right)\frac{\partial \hat{\sigma}_0}{\partial \underline{u}} \tag{A.9}$$

Equation A.9 allows to solve for $\hat{\sigma}_0$ which, by successive inverse Fourier transforms leads to the solution for C_4. The integral form of C_4 is given by:

$$C_4\left(\acute{x},0,0\right) = \int d\acute{u}\; e^{-2\int_0^{\acute{x}} dx'\left(1-p\left(\acute{\psi}\acute{u}x'\right)\right)} \frac{1}{2\pi} \int d\acute{\xi}\; e^{i\acute{u}\acute{\xi}} e^{\int_0^{\acute{x}} dx'\left[2p\left(\acute{\psi}\acute{\xi}\right)-p\left(\acute{\psi}\left(\acute{\xi}-\acute{u}x'\right)\right)-p\left(\acute{\psi}\left(\acute{\xi}+\acute{u}x'\right)\right)\right]} \quad \text{(A.10)}$$

The neighborhood of $\acute{u} = 0$ and $\acute{\xi} = 0$ predominates the last integral term, which leads to the final form of C_4:

$$C_4\left(\acute{x},0,0\right) \approx \mathcal{J}_1 + \mathcal{J}_2, \quad \text{(A.11)}$$

where

$$\mathcal{J}_1 = \frac{1}{\acute{\psi}^2\acute{x}} \int_{-\infty}^{\infty} du' \frac{1}{2\pi} \int_{-u'}^{u'} d\acute{\vartheta}\; e^{i\frac{u'\acute{\vartheta}}{\acute{\psi}^2\acute{x}}}\; e^{\acute{x}\acute{\vartheta}^2\left(p^{(2)}(0)-\frac{p'\left(u'\right)-p'(0)}{u'}\right)} \quad \text{(A.12)}$$

If we now let $\acute{x} = x_3\acute{\psi}^{-4/3}$, $\vartheta_2 = \vartheta\acute{\psi}^{-2/3}$ and write $\underline{\omega} = \frac{u'\vartheta_2}{x_3}$, equation A.12 becomes:

$$\mathcal{J}_1 = \int_0^{\infty} d\varsigma \frac{1}{\varsigma} \int_0^{\varsigma/2\Lambda} d\underline{\omega} \cos\left(\underline{\omega}\right)\; e^{-4\underline{\omega}^2\Lambda^2\Phi^2\mathcal{C}\mathcal{H}(\varsigma)} \quad \text{(A.13)}$$

where $\mathcal{H}\left(\varsigma\right) = \left(p^{(2)}\left(0\right) - \frac{p'(u')-p'(0)}{u'}\right)/u'^2$ and $\mathcal{C}$ is chosen so that $\mathcal{H}(0) = 1$.

Similarly, we obtain:

$$\mathcal{J}_2 = \frac{1}{\pi} \int_0^{\infty} d\varsigma \frac{1}{\varsigma} \int_0^{\varsigma/2\Lambda} d\underline{\omega} \cos\left(\underline{\omega}\right)\; e^{-4\frac{\underline{\omega}^2}{3}\Lambda^2\Phi^2\mathcal{B}\mathcal{G}(\varsigma)} \quad \text{(A.14)}$$

where $\mathcal{G}\left(\varsigma\right) = \frac{p^{(2)}(0)-p^{(2)}(\vartheta)}{\vartheta^2}$ and $\mathcal{B}$ is chosen so that $\mathcal{G}(0) = 1$. Note the appearance of Flatté's parameter Λ and Φ in the expressions of $\mathcal{J}_1$ and $\mathcal{J}_2$.

A.2 C_4 in the lens case

We now present the calculations of C_4 in the case of propagation through an acoustic lens. For simplicity, the transmitted wave is considered here to be a plane wave, so that the measured wave after propagation through the rough phase screen is:

$$p(x,z) = \int dz'\; \mathscr{G}\left(x, z-z'\right) e^{i\Delta\phi(z')} \quad \text{(A.15)}$$

where $\mathscr{G}(x, z-z') \approx \frac{k_0}{2\pi}\int d\theta\, e^{-i\frac{k_0}{2}\theta^2 x} e^{ik_0(z-z')}$.
$C_4(x,0,0)$ can here be written as:

$$C_4(x,0,0) = \int du\, e^{-2\sigma_\phi^2\left(1-p\left(\frac{u}{k_0 L_Z}\right)\right)} \frac{1}{2\pi}\int d\tau\, e^{iu\tau} e^{\sigma_\phi^2\left[2p\left(\frac{\tau x}{L_Z}\right)-p\left(\frac{\tau x}{L_Z}-\frac{u}{k_0 L_Z}\right)-p\left(\frac{\tau x}{L_Z}+\frac{u}{k_0 L_Z}\right)\right]}. \tag{A.16}$$

The rms phase variance is noted σ_ϕ. Similarly to what was done in the extended 3D medium case, we apply the following change of variable: $t\acute{a}u = \tau\frac{x}{L_Z}$ and $\acute{u} = \frac{u}{k_0 L_Z}$. This leads equation A.16 to become:

$$C_4(x,0,0) = \frac{k_0 L_z^2}{x}\int d\acute{u}\, e^{-2\sigma_\phi^2(1-p(\acute{u}))}\frac{1}{2\pi}\int d\acute{\tau}\, e^{i\frac{k_0 L_z^2}{x}\acute{\tau}\acute{u}} e^{\sigma_\phi^2[2p(\acute{\tau})-p(\acute{\tau}-\acute{u})-p(\acute{\tau}+\acute{u})]} \tag{A.17}$$

In the neighborhood of $\acute{u} = 0$ and $\acute{\tau} = 0$, $C_4(x,0,0)$ takes the following form:

$$C_4(x,0,0) = \mathcal{I}_1 + \mathcal{I}_2 \tag{A.18}$$

where

$$\mathcal{I}_1 = \frac{k_0 L_z^2}{x}\int_\infty^\infty d\acute{u}\, \frac{1}{2\pi}\int_{\acute{u}}^{\acute{u}} d\acute{\tau}\, e^{i\frac{k_0 L_z^2}{x}\acute{u}\acute{\tau}} e^{\sigma_\phi^2\acute{\tau}^2\left(p^{(2)}(0)-p^{(2)}(\acute{u})\right)} \tag{A.19}$$

and

$$\mathcal{I}_2 = \frac{k_0 L_z^2}{x}\int_\infty^\infty d\acute{\tau}\, \frac{1}{2\pi}\int_{\acute{\tau}}^{\acute{\tau}} d\acute{u}\, e^{i\frac{k_0 L_z^2}{x}\acute{u}\acute{\tau}} e^{\sigma_\phi^2\acute{\tau}^2\left(p^{(2)}(0)-p^{(2)}(\acute{\tau})\right)} \tag{A.20}$$

Letting $\varpi = \frac{k_0 L_z^2}{x}\acute{u}\acute{\tau}$ and $\varsigma = \acute{u}^2$ leads to a new expression for $\mathcal{I}_1$:

$$\mathcal{I}_1 = \frac{1}{\pi}\int_0^\infty d\varsigma\, \frac{1}{\varsigma}\int_0^{\varsigma/\Lambda} d\varpi\, \cos(\varpi)\, e^{-\Phi^2\Lambda^2\mathcal{D}\mathcal{F}(\varsigma)} \tag{A.21}$$

where $\mathcal{F}(\varsigma) = \frac{p^{(2)}(0)-p^{(2)}(\sqrt{\varsigma})}{\varsigma}$ and $\mathcal{D}$ is chosen so that $\mathcal{F}(\varsigma) = 1$.
Similarly, we obtain for $\mathcal{I}_2$, with $\varsigma_2 = \acute{\tau}^2$:

$$\mathcal{I}_2 = \frac{1}{\pi}\int_0^\infty d\varsigma_2\, \frac{1}{\varsigma_2}\int_0^{\varsigma_2/\Lambda} d\varpi\, \cos(\varpi)\, e^{-\Phi^2\Lambda^2\mathcal{K}\mathcal{E}(\varsigma_2)} \tag{A.22}$$

where $\mathcal{E}(\varsigma_2) = \frac{p^{(2)}(0)-p^{(2)}(\sqrt{\varsigma_2})}{\varsigma_2}$ and $\mathcal{K}$ is chosen so that $\mathcal{E}(\varsigma) = 1$.
In this case too, Λ and Φ appear in the expression of the fourth-order moment. If they are not

absolutely equal, the expressions of $C_4(x, 0, 0)$ in the case of a 3D extended medium and in the case of a rough phase screen are extremely similar. This confirms the fact that distortions comparable to what can be observed in an oceanic medium perturbed by IW can be measured with out experimental protocol, at least in terms of stochastic moment of the acoustic pressure up to the fourth order.

Appendix B

Average number of eigenrays calculation

Contents

In this appendix the average number of eigenrays in the case of a 3D fluctuating medium is analytically derived. The expression of the ray divergence is obtained from the moments of the ray geometrical parameters. The behavior of the average number of eigenrays as a function of the distance of propagation highlights the validity of the approach used in this thesis: three regions can be sorted out, leading to the idea that three regimes of fluctuations can be defined.

The standard parabolic equation applied to the fourth-order moment of the acoustic pressure in a three dimensional environment is given by:

$$
\begin{aligned}
& i\frac{\partial C_4}{\partial x} - \frac{\partial^2 C_4}{\partial z_1 \partial u_1} - \frac{\partial^2 C_4}{\partial y_1 \partial v_1} - \frac{\partial^2 C_4}{\partial z_2 \partial u_2} - \frac{\partial^2 C_4}{\partial y_2 \partial v_2} + i[-\frac{1}{2}(u_1^2+u_2^2)\frac{\partial^2 \Phi_\delta}{\partial \zeta^2}\bigg|_{0,0} - \frac{1}{2}(v_1^2+v_2^2)\frac{\partial^2 \Phi_\delta}{\partial v^2}\bigg|_{0,0} \\
& - (u_1u_2+v_1v_2)\frac{\partial^2 \Phi_\delta}{\partial v \partial \zeta}\bigg|_{0,0} - u_1u_2\frac{\partial^2 \Phi_\delta}{\partial \zeta^2}\bigg|_{z_1-z_2,y_1-y_2} - v_1v_2\frac{\partial^2 \Phi_\delta}{\partial v^2}\bigg|_{z_1-z_2,y_1-y_2} \\
& - (u_1u_2+v_1v_2)\frac{\partial^2 \Phi_\delta}{\partial v \partial \zeta}\bigg|_{z_1-z_2,y_1-y_2}]C_4 = 0;
\end{aligned}
\tag{B.1}
$$

where $u_i = k_0\zeta_i$, $v_i = k_0 \upsilon_i (i \in [1;2])$. We also define the normalized cross-correlation as $F(\frac{\zeta}{L_V}, \frac{\upsilon}{L_H}) = \Phi_\delta(\zeta, \upsilon)$. equation B.1 was obtained under the assumption that the correlation function of the sound speed fluctuations is Gaussian or exponential.

Similarly, for the second order moment C, we find:

$$i\frac{\partial C}{\partial x} - \frac{\partial^2 C}{\partial z \partial u} + i\left[-\frac{1}{2}u^2 \frac{\partial^2 \Phi_\delta}{\partial \zeta^2}\bigg|_{0,0} - \frac{1}{2}v^2 \frac{\partial^2 \Phi_\delta}{\partial \upsilon^2}\bigg|_{0,0} - (uv)\frac{\partial^2 \Phi_\delta}{\partial \upsilon \partial \zeta}\bigg|_{0,0} \right] C = 0; \tag{B.2}$$

If we now define the spatial Fourier transform of the fourth order moment C_4 as follows:

$$J_4(x, y_1, z_1, y_2, z_2, \varphi_1, \varphi_2, \theta_1, \theta_2) = \frac{1}{(2\pi)^4} \iiiint du_1 dv_1 du_2 dv_2 e^{i\theta_1 u_1} e^{i\theta_2 u_2} e^{i\varphi_1 v_1} e^{i\varphi_2 v_1} C_4; \tag{B.3}$$

this definition of the Fourier transform of the fourth order moment of the acoustic pressure leads to a new form of the standard parabolic equation in three dimensions:

$$\begin{aligned}
&\frac{\partial J_4}{\partial x} + \theta_1 \frac{\partial J_4}{\partial z_1} + \varphi_1 \frac{\partial J_4}{\partial y_1} + \theta_2 \frac{\partial J_4}{\partial z_2} + \varphi_2 \frac{\partial J_4}{\partial y_2} \\
&+ \frac{1}{2}\frac{\partial^2 \Phi_\delta}{\partial \zeta^2}\bigg|_{0,0} \left[\frac{\partial^2 J_4}{\partial \theta_1^2} + \frac{\partial^2 J_4}{\partial \theta_2^2} \right] + \frac{1}{2}\frac{\partial^2 \Phi_\delta}{\partial \upsilon^2}\bigg|_{0,0} \left[\frac{\partial^2 J_4}{\partial \varphi_1^2} + \frac{\partial^2 J_4}{\partial \varphi_2^2} \right] + \frac{\partial^2 \Phi_\delta}{\partial \upsilon \partial \zeta}\bigg|_{0,0} \left[\frac{\partial^2 J_4}{\partial \varphi_1 \partial \theta_1} + \frac{\partial^2 J_4}{\partial \varphi_2 \partial \theta_2} \right] \\
&+ \frac{\partial^2 \Phi_\delta}{\partial \zeta^2}\bigg|_{z_1 - z_2, y_1 - y_2} \left[\frac{\partial^2 J_4}{\partial \theta_1 \partial \theta_2} \right] + \frac{\partial^2 \Phi_\delta}{\partial \upsilon^2}\bigg|_{z_1 - z_2, y_1 - y_2} \left[\frac{\partial^2 J_4}{\partial \varphi_1 \partial \varphi_2} \right] + \frac{\partial^2 \Phi_\delta}{\partial \upsilon \partial \zeta}\bigg|_{z_1 - z_2, y_1 - y_2} \left[\frac{\partial^2 J_4}{\partial \varphi_2 \partial \theta_1} + \frac{\partial^2 J_4}{\partial \varphi_1 \partial \theta_2} \right] \\
&= 0;
\end{aligned} \tag{B.4}$$

Once again, a simple analogy allows us to write the equivalent of equation B.4 for the second order moment, using the fact that:

$$J_2(x, y, z, \varphi, \theta) = \frac{1}{(2\pi)^2} \iint du dv e^{i\theta u} e^{i\varphi v} C; \tag{B.5}$$

This would give us:

$$\frac{\partial J_2}{\partial x} + \theta \frac{\partial J_2}{\partial z} + \varphi \frac{\partial J_2}{\partial y} + \frac{1}{2}\frac{\partial^2 \Phi_\delta}{\partial \zeta^2}\bigg|_{0,0} \left[\frac{\partial^2 J_2}{\partial \theta^2} \right] + \frac{1}{2}\frac{\partial^2 \Phi_\delta}{\partial \upsilon^2}\bigg|_{0,0} \left[\frac{\partial^2 J_2}{\partial \varphi^2} \right] + \frac{\partial^2 \Phi_\delta}{\partial \upsilon \partial \zeta}\bigg|_{0,0} \left[\frac{\partial^2 J_2}{\partial \varphi \partial \theta} \right] = 0; \tag{B.6}$$

The solution of equation B.6, denoted j_2, may be physically interpreted as the probability density function of the random variable ensemble $\{Y, Z, \Psi, \Theta\}$. j_2 can therefore be developed in terms of moments of the statistics of depths and angles of a single ray, provided the pertinent initial condition:

$$j_2(x_0, y, z, \varphi, \theta; y_0, z_0, \varphi_0, \theta_0) = \delta(y - y_0)\delta(z - z_0)\delta(\varphi - \varphi_0)\delta(\theta - \theta_0); \tag{B.7}$$

$$\begin{aligned}
&j_2(x, y, z, \varphi, \theta; y_0, z_0, \varphi_0, \theta_0) \\
&= \frac{1}{(4\pi)^4} \iiiint dz' dy' d\varphi' d\theta' \\
&\times e^{i[z'(z-<Z>)+y'(y-<Y>)+\varphi'(\varphi-<\Psi>)+\theta'(\theta-<\Theta>)]} \\
&\times e^{-\frac{1}{2}(z'^2<\Delta Z^2>+y'^2<\Delta Y^2>+\varphi'^2<\Delta\Psi^2>+\theta'^2<\Delta\Theta^2>)} \\
&\times e^{-(z'y'<\Delta Z\Delta Y>+\varphi'\theta'<\Delta\Psi\Delta\Theta>+z'\varphi'<\Delta Z\Delta\Psi>+z'\theta'<\Delta Z\Delta\Theta>+y'\varphi'<\Delta Y\Delta\Psi>+y'\theta'<\Delta Y\Delta\Theta>)};
\end{aligned} \tag{B.8}$$

In equation B.8, the fact that we need to evaluate the statistical moments related to the random variable ensemble $\{Y, Z, \Psi, \Theta\}$ is highlighted. An analysis of the fourth order moment equation leads to the idea that the solution for equation B.4 is a simple generalization of the solution of the second order moment equation.
This extension would consist in taking into consideration the random variable ensemble $\{Y_1, Y_2, Z_1, Z_2, \Psi_1, \Psi_2, \Theta_1, \Theta_2\}$ corresponding to a pair of rays. This leads to the need of evaluating not only the mean of the random variables, but also the variance and the covariance of all the random variables in the ensemble taken into account here. Multiplying equation B.4 by one of the random variable, for example z_1, and integrating the resulting equation over the random variable ensemble would provide us an expression for $< Z_1 >$. The first term of B.4 would therefore be :

$$\begin{aligned}
&\int\int\int\int\int\int\int\int dz_1 dy_1 dz_2 dy_2 d\theta_1 d\varphi_1 d\theta_2 d\varphi_2 z_1 \frac{\partial J_4}{\partial x} \\
&= \frac{\partial}{\partial x} \int\int\int\int\int\int\int\int dz_1 dy_1 dz_2 dy_2 d\theta_1 d\varphi_1 d\theta_2 d\varphi_2 z_1 J_4 \\
&= \frac{\partial}{\partial x} < Z_1 >;
\end{aligned} \tag{B.9}$$

A similar evaluation for all the terms in equation B.4 ends up with the following relation:

$$\frac{\partial}{\partial x} < Z_1 > = < \Theta_1 > \tag{B.10}$$

Applying this procedure to all the R.V. (Random Variables) taken into consideration in this study, we obtain the following systems

$$\begin{cases} \frac{d}{dx} < Z_i >=< \Theta_i >; \\ \frac{d}{dx} < Y_i >=< \Psi_i >; \\ \frac{d}{dx} < \Theta_i >= \frac{d}{dx} < \Psi_i >= 0; \end{cases} \tag{B.11}$$

In the following systems, we limit our analysis to cases where $\Phi_\delta(\upsilon, \zeta)$ may be separated as product of functions of vertical and horizontal directions:

$$\Phi_\delta(\upsilon, \zeta) = \frac{1}{4\pi^2} \int d\lambda e^{i\lambda\zeta} \phi_V(\lambda) \int d\mu e^{i\mu\upsilon} \phi_H(\mu). \tag{B.12}$$

The covariance moments of the R.V. ensemble are governed by the following systems of equation:

$$\begin{cases} \frac{d}{dx} < \Delta Z_i \Delta Z_j >=< \Delta Z_j \Delta\Theta_i > + < \Delta Z_i \Delta\Theta_j >; \\ \frac{d}{dx} < \Delta Z_i \Delta\Theta_j >=< \Delta\Theta_i \Delta\Theta_j >; \\ \frac{d}{dx} < \Delta\Theta_i \Delta\Theta_j >= \frac{1}{4\pi^2} \iint d\lambda d\mu \lambda^2 \mathcal{M} \phi_V(\lambda) \phi_H(\mu); \end{cases} \tag{B.13}$$

$$\begin{cases} \frac{d}{dx} < \Delta Z_i \Delta Y_j >=< \Delta Y_j \Delta\Theta_i > + < \Delta Z_i \Delta\Psi_j >; \\ \frac{d}{dx} < \Delta\Theta_i \Delta Y_j >= \frac{d}{dx} < \Delta\Psi_j \Delta Z_i >=< \Delta\Theta_i \Delta\Psi_j >; \\ \frac{d}{dx} < \Delta\Theta_i \Delta\Psi_j >= \frac{1}{4\pi^2} \iint d\lambda d\mu \lambda\mu \mathcal{M} \phi_V(\lambda) \phi_H(\mu); \end{cases} \tag{B.14}$$

$$\begin{cases} \frac{d}{dx} < \Delta Y_i \Delta Y_j >=< \Delta Y_j \Delta\Psi_i > + < \Delta Y_i \Delta\Psi_j >; \\ \frac{d}{dx} < \Delta Y_i \Delta\Psi_i >=< \Delta\Psi_i \Delta\Psi_j >; \\ \frac{d}{dx} < \Delta\Phi_i \Delta\Psi_j >= \frac{1}{4\pi^2} \iint d\lambda d\mu \mu^2 \mathcal{M} \phi_V(\lambda) \phi_H(\mu); \end{cases} \tag{B.15}$$

where the quantity $\mathcal{M}$ is defined as follows:

$$\begin{aligned} \mathcal{M} =& e^{i[\lambda(<Z_i>-<Z_j>)+\mu(<Y_i>-<Y_j>)]} \\ & e^{-\frac{\lambda^2}{2}(<\Delta Z_i^2>+<\Delta Z_j^2>-2<\Delta Z_i \Delta Z_j>)} \\ & e^{-\frac{\mu^2}{2}(<\Delta Y_i^2>+<\Delta Y_j^2>-2<\Delta Y_i \Delta Y_j>)} \\ & e^{\lambda\mu(<\Delta Z_i \Delta Y_i>-<\Delta Z_i \Delta Y_j>-<\Delta Y_i \Delta Z_j>+<\Delta Z_j \Delta Y_j>)}. \end{aligned} \tag{B.16}$$

If we now define α_0 and β_0 as two geometrical parameters related to the considered ray , we can write:

$$\begin{cases} R_{ZZ}(x,\alpha_0^i-\alpha_0^j,\beta_0^i-\beta_0^j) =< \Delta Z(x,\alpha_0^i,\beta_0^i)\Delta Z(x,\alpha_0^j,\beta_0^j) >; \\ R_{Z\Theta}(x,\alpha_0^i-\alpha_0^j,\beta_0^i-\beta_0^j) =< \Delta Z(x,\alpha_0^i,\beta_0^i)\Delta \Theta(x,\alpha_0^j,\beta_0^j) >; \\ R_{\Theta\Theta}(x,\alpha_0^i-\alpha_0^j,\beta_0^i-\beta_0^j) =< \Delta \Theta(x,\alpha_0^i,\beta_0^i)\Delta \Theta(x,\alpha_0^j,\beta_0^j) >; \\ R_{YY}(x,\alpha_0^i-\alpha_0^j,\beta_0^i-\beta_0^j) =< \Delta Y(x,\alpha_0^i,\beta_0^i)\Delta Y(x,\alpha_0^j,\beta_0^j) >; \\ R_{ZY}(x,\alpha_0^i-\alpha_0^j,\beta_0^i-\beta_0^j) =< \Delta Z(x,\alpha_0^i,\beta_0^i)\Delta Y(x,\alpha_0^j,\beta_0^j) >; \\ R_{Y\Theta}(x,\alpha_0^i-\alpha_0^j,\beta_0^i-\beta_0^j) =< \Delta Y(x,\alpha_0^i,\beta_0^i)\Delta \Theta(x,\alpha_0^j,\beta_0^j) >; \\ R_{Z\Phi}(x,\alpha_0^i-\alpha_0^j,\beta_0^i-\beta_0^j) =< \Delta Z(x,\alpha_0^i,\beta_0^i)\Delta \Psi(x,\alpha_0^j,\beta_0^j) >; \\ R_{\Theta\Psi}(x,\alpha_0^i-\alpha_0^j,\beta_0^i-\beta_0^j) =< \Delta \Theta(x,\alpha_0^i,\beta_0^i)\Delta \Psi(x,\alpha_0^j,\beta_0^j) >; \\ R_{Y\Psi}(x,\alpha_0^i-\alpha_0^j,\beta_0^i-\beta_0^j) =< \Delta Y(x,\alpha_0^i,\beta_0^i)\Delta \Psi(x,\alpha_0^j,\beta_0^j) >; \\ R_{\Psi\Psi}(x,\alpha_0^i-\alpha_0^j,\beta_0^i-\beta_0^j) =< \Delta \Psi(x,\alpha_0^i,\beta_0^i)\Delta \Psi(x,\alpha_0^j,\beta_0^j) >; \end{cases} \tag{B.17}$$

In practice, α_0 and β_0 represent either the initial angles θ_0 and φ_0 of a ray, in the case of a point source, or the initial coordinates of the ray z_0, y_0 if the wave is originally plane. Similarly, in the three dimensions case, $\alpha_0^{i,j}$ and $\beta_0^{i,j}$ would correspond to the same quantities related, this time, to a pair of rays i, j.
The systems B.13 to B.15 translate into the following systems:

$$\begin{cases} \frac{d}{dx}R_{ZZ} = 2R_{Z\Theta}; \\ \frac{d}{dx}R_{Z\Theta} = R_{\Theta\Theta}; \\ \frac{d}{dx}R_{\Theta\Theta} = \frac{1}{4\pi^2}\iint d\lambda d\mu \lambda^2 \mathscr{N}\phi_V(\lambda)\phi_H(\mu); \end{cases} \tag{B.18}$$

$$\begin{cases} \frac{d}{dx}R_{ZY} = R_{Z\Psi} + R_{Y\Theta}; \\ \frac{d}{dx}R_{Y\Theta} = \frac{d}{dx}R_{Z\Psi} = R_{\Phi\Theta}; \\ \frac{d}{dx}R_{\Psi\Theta} = \frac{1}{4\pi^2}\iint d\lambda d\mu \lambda\mu \mathscr{N}\phi_V(\lambda)\phi_H(\mu); \end{cases} \tag{B.19}$$

$$\begin{cases} \frac{d}{dx}R_{YY} = 2R_{Y\Psi}; \\ \frac{d}{dx}R_{Y\Psi} = R_{\Psi\Psi}; \\ \frac{d}{dx}R_{\Psi\Psi} = \frac{1}{4\pi^2}\iint d\lambda d\mu \mu^2 \mathscr{N}\phi_V(\lambda)\phi_H(\mu); \end{cases} \tag{B.20}$$

where $\mathscr{N}$ is define as:

$$\begin{aligned} \mathscr{N} =& e^{i[\lambda\alpha_0 x+\mu\beta_0 x]} \\ & e^{-\lambda^2(R_{ZZ}(x,0,0)-R_{ZZ}(x,\alpha_0,\beta_0))} \\ & e^{-\mu^2(R_{YY}(x,0,0)-R_{YY}(x,\alpha_0,\beta_0))} \\ & e^{-2\lambda\mu(R_{ZY}(x,0,0)-R_{ZY}(x,\alpha_0,\beta_0))}. \end{aligned} \tag{B.21}$$

Systems B.18 to B.20 will be used in the evaluation of the divergence of the rays, which is the main point of the next section.

B.1 Divergence of the rays

The divergence is an important feature of a ray. Indeed, in order to characterize the regime of fluctuations related to a configuration, the number of eigenrays is used. This number of eigenrays, denoted N_{eig} is evaluated from the divergence of the rays. The divergence is defined as being inversely proportional to the acoustic intensity:

$$|U| = \frac{1}{|p|^2} = \iint d\alpha_0 d\beta_0 \delta\left(z - Z\left(x, \alpha_0, \beta_0\right)\right) \delta\left(y - Y\left(x, \alpha_0, \beta_0\right)\right), \tag{B.22}$$

with

$$\begin{cases} \delta\left(z - Z(x, \alpha_0, \beta_0)\right) = \frac{\partial Z}{\partial \alpha_0}\Big|_R \left(\alpha_0 - \alpha_{0_R}\right) + \frac{\partial Z}{\partial \beta_0}\Big|_R \left(\beta_0 - \beta_{0_R}\right); \\ \delta(y - Y(x, \alpha_0, \beta_0)) = \frac{\partial Y}{\partial \alpha_0}\Big|_R \left(\alpha_0 - \alpha_{0_R}\right) + \frac{\partial Y}{\partial \beta_0}\Big|_R \left(\beta_0 - \beta_{0_R}\right); \end{cases} \tag{B.23}$$

The expression of the divergence in three dimensions is given by:

$$U = \frac{\partial Z}{\partial \alpha_0}\frac{\partial Y}{\partial \beta_0} - \frac{\partial Z}{\partial \beta_0}\frac{\partial Y}{\partial \alpha_0}. \tag{B.24}$$

A useful quantity for the calculation of $< N_{eig} >$ is the normalized standard deviation of the divergence U. This quantity is denoted $\frac{\sigma_U}{<U>}$. In order to evaluate the normalized standard deviation, we first need an expression for $< U^2 >$:

$$\left\langle U^2 \right\rangle = \left\langle \left(\frac{\partial Z}{\partial \alpha_0}\frac{\partial Y}{\partial \beta_0}\right)^2 + \left(\frac{\partial Z}{\partial \beta_0}\frac{\partial Y}{\partial \alpha_0}\right)^2 - 2\frac{\partial Z}{\partial \alpha_0}\frac{\partial Y}{\partial \beta_0}\frac{\partial Z}{\partial \beta_0}\frac{\partial Y}{\partial \alpha_0} \right\rangle. \tag{B.25}$$

By definition, the eigen rays are the rays such that the pair of variables (α_0, β_0) is solution to the algebraic system:

$$\begin{cases} Z(x, \alpha_0, \beta_0) = \left\langle Z(x, \alpha_0, \beta_0) \right\rangle + \Delta Z(x, \alpha_0, \beta_0) = z; \\ Y(x, \alpha_0, \beta_0) = \left\langle Y(x, \alpha_0, \beta_0) \right\rangle + \Delta Y(x, \alpha_0, \beta_0) = y. \end{cases} \tag{B.26}$$

Given the expression of Z and Y in equation B.26, equation B.25 can be expanded as follows:

$$\left\langle U^2 \right\rangle = \bar{U}^4 + 4\bar{U}^2 \left\langle \frac{\partial \Delta Z}{\partial \alpha_0} \frac{\partial \Delta Y}{\partial \beta_0} \right\rangle + \bar{U}^2 \left[\left\langle (\frac{\partial \Delta Y}{\partial \beta_0})^2 \right\rangle + \left\langle (\frac{\partial \Delta Z}{\partial \alpha_0})^2 \right\rangle \right]$$
$$+ \left\langle \left(\frac{\partial \Delta Z}{\partial \alpha_0} \right)^2 \left(\frac{\partial \Delta Y}{\partial \beta_0} \right)^2 \right\rangle + \left\langle \left(\frac{\partial \Delta Z}{\partial \beta_0} \right)^2 \left(\frac{\partial \Delta Y}{\partial \alpha_0} \right)^2 \right\rangle - 2\bar{U}^2 \left\langle \frac{\partial \Delta Z}{\partial \beta_0} \frac{\partial \Delta Y}{\partial \alpha_0} \right\rangle$$
$$- 2 \left\langle \frac{\partial \Delta Z}{\partial \alpha_0} \frac{\partial \Delta Y}{\partial \beta_0} \frac{\partial \Delta Z}{\partial \beta_0} \frac{\partial \Delta Y}{\partial \alpha_0} \right\rangle, \tag{B.27}$$

where $\bar{U} =< U >$ (for visiblity). Equation B.27 can be rewritten as follows:

$$< U^2 >= \bar{U}^4 - 4\bar{U}^2 \frac{\partial^2 R_{ZY}}{\partial \beta_0 \alpha_0}\bigg|_{x,0,0} - \bar{U}^2 \left[\frac{\partial^2 R_{ZZ}}{\partial \alpha_0^2}\bigg|_{x,0,0} + \frac{\partial^2 R_{YY}}{\partial \beta_0^2}\bigg|_{x,0,0} \right] + \frac{\partial^2 R_{ZZ}}{\partial \alpha_0^2}\bigg|_{x,0,0} \frac{\partial^2 R_{YY}}{\partial \beta_0^2}\bigg|_{x,0,0}$$
$$+ 2 \left(\frac{\partial^2 R_{ZY}}{\partial \beta_0 \alpha_0}\bigg|_{x,0,0} \right) + \frac{\partial^2 R_{YY}}{\partial \alpha_0^2}\bigg|_{x,0,0} \frac{\partial^2 R_{ZZ}}{\partial \beta_0^2}\bigg|_{x,0,0} + 2 \left(\frac{\partial^2 R_{ZY}}{\partial \beta_0 \alpha_0}\bigg|_{x,0,0} \right)^2 + 2\bar{U}^2 \frac{\partial^2 R_{ZY}}{\partial \beta_0 \alpha_0}\bigg|_{x,0,0}$$
$$- 2 \left(\frac{\partial^2 R_{ZZ}}{\partial \alpha_0^2}\bigg|_{x,0,0} \frac{\partial^2 R_{YY}}{\partial \beta_0^2}\bigg|_{x,0,0} + \frac{\partial^2 R_{ZY}}{\partial \alpha_0^2}\bigg|_{x,0,0} \frac{\partial^2 R_{ZY}}{\partial \beta_0^2}\bigg|_{x,0,0} + \left(\frac{\partial^2 R_{ZY}}{\partial \beta_0 \alpha_0}\bigg|_{x,0,0} \right)^2 \right) \tag{B.28}$$

which simplifies into:

$$< U^2 >= \bar{U}^4 - 2\bar{U}^2 \frac{\partial^2 R_{ZY}}{\partial \beta_0 \alpha_0}\bigg|_{x,0,0} - \bar{U}^2 [\frac{\partial^2 R_{ZZ}}{\partial \alpha_0^2}\bigg|_{x,0,0} + \frac{\partial^2 R_{YY}}{\partial \beta_0^2}\bigg|_{x,0,0}] + \frac{\partial^2 R_{ZZ}}{\partial \alpha_0^2}\bigg|_{x,0,0} \frac{\partial^2 R_{YY}}{\partial \beta_0^2}\bigg|_{x,0,0}$$
$$+ 2 \left(\frac{\partial^2 R_{ZY}}{\partial \beta_0 \alpha_0}\bigg|_{x,0,0} \right)^2 + \frac{\partial^2 R_{YY}}{\partial \alpha_0^2}\bigg|_{x,0,0} \frac{\partial^2 R_{ZZ}}{\partial \beta_0^2}\bigg|_{x,0,0} \tag{B.29}$$

In order to evaluate $< U^2 >$, expressions for $\frac{\partial^2 R_{ZY}}{\partial \beta_0 \alpha_0}\Big|_{x,0,0}$, $\frac{\partial^2 R_{ZZ}}{\partial \alpha_0^2}\Big|_{x,0,0}$, $\frac{\partial^2 R_{ZZ}}{\partial \beta_0^2}\Big|_{x,0,0}$, $\frac{\partial^2 R_{YY}}{\partial \alpha_0^2}\Big|_{x,0,0}$ and $\frac{\partial^2 R_{YY}}{\partial \beta_0^2}\Big|_{x,0,0}$ are needed. These terms can be obtained by solving systems B.18 to B.20 (complete derivation given at the end of Appendix B). The solutions are of the form:

$$\begin{cases} \frac{\partial^2 R_{ZZ}}{\partial \alpha_0^2}\Big|_{x,0,0} = \frac{D_0 e^{\xi_0} + D_p e^{\lambda_p \xi_0} + D_m e^{\lambda_m \xi_0} + x^2}{1 + (\frac{L_V}{L_H})^4} \\ \frac{\partial^2 R_{YY}}{\partial \beta_0^2}\Big|_{x,0,0} = (\frac{L_V}{L_H})^2 \frac{\partial^2 R_{ZZ}}{\partial \alpha_0^2}\Big|_{x,0,0} ; \end{cases} \tag{B.30}$$

where

$$\begin{cases} D_0 = -2\psi_0^{-\frac{2}{3}}\frac{1}{3}; \\ D_p = 2\psi_0^{-\frac{2}{3}}(\frac{1}{6} - 0.2887i); \\ D_m = 2\psi_0^{-\frac{2}{3}}(\frac{1}{6} + 0.2887i); \\ \lambda_p = e^{\frac{2i\pi}{3}}; \\ \lambda_m = e^{-\frac{2i\pi}{3}}; \\ \psi_0 = 2\Phi_\delta(0,0)(\frac{1}{L_V^4} + \frac{1}{L_H^4}); \end{cases} \tag{B.31}$$

$$\begin{cases} \left.\frac{\partial^2 R_{YY}}{\partial \alpha_0^2}\right|_{x,0,0} = \frac{D_0 e^{\xi_0} + D_p e^{\lambda_p \xi_0} + D_m e^{\lambda_m \xi_0} + x^2}{1+(\frac{L_V}{L_H})^4} \\ \left.\frac{\partial^2 R_{ZZ}}{\partial \beta_0^2}\right|_{x,0,0} = (\frac{L_H}{L_V})^2 \left.\frac{\partial^2 R_{YY}}{\partial \alpha_0^2}\right|_{x,0,0}; \end{cases} \tag{B.32}$$

$$\left.\frac{\partial^2 R_{ZY}}{\partial \beta_0 \alpha_0}\right|_{x,0,0} = E_0 e^{\xi_0} + E_p e^{\lambda_p \xi_0} + E_m e^{\lambda_m \xi_0} + \frac{1}{2}x^2; \tag{B.33}$$

where

$$\begin{cases} E_0 = -\psi_1^{-\frac{2}{3}}\frac{1}{3}; \\ E_p = \psi_1^{-\frac{2}{3}}(\frac{1}{6} - 0.2887i); \\ E_m = \psi_1^{-\frac{2}{3}}(\frac{1}{6} + 0.2887i); \\ \psi_1 = \frac{4\Phi_\delta(0,0)}{L_H^2 L_V^2} \end{cases} \tag{B.34}$$

Figure B.1 displays a numerical example of the calculation of the normalized standard deviation of the divergence $\frac{\sigma_U}{<U>}$ as a function of the distance of propagation. The parameters chosen for this example were $\delta_c = 2m/s$, $c_0 = 1500m/s$, $L_H = 300m$ and $L_V = 30m$. The quantity displayed here is evaluated using the analytical results previously detailed (equation B.29 to B.34) and the fact that $< U >= \bar{U} = x^2$, and $\sigma_U = \sqrt{< U^2 > - < U >^2)} = \sqrt{< U^2 > - \bar{U}^2)}$.

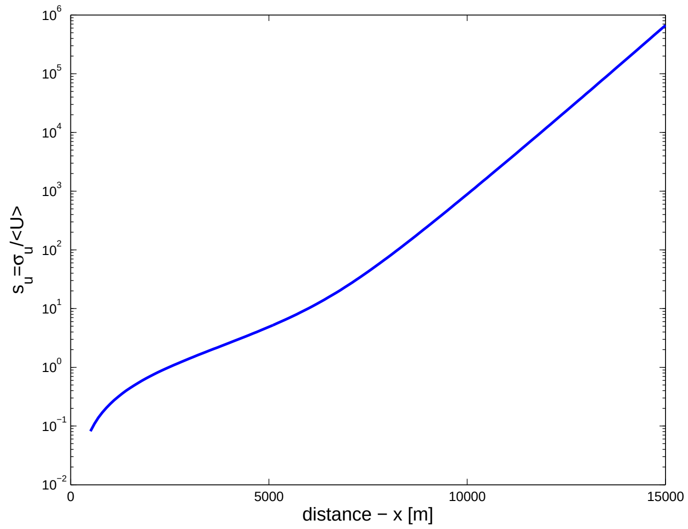

FIGURE B.1: $s = \frac{\sigma_U}{\bar{U}}$: Normalized Standard Deviation of the Divergence U as a Function of Distance x. $\delta_c = 2m/s$, $c_0 = 1500m/s$, $L_H = 300m$ and $L_V = 30m$

B.2 Average number of eigenrays

We define an eigen ray as a ray linking source to receiver. The number of eigen rays N_{eig} is characteristic of perturbation regimes. Indeed, a high number of eigen rays, especially if they are uncorrelated, is synonym of full saturation ; a small number of correlated eigen rays would lead to partial saturation, and the final case of unsaturation is obtained when we only observe one -possibly perturbed- eigen ray. The knowledge of this quantity's behavior is of great influence on the theory of the problem studied here. As explained in section 2.1.1.2, the eigen rays are associated with the solutions of system B.26. Therefore, we can define N_{eig} as follows:

$$N_{eig} = \iint d\alpha_0 d\beta_0 |U| \delta(z - Z(x, \alpha_0, \beta_0)) \delta(y - Y(x, \alpha_0, \beta_0)) \tag{B.35}$$

Taking the average value of equation B.35 leads to the following expression of $< N_{eig} >$:

$$\begin{aligned} < N_{eig} > &= \iiint d\alpha_0 d\beta_0 du |u| < \delta(u - U(\alpha_0, \beta_0)) \delta(z - Z(x, \alpha_0, \beta_0)) \delta(y - Y(x, \alpha_0, \beta_0)) > \\ &= \int du |u| \frac{e^{-\frac{1}{2}\frac{(u - <U>)^2}{\sigma_U^2}}}{\sqrt{2\pi}\sigma_U} \iint < \delta(z - Z(x, \alpha_0, \beta_0)) \delta(y - Y(x, \alpha_0, \beta_0)) > \\ &= \int du \frac{|u|}{\bar{U}} \frac{e^{-\frac{1}{2}\frac{(u - <U>)^2}{\sigma_U^2}}}{\sqrt{2\pi}\sigma_U}; \end{aligned} \tag{B.36}$$

Finally, we obtain:

$$< N_{eig} >= \text{erf}\left(\frac{\sqrt{2}}{s}\right) + s\sqrt{\frac{2}{\pi}}e^{-\frac{1}{2s^2}}; \quad \text{(B.37)}$$

where $s_u = \frac{\sigma_U}{<U>}$.

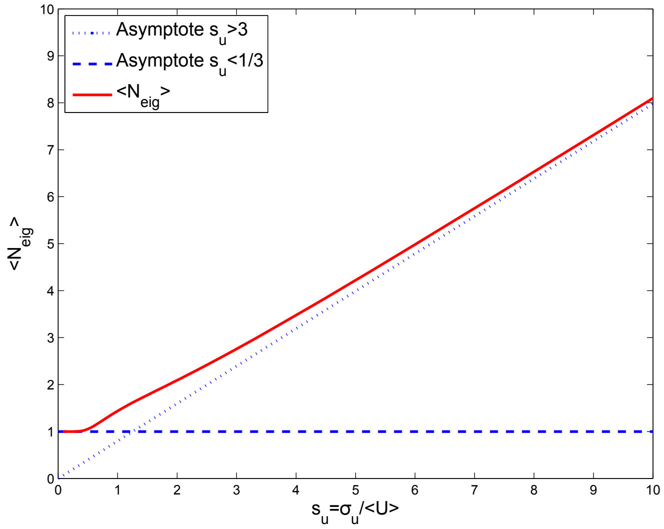

FIGURE B.2: $N_{eig}(s_u)$: Average Number of Eigen Rays as a Function of the Normalized Standard Deviation of the Divergence. $\delta_c = 2m/s$, $c_0 = 1500m/s$, $L_H = 300m$ and $L_V = 30m$

We represent the asymptotic behavior of the average number of eigen rays as a function of the normalized standard deviation of the divergence in Figure B.2: for small values of s_u, N_{eig} tends to 1, which can be interpreted as translating the fact that small values of the normalized standard deviation of the divergence leads to unsaturation.

For high values of s_u, typically for $s_u > 3$, we observe an increase of the average number for eigenrays following a linear asymptote in $\sqrt{(2/\pi)}s_u$. In this "region", the number of eigenrays is high, so is the normalized standard deviation of the divergence, meaning that this would correspond to the saturated case.

For values of s_u included in the interval $[\frac{1}{3}; 3]$, a transition is noted in the evolution of the number of eigen rays: the sweetspot corresponding to $N_{eig} = 1$ is exceeded, and $N_{eig} = 1$ tends to get closer and closer to the asymptote in $\sqrt{(2/\pi)}s_u$. This would correspond to partial saturation.

This result confirms the theory of classification of signal distortions into regimes of fluctuations.

B.3 Derivation of $< U^2 >$.

As a reminder, in order to evaluate $< U^2 >$ (given in equation B.29), we need on expression for $\left.\frac{\partial^2 R_{ZY}}{\partial\beta_0\alpha_0}\right|_{x,0,0}$, $\left.\frac{\partial^2 R_{ZZ}}{\partial\alpha_0^2}\right|_{x,0,0}$, $\left.\frac{\partial^2 R_{ZZ}}{\partial\beta_0^2}\right|_{x,0,0}$, $\left.\frac{\partial^2 R_{YY}}{\partial\alpha_0^2}\right|_{x,0,0}$ and $\left.\frac{\partial^2 R_{YY}}{\partial\beta_0^2}\right|_{x,0,0}$.

First, we can evaluate $\left.\frac{\partial^2 R_{ZZ}}{\partial\alpha_0^2}\right|_{x,0,0}$ and $\left.\frac{\partial^2 R_{YY}}{\partial\alpha_0^2}\right|_{x,0,0}$ together, given that:

$$\begin{cases} \frac{d^3u}{dx^3} = 2\Phi_v^{(4)}(0)\Phi_h(0)(u-x^2) + 2\Phi_v^{(2)}(0)\Phi_h^{(2)}(0)v; \\ \frac{d^3v}{dx^3} = 2\Phi_v^{(2)}(0)\Phi_h^{(2)}(0)(u-x^2) + 2\Phi_v^{(4)}(0)\Phi_h(0)v; \end{cases} \tag{B.38}$$

where $u = \left.\frac{\partial^2 R_{ZZ}}{\partial\alpha_0^2}\right|_{x,0,0}$ and $v = \left.\frac{\partial^2 R_{YY}}{\partial\alpha_0^2}\right|_{x,0,0}$. B.38 can be rewritten as follows:

$$\frac{d^3}{dx^3}\begin{pmatrix} u \\ v \end{pmatrix} = 2\phi_0 \begin{pmatrix} \frac{1}{L_V^4} & \frac{1}{L_H^2L_V^2} \\ \frac{1}{L_H^2L_V^2} & \frac{1}{L_H^4} \end{pmatrix}\begin{pmatrix} u \\ v \end{pmatrix} - 2\phi_0 x^2 \begin{pmatrix} \frac{1}{L_V^4} \\ \frac{1}{L_H^2L_V^2} \end{pmatrix}. \tag{B.39}$$

Looking for the eigen values of equation B.39 gives us:

$$\begin{vmatrix} \frac{1}{L_V^4} - \lambda & \frac{1}{L_H^2L_V^2} \\ \frac{1}{L_H^2L_V^2} & \frac{1}{L_H^4} - \lambda \end{vmatrix} = \left(\frac{1}{L_V^4} - \lambda\right)\left(\frac{1}{L_H^4} - \lambda\right) - \frac{1}{L_H^4L_V^4} = \lambda\left(\lambda - \left(\frac{1}{L_V^4} + \frac{1}{L_H^4}\right)\right). \tag{B.40}$$

Solving for the roots of equation B.40 provides the two following eigen values:

$$\begin{cases} \lambda_1^1 = 0; \\ \lambda_2^1 = \frac{1}{L_V^4} + \frac{1}{L_H^4}; \end{cases} \tag{B.41}$$

The associated eigen vectors w_1^1 and w_2^1 are obtained by solving the two following equations:

$$\left(A_1 - \lambda_1^1 I\right) w_1^1 = 0; \tag{B.42}$$

$$\left(A_1 - \lambda_2^1 I\right) w_2^1 = 0; \tag{B.43}$$

where $A_1 = \begin{pmatrix} \frac{1}{L_V^4} & \frac{1}{L_H^2L_V^2} \\ \frac{1}{L_H^2L_V^2} & \frac{1}{L_H^4} \end{pmatrix}$ and I is the identity matrix.

The solutions for the eigen vectors are:

$$\begin{cases} w_1^1 = \begin{pmatrix} 1 \\ -\frac{L_H^2}{L_V^2} \end{pmatrix}; \\ w_2^1 = \begin{pmatrix} 1 \\ \frac{L_V^2}{L_H^2} \end{pmatrix}; \end{cases} \tag{B.44}$$

Multiplying equation B.39 by w_1^1 gives:

$$\begin{aligned} &\frac{d^3}{dx^3}\left(u - \frac{L_H^2}{L_V^2}v\right) = 2\phi_0\lambda_1^1\left(u - \frac{L_H^2}{L_V^2}v\right) - 2\phi_0 x^2\left(\frac{1}{L_V^4} - \frac{L_H^2}{L_V^2}\frac{1}{L_H^2 L_V^2}\right) = 0 \\ \leftrightarrow\ &\frac{d^3}{dx^3}\left(u - \frac{L_H^2}{L_V^2}v\right) = -2\phi_0 x^2\left(\frac{1}{L_V^4} - \frac{1}{L_H^4}\right) = 0 \\ \leftrightarrow\ &u = \frac{L_H^2}{L_V^2}v. \end{aligned} \tag{B.45}$$

Multiplying equation B.39 by w_2^1 gives:

$$\begin{aligned} &\frac{d^3}{dx^3}\left(u + \frac{L_V^2}{L_H^2}v\right) = 2\phi_0\lambda_2^1\left(u + \frac{L_V^2}{L_H^2}v\right) - 2\phi_0 x^2\left(\frac{1}{L_V^4} + \frac{L_V^2}{L_H^2}\frac{1}{L_H^2 L_V^2}\right) = 0 \\ \leftrightarrow\ &\frac{d^3}{dx^3}\left(u - \frac{L_H^2}{L_V^2}v\right) = 2\phi_0\left(\frac{1}{L_H^4} + \frac{1}{L_V^4}\right)\left(u - \frac{L_H^2}{L_V^2}v\right) - 2\phi_0 x^2\left(\frac{1}{L_V^4} - \frac{1}{L_H^4}\right) = 0; \\ \leftrightarrow\ &\frac{d^3}{dx^3}\left(u - \frac{L_H^2}{L_V^2}v\right) = 2\phi_0\left(\frac{1}{L_H^4} + \frac{1}{L_V^4}\right)\left(u - \frac{L_H^2}{L_V^2}v - x^2\right); \\ \leftrightarrow\ &\frac{d^3}{dx^3}V = \Psi_0 V; \end{aligned} \tag{B.46}$$

where $V = \left(u - \frac{L_H^2}{L_V^2}v - x^2\right)$ and $\Psi_0 = 2\phi_0\left(\frac{1}{L_H^4} + \frac{1}{L_V^4}\right)$. Since $\frac{d^3}{dx^3}\left(u - \frac{L_H^2}{L_V^2}v - x^2\right) = \frac{d^3}{dx^3}\left((u - \frac{L_H^2}{L_V^2}v\right)$, we can write $\frac{d^3}{dx^3}V = \Psi_0 V$. In order to adimensionize the equation, we write $\psi = \Psi_0^{\frac{1}{3}}x$, which gives:

$$\begin{cases} \frac{d^3}{d\psi^3}V = V; \\ \frac{d}{d\psi}V = W; \\ \frac{d}{d\psi}W = X; \end{cases} \tag{B.47}$$

We obtain the following equation:

$$\frac{d}{d\psi}\begin{pmatrix} V \\ W \\ X \end{pmatrix} = \begin{pmatrix} 0 & 1 & 0 \\ 0 & 0 & 1 \\ 1 & 0 & 0 \end{pmatrix}\begin{pmatrix} V \\ W \\ X \end{pmatrix}, \tag{B.48}$$

with

$$\begin{cases} V(0) = 0; \\ W(0) = 0; \\ X(0) = -2\Psi^{-\frac{2}{3}}; \end{cases} \tag{B.49}$$

Looking for the eigen values of B.58 gives:

$$\begin{aligned} &\begin{vmatrix} -\lambda & 1 & 0 \\ 0 & -\lambda & 1 \\ 1 & 0 & -\lambda \end{vmatrix} = 0: \\ &\leftrightarrow -\lambda^3 + 1 = 0; \\ &\leftrightarrow \lambda^3 = 1. \end{aligned} \tag{B.50}$$

Leading to:

$$\begin{cases} \lambda_1^2 = 1; \\ \lambda_2^2 = \lambda_p = e^{i2\pi/3}; \\ \lambda_3^2 = \lambda_m = e^- i2\pi/3; \end{cases} \tag{B.51}$$

The solution is therefore of the form:

$$\begin{cases} V = D_0 e^{\lambda_1^2 \xi} + D_p e^{\lambda_p \xi} + D_m e^{\lambda_m \xi}; \\ W = D_0 \lambda_1^2 e^{\lambda_1^2 \xi} + D_p \lambda_+ e^{\lambda_p \xi} + D_m \lambda_m e^{\lambda_m \xi}; \\ X = D_0 \left(\lambda_1^2\right)^2 e^{\lambda_1^2 \xi} + D_p \left(\lambda_p\right)^2 e^{\lambda_p \xi} + D_m \left(\lambda_m\right)^2 e^{\lambda_m \xi}; \end{cases} \tag{B.52}$$

with,

$$\begin{cases} V(0) = D_0 + D_p + D_m; \\ W(0) = D_0 \lambda_1^2 + D_p \lambda_p + D_m \lambda_m; \\ X(0) = D_0 (\lambda_1^2)^2 + D_p (\lambda_p)^2 + D_m (\lambda_m)^2; \end{cases} \tag{B.53}$$

with the following initial condition:

$$\begin{cases} D_0 = -2\Psi_0^{-2/3}\frac{1}{3}; \\ D_p = 2\Psi_0^{-2/3}(\frac{1}{6} - 0.2887i); \\ D_m = 2\Psi_0^{-2/3}(\frac{1}{6} + 0.2887i); \end{cases} \tag{B.54}$$

We now have an expression for V, therefore we know $\left(u - \frac{L_H^2}{L_V^2}v\right)$. Hence, we know $\frac{\partial^2 R_{ZZ}}{\partial \alpha_0^2}\Big|_{x,0,0}$ and $\frac{\partial^2 R_{YY}}{\partial \alpha_0^2}\Big|_{x,0,0}$.

A similar scheme gives us the expression of $\frac{\partial^2 R_{ZZ}}{\partial \beta_0^2}\Big|_{x,0,0}$ and $\frac{\partial^2 R_{YY}}{\partial \beta_0^2}\Big|_{x,0,0}$. As for the last moment to evaluate, $\frac{\partial^2 R_{ZY}}{\partial \beta_0 \partial \alpha_0}\Big|_{x,0,0}$, if we take the derivative of system(B.19) with respect to $\partial\alpha_0\partial\beta_0$, we obtain:

$$\frac{\partial^3}{dx^3}\left(\frac{\partial^2 R_{ZY}}{\partial \beta_0 \partial \alpha_0}\Big|_{x,0,0}\right) = 2\left[\Phi_h^{(2)}(0)\Phi_v^{(2)}(0)\left(2\frac{\partial^2 R_{ZY}}{\partial \beta_0 \partial \alpha_0}\Big|_{x,0,0} - x^2\right)\right]. \tag{B.55}$$

Equation B.55 can be rewritten:

$$\frac{d^3}{dx^3}w = 4\phi_0\frac{1}{L_H^2 L_V^2}w - 2\phi_0\frac{1}{L_H^2 L_V^2}x^2; \tag{B.56}$$

where $w = \frac{\partial^2 R_{ZY}}{\partial \beta_0 \partial \alpha_0}\Big|_{x,0,0}$. If we note $W = \left(w - \frac{1}{2}x^2\right)$ and $\Psi_1 = 4\phi_0\frac{1}{L_H^2 L_V^2}$, we obtain:

$$\frac{d^3}{dx^3}W = \Psi_1 W, with \begin{cases} W(0) = 0; \\ W'(0) = 0; \\ W''(0) = -1 \end{cases} \tag{B.57}$$

We repeat the adimensionalization step, so that $\xi = \Psi_1^{1/3}x$, which gives:

$$\frac{d}{d\xi}\begin{pmatrix} W \\ X \\ T \end{pmatrix} = \begin{pmatrix} 0 & 1 & 0 \\ 0 & 0 & 1 \\ 1 & 0 & 0 \end{pmatrix}\begin{pmatrix} W \\ X \\ T \end{pmatrix}, \tag{B.58}$$

with

$$\begin{cases} W(0) = 0; \\ X(0) = 0; \\ T(0) = -\Psi_1^{-\frac{2}{3}}; \end{cases} \tag{B.59}$$

Once again, we find a solution of the form:

$$\begin{cases} W = E_0 e^{\lambda_1^2 \xi} + E_p e^{\lambda_p \xi} + E_m e^{\lambda_m \xi}; \\ X = E_0 \lambda_1^2 e^{\lambda_1^2 \xi} + E_p \lambda_+ e^{\lambda_p \xi} + E_m \lambda_m e^{\lambda_m \xi}; \\ T = E_0 \left(\lambda_1^2\right)^2 e^{\lambda_1^2 \xi} + E_p \left(\lambda_p\right)^2 e^{\lambda_p \xi} + E_m \left(\lambda_m\right)^2 e^{\lambda_m \xi}; \end{cases} \tag{B.60}$$

with the initial conditions given in B.59, we obtain finally:

$$\begin{cases} E_0 = -\Psi_1^{-2/3} \frac{1}{3}; \\ E_p = \Psi_1^{-2/3} (\frac{1}{6} - 0.2887i); \\ E_m = \Psi_1^{-2/3} (\frac{1}{6} + 0.2887i); \end{cases} \tag{B.61}$$

Appendix C

Intercorrelation calculation details

In equation 2.42, the term between brackets can be expressed as follows:

$$
\begin{aligned}
&\left\langle \Pi\left(x,\Theta-\frac{1}{2}\upsilon\right)\Pi^{*}\left(x,\Theta+\frac{1}{2}\upsilon\right)\right\rangle \\
=&C_1\frac{1}{4\pi^2}\iint dz_p\,dz_m\,e^{i\Theta z_m}e^{i\upsilon z_p}\frac{1}{4\pi^2}\iint d\upsilon_p\,d\upsilon_m\,e^{-i\upsilon_p z_m}e^{-i\upsilon_m z_p}e^{i\upsilon_p\upsilon_m\left(\frac{x_1}{k_1}+\frac{x-x_1}{k_2}\right)}e^{-\frac{1}{8}\rho^2 2\left(\upsilon_p^2+\frac{\upsilon_m^2}{4}\right)} \\
&\times\left\langle e^{-i\left[\left(k_1-\frac{1}{2}\frac{\left(\Theta-\frac{1}{2}\upsilon\right)^2}{k_1}\right)\xi(z_1)+\left(k_1-\frac{1}{2}\frac{\left(\Theta+\frac{1}{2}\upsilon\right)^2}{k_1}\right)\xi(z_2)+\left(k_2-\frac{1}{2}\frac{\left(\upsilon_p-\frac{1}{2}\mu\right)^2}{k_2}\right)\xi(z_1)+\left(k_2-\frac{1}{2}\frac{\left(\upsilon_p+\frac{1}{2}\mu\right)^2}{k_2}\right)\xi(z_2)\right]}\right\rangle
\end{aligned}
\tag{C.1}
$$

where the changes of variables operated are $z_m = z_2 - z_1$, $z_p = \frac{z_1+z_2}{2}$, $\upsilon_m = \upsilon_2 - \upsilon_1$ and $\upsilon_p = \frac{\upsilon_1+\upsilon_2}{2}$ and C_1 is a constant coefficient.

Noticing, once again, that $\frac{1}{4\pi^2}\int dz_p\, e^{i\upsilon z_p}e^{-i\upsilon_m z_p} = 2\pi\delta(\upsilon_m - \upsilon)$, equation C.1 may be rewritten as follows:

$$
\begin{aligned}
&\left\langle \Pi\left(x,\Theta-\frac{1}{2}\upsilon\right)\Pi^{*}\left(x,\Theta+\frac{1}{2}\upsilon\right)\right\rangle \\
&= C_1\frac{1}{2\pi}\int dz_m e^{i\Theta z_m}\frac{1}{4\pi^2}\int d\upsilon_p e^{-i\Upsilon z_m}e^{i\upsilon_p\upsilon\left(\frac{x_1}{k_1}+\frac{x-x_1}{k_2}\right)}e^{-\frac{1}{4}\rho^2\left(\upsilon_p^2+\frac{\upsilon^2}{4}\right)}\left\langle e^{i\left[A_1\xi\left(-\frac{1}{2}z_m\right)-A_2\xi\left(\frac{1}{2}z_m\right)\right]}\right\rangle.
\end{aligned}
\tag{C.2}
$$

where A_1 and A_2 are constant coefficients. The term between brackets may be approximated in the geometrical limit, so that an analytical expression can be found for the radius of curvature of the Fourier transform of the intercorrelation function $\tilde{C}$. This translates into the following:

$$\begin{aligned}
\left\langle e^{i\left[A_1\xi\left(-\frac{1}{2}z_m\right)-A_2\xi\left(\frac{1}{2}z_m\right)\right]}\right\rangle &= e^{-\frac{1}{2}\left[\left(A_1^2+A_2^2\right)R_\xi(0)-2A_1A_2R_\xi(z_m)\right]} \\
&= e^{-(k_1-k_2)^2\left(R_\xi(0)-R_\xi(z_m)\right)} \\
&\approx e^{-(k_1-k_2)^2\frac{1}{2}\xi_0^2\frac{z_m^2}{L_V^2}} \\
&= e^{-\frac{1}{2}k_1^2\xi_0^2\left(1-\frac{c_1}{c_2}\right)^2\frac{z_m^2}{L_V^2}}
\end{aligned} \tag{C.3}$$

Starting from equation C.3, we are able to go back to the evaluation of $\left\langle \Pi\left(x,\Theta-\frac{1}{2}\upsilon\right)\Pi^*\left(x,\Theta+\frac{1}{2}\upsilon\right)\right\rangle$:

$$\begin{aligned}
\left\langle \Pi\left(x,\Theta-\frac{1}{2}\upsilon\right)\Pi^*\left(x,\Theta+\frac{1}{2}\upsilon\right)\right\rangle &= c_1^2\frac{1}{2\pi}\int d^s e^{i\Theta s} \\
&\times \frac{1}{4\pi^2}\int d\Upsilon e^{-i\Upsilon\left(s-\upsilon\left(\frac{x_1}{k_1}+\frac{x-x_1}{k_2}\right)\right)} \\
&\times e^{-\frac{1}{4}\rho^2\left(\Upsilon^2+\upsilon^2/4\right)}e^{-\frac{1}{2}k_1^2\xi_0^2\left(1-\frac{c_1}{c_2}\right)^2\frac{s^2}{L_V^2}}
\end{aligned} \tag{C.4}$$

Setting $b=\frac{x_1}{k_1}+\frac{x-x_1}{k2}$ and $d^2=k_1^2\xi_0^2\left(1-\frac{c_1}{c_2}\right)^2\frac{1}{L_V^2}$ leads to:

$$\begin{aligned}
\left\langle \Pi\left(x,\Theta-\frac{1}{2}\upsilon\right)\Pi^*\left(x,\Theta+\frac{1}{2}\upsilon\right)\right\rangle &= C_1^2\frac{1}{4\pi^2}e^{-\frac{1}{16}\rho^2\upsilon^2}\int dse^{i\Theta s} \\
&\times \frac{e^{-\frac{1}{2}\frac{1}{\rho^2/2}\left[\left(d^2\rho^2/2+1\right)s^2-2\upsilon sb+\upsilon^2b^2\right]}}{\sqrt{2\pi}\rho/\sqrt{2}}.
\end{aligned} \tag{C.5}$$

Writing $q=1+d^2\frac{\rho^2}{2}$ allows to rewrite equation C.5:

$$\begin{aligned}
\left\langle \Pi\left(x,\Theta-\frac{1}{2}\upsilon\right)\Pi^*\left(x,\Theta+\frac{1}{2}\upsilon\right)\right\rangle &= C_1^2\frac{1}{(2\pi)^{3/2}}\frac{1}{\rho/\sqrt{2}}e^{-\frac{1}{16}\rho^2\upsilon^2} \\
&\times e^{-\frac{1}{2}\frac{\upsilon^2b^2}{\rho^2/2}}\frac{1}{2\pi}\int dse^{i\Theta s}e^{-\frac{1}{2}\frac{q}{\rho^2/2}\left(s-\upsilon\frac{b}{q}\right)^2}e^{\frac{1}{2}\frac{\upsilon^2b}{q\rho^2/2}}
\end{aligned} \tag{C.6}$$

which rewrites into:

$$\left\langle \Pi\left(x,\Theta-\frac{1}{2}\upsilon\right)\Pi^*\left(x,\Theta+\frac{1}{2}\upsilon\right)\right\rangle = C_1^2\frac{1}{(2\pi)^{3/2}}\frac{1}{\rho/\sqrt{2}}e^{-\frac{1}{16}\rho^2\upsilon^2} \times e^{-\frac{1}{2}\upsilon^2 b^2\frac{d^2}{1+d^2\rho^2/2}} \times \frac{1}{2\pi}\int dse^{i\Theta s}e^{-\frac{1}{2}\frac{q}{\rho^2/2}\left(s-\upsilon\frac{b}{q}\right)^2} \tag{C.7}$$

Equation C.7 can be astutely revised into:

$$\left\langle \Pi\left(x,\Theta-\frac{1}{2}\upsilon\right)\Pi^*\left(x,\Theta+\frac{1}{2}\upsilon\right)\right\rangle = C_1^2\frac{1}{(2\pi)^{3/2}}e^{-\frac{1}{2}\upsilon^2\left(\frac{\rho^2}{8}+\frac{b^2d^2}{1+d^2\rho^2/2}\right)} \times \frac{1}{2\pi}e^{i\Theta\frac{\upsilon b}{q}}\int dse^{i\Theta\left(s-\frac{\upsilon b}{q}\right)}e^{-\frac{1}{2}\frac{q}{\rho^2/2}\left(s-\frac{\upsilon b}{q}\right)} \tag{C.8}$$

The simplification of the Gaussian term in the integral in equation C.8 leads to the expression given in equation 2.4.2.

Appendix D

The Fresnel radius and the Phase Sensitivity Kernel.

In this appendix, we propose a derivation of the acoustic field sensitivity kernel (in phase and amplitude) in order to relate its width to he Fresnel radius R_F. The link between these quantities was tackled in Marquering et al. (1999), Dahlen and Baig (2002), Skarsoulis and Cornuelle (2004), Spetzler and Snieder (2004). The first step is to derive the expression of the Frechet derivative of $p_3(x,y,z) = p(x > x_2, y, z)$:

$$
\begin{aligned}
&\left.\frac{\delta p_3(x,y,z)}{\delta \xi(y_1,z_1)}\right|_{\xi=0} = K_p \\
&= \int d\mu e^{i(\mu z)} e^{i\left(k_1 - \frac{1}{2}\frac{\mu^2}{k_1}\right)(x-x_2)} K_\Pi(\mu, H) \\
&= \int d\mu e^{i(\mu(z-z_1))} e^{i\left(k_1 - \frac{i}{2}\frac{\mu^2}{k_1}\right)(x-x_2)} \frac{2k_2}{k_1+k_2} 2\pi\rho^2 \frac{A_S}{4\pi} e^{ik_1 x_1} e^{ik_2(x_2-x_1)} \frac{e^{-\frac{1}{2}\frac{z_1^2}{\alpha^2}}}{2\pi\alpha^2}.
\end{aligned}
\tag{D.1}
$$

Equation (D.1) can be rewritten as:

$$
\begin{aligned}
K_p &= \frac{2k_2}{k_1+k_2} 2\pi\rho^2 \frac{A_S}{2} e^{ik_1(x-H+F)} e^{ik_2(H-F)} \frac{e^{-\frac{1}{2}\frac{z_1^2+y_1^2}{\alpha^2}}}{2\pi\alpha^2} \\
&\times \frac{1}{4\pi^2} \iint d\lambda d\mu e^{i(\lambda\Delta z + \mu\Delta y)} e^{-\frac{i}{2}\left(\frac{\lambda^2+\mu^2}{k_1}\right)(x-H)} \\
&= \frac{2k_2}{k_1+k_2} 2\pi\rho^2 \frac{A_S}{2} e^{ik_1(x-H+F} e^{ik_2(H-F)} \frac{e^{-\frac{1}{2}\frac{z_1^2+y_1^2}{\alpha^2}}}{2\pi\alpha^2} \frac{e^{-\frac{1}{2}\frac{\Delta z^2+\Delta y^2}{\gamma^2}}}{2\pi\gamma^2},
\end{aligned}
\tag{D.2}
$$

with $\gamma^2 = i\frac{x-H}{k_1}$. We conclude here that:

$$K_p = \frac{2k_2}{k_1+k_2} 2\pi\rho^2 \frac{A_S}{2} e^{ik_1(x-H+F)} = e^{ik_2(H-F)} \frac{e^{-\frac{1}{2}\frac{z_1^2+y_1^2}{\alpha^2}}}{2\pi\alpha^2} \frac{e^{-\frac{1}{2}\frac{\Delta z^2+\Delta y^2}{\gamma^2}}}{2\pi\gamma^2}. \tag{D.3}$$

For the particular point where $z = y = 0$, we can write:

$$K_{p(x,0,0)} = \frac{2k_2}{k_1+k_2} 2\pi\rho^2 \frac{A_S}{2} e^{ik_1(x-H+F)} e^{ik_2(H-F)} \frac{e^{-\frac{1}{2}\frac{z_1^2+y_1^2}{\alpha^2}}}{2\pi\alpha^2} \frac{e^{-\frac{1}{2}\frac{z_1^2+y_1^2}{\gamma^2}}}{2\pi\gamma^2}. \tag{D.4}$$

If we go back to the evaluation of $p_3(x, y, z)$, we obtain:

$$p_3(x,y,z) = \frac{2k_2}{(k_1+k_2)^2} 2\pi\rho^2 A_S \frac{-i}{8\pi^2} e^{ik_1(x-H+F)} e^{ik_2(H-F)} e^{i(k_1+k_2)\xi(y,z)} \frac{e^{-\frac{1}{2}\frac{z^2+y^2}{\alpha^2}}}{2\pi\alpha^2}. \tag{D.5}$$

Again, for the particular point in $z = y = 0$:

$$p_3(x,0,0) = \frac{2k_2}{(k_1+k_2)^2} 2\pi\rho^2 A_S \frac{-i}{8\pi^2} e^{ik_1(x-H+F} e^{ik_2(H-F)} e^{i(k_1+k_2)\xi(0,0)} \frac{1}{2\pi\alpha^2}. \tag{D.6}$$

From equations (D.4) and (D.6), we notice that:

$$\begin{aligned} K_{p(x,0,0)} &= p_3(x,0,0)\Big|_{\xi=0} 4\pi^2 i(k_1+k_2) e^{-\frac{1}{2}\frac{z_1^2+y_1^2}{\alpha^2}} \frac{e^{-\frac{1}{2}\frac{z_1^2+y_1^2}{\gamma^2}}}{2\pi\gamma^2} \\ &= p_3(x,0,0)\Big|_{\xi=0} 4\pi^2 \frac{k_1(k_1+k_2)}{2\pi(x-H)} e^{-\frac{1}{2}\frac{z_1^2+y_1^2}{\alpha^2}} e^{i\frac{1}{2}\frac{z_1^2+y_1^2}{(x-H)}}. \end{aligned} \tag{D.7}$$

We can therefore write :

$$K_{p(x,0,0)} = p_3(x,0,0)\Big|_{\xi=0} 2\pi \frac{k_1(k_1+k_2)}{(x-H)} e^{R} e^{i\frac{1}{2}B}; \begin{cases} R = \frac{1}{2}\frac{(z_1^2+y_1^2)\rho^2/4}{\frac{\rho^4}{16}+\left(\frac{F}{k_1}+\frac{H-F}{k_2}\right)^2}; \\ B = \frac{z_1^2+y_1^2}{x-H} + \frac{(z_1^2+y_1^2)\left(\frac{F}{k_1}+\frac{H-F}{k_2}\right)}{\frac{\rho^4}{16}+\left(\frac{F}{k_1}+\frac{H-F}{k_2}\right)^2}; \end{cases} \tag{D.8}$$

The acoustic pressure p_3 can be written as: $p_3 = Ae^{i\omega T}$, so that:

$$
\begin{aligned}
\left.\frac{\delta A^2}{\delta\xi(z_1,y_1)}\right|_{\xi=0} &= \left.\frac{\delta p_3}{\delta\xi(z_1,y_1)}\right|_{\xi=0} p_3^* + \left.\frac{\delta p_3^*}{\delta\xi(z_1,y_1)}\right|_{\xi=0} p_3 \\
&= A^2 2\pi \frac{k_1(k_1+k_2)}{(x-H)} e^R 2R\{e^{i\frac{1}{2}B}\}.
\end{aligned}
\tag{D.9}
$$

This gives us an expression for the amplitude sensitivity kernel (ASK):

$$
\left.\frac{\delta A^2}{\delta\xi(z_1,y_1)}\right|_{\xi=0} = A^2 2\pi \frac{k_1(k_1+k_2)}{(x-H)} e^R 2cos\left(\frac{1}{2}B\right). \tag{D.10}
$$

If we now write $p_3^2 = A^2 e^{2i\phi}$, we have:

$$
\begin{aligned}
2p_3 \left.\frac{\delta p_3}{\delta\xi(z_1,y_1)}\right|_{\xi=0} &= \frac{1}{2}\left.\frac{\delta A^2}{\delta\xi(z_1,y_1)}\right|_{\xi=0} e^{2i\phi} + 2i \left.\frac{\delta\phi}{\delta\xi(z_1,y_1)}\right|_{\xi=0} A^2 e^{2i\phi} \\
\Leftrightarrow A^2 e^{2i\phi} 2\pi \frac{k_1(k_1+k_2)}{(x-H)} e^R e^{i\frac{1}{2}B} &= A^2 2\pi \frac{k_1(k_1+k_2)}{(x-H)} e^R cos\left(\frac{1}{2}B\right) e^{2i\phi} + i \left.\frac{\delta\phi}{\delta\xi(z_1,y_1)}\right|_{\xi=0} A^2 e^{2i\phi}
\end{aligned}
\tag{D.11}
$$

Which gives us an expression for the phase sensitivity kernel (PSK) :

$$
\left.\frac{\delta\phi}{\delta\xi(z_1,y_1)}\right|_{\xi=0} = 2\pi \frac{k_1(k_1+k_2)}{(x-H)} e^R sin\left(\frac{1}{2}B\right). \tag{D.12}
$$

Overall, a new approach aiming to obtain the Fresnel radius was presented here. Comparing the results obtained in this section with the - more classical - calculations of R_F in Chapter 2 leads to the following analysis: the Fresnel radius seems, in fact, to be related to the phase sensitivity kernel since it corresponds to an inflection point of the PSK. Figures D.1 to D.3 show the comparison between the calculations in Chapter 2, the results obtained here and the second-order derivative of the PSK for three propagation ranges (the shortest in figure D.1, the longest in figure D.3 and a transitional distance in figure D.2).

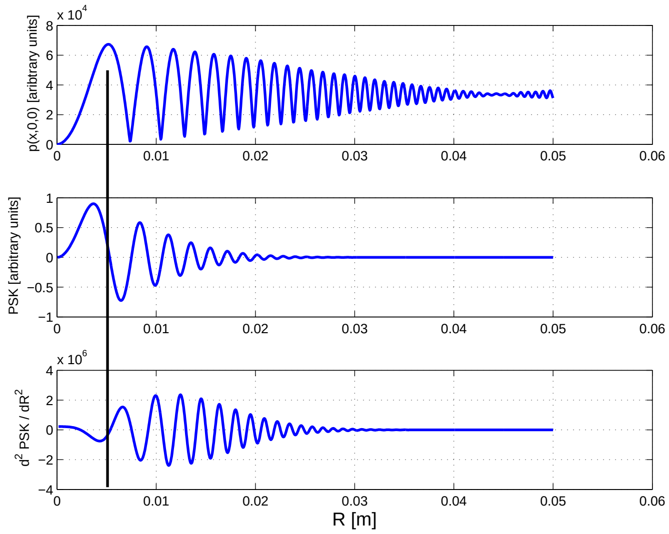

FIGURE D.1: Top figure: Central propagation axis pressure field, as calculated in Chapter 2 - center figure: Phase sensitivity kernel on the central propagation axis - bottom figure: second-order derivative of the PSK. Propagation range x_{dist} = 50 mm

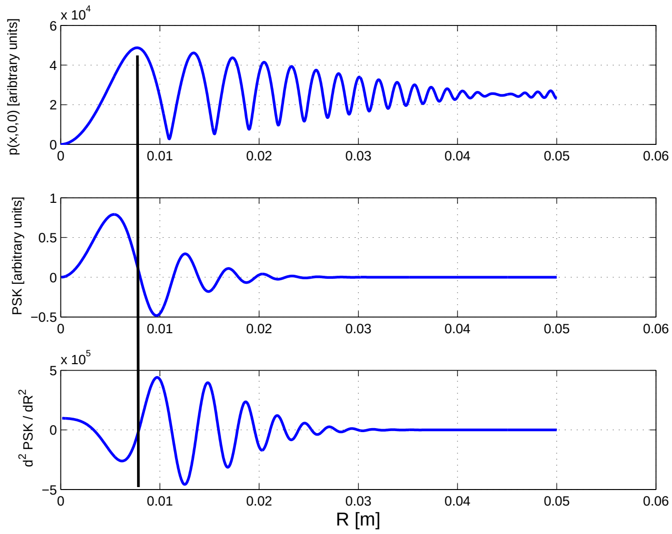

FIGURE D.2: Top figure: Central propagation axis pressure field, as calculated in Chapter 2 - center figure: Phase sensitivity kernel on the central propagation axis - bottom figure: second-order derivative of the PSK. Propagation range x_{dist} = 150 mm

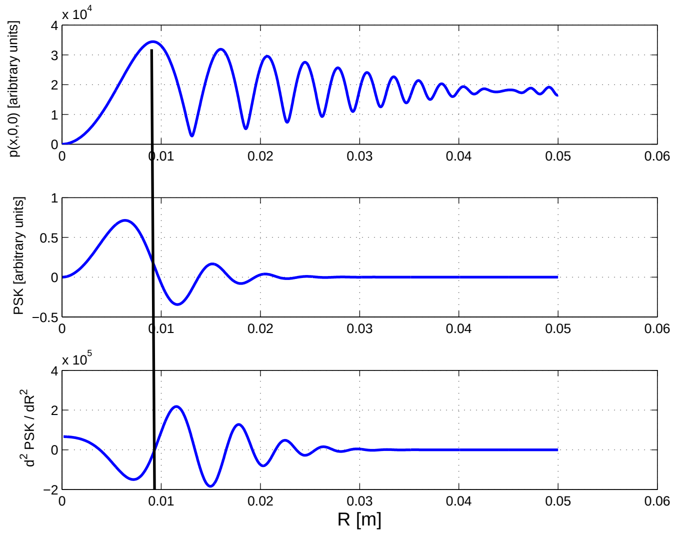

FIGURE D.3: Top figure: Central propagation axis pressure field, as calculated in Chapter 2 - center figure: Phase sensitivity kernel on the central propagation axis - bottom figure: second-order derivative of the PSK. Propagation range x_{dist} = 300 mm

Figures D.1 to D.3 show that the Fresnel radius is indeed related to the PSK but can not be considered as the first maximum of the kernel on the central axis.

Appendix E

Numerical techniques

In this appendix, more technical details about the method of resolution used in the numerical codes are given.

E.1 Propagation in the 3-Dimension Corresponding Oceanic Medium (P3DCOM)

The code presented here was written in FORTRAN. The propagation through a medium characterized by Gaussian sound speed fluctuations is handled using a Split-Step Fourier solution to the $3D$ standard parabolic equation:

$$2\imath k\frac{\partial\psi}{\partial x} + \frac{\partial^2\psi}{\partial y^2} + \frac{\partial^2\psi}{\partial z^2} + k^2\epsilon\psi = 0 \tag{E.1}$$

where $\epsilon = \left(n^2 - 1 - 2\delta_c/c_0\right)$. We recall that the refraction index is defined as $n = c_0/c$.

We introduce the 2D Fourier transform of ψ, denoted Ψ and defined as:

$$\Psi = \frac{1}{4\pi^2}\iint\limits_{-\infty}^{\infty} \psi(x,y,z)e^{-\imath(\mathcal{L}y+\mu z)}dy\,dz \tag{E.2}$$

Numerically, the Fourier transform is performed with a 2D Cooley-Tukey algorithm. Under the first hypothesis that the refraction index (in other words the sound speed) fluctuations remain weak -typically $\delta_c/c \approx 1.10^{-3}$- and sufficiently slow so that we can write:

$$\int_x^{x+\Delta x} \epsilon dx \approx \epsilon\Delta x \tag{E.3}$$

The second hypothesis is that ψ and its derivative tend to zero when the distance tends to infinity (Sommerfeld conditions (Sommerfeld 1912)). Equation E.1 becomes:

$$\frac{\partial \Psi}{\partial x} = -\frac{k^2\epsilon - (\mathcal{L} + \mu)^2}{2ik}\Psi\left(x, \mathcal{L}, \mu\right) \tag{E.4}$$

which can be solved in the following manner:

$$\Psi\left(x + \Delta x, \mathcal{L}, \mu\right) = e^{\frac{k^2\epsilon - (\mathcal{L}+\mu)^2}{2ik}\Delta x}\Psi\left(x, \mathcal{L}, \mu\right) \tag{E.5}$$

An inverse Fourier transform of this equation leads to:

$$\psi\left(x + \Delta x, y, z\right) = e^{\imath\frac{k}{2}\epsilon\Delta x}F^{-1}\{e^{-\imath\frac{(\mathcal{L}+\mu)^2}{2k}\Delta x}F\{\psi\left(x, y, z\right)\}\} \tag{E.6}$$

Hence, given this transition relationship establishing the wavefront $\psi\left(x + \Delta x, y, z\right)$ (at distance $x = x + \Delta x$) from the wavefront $\psi\left(x, y, z\right)$ at distance x, we are able to construct the wavefront from the initial condition at $x = x_0$, $\psi\left(x_0, y, z\right)$ step by step.

The resolution step Δx is here $25\ m$. The other numerical parameters involved with this code are given in table 3.5.
The code runs under deep water conditions, so that interaction with the sea surface of the seabed can be neglected. To do so, an artificial attenuation is used on a small slice (of $50\ m$) near these interfaces. Its value is $0.1dB/m$. Therefore, any non negligible wave entering one of these slices would be strongly attenuated and would not be significant anymore.
The initial conditions here are those of a point source, so that:

$$\psi\left(0, y, z\right) = Ae^{-\frac{k}{2}(y-y_z)^2(z-z_s)^2} \tag{E.7}$$

where A is the initial amplitude and $(0, y_s, z_s)$ are the source coordinates.

E.2 Propagation in the 3-Dimension Tank Experiment (P3DTEx)

This code was developed, in FORTRAN as well, in order to anticipate for the experimental results and compare the recorded signals with a numerical "reference". In the tank experiment configuration, two cases are noticed: the propagation of the acoustic wave in water (deterministic and unperturbed) and the propagation in the RAFAL (perturbed by its randomly rough output face).
In the latter case, the same procedure as the one described in section E.1 is used: the RAFAL is discretized and the Split-Step Fourier algorithm is applied to its interior and its rough surface.

Outside of the RAFAL, rougher steps are sufficient to carry on the propagation, since no medium fluctuations occur. Hence, the resolution step inside the RAFAL (between coordinates x^{ℓ}_{min} and x^{ℓ}_{max}) is chosen to be ten times smaller than the resolution step in the water (see section 3.5.1). The discontinuity at the rough interface is handled in a manner analogous to what can be observed with Fresnel lenses, meaning that the roughness can be considered continuous after propagation through a certain distance.

The source is here defined using the plane circular piston directivity pattern as initial condition.

Bibliography

Abado, S., Gordeyev, S., and Jumper, E. (2010). Two-dimensional high-bandwidth shack-hartmann wavefront sensor: design guidelines and evaluation testing. *Optical Engineering*, 49(6):064403–064403.

Aki, K. (1980). Attenuation of shear-waves in the lithosphere for frequencies from 0.05 to 25 hz. *Physics of the Earth and Planetary Interiors*, 21(1):50–60.

Ancey, R. (1973). Cohérence spatiale de signaux acoustiques propages par petits fonds. In *4° Colloque sur le traitement du signal et des images, FRA, 1973*. GRETSI, Groupe d'Etudes du Traitement du Signal et des Images.

Anderson, M., Soo, M., and Trahey, G. (2001). In vivo breast tissue backscatter measurements with 7.5-and 10-mhz transducers. *Ultrasound in medicine & biology*, 27(1):75–81.

Andrews, L., Phillips, R., and Weeks, A. (1997). Propagation of a gaussian-beam wave through a random phase screen. *Waves in Random Media*, 7(2):229–244.

Aragón, J., Naumis, G., Bai, M., Torres, M., and Maini, P. (2008). Turbulent luminance in impassioned van gogh paintings. *Journal of Mathematical Imaging and Vision*, 30(3):275–283.

Badiey, M., Katsnelson, B., Lynch, J., Pereselkov, S., and Siegmann, W. (2005). Measurement and modeling of three-dimensional sound intensity variations due to shallow-water internal waves. *The Journal of the Acoustical Society of America*, 117(2):613–625.

Badiey, M., Mu, Y., Lynch, J., Apel, J., and Wolf, S. (2002). Temporal and azimuthal dependence of sound propagation in shallow water with internal waves. *Oceanic Engineering, IEEE Journal of*, 27(1):117–129.

Baggeroer, A., Kuperman, W., and Schmidt, H. (1988). Matched field processing: Source localization in correlated noise as an optimum parameter estimation problem. *The Journal of the Acoustical Society of America*, 83(2):571–587.

Ballard, J., Culver, R., et al. (2009). The estimated signal parameter detector: Incorporating signal parameter statistics into the signal processor. *Oceanic Engineering, IEEE Journal of*, 34(2):128–139.

Beckers, J. (1993). Adaptive optics for astronomy-principles, performance, and applications. *Annual review of astronomy and astrophysics*, 31:13–62.

Bensimon, D., Englander, A., Karoubi, R., and Weiss, M. (1981). Measurement of the probability of getting a lucky shortexposure image through turbulence. *The Journal of the Optical Society of America*, 71(9):1138–1139.

Bienvenu, G. and Kopp, L. (1983). Optimality of high resolution array processing using the eigensystem approach. *Acoustics, Speech and Signal Processing, IEEE Transactions on*, 31(5):1235–1248.

Blanc-Benon, P. (1981). *Effet d'une turbulence cinématique sur la propagation des ondes acoustiques*. PhD thesis.

Blanc-Benon, P. and Juvé, D. (1993). Intensity fluctuations of spherical acoustic waves propagating through thermal turbulence. *Waves in random media*, 3(2):71–83.

Booker, H., Ferguson, J., and Vats, H. (1985). Comparison between the extended-medium and the phase-screen scintillation theories. *Journal of atmospheric and terrestrial physics*, 47(4):381–399.

Boyce, F. (1975). Internal waves in the straits of gibraltar. In *Deep Sea Research and Oceanographic Abstracts*, volume 22, pages 597–610. Elsevier.

Briggs, B. and Parkin, I. (1963). On the variation of radio star and satellite scintillations with zenith angle. *Journal of Atmospheric and Terrestrial Physics*, 25(6):339–366.

Brühl, M., Vermeer, G., and Kiehn, M. (1996). Fresnel zones for broadband data. *Geophysics*, 61(2):600–604.

Bucker, H. (1976). Use of calculated sound fields and matched-field detection to locate sound sources in shallow water. *The Journal of the Acoustical Society of America*, 59(2):368–373.

Buckley, R. (1975). Diffraction by a random phase-changing screen: A numerical experiment. *Journal of Atmospheric and Terrestrial Physics*, 37(11):1431–1446.

Buffington, A., Crawford, F., Muller, R., Schwemin, A., and Smits, R. (1977). Correction of atmospheric distortion with an image-sharpening telescope. *JOSA*, 67(3):298–303.

Calvo, D., Canepa, G., Soukup, R., Kunz, E., Sessarego, J.-P., and Rudd, K. (2008). Benchmarking of computational scattering models using underwater acoustic data from a corrugated wax slab. *The Journal of the Acoustical Society of America*, 123(5):3602–3602.

Campanella, S. and Favret, A. (1969). Time autocorrelation of sonic pulses propagated in a random medium. *The journal of the Acoustical Society of America*, 46(5B):1234–1245.

Carey, W. (1998). The determination of signal coherence length based on signal coherence and gain measurements in deep and shallow water. *The Journal of the Acoustical Society of America*, 104(2):831–837.

Carey, W., Lynch, J., Siegmann, W., Rozenfeld, I., and Sperry, B. (2006). Sound transmission and spatial coherence in selected shallow-water areas: Measurements and theory. *Journal of Computational Acoustics*, 14(02):265–298.

Chandrayadula, T., Colosi, J., Worcester, P., Dzieciuch, M., Mercer, J., Andrew, R. K., and Howe, B. (2013). Observations and transport theory analysis of low frequency, acoustic mode propagation in the eastern north pacific ocean. *The Journal of the Acoustical Society of America*, 134(4):3144–3160.

Chapman, R. and Harris, J. (1962). Surface backscattering strengths measured with explosive sound sources. *The Journal of the Acoustical Society of America*, 34(10):1592–1597.

Chotiros, N. and Smith, B. (1979). Sound amplitude fluctuations due to a temperature microstructure. *Journal of Sound and Vibration*, 64(3):349–369.

Collis, J., Duda, T., Lynch, J., and DeFerrari, H. (2008). Observed limiting cases of horizontal field coherence and array performance in a time-varying internal wavefield. *The Journal of the Acoustical Society of America*, 124(3):EL97–EL103.

Colosi, J., Chandrayadula, T., Voronovich, A., and Ostashev, V. (2013). Coupled mode transport theory for sound transmission through an ocean with random sound speed perturbations: Coherence in deep water environments. *The Journal of the Acoustical Society of America*, 134(4):3119–3133.

Colosi, J., Tappert, F., and Dzieciuch, M. (2001). Further analysis of intensity fluctuations from a 3252-km acoustic propagation experiment in the eastern north pacific ocean. *The Journal of the Acoustical Society of America*, 110(1):163–169.

Cotté, B. and Blanc-Benon, P. (2007). Estimates of the relevant turbulent scales for acoustic propagation in an upward refracting atmosphere. *Acta Acustica united with Acustica*, 93(6):944–958.

Cox, H. (1973a). Line array performance when the signal coherence is spatially dependent. *The Journal of the Acoustical Society of America*, 54(6):1743–1746.

Cox, H. (1973b). Resolving power and sensitivity to mismatch of optimum array processors. *The Journal of the acoustical society of America*, 54(3):771–785.

Creamer, D. (2006). On using polynomial chaos for modeling uncertainty in acoustic propagation. *The Journal of the Acoustical Society of America*, 119(4):1979–1994.

Cristol, X. (1996). Validation expérimentale de modèles de propagation. Unpublished technical report.

Cristol, X. (2005). Narcissus-2005: A global model of fading channel for application to acoustic communication in marine environment. In *Oceans 2005-Europe*, volume 1, pages 655–662. IEEE.

Cristol, X. (2008). Modeling the acoustic reflection on a rough interface with the simplified small slope approximation (simplified ssa). Unpublished technical report.

Cristol, X., Fattaccioli, D., and Couvrat, A.-S. (2012). Alternative criteria for sonar array-gain limits from linear internal waves. *Proceedings of the European Conference of Underwater Acoustics, Edimburgh, Scotland*.

Crowther, P. (1980). Acoustical scattering from near-surface bubble layers. In *Cavitation and Inhomogeneities in Underwater Acoustics*, pages 194–204. Springer.

Dahlen, F. and Baig, A. (2002). Fréchet kernels for body-wave amplitudes. *Geophysical Journal International*, 150(2):440–466.

Dashen, R., Flatté, S., Munk, W., Watson, K., and Zachariasen, F. (2010). *Sound transmission through a fluctuating ocean*. Cambridge University Press.

Dashen, R., Flatté, S., and Reynolds, S. (1985). Path-integral treatment of acoustic mutual coherence functions for rays in a sound channel. *The Journal of the Acoustical Society of America*, 77(5):1716–1722.

Del Grosso, V. and Mader, C. (1972). Speed of sound in pure water. *the Journal of the Acoustical Society of America*, 52(5B):1442–1446.

Derode, A., Roux, P., and Fink, M. (1995). Robust acoustic time reversal with high-order multiple scattering. *Physical review letters*, 75(23):4206.

Desaubies, Y. (1976). Analytical representation of internal wave spectra. *Journal of Physical Oceanography*, 6(6):976–981.

Dessler, A. (1966). *Solar wind and interplanetary magnetic field*. Department of Space Science, Rice University.

Dianis, S. and von Ramm, O. (2011). Harmonic source wavefront aberration correction for ultrasound imaging. *The Journal of the Acoustical Society of America*, 129(1):507–517.

Dobbins, P. (1989). *Degradation of Coherence of Acoustic Signals Resulting from Inhomogeneities in the Sea.* PhD thesis, University of Bath (UK).

Dobbins, P. (1994). ystèmes sous-marins. *Traitement du Signal*, 11(4).

Dungan, M. and Dowling, D. (2000). Computed narrow-band time-reversing array retrofocusing in a dynamic shallow ocean. *The Journal of the Acoustical Society of America*, 107(6):3101–3112.

Eckart, C. (1953). The scattering of sound from the sea surface. *The Journal of the Acoustical Society of America*, 25(3):566–570.

Ehrhardt, L., Cheinet, S., Juvé, D., and Blanc-Benon, P. (2013). Evaluating a linearized euler equations model for strong turbulence effects on sound propagation. *The Journal of the Acoustical Society of America*, 133(4):1922–1933.

Elfouhaily, T., Chapron, B., Katsaros, K., and Vandemark, D. (1997). A unified directional spectrum for long and short wind-driven waves. *Journal of Geophysical Research-Oceans*, 102(C7):15781–15796.

Esswein, R. and Flatté, S. (1980). Calculation of the strength and diffraction parameters in oceanic sound transmission. *The Journal of the Acoustical Society of America*, 67(5):1523–1531.

Esswein, R. and Flatté, S. (1981). Calculation of the phase-structure function density from oceanic internal waves. *The Journal of the Acoustical Society of America*, 70(5):1387–1396.

Evans, R. (1983). A coupled mode solution for acoustic propagation in a waveguide with stepwise depth variations of a penetrable bottom. *The Journal of the Acoustical Society of America*, 74(1):188–195.

Fattaccioli, D. (2015). Alma: a new experimental acoustic system to explore coastal waters. In *Proceedings of the 3rd Underwater Acoustic Conference, Chania, GREECE*, pages 1–6.

Fattaccioli, D., Cristol, X., Picard Destelan, G., and Danet, P. (2009). Sonar processing performance in random environments. In *Proceedings Of Underwater Acoustic Measurements (UAM 09), Nafplion, Greece, 21-26 June 2009*.

Finette, S. (2006). A stochastic representation of environmental uncertainty and its coupling to acoustic wave propagation in ocean waveguides. *The Journal of the Acoustical Society of America*, 120(5):2567–2579.

Flatté, S. (2002). Calculations of wave propagation through statistical random media, with and without a waveguide. *Optics express*, 10(16):777–804.

Flatte, S. (1983). Wave propagation through random media: Contributions from ocean acoustics. *Proceedings of the IEEE*, 71(11):1267–1294.

Flatté, S. (1986). The schrödinger equation in classical physics. *American Journal of Physics*, 54(12):1088–1092.

Flatté, S., Reynolds, S., Dashen, R., Buehler, B., and Maciejewski, P. (1987). Afar measurements of intensity and intensity moments. *The Journal of the Acoustical Society of America*, 82(3):973–980.

Flatté, S. and Rovner, G. (2000). Calculations of internal-wave-induced fluctuations in ocean-acoustic propagation. *The Journal of the Acoustical Society of America*, 108(2):526–534.

Flatté, S. and Stoughton, R. (1988). Predictions of internal-wave effects on ocean acoustic coherence, travel-time variance, and intensity moments for very long-range propagation. *The Journal of the Acoustical Society of America*, 84(4):1414–1424.

Flatté, S. and Tappert, F. (1975). Calculation of the effect of internal waves on oceanic sound transmission. *The Journal of the Acoustical Society of America*, 58(6):1151–1159.

Flatté, S. and Vera, M. (2003). Comparison between ocean-acoustic fluctuations in parabolic-equation simulations and estimates from integral approximations. *The Journal of the Acoustical Society of America*, 114(2):697–706.

Frankenthal, S., Whitman, A., and Beran, M. (1984). Two-scale solutions for intensity fluctuations in strong scattering. *The Journal of the Acoustical Society of America*, 75(S1):S51–S51.

Freedman, D. and Diaconis, P. (1981). On the histogram as a density estimator: L 2 theory. *Probability theory and related fields*, 57(4):453–476.

Fried, D. (1966). Optical resolution through a randomly inhomogeneous medium for very long and very short exposures. *Journal of the Optical Society of America*, 56(10):1372–1379.

Frisk, G. V. (1994). *Ocean and seabed acoustics: a theory of wave propagation*. Pearson Education.

Fugate, R., Spinhirne, J., Moroney, J., Cleis, R., Oliker, M., Boeke, B., Ellerbroek, B., Higgins, C., Ruane, R., Swindle, D., et al. (1994). Two generations of laser-guide-star adaptive-optics experiments at the starfire optical range. *Journal of the Optical Society of America*, 11(1):310–324.

Garrett, C. and Munk, W. (1972). Space-time scales of internal waves. *Geophysical & Astrophysical Fluid Dynamics*, 3(1):225–264.

Garrett, C. and Munk, W. (1975). Space-time scales of internal waves: A progress report. *Journal of Geophysical Research*, 80(3):291–297.

Gaskill, J. (1978). *Linear systems, Fourier transforms, and optics*. Wiley New York.

Gladysz, S. and Christou, J. (2008a). Detection of faint companions through stochastic speckle discrimination. *The Astrophysical Journal*, 684(2):1486.

Gladysz, S. and Christou, J. (2008b). Detection of faint companions through stochastic speckle discrimination. *The Astrophysical Journal*, 684(2):1486.

Gladysz, S. and Christou, J. C. (2009). Reference-less detection, astrometry, and photometry of faint companions with adaptive optics. *The Astrophysical Journal*, 698(1):28.

Gladysz, S., Gallé, R., Christou, J., and Roberts Jr, L. (2010). Differential photometry in adaptive optics imaging. In *Advanced Maui Optical and Space Surveillance Technologies Conference*, volume 1, page 24.

Gorodetskaya, E., Malekhanov, A., Sazontov, A., Vdovicheva, N., et al. (1999). Deep-water acoustic coherence at long ranges: Theoretical prediction and effects on large-array signal processing. *Oceanic Engineering, IEEE Journal of*, 24(2):156–171.

Gosling, J., Baker, D., Bame, S., Feldman, W., Zwickl, R., and Smith, E. (1987). Bidirectional solar wind electron heat flux events. *Journal of Geophysical Research: Space Physics (1978–2012)*, 92(A8):8519–8535.

Graham, W. (1979). *The Coherence of Acoustic Signals in the Ocean and Application to the Design of Very Large Arrays*. PhD thesis.

Graham, W. (1982). The multipath coherence function for uncorrelated underwater channels. *The Journal of the Acoustical Society of America*, 72(3):908–915.

Graham, W. (1993). Spatio-temporal scale assessment of an "upwelling shadow" in northern monterey bay, california. *Estuaries*, 16(1):83–91.

Hemingway, E. (1963). *The old man and the sea*, volume 7. Kiddy Monster Publication.

Hinkelman, L., Liu, D.-L., Metlay, L., and Waag, R. (1994). Measurements of ultrasonic pulse arrival time and energy level variations produced by propagation through abdominal wall. *The Journal of the Acoustical Society of America*, 95(1):530–541.

Hippler, S., Hormuth, F., Butler, D., Brandner, W., and Henning, T. (2006). Atmosphere-like turbulence generation with surface-etched phase-screens. *Optics express*, 14(22):10139–10148.

Hodgkiss, W., Song, H., Kuperman, W., Akal, T., Ferla, C., and Jackson, D. (1999). A long-range and variable focus phase-conjugation experiment in shallow water. *The Journal of the Acoustical Society of America*, 105(3):1597–1604.

Hufnagel, R. (1966). Restoration of atmospherically degraded images. *National Academy of Sciences-National Research Council*, 3:11.

Ishimaru, A. (1978). *Wave propagation and scattering in random media*, volume 2. Academic press New York.

Jackson, D., Briggs, K., Williams, K., and Richardson, M. (1996). Tests of models for high-frequency seafloor backscatter. *Oceanic Engineering, IEEE Journal of*, 21(4):458–470.

Jackson, D., Winebrenner, D., and Ishimaru, A. (1986). Application of the composite roughness model to high-frequency bottom backscattering. *The Journal of the Acoustical Society of America*, 79(5):1410–1422.

Jensen, F., Kuperman, W., Porter, M., and Schmidt, H. (2011). *Computational ocean acoustics*. Springer Science & Business Media.

Jin, Y. and Friedlander, B. (2004). Detection of distributed sources using sensor arrays. *Signal Processing, IEEE Transactions on*, 52(6):1537–1548.

Kim, S., Kuperman, W., Hodgkiss, W., Song, H., Edelmann, G., and Akal, T. (2003). Robust time reversal focusing in the ocean. *The Journal of the Acoustical Society of America*, 114(1):145–157.

Kinsler, L., Frey, A., Coppens, A., and Sanders, J. (1999). *Fundamentals of acoustics*. Wiley - VCH.

Knapp, R. (1991). Fresnel zones in the light of broadband data. *Geophysics*, 56(3):354–359.

Kolmogorov, A. N. (1941). Dissipation of energy in locally isotropic turbulence. In *Dokl. Akad. Nauk SSSR*, volume 32, pages 16–18.

Kuperman, W., Cornuelle, B., Hodgkiss, W., and Roux, P. (2012). Group speed versus phase speed analysis of sound speed fluctuations in a shallow water ocean. *The Journal of the Acoustical Society of America*, 131(4):3450–3450.

Kuperman, W., Hodgkiss, W., Song, H., Akal, T., Ferla, C., and Jackson, D. (1998). Phase conjugation in the ocean: Experimental demonstration of an acoustic time-reversal mirror. *The journal of the Acoustical Society of America*, 103(1):25–40.

Kuperman, W. and Ingenito, F. (1977). Attenuation of the coherent component of sound propagating in shallow water with rough boundaries. *The Journal of the Acoustical Society of America*, 61(5):1178–1187.

Kuperman, W. and Lynch, J. (2004). Shallow-water acoustics. *Physics Today*, 57(10):55–61.

Kuperman, W. and Schmidt, H. (1989). Self-consistent perturbation approach to rough surface scattering in stratified elastic media. *The Journal of the Acoustical Society of America*, 86(4):1511–1522.

Labeyrie, A. (1970). Attainment of diffraction limited resolution in large telescopes by fourier analysing speckle patterns in star images. *Astronomy and Astrophysics*, 6(1):85–87.

LaCasce Jr, E., Stone, R., and Mintzer, D. (1962). Frequency dependence of acoustic fluctuations in a randomly inhomogeneous medium. *Journal of Applied Physics*, 33(9):2710–2714.

Laval, R. and Labasque, Y. (1981). Medium inhomogeneities and instabilities: Effects on spatial and temporal processing. In *Underwater Acoustics and Signal Processing*, pages 41–70. Springer.

Leclere, J., Collins, M., and Del Balzo, D. (1997). Environmental impact on active-sonar performance predictions in shallow water. *The Journal of the Acoustical Society of America*, 101(5):3198–3198.

Lee, J., Joung, J., and Kim, J. (2008). A method for the direction-of-arrival estimation of incoherently distributed sources. *Vehicular Technology, IEEE Transactions on*, 57(5):2885–2893.

Levine, M. and Irish, J. (1981). A statistical description of temperature finestructure in the presence of internal waves. *Journal of Physical Oceanography*, 11(5):676–691.

Li, J. and Stoica, P. (2006). *Robust adaptive beamforming*. Wiley Online Library.

Li, W. and Preisig, J. (2007). Estimation of rapidly time-varying sparse channels. *Oceanic Engineering, IEEE Journal of*, 32(4):927–939.

Liang, J., Grimm, B., Goelz, S., and Bille, J. (1994). Objective measurement of wave aberrations of the human eye with the use of a hartmann–shack wave-front sensor. *Journal of the Optical Society of America*, 11(7):1949–1957.

Lorimer, D. and Kramer, M. (2005). *Handbook of pulsar astronomy*, volume 4. Cambridge University Press.

Mackay, C. (2013). High-efficiency lucky imaging. *Monthly Notices of the Royal Astronomical Society*, 432(1):702–710.

Mantravadi, S., Rhoadarmer, T., and Glas, R. (2004). Simple laboratory system for generating well-controlled atmospheric-like turbulence. In *Optical Science and Technology, the SPIE 49th Annual Meeting*, pages 290–300. International Society for Optics and Photonics.

Marquering, H., Dahlen, F., and Nolet, G. (1999). Three-dimensional sensitivity kernels for finite-frequency traveltimes: the banana-doughnut paradox. *Geophysical Journal International*, 137(3):805–815.

Marsh, H. W., Schulkin, M., and Kneale, S. (1961). Scattering of underwater sound by the sea surface. *The Journal of the Acoustical Society of America*, 33(3):334–340.

Massey, F. (1951). The kolmogorov-smirnov test for goodness of fit. *Journal of the American statistical Association*, 46(253):68–78.

Matthaeus, W. and Goldstein, M. (1982). Measurement of the rugged invariants of magnetohydrodynamic turbulence in the solar wind. *Journal of Geophysical Research*, 87:6011–6028.

McDaniel, S. (1993). Sea surface reverberation: A review. *The Journal of the Acoustical Society of America*, 94(4):1905–1922.

Metchev, S., Hillenbrand, L., and White, R. (2003). Adaptive optics observations of vega: eight detected sources and upper limits to planetary-mass companions. *The Astrophysical Journal*, 582(2):1102.

Morgan, D. and Smith, T. (1990). Coherence effects on the detection performance of quadratic array processors, with applications to large-array matched-field beamforming. *The Journal of the Acoustical Society of America*, 87(2):737–747.

Muller, R. and Buffington, A. (1974). Real-time correction of atmospherically degraded telescope images through image sharpening. *Journal of the Optical Society of America*, 64(9):1200–1210.

Munk, W. and Zachariasen, F. (1976). Sound propagation through a fluctuating stratified ocean: Theory and observation. *The Journal of the Acoustical Society of America*, 59(4):818–838.

Neil, M., Booth, M., and Wilson, T. (1998). Dynamic wave-front generation for the characterization and testing of optical systems. *Optics letters*, 23(23):1849–1851.

Newton, I. (1704). *Opticks*. Fourth Edition.

Oba, R. and Finette, S. (2002). Acoustic propagation through anisotropic internal wave fields: Transmission loss, cross-range coherence, and horizontal refraction. *The Journal of the Acoustical Society of America*, 111(2):769–784.

Ogden, P. and Erskine, F. (1992). An empirical prediction algorithm for low-frequency acoustic surface scattering strengths. Technical report, DTIC Document.

Papadakis, P., Taroudakis, M., Sturm, F., Sanchez, P., and Sessarego, J.-P. (2008). Scaled laboratory experiments of shallow water acoustic propagation: Calibration phase. *Acta Acustica united with Acustica*, 94(5):676–684.

Petit, C., Fusco, T., Sauvage, J., Sevin, A., Suarez, M., Charton, J., Baudoz, P., Beuzit, J., Buey, T., Dohlen, K., et al. (2011). Integration, tests and laboratory performance of saxo, the vlt-sphere extreme ao system. *AO for ELT,*.

Picinbono, B. (1995). On deflection as a performance criterion in detection. *Aerospace and Electronic Systems, IEEE Transactions on*, 31(3):1072–1081.

Platt, B. et al. (2001). History and principles of shack-hartmann wavefront sensing. *Journal of Refractive Surgery*, 17(5):S573–S577.

Primmerman, C., Murphy, D., Page, D., Zollars, B., and Barclay, H. (1991). Compensation of atmospheric optical distortion using a synthetic beacon. *Nature*, 353(6340):141–143.

Rampy, R., Gavel, D., Dillon, D., and Thomas, S. (2012). Production of phase screens for simulation of atmospheric turbulence. *Applied optics*, 51(36):8769–8778.

Real, G., Cristol, X., Habault, D., Sessarego, J.-P., and Fattaccioli, D. (2015a). Influence of decoherence effects on sonar array gain: scaled experiment, simulations and simplified theory comparison. In *Proceedings of the 3rd Underwater Acoustic Conference, Chania, GREECE*, pages 1–6.

Real, G., Cristol, X., Habault, D., Sessarego, J.-P., and Fattaccioli, D. (2015b). Rafal: Random faced acoustic lens used to model internal waves effect on underwater acoustic propagation. In *Proceedings of the 3rd Underwater Acoustic Conference, Chania, GREECE*, pages 1–6.

Real, G., Cristol, X., Sessarego, J.-P., and Fattaccioli, D. (2014a). Propagation of acoustic waves through a spatially fluctuating medium: theoretical study of the physical phenomena. In *Proceedings of the 2nd Underwater Acoustic Conference, Rhodes, GREECE*, pages 20–26.

Real, G., Sessarego, J.-P., Cristol, X., and Fattaccioli, D. (2013). Experimental study of the influence of spatial inhomogeneities in underwater acoustic propagation. In *Proceedings of the 1st Underwater Acoustic Conference, Corfu, GREECE*, pages 23–28.

Real, G., Sessarego, J.-P., Cristol, X., and Fattaccioli, D. (2014b). De-coherence effects in underwater acoustics: scaled experiments. In *Proceedings of the 2nd Underwater Acoustic Conference, Rhodes, GREECE*, pages 20–26.

Reynolds, S., Flatté, S., Dashen, R., Buehler, B., and Maciejewski, P. (1985). Afar measurements of acoustic mutual coherence functions of time and frequency. *The Journal of the Acoustical Society of America*, 77(5):1723–1731.

Rhoadarmer, T., Angel, J., et al. (2001). Low-cost, broadband static phase plate for generating atmosphericlike turbulence. *Applied Optics*, 40(18):2946–2955.

Rickett, B. (1977). Interstellar scattering and scintillation of radio waves. *Annual review of astronomy and astrophysics*, 15:479–504.

Rickett, B. (1990). Radio propagation through the turbulent interstellar plasma. *Annual review of astronomy and astrophysics*, 28:561–605.

Robert, J.-L. and Fink, M. (2008). Green's function estimation in speckle using the decomposition of the time reversal operator: Application to aberration correction in medical imaging. *The Journal of the Acoustical Society of America*, 123(2):866–877.

Rouseff, D., Turgut, A., Wolf, S., Finette, S., Orr, M., Pasewark, B., Apel, J., Badiey, M., Chiu, C.-S., Headrick, R., et al. (2002). Coherence of acoustic modes propagating through shallow water internal waves. *The Journal of the Acoustical Society of America*, 111(4):1655–1666.

Roux, P., Iturbe, I., Nicolas, B., Virieux, J., and Mars, J. (2011). Travel-time tomography in shallow water: Experimental demonstration at an ultrasonic scale. *The Journal of the Acoustical Society of America*, 130(3):1232–1241.

Roux, P., Kuperman, W., Cornuelle, B., Aulanier, F., Hodgkiss, W., and Song, H. (2013). Analyzing sound speed fluctuations in shallow water from group-velocity versus phase-velocity data representation. *The Journal of the Acoustical Society of America*, 133(4):1945–1952.

Schmidt, R. (1986). Multiple emitter location and signal parameter estimation. *Antennas and Propagation, IEEE Transactions on*, 34(3):276–280.

Schwiegerling, J. and Neal, D. (2005). Historical development of the shack-hartmann wavefront sensor. *Robert Shannon and Roland Shack: Legends in Applied Optics, edited by JE Harvey and RB Hooker—SPIE, Bellingham, WA*, pages 132–139.

Sears, F. (1949). *Optics*. Addison Wesley Publishing Company (not provided).

Sederowitz, W. and Favret, A. (1969). Covariance between acoustic signals traveling diverging paths in a random medium. *The Journal of the Acoustical Society of America*, 45(2):386–391.

Skarsoulis, E. and Cornuelle, B. (2004). Travel-time sensitivity kernels in ocean acoustic tomography. *The Journal of the Acoustical Society of America*, 116(1):227–238.

Sommerfeld, A. (1912). Die greensche funktionen der schwingungsgleichung. *Jahresber. Deutsch. Math. Verein.*, 21:309–353.

Song, H., Hodgkiss, W., Kuperman, W., Stevenson, M., and Akal, T. (2006). Improvement of time-reversal communications using adaptive channel equalizers. *Oceanic Engineering, IEEE Journal of*, 31(2):487–496.

Spetzler, J. and Snieder, R. (2004). The fresnel volume and transmitted waves. *Geophysics*, 69(3):653–663.

Stone, R. and Mintzer, D. (1962). Range dependence of acoustic fluctuations in a randomly inhomogeneous medium. *The Journal of the Acoustical Society of America*, 34(5):647–653.

Stone, R. and Mintzer, D. (1965). Transition regime for acoustic fluctuations in a randomly inhomogeneous medium. *The Journal of the Acoustical Society of America*, 38(5):843–846.

Strohbehn, J., Wang, T., and Speck, J. (1975). On the probability distribution of line-of-sight fluctuations of optical signals. *Radio Science*, 10(1):59–70.

Svet, V. (2014). Acoustical imaging in heterogeneous environments. *Advances in Signal Processing*, 2(2):29–45.

Tang, D., Moum, J., Lynch, J., Abbot, P., Chapman, R., Dahl, P., Duda, T., Gawarkiewicz, G., Glenn, S., Goff, J., et al. (2007). Shallow water'06: A joint acoustic propagation/nonlinear internal wave physics experiment.

Tatarskii, V. (1971). *The Effects of the Turbulent Atmosphere on Wave Propagation*. National Technical Information Servie, Springfield, VA.

Texereau, J. (1948). La construction du télescope d'amateur. *L'Astronomie*, 62:257–264.

Tielbürger, D., Finette, S., and Wolf, S. (1997). Acoustic propagation through an internal wave field in a shallow water waveguide. *The Journal of the Acoustical Society of America*, 101(2):789–808.

Tychensky, A. and Carton, X. (1998). Hydrological and dynamical characterization of meddies in the azores region: a paradigm for baroclinic vortex dynamics. *Journal of Geophysical Research: Oceans (1978–2012)*, 103(C11):25061–25079.

Urick, R. (1973). Measurements of the vertical coherence of the sound from a near-surface source in the sea and the effect on the gain of an additive vertical array. *The Journal of the Acoustical Society of America*, 54(1):115–120.

Van Trees, H. (2004). *Detection, estimation, and modulation theory*. John Wiley & Sons.

Vera, M. (2007). Comparison of ocean-acoustic horizontal coherence predicted by path-integral approximations and parabolic-equation simulation results. *The Journal of the Acoustical Society of America*, 121(1):166–174.

Voronovich, A. (2012). *Wave scattering from rough surfaces*, volume 17. Springer Science & Business Media.

Voronovich, A. and Ostashev, V. (2006). Low-frequency sound scattering by internal waves in the ocean. *The Journal of the Acoustical Society of America*, 119(3):1406–1419.

Waite, A. (2001). *SONAR for Practicing Engineers, Hoboken*. NJ: Wiley.

Wilcox, C., Andrews, J., Restaino, S., and Martinez, T. (2007). Atmospheric turbulence generator using a liquid crystal spatial light modulator. In *Aerospace Conference, 2007 IEEE*, pages 1–8. IEEE.

Wilson, D. (1998). Performance bounds for acoustic direction-of-arrival arrays operating in atmospheric turbulence. *The Journal of the Acoustical Society of America*, 103(3):1306–1319.

Wilson, H. and Tappert, F. (1979). Acoustic propagation in random oceans using the radiation transport equation. *The Journal of the Acoustical Society of America*, 66(1):256–274.

Wilson, R., Wooder, N., Rigal, F., and Dainty, J. (2003). Estimation of anisoplanatism in adaptive optics by generalized scidar profiling. *Monthly Notices of the Royal Astronomical Society*, 339(2):491–494.

Wolf, D. (1975). Propagation regimes for turbulent atmospheres. *Radio Science*, 10(1):53–57.

Wu, R.-S. and Aki, K. (1988). Multiple scattering and energy transfer of seismic waves—separation of scattering effect from intrinsic attenuation ii. application of the theory to hindu kush region. *Pure and Applied Geophysics*, 128(1-2):49–80.

Yang, T. (2008). Temporal coherence of sound transmissions in deep water revisited. *The Journal of the Acoustical Society of America*, 124(1):113–127.

Yang, T. and Yoo, K. (1999). Internal wave spectrum in shallow water: Measurement and comparison with the garrett-munk model. *Oceanic Engineering, IEEE Journal of*, 24(3):333–345.

Zank, G. (1999). Interaction of the solar wind with the local interstellar medium: A theoretical perspective. *Space Science Reviews*, 89(3-4):413–688.

Zhou, J.-X., Zhang, X.-Z., Peng, Z., and Martin, J. (2007). Sea surface effect on shallow-water reverberation. *The Journal of the Acoustical Society of America*, 121(1):98–107.

Zhu, Q. and Steinberg, B. (1992). Large-transducer measurements of wavefront distortion in the female breast. *Ultrasonic Imaging*, 14(3):276–299.

Publications associated with the dissertation topic.

- **Refereed academic journals**:
  - G. Real, D. Habault, X. Cristol, J.-P. Sessarego and D. Fattaccioli, "Ultrasonic test-bench for emulating the degradation of sonar performance in random ocean", *in prep.*
  - G. Real, D. Habault, X. Cristol, J.-P. Sessarego and D. Fattaccioli, "Dimensional analysis adapted to scaled experiments in underwater acoustics", *in prep.*
- **International peer reviewed conference proceedings**:
  - G. Real, X. Cristol, D. Habault, J.-P. Sessarego and D. Fattaccioli, "Influence of de-coherence effects on sonar array gain: scaled experiments, simulations and simplified theory comparison", *Proc. of the 3rd Underwater Acoustic Conference and Exhibition, June 2015, Chania, Greece.*
  - G. Real, X. Cristol, D. Habault, J.-P. Sessarego and D. Fattaccioli, "RAFAL: RAndom Faced Acoustic Lens used to model internal waves effects on underwater acoustic propagation", *Proc. of the 3rd Underwater Acoustic Conference and Exhibition, June 2015, Chania, Greece.*
  - G. Real, J.-P. Sessarego, X. Cristol and D. Fattaccioli, "De-coherence effects in underwater acoustics: scaled experiments", *Proc. of the 2nd Underwater Acoustic Conference and Exhibition, June 2014, Rhodes, Greece.*
  - G. Real, X. Cristol, J.-P. Sessarego and D. Fattaccioli, "Propagation of acoustic waves through a spatially fluctuating medium: theoretical study of the physical phenomena", *Proc. of the 2nd Underwater Acoustic Conference and Exhibition, June 2014, Rhodes, Greece.*
  - G. Real, J.-P. Sessarego, X. Cristol and D. Fattaccioli, "Experimental study of the influence of spatial inhomogeneities in underwater acoustic propagation", *Proc. of the 1st Underwater Acoustic Conference and Exhibition, June 2013, Corfu, Greece.*
- **National conference communications**:
  - G. Real, D. Habault, X. Cristol and D. Fattaccioli, "Dimensional analysis adapted to scaled experiments", *Congrès Français de Mécanique, August 2015, Lyon, France.*
  - G. Real, "Comprendre les Fluctuations Océaniques pour Améliorer la Détection des Sonars", *Poster and Experimental Demonstration, 19 Nov. 2014, Forum DGA Innovation, École Polytechnique, Palaiseau, France.*
  - G. Real, X. Cristol, J.-P. Sessarego, D. Habault and D. Fattaccioli, "Décohérence des Signaux Marin en Milieu Marin Fluctuant", *Workshop SERENADE, 3-5 Nov. 2014, GIPSA-Lab, Grenoble, FRANCE.*

– G. Real, J.-P. Sessarego, X. Cristol and D. Fattaccioli, "Etude théorique et expérimentale de la décohérence spatiale des signaux acoustiques en milieu marin fluctuant", *Journée d'Acoustiques et Applications Navales (JAAN), 8-9 Oct. 2013, Nice, FRANCE.*

- **Awards**:

  – *Young Scientist Award for the Best Paper Presented by a Graduate Student*, committee: Dr. Mike Buckingham, Dr. David Bradley and Dr. Michael Taroudakis, 2nd Underwater Acoustic Conference and Exhibition, June 2014, Rhodes, Greece.

Title - An ultrasonic testbench for reproducing the degradation of sonar performance in a fluctuating ocean 1.2

Abstract - This thesis focuses on wave propagation in random media. Especially, the ocean medium is subject to many sources of fluctuations. The most critical ones were found to be internal waves, occurring frequently and inducing fluctuations of the spatial distribution of the sound speed field. Because of the fairly long period of this phenomenon as compared to the propagation time of acoustic waves for sonar applications (typically for frequencies of 1 to 15 kHz and propagation ranges of 1 to 10 km), the process can be considered frozen in time for each stochastic realization of the medium. The intrinsic objective of this project is to develop and benchmark corrective signal processing techniques allowing to mitigate the degradation of performance induced by the medium fluctuations. The development of testbenches allowing to reproduce the effect of atmospheric turbulence on optic waves propagation under laboratory conditions lead to considerable advancements in the field of adaptive optics. We therefore see a vivid interest in being able to reproduce the effects of internal waves on sound propagation in controlled environments. An experimental protocol in a water tank is proposed: an ultrasonic wave is transmitted through a randomly rough acoustic lens, producing distortions of the received wavefront. The induced signal fluctuations are controlled by tuning the statistical parameters of the roughness of the lens. Especially, they are linked to dimensional parameters allowing to classify the configurations into regimes of fluctuations and to predict the statistical moment of the acoustic pressure up to the fourth order. A remarkable relevance of our experimental scheme is found when compared to theoretical and simulation results. The degradation of classical signal processing techniques when applied to our acquired data highlights the need for corrective detection techniques. A review of the existing techniques in other domains is proposed.

Keywords - loss of coherence, ocean fluctuations, tank experiment, dimensional analysis, detection performance.